UNIVERSITEIT VAN PRETORIA
UNIVERSITY OF PRETORIA
YUNIBESITHI YA PRETORIA

Finite Element Developments and Applications in Structural Topology Optimization

by

Craig Stephen Long

Submitted in partial fulfilment of the requirements for the degree

Philosophiae Doctor (Mechanical Engineering)

in the Faculty of Engineering, Built Environment and Information Technology, University of Pretoria, Pretoria

July 2007

Summary

Title:	Finite element developments and applications in structural topology optimization
Author:	Craig Stephen Long
Supervisor:	Prof. A.A. Groenwold
Co-supervisor:	Dr. P.W. Loveday
Department:	Department of Mechanical Engineering
Degree:	Philosophiae Doctor (Mechanical Engineering)
Keywords:	Finite element; piezoelectric; drilling degrees of freedom; reduced numerical integration; topology optimization; one-node hinge; checkerboard; compliant mechanism

In this two-part study, developments in finite element technology and the application thereof to topology optimization are investigated. Ultimately, the developed finite elements and corresponding topology optimization procedures are aimed at, but not restricted to, aiding the design of piezoelectrically driven compliant mechanisms for micropositioning applications. The objective is to identify and exploit existing, or to develop new, finite element technologies to alleviate the numerical instabilities encountered in topology optimization. Checkerboarding and one-node connected hinges are two commonly encountered examples which can directly be attributed to inadequacies or deficiencies in the finite element solution of structural problems using 4-node bilinear isoparametric finite elements (denoted Q4). The numerical behaviour leading to checkerboard layouts stems from an over-stiff estimation of a checkerboard patch of Q4 elements. The numerical model of a one-node connected hinge using Q4 elements, on the other hand, possesses no (or very little) stiffness in rotation about the common node.

In the *first* part of the study, planar finite elements with in-plane rotational (drilling) degrees of freedom are investigated. It is shown that the skew-symmetric part of the stress tensor can directly be used to quantitatively assess the validity of the penalty parameter γ, which relates the in-plane translations to the rotations. Thereafter, the variational formulations used to develop these planar finite elements with drilling degrees of freedom are extended to account for the piezoelectric effect. Several new piezoelectric elements that include in-plane rotational degrees of freedom (with and without assumed stress and electric flux density) are implemented, evaluated and shown to be accurate and stable.

Furthermore, the application of alternative reduced order integration schemes to quadratic serendipity (Q8) and Lagrangian (Q9) elements is investigated. Reduced or selective reduced integration schemes are often used to enhance element accuracy by 'softening' higher order deformation modes. However, application of reduced integration schemes to Q8 and Q9 elements is usually accompanied by element rank deficiencies. It is shown how the application of five and eight point modified integration schemes preserve the accuracy benefits of reduced integration, while preventing element rank deficiencies.

In the *second* part of the investigation, the salient features of elements with drilling degrees are utilized in two schemes to prevent, or improve the modelling of, one-node connected hinges. In principle, the first scheme uses the rotations computed at interior nodes to detect excessive rotations at suspect nodes. The second scheme essentially replaces planar elements forming a one-node hinge, where appropriate, with a more realistic beam model of the material layout while other elements in the mesh are modelled using planar elements as usual.

Next, the dependence of optimal topologies on element formulation is demonstrated. Attention is especially paid to plate and shell applications. It is shown that Mindlin-Reissner based elements, which employ selective reduced integration on shear terms, are not reliable in topology optimization problems. Conversely, elements based on an assumed natural strain formulation are shown to be stable and capable of reproducing thin plate topology results computed using shear-rigid elements. Furthermore, it is shown that an *ad hoc* treatment of rotational degrees of freedom in shell problems is sensitive to the related adjustable parameter, whereas optimal topologies, using a proper treatment of drilling degrees of freedom are not.

Finally, the use of reduced order integration schemes as a strategy to reduce the stiffness of a checkerboard patch of elements is considered. It is demonstrated that employing the five and eight point integration schemes, used to enhance the accuracy of Q8 and Q9 elements, also significantly reduce the stiffness of a checkerboard patch of elements, thereby reducing the probability of observing checkerboard layouts in optimal topologies.

Acknowledgements

It is my great pleasure and a tremendous honour to be able to acknowledge all the wonderful people who have contributed to the completion of this thesis. Looking back over the years I have spent at university, I can only now fully appreciate how privileged I have been to have received so much support and encouragement in perusing my interests.

Firstly to my Ph.D. supervisor, Prof. Albert Groenwold, I wish to extend my immeasurable thanks and appreciation for the enthusiasm, patients, encouragement, advice and wisdom, which you have so generously shared during the years we have worked together. It has been a real education, not only in structural optimisation, but in life. Thank you for being my guide on this adventure. I sincerely hope that our paths will cross frequently!

I would also like to thank my co-supervisor, Dr. Philip Loveday for the faith you have shown in me, and for the patience you exercised in the time while I was completing my write-up. Thanks also for the dedication and vigour with which you have approached each undertaking I have consulted you on. I am grateful to be working with you now, and hope to do so for many years to come.

I would also like to express my gratitude to the faculty of the Department of Mechanical Engineering at the University of Pretoria who have helped shape my life. I would especially like to acknowledge Prof. Jan Snyman, not only for the technical guidance you have provided during my Masters and Ph.D. studies, but for brightening up life with the many colourful tales of your travels and other exploits. It has been an honour to have known you. Also, to Prof. Schalk Kok who was always willing to share his seemingly boundless knowledge. Thank you. Also, to my friends and colleagues at CSIR, thank you for your support and encouragement over the past year and a half.

To the Structural Optimization Research Group (SORG), and some honorary members, especially Albert, Schalk, Nico, Carl, Cheng, Derren, Lize, Antoinette, Michael, Sannelie, Christiaan, Gerhard, Jaco and Neo. Also, to all my friends especially Justin and Jonathan. The heated debates over a cup of steaming coffee, the cheap beer from various establishments in Hatfield, working together on assignments until late, stories of weekend adventures, chess and go tournaments, etc. are what made my varsity days the best of my life. Thank you for sharing in my life and for letting me share in yours.

Financial support provided by

- the South African National Research Foundation (NRF), who provided funding via the THRIP initiative (project number 2769), as well as general studentship funding,
- the Council for Scientific and Industrial Research (CSIR), and
- the University of Pretoria,

is most gratefully acknowledged.

Thanks go also to Prof. Krister Svanberg, for supplying me with his MMA implementation.

I would also like to acknowledge my family-in-law. Mr. and Mrs. Bredenkamp, thank you for letting me stay with you for so long and for treating me like a son. Also to Louis and Janine, thank you for making me part of your family. Lastly, but certainly not least, I would like to thank my family. Thank you Mom and Dad for all the sacrifices you've made to give your children every opportunity to succeed. Thanks also to my brothers, Mark, Gavin and Anthony and to my sister Sharon, and family, for always being there during the tough times and for supporting all my ventures. I love you all!

To **Michele**, my wife, my love and my best friend.

> Let me not to the marriage of true minds
> Admit impediments. Love is not love
> Which alters when it alteration finds,
> Or bends with the remover to remove.
> O no, it is an ever fixed mark
> That looks on tempests and is never shaken;
> It is the star to every wand'ring barque,
> Whose worth's unknown although his height be taken.
> Love's not time's fool, though rosy lips and cheeks
> Within his bending sickle's compass come;
> Love alters not with his brief hours and weeks,
> But bears it out even to the edge of doom.
> If this be error and upon me proved,
> I never writ, nor no man ever loved.
>
> – William Shakespeare

Shell, these words are as true now as they were the day I first recited them to you, over 13 years ago. I truly love you and I dedicate this thesis to you.

Contents

List of Figures

List of Tables

Chapter 1

Introduction

The analysis of modern designs and systems is becoming ever more complex. Closed form analytical solutions to problems, although extremely important, are often limited to relatively simple geometries or restricted to specific loadings, and are therefore difficult to generalise to industrial applications. For some time now numerical solution techniques, implemented on digital computers, have been an invaluable tool in the analysis of complex physical problems. Indeed, commercial, general purpose, finite element analysis (FEA) and computational fluid dynamics (CFD) software are now commonplace in the engineering community.

Although numerical methods are commonly used commercially in the *analysis* of mechanical designs, they are often not fully exploited in the *design process* itself. Generally this process starts with the designer conceiving an initial concept design which is analysed, possibly using numerical methods, and the results are judged based on predetermined objectives or criteria. If the design is not satisfactory the designer then, based on past experience, predicts an improved design. This process is repeated until a satisfactory design is found, upon which the process is terminated. Some of the disadvantages of such a procedure include:

- There is no guarantee that the design is optimal, or even good, although it satisfies the prescribed requirements. That is to say, unknown to the designer, significant improvements may still be possible.
- The process relies on the experience of the designer (and often trial-and-error) to predict design improvements. This process may not be systematic, and in fact the designer's intuition or experience could at times be misleading.
- The process is not repeatable, and is difficult to describe as a fixed procedure. If a designer gains experience with a given problem, it is would take a significant effort to pass this experience on, or document a procedure, to repeatably come up with a good design for similar problems.

Structural optimization holds the potential to improve upon or optimize designs conceived by designers in a *systematic*, *repeatable* manner. Furthermore, using structural topology optimization, the design process itself can largely be described and automated[1]. Structural

[1]Within reason and for specific components only.

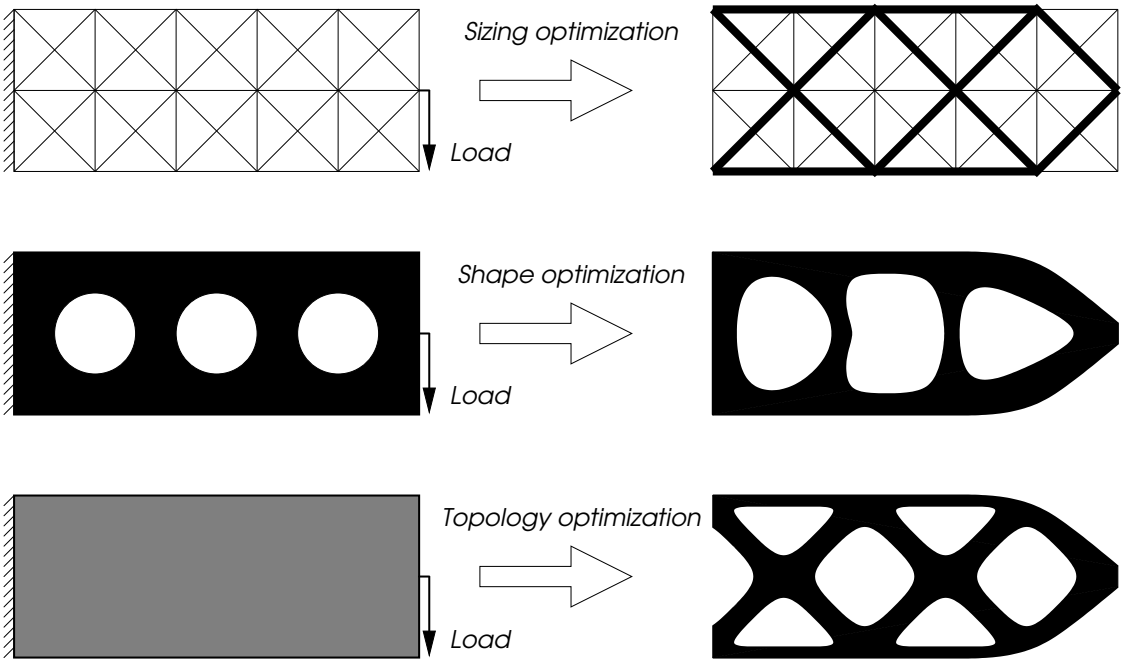

Figure 1.1: Three categories of structural optimization. Initial design and problem description on the left, optimal designs on the right. Note that optimal designs in this figure are for illustrative purposes only.

optimization is therefore an important tool which can assist in finding not only good, but *optimal* solutions to structural design problems.

1.1 Structural topology optimization

Structural optimization seeks to find the *best* design (out of all possible designs) which is capable of satisfying a number of prescribed criteria. The measure of how good the design is and the criteria which the design is required to fulfil are usually conflicting. A simple example of such a problem is to determine the stiffest possible structure, under given loading and support conditions, such that the weight of the structure is limited. The requirements are conflicting because physically the more material the structure contains, the stiffer it will generally be, but the heavier it becomes.

Broadly speaking, structural optimization problems can be classified into one of three categories, namely *sizing*, *shape* or *topology* optimization. These three classes are schematically depicted in Figure 1.1.

Sizing optimization generally uses truss or grillage member cross-sectional areas, or membrane, plate or shell component thicknesses as design variables in the optimization process. More specifically, in sizing optimization problems the shape and topology of the design analysis domain considered are fixed, and do not change during the optimization process, as shown in Figure 1.1. Therefore, if a finite element model is used, the nodes remain in fixed positions throughout the process.

On the other hand, shape optimization generally involves finding the analysis domain shape which optimally performs a given function, subject to certain constraints. The design domain is usually determined parametrically by the design variables. If gradient based optimization methods are employed, considerable difficulties would be encountered if holes were to merge during the process, and it is certainly not a trivial task to determine the effect of adding or removing holes *a priori*, or indeed to determine *where* to introduce additional holes if necessary. Therefore, during this process the topology is generally fixed. For example, in the shape optimization illustration in Figure 1.1, the starting design has three holes and the final design also has three holes.

Finally, topology optimization can be considered the most general type of structural optimization. In topology optimization, the optimal boundary and connectivity, as well as the optimal size, shape, location and number of features (including holes) in an analysis domain are sought. Topology optimization is therefore also sometimes referred to as generalised shape or layout optimization.

These classes of problems can be combined in procedures to exploit the advantages of the different techniques. For example, some authors have combined shape and topology optimization to take advantage of the salient features of both classes simultaneously, especially in the design of generally curved shell structures [1, 2]. In this work, however, attention is exclusively focused on the topology optimization problem.

Furthermore, the optimization of low volume fraction, inherently discrete, structures (such as truss structures) is not considered, and attention is focused on continuum structural problems only. Having said that, much of the theory and many techniques employed in the optimization of continuum structures are derived from the topology optimization of truss and grillage problems, see [3, 4] for examples. Furthermore, many of the difficulties encountered are similar, for example singularity problems with stress constraints [4, 5, 6, 7].

The iterative process of structural topology optimization used in this study is schematically depicted in Figure 1.2. In the remainder of this section, an informal description of the process is presented in more detail for readers unfamiliar with the process.

Initial design and design parameterization

The first step in the process is to select an initial or starting design. This design could be based on the experience of the designer, but could also simply be randomly selected within a given design domain or could be the result of a previous (more general) optimization procedure.

At this stage the parameters that describe the design, and which will be allowed to change during the process (the *design variables*, $\boldsymbol{x}$) are defined. The initial design is accordingly described by an initial design vector $\boldsymbol{x}^0$. The type of parameterization chosen will dictate (or is dictated by) the type or category of structural optimization that is employed. The design variables used in topology optimization typically describe the material distribution within the design domain using a density function.

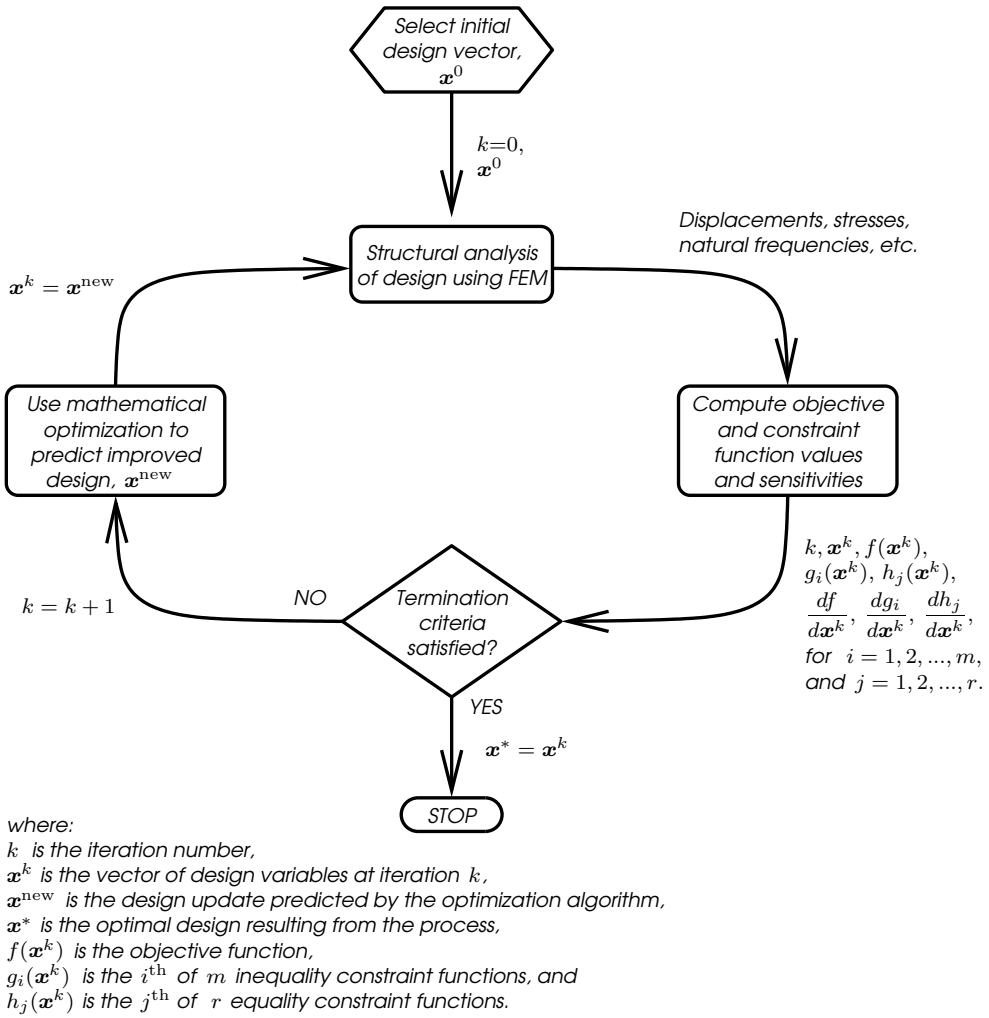

Figure 1.2: Schematic of the process of structural topology optimization.

Structural analysis

After the physical problem has been identified and a representative mathematical model constructed, the initial design can be analysed. If necessary, simplifying assumptions are made in the construction of the mathematical model. Often, the model of the physical problem results in a system of differential equations. These equations can be solved using classical analytical methods, the finite element method (FEM), the boundary element method (BEM) or any of numerous other numerical methods. In this work, the finite element method is exclusively used to perform the structural analyses.

Design evaluation and sensitivity analysis

The next step in the process involves the computation of the measure of how good the design is (the *objective function* denoted $f(\boldsymbol{x})$) and the criteria which the design is required to fulfil (the *constraint functions*, with inequality and equality constraints denoted $g_i(\boldsymbol{x})$ and $h_j(\boldsymbol{x})$

respectively).

Often the structural analysis is rather general, especially if general purpose finite element software is used, and it may therefore be necessary to post-process the results in order to extract the specific information used to construct the objective and constraint functions.

Furthermore, if a gradient based optimization procedure is to be employed, gradient or sensitivity information is also required. The process by which sensitivity information is obtained is usually referred to as design *sensitivity analysis*. For the problems considered in this work, sensitivity information is relatively easily and numerically inexpensively obtained, and therefore solely gradient based methods will be used.

Systematic design improvement

The step in which a prediction is made for an improved design is at the heart of the structural optimization process. Mathematical optimization techniques are employed to systematically generate a series of improving designs. Mathematical optimization can be described as consisting of the formulation and the solution of a constrained optimization problem of the general mathematical form:

$$\begin{aligned} &\min_{\boldsymbol{x}} \ f(\boldsymbol{x}) \\ \text{subject to}: \ &g_i(\boldsymbol{x}) \leq 0, i = 1, 2, ..., m \\ &h_j(\boldsymbol{x}) = 0, j = 1, 2, ..., r \end{aligned} \tag{1.1}$$

where $\boldsymbol{x} = [x_1, x_2, ..., x_n]^T \in \mathbb{R}^n$ is the vector of real numbered design variables. The real scalar functions f, g and h represent the objective function and inequality and equality constraint functions respectively. For more details see for example Haftka *et al.* [8] or Snyman [9].

Over the years, many techniques have been developed to solve the optimization problem, each well suited to particular problems. Many of the classical methods for solving convex problems are gradient-based, including classical line search methods and sequential approximation methods.

In this study, two different gradient based methods are used, namely the Method of Moving Asymptotes (MMA) of Svanberg [10], and the well known heuristic updating scheme based on Optimality Criteria (OC) [4].

Stopping criterion

The above process is repeated until some termination criterion has been satisfied, upon which the process is stopped. The stopping criterion can be based on the number of iterations performed, the norm of the change in function value, the norm of the change in design variables, the gradient of the objective function or any combination of the above. If it is not possible to further improve upon this design with a given algorithm, it is considered a *local optimal* solution, usually denoted $\boldsymbol{x}^*$.

For some classes of problems, such as problems with strictly convex objective and constraint functions, this local optimum may be shown to also be the *global optimal* solution. However, if this is not possible (as is the case with topology optimization) this local optimum is often accepted as a reasonable approximation to the global optimum.

1.2 Background to the study

Arguably one of the most popular and immediately useful applications of structural topology optimization is in the synthesis of compliant mechanisms. Whereas traditional mechanisms employ rigid links connected by movable joints, compliant mechanisms are mechanical devices used to transfer or transform motion, force or energy via mobility gained through the deflection of flexible members. Manually designing compliant mechanisms to carry out all but the simplest of tasks is a challenging exercise. Therefore, finite element modelling and topology optimization have become increasingly useful design tools of late.

Compliant mechanisms have a number of advantages over conventional jointed mechanisms. For example, they have fewer moving parts, reducing or eliminating backlash, play, noise as well as weight. Furthermore, compliant mechanisms are easily miniaturized making them ideal for use in Micro Electro Mechanical Systems (MEMS) or precision engineering applications where smart materials are regularly used as transducers.

Piezoelectric materials in particular are very attractive as actuator smart materials for compliant mechanisms due to their high energy density, large force capacity and excellent operational bandwidth. However their low induced strain (typically in the order of $0.1-0.2\%$[2]) means that output displacements are small, limiting their direct application. To convert these small induced strains to usable displacements, piezoelectric ceramics commonly employ some form of mechanical amplification. Often, this mechanical amplification takes the form of a compliant mechanism.

In 2003 the Department of Mechanical Engineering, and in particular the Structural Optimization Research Group (SORG) at the University of Pretoria, and the Centre for Integrated Sensing Systems (CISS)[3] at the Council for Scientific and Industrial Research (CSIR) in South Africa became jointly involved in a project aimed at investigating the development of novel finite elements and structural optimization techniques for application in compliant, piezoelectrically actuated, micropositioning systems.

The goal of this study was to develop accurate finite elements, or procedures used in their calculation, which could be used for (but are not limited to) the modelling of piezoelectrically driven compliant mechanisms. Furthermore, the study aimed to show how the salient features of these specially developed finite elements and procedures could be exploited in a topology optimization environment to overcome common numerical instabilities such as checkerboarding. In the remainder of this section a very brief background to relevant topics in topology optimization and the finite element method, is presented.

[2]However, new relaxor ferroelectric single crystals (PZN-PT and PMN-PT) can reportedly deliver in excess of 1% strain [11, 12].

[3]Now known as Sensor Science and Technology (SST).

1.2.1 Topology optimization

In topology optimization, there are several acknowledged fundamental, theoretical issues which need to be appropriately addressed if sensible results are to be achieved [13]. These issues include *non-existence* of the solution (mesh dependency), *multiple local optima*, and *non-uniqueness* of the solution.

Firstly, it is well known that the 0-1 problem statement in topology optimization lacks existence of solution in a continuum setting [4]. This problem exists due to a lack of closedness of the set of admissible designs.[4] In a discrete (finite element) setting, this problem manifests itself as a mesh dependency problem. One possible way to deal with this problem is to *a priori* allow composite materials constructed from the original isotropic material (and void). This method extends the design space and sufficiently *relaxes* the original problem. Alternatively, the design space can be *restricted* by limiting local or global variations in material distribution, thereby sufficiently closing the the set of admissible designs.

Another common complication is that of multiple (local) optima. If one observes the many different optimal solutions which have been published for benchmark problems, for example the well known MBB beam problem, it is clear that there are many local optima present. This is due to the fact that most topology optimization problems are non-convex. Unfortunately, there is no way to overcome this problem, although a popular method to alleviate non-convexity is the use of *continuation methods*. Continuation methods gradually change problems from artificial (strictly) convex, or nearly convex, problems to the original non-convex problem.

Finally, problems with multiple globally optimal solutions are termed non-unique. An example commonly cited is that of a structure under uniaxial tension, in which only the cross-sectional area is of importance and not the topology. The only sensible way to deal with this problem is to impose manufacturing preference constraints.

Unfortunately these fundamental issues cannot be resolved solely through the use of finite element technology, no matter how sophisticated the finite element. Therefore attention in this study is rather focused on problems which occur *locally* in material distributions, and which can be attributed to the numerical deficiencies of the finite element model, such as *checkerboarding* and *one-node connected hinges*.

The checkerboarding problem is characterised by material in 'optimal topologies' being distributed in alternating solid and void elements, similar to the pattern created by the squares on a checkerboard. Checkerboarding is largely a result of poor numerical modelling of this spurious material distribution, as shown by Díaz and Sigmund [14]. In essence, the numerical behaviour of this material distribution is over-stiff and is therefore especially common in the solutions of minimum compliance problems.

The one-node connected hinge is characterised by four elements surrounding a node, where two diagonally opposite elements are solid and the other two are void, see for example

[4] As more holes are introduced without changing the volume of the structure, the efficiency of the structure is generally improved. Eventually, variations on the microstructural level are introduced (requiring composite material descriptions) which cannot be described by the original problem which permits isotropic material only.

Poulsen [15]. This material distribution is somewhat common in the design of compliant mechanisms such as those for which this work is ultimately aimed. This is due to the fact that in compliant mechanism design, solid state hinges are employed to achieve the required motion and the numerical model of a one-node hinge employing standard elements is ideal (albeit unrealistic) since it offers zero resistance to rotation about the common node.

For a more detailed introduction to the topology optimization problem, the reader is referred to Appendix A.

1.2.2 The finite element method

The finite element method (FEM) is essentially a numerical method for the solution of differential equations [16]. Originally, FEM gained popularity among engineers as a method for structural stress analysis. With the advent of ever faster and less expensive digital computers, FEM found application in other fields including heat transfer, fluid dynamics, as well as electric, piezoelectric and electromagnetic analysis. In fact, many commercial finite element codes now support these types of analyses as standard and some even have structural optimization algorithms included.

FEM topics for consideration in this study were identified based on the topology optimization problems selected for attention, namely checkerboarding and one-node connected hinges. Finite element procedures which could alleviated or eliminate the numerical modelling deficiencies associated with, or leading, to these material distributions were sought.

Since checkerboarding has been attributed to an over-stiff numerical model of a checkerboard layout, a procedure to effectively soften elements in this layout was sought. One common technique used to soften (especially higher order deformation modes) is to employ a reduced numerical integration scheme in the calculation of elemental quantities.

In the finite element method, the equilibrium equations involve integration over the element volume. This is also true for the expressions for consistent nodal loads, mass matrices, penalty matrices, etc. For simple elements the integrand may be formed explicitly, resulting in *exact* integration. However, numerical integration schemes are necessary when element geometries are distorted, of which the Gaussian rules are possibly the best known and most frequently employed. The effects of numerical integration schemes are summarized in a clear manner by Cook *et al.* [17].

A lower-order quadrature rule, called reduced integration, may be desirable for two reasons. Firstly, since the expense of generating the stiffness matrix by numerical integration is proportional to the number of sampling points, fewer points results in lower computational cost. Secondly, a low order rule tends to soften an element, thus countering the overly-stiff behavior associated with assumed displacement fields. (The displacement based finite element method is monotonically convergent from below.) Softening comes about because certain higher-order polynomial terms happen to vanish at Gauss points of a low-order rule. Simply stated, with fewer sampling points, some of the more complicated displacement modes offer less resistance to deformation.

Conversely, the numerical model of a one-node hinge comprised of standard displacement-based elements is known to possess little or no stiffness in rotation. In fact, for planar

problems most elements do not possess in-plane rotational degrees of freedom at all. However, elements with in-plane rotational degrees of freedom do exist, and their use in schemes to effectively stiffen one-node connected hinges is evaluated.

In recent times, elements with in-plane rotational (drilling) degrees of freedom have become quite popular. Apart from enrichment of the displacement field, which increases element accuracy, drilling degrees of freedom allow for the modelling of, for instance, folded plates and beam-slab intersections.

The membrane elements used in this study account for in-plane rotations based on a continuum mechanics definition of rotation. The approach relies on a variational formulation employing an independent rotation field, as presented by Hughes and Brezzi [18]. It utilizes the skew-symmetric part of the stress tensor as a Lagrange multiplier to enforce equality of independent rotations and the skew-symmetric part of the displacement gradient in a weak sense. The stress tensor is therefore not *a priori* assumed to be symmetric.

1.3 Objectives of the study

There has been a steady stream of publications reporting on improvements and advances in finite element technology since the 1970's, when FEM was conceived as a general computer implementation [19]. Improvements can be judged on several measures, including accuracy, numerical robustness or computational cost. Unfortunately though, as with most things, there is 'no free lunch', and generally accuracy is traded for robustness or computational effort, or *vice versa*.

Advances in finite element technology are of particular interest to practitioners of structural optimization, since multiple finite element analyses (at least one per iteration) are required to determine the optimal structure. Procedures which increase accuracy or decrease computational effort are of significant benefit in such an iterative environment, and are therefore *per se* of interest.

However, finite element formulation does not only affect the accuracy (and/or numerical effort) required to perform the structural analyses in topology optimization, it can actually influence the resulting topology itself. For example, the use of higher order elements are known to lessen or eliminate checkerboarding, common in minimum compliance solutions employing 4-node planar elements. Although it may be argued that topology results containing checkerboarding are physically unreasonable, the conclusion is that under certain circumstances finite element formulation indeed affects the results of a topology optimization procedure.

The goal of this work is essentially to investigate this observation further. In principal, the intention is to develop new finite elements and/or procedures (or to identify existing elements and procedures) and to exploit their unique characteristics to overcome numerical instabilities or deficiencies in a topology optimization setting.

Firstly, traditional planar elements do not possess nodal rotational degrees of freedom. Therefore if two of these elements are connected at a single node, the assembly offers no resistance to rotation about the common node. Although this model of a compliant hinge is

completely unrealistic and therefore undesirable in topological results, one-node hinges are regularly encountered in compliant mechanism design using topology optimization. Consequently, the idea to exploiting the nodal rotational stiffness associated with elements with drilling degrees of freedom to prevent (or at least improve the numerical model of) a one-node connected hinge is investigated.

Ultimately, the practical application of this investigation is in the design of piezoelectrically driven compliant mechanisms. Therefore new piezoelectric elements with drilling degrees of freedom are required. Furthermore, although it was decided to focus the finite element development on 2-D planar elements, planar membrane elements also form part of flat shell elements, and therefore developments in planar element technology are not restricted to planar problems. Accordingly, the effects of membrane (and plate) element formulations on flat shell topology optimization results are also investigated.

Secondly, since the model of a checkerboard patch of elements is commonly known to exhibit over-stiff behaviour, a method to soften the finite element model is sought. A popular method of softening (especially higher-order) deformation modes associated with elements is to employ reduced integration schemes. Subsequently, the notion of employing alternative reduced order integration schemes to soften patches of elements arranged in a checkerboard layout is investigated.

In summary, the primary objectives of this study are to:

1. Develop new finite elements, or elemental procedures, which not only improve model accuracy, robustness and/or efficiency, but can also be used in schemes which alleviate or eliminate the numerical instabilities, or improper modelling, associated with spurious material layouts in topology optimization. Attention is focused on the following topics in particular:

   - Determining the sensitivity of elements with drilling degrees of freedom to the penalty parameter, usually denoted γ.
   - The formulation, implementation and evaluation of planar piezoelectric finite elements with drilling degrees of freedom.
   - Investigating the use of reduced order integration rules in higher order elements to enhance element accuracy.

   Note that application of these finite element developments is not restricted to structural topology problems. Their increased accuracy, modelling capacity or numerical efficiency could also be applied in general purpose finite element codes.

2. To develop procedures which exploit the salient features of the new finite elements, or elemental procedures, in order to overcome or alleviate the numerical instabilities, or modelling deficiencies, leading to spurious material layouts in topology optimization. More specifically, the topics under consideration include:

   - Exploiting elements with drilling degrees of freedom in schemes to prevent undesirable local material distributions in topology optimization.

- Evaluating the effect of element formulation in plate and shell topology optimization problems.
- Quantifying the effect of reduced order integration rules on the stiffness of a checkerboard patch of elements.

1.4 Thesis overview and list of contributions

The thesis is divided into six main research chapters. Each of these chapters represent scientific contributions (in the form of conference or journal papers) made during the course of this work. As such, each chapter is intended to be self-contained and can be read independently of the other chapters. Note also that the notation in each chapter is therefore slightly different.

A schematic depiction of the thesis layout is presented in Figure 1.3. As indicated in the figure, the thesis body is divided into two parts. The first part contains Chapters 2 to 4, and details contributions made in finite element development and technology. The second, comprising Chapters 5 to 7, explores the application of finite element technology in a topology optimization environment. Furthermore, the finite element developments presented in Chapters 2 and 3 are related to topology optimization topics communicated in Chapters 5 and 6. Similarly the finite element developments offered in Chapter 4 find application in Chapter 7.

In **Chapter 2** an introduction to elements with drilling degrees of freedom (DOFs) is presented. Furthermore, the effect of the parameter which relates in-plane displacements and rotations, usually denoted γ, is studied. A unique feature of this study is the novel use of the skew symmetric part of the stress tensor to assess element accuracy. This contribution has been published in *Finite Elements in Analysis and Design*, with the full reference:

- C.S. Long, S. Geyer, and A.A. Groenwold. A numerical study of the effect of penalty parameters for membrane elements with independent rotation fields and penalized equilibrium. *Finite Elements in Analysis and Design*, 42:757–765, 2006.

Chapter 3 details the development of planar 4-node piezoelectric elements with drilling DOFs. Firstly, two families of variational formulations accounting for piezoelectricity and in-plane rotations are derived. The first retains the skew-symmetric part of the stress tensor, while in the second, the skew part of stress is eliminated from the functional. The finite elements derived from the variational formulations are then benchmarked against existing elements.

Much of the work presented in this chapter is summarised in the journal article:

- C.S. Long, P.W. Loveday, and A.A. Groenwold. Planar four node piezoelectric elements with drilling degrees of freedom. *International Journal for Numerical Methods in Engineering*, 65:1802–1830, 2006.

However, due to space limitations in the journal article, not all variational formulations are given in detail and only two of the eight elements presented in this chapter are evaluated.

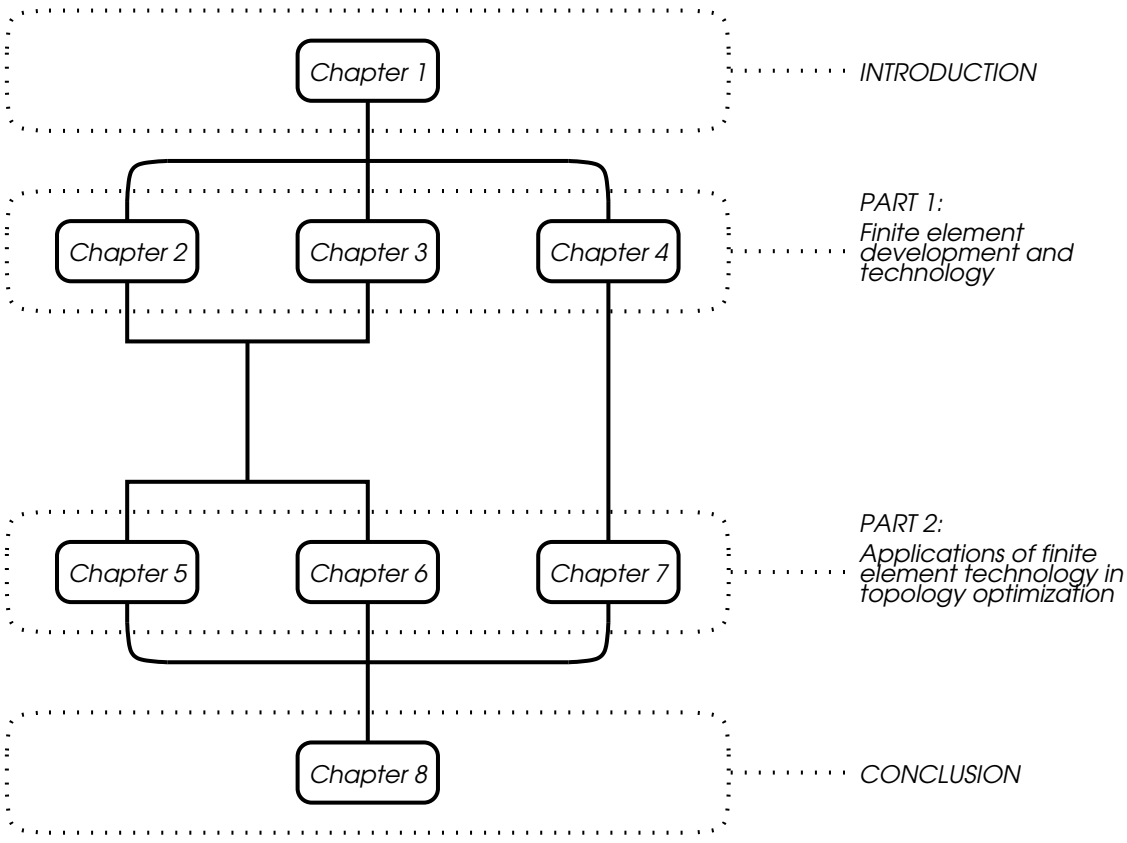

Figure 1.3: Schematic of thesis layout.

Here, the complete compilation of variational formulations, as well as a numerical evaluation of all eight elements (with and without assumed stress and electric flux density) are presented.

Chapter 4 explores the application of modified (5- and 8-point) integration schemes in higher order Q8 and Q9 elements. Reduced integration schemes are often employed to enhance element accuracy. Application of a 4-point reduced integration rule in quadratic elements however, results in spurious zero energy modes. The application of modified integration rules in elemental calculations of Q8 and Q9 elements is shown to suppress these spurious modes while, maintaining element accuracy comparable to that of their under-integrated counterparts.

The journal article resulting from this work is

- C.S. Long and A.A. Groenwold. Reduced modified quadrature for quadratic membrane finite elements. *International Journal for Numerical Methods in Engineering*, 61:837–855, 2004.

Chapter 5 explores the use of elements with drilling DOFs in developing new schemes to prevent checkerboarding, one-node connected hinges and diagonal members. As an application, topology optimization is applied to the design of a piezoelectrically driven mirror scanning device. The new method to deal with one-node connected hinges and diagonal members is employed in order to improve upon the designs achieved using conventional Q4

elements and filter strategies.

The presentation in this chapter is largely adapted from work that was presented at the 5th and 6th World Congress of Structural and Multidisciplinary Optimization (WCSMO5 and WCSMO6). For further details, the reader is referred to the articles:

- C.S. Long, P.W. Loveday, and A.A. Groenwold. On membrane elements with drilling degrees of freedom in topology optimization. In *Proc. Fifth World Congress on Structural and Multidisciplinary Optimization*, Lido di Jesolo, Venice, Italy, May 2003. Paper no. 83.

- C.S. Long, P.W. Loveday, and A.A. Groenwold. Design of a piezoelectric mirror scanning device using topology optimization. In *Proc. Sixth World Congress on Structural and Multidisciplinary Optimization*, Rio de Janeiro, Brazil, May 2005. Paper no. 4031.

Chapter 6 deals with generally curved shell problems in topology optimization. The differences in optimal topologies obtained when employing *ad hoc* versus mathematically sound methods to include in-plane rotations, are investigated. The sensitivity of optimal topologies to the parameter γ, studied in Chapter 2, for membrane and shell problems is quantified. Furthermore, the effect of the plate component of flat shell elements on optimal topologies is determined. Differences between the popular Discrete Kirchhoff Quadrilateral (DKQ) elements, and two frequently employed Mindlin Reissner plate elements, are presented.

Parts of this work were presented at the Second International Conference on Structural Engineering, Mechanics and Computation held in Cape Town

- C.S. Long, A.A. Groenwold, and P.W. Loveday. Implications of finite element formulation in optimal topology design. In A. Zingoni, editor, *Progress in Structural Engineering, Mechanics and Computation*, pages 1015–1019, Cape Town, South Africa, July 2004.

Furthermore, the work in this chapter is to form the basis of an article:

- C.S. Long, A.A. Groenwold, and P.W. Loveday. Effect of element formulation on membrane, plate and shell topology optimization problems. *Finite Elements in Analysis and Design*, 2007. To be submitted.

Chapter 7 reports on the application of reduced order integration schemes in topology optimization. It is widely known that a patch of elements, with material distributed in a checkerboard pattern, exhibits artificially high stiffness. This is generally accepted as the cause of checkerboarding, a phenomena characterised by significant areas of 'optimal' topologies in which material is distributed in a checkerboard-like pattern. Therefore, particular attention is paid to the effect of reduced order integration on the stiffness of higher order (Q8 and Q9) checkerboard patches.

A journal article summarising this work is in preparation:

- C.S. Long, A.A. Groenwold, and P.W. Loveday. Effect of reduced order integration schemes on checkerboard patterns in topology optimization. *Structural and Multidisciplinary Optimization*, 2007. To be submitted.

Finally, in **Chapter 8** a retrospective summary of the work is offered. Some concluding remarks regarding the study are offered, as well as recommendations for future work.

In **Appendix A** a brief introduction to topology optimization is offered, while **Appendix B** presents some additional topology optimization results not included in Chapter 6.

Part 1:

Finite Element Development and Technology

Chapter 2

Stability of elastostatic elements with drilling degrees of freedom

2.1 Summary

This chapter presents a short introduction and background to finite element formulations with drilling degrees of freedom (DOFs). Early parts of the chapter are largely given as a background to the formulation of elements with drilling DOFs. However, this chapter also presents a new contribution which has been made in the stability analysis of these elements. In particular, the novel idea of using the skew-symmetric part of stress as an error estimate has been proposed.

In particular, a numerical investigation into the effect of the penalty parameter in elements with drilling DOFs, for which the stress tensor $\boldsymbol{\sigma}$ is not *a priori* assumed to be symmetric, is offered. The parameter under investigation is γ, which relates the in-plane translations to the rotations for elements with drilling DOFs. Rather than simply reporting on the quantitative influence of γ on measures like displacement, rotation and stress, the skewness of the nonsymmetric stress tensor is directly assessed. Results are presented for both isotropic and orthotropic constitutive relationships.

2.1.1 A word on notation

Before starting with the presentation, some brief notes on the notation employed are called for. Firstly, the notations employed to denote variables in this chapter, and in Chapter 3, differ somewhat. In the present chapter, the conventional mechanical symbolic designations are used, whereas in Chapter 3 the symbols traditionally used in the piezoelectric research community are employed. For example in what is to follow, $\boldsymbol{\epsilon}$ denotes the mechanical strain tensor, which is denoted $\boldsymbol{S}$ in Chapter 3. Furthermore, in Chapter 3 the symbol $\boldsymbol{\epsilon}$ is reserved for the dielectric constitutive properties. To avoid confusion, the notation employed is explained in detail in the text of each chapter and should not be assumed to be consistent throughout this work.

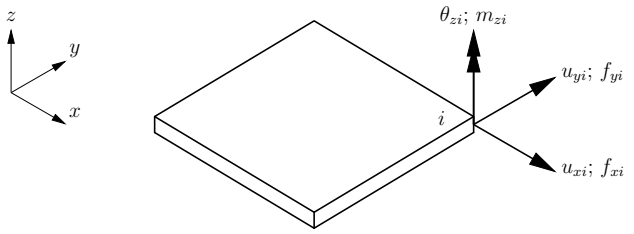

(a) Membrane deformations and forces.

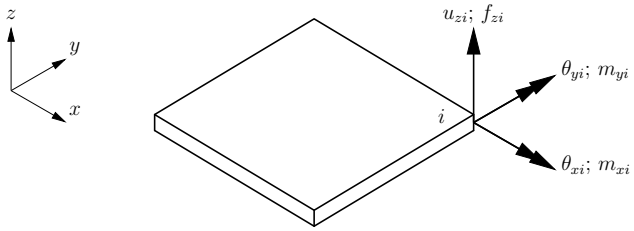

(b) Bendng deformations and forces.

Figure 2.1: Flat element subject to in-plane membrane and bending actions.

Secondly, a conventional tensor notation, similar to that employed by for example Pimpinelli [20], where "·" is reserved for the scalar inner product between tensors of given order, is used. This notation is slightly different to that employed for example by Hughes and Brezzi [18] or Ibrahimbegovic *et al.* [21].

2.2 Introduction

In this section some background is presented on finite elements with drilling degrees of freedom (DOFs). Much of the work in the early part of this chapter is relatively widely known, but is given here as an introduction for those readers unfamiliar with the topic.

In recent times, elements with in-plane rotational (drilling) degrees of freedom have become quite popular. Apart from enrichment of the displacement field, which increases element accuracy, drilling degrees of freedom allow for the modelling of, for instance, folded plates and beam-slab intersections. Although only planar membrane elements are considered in this chapter, the need for elements with an in-plane rotational DOFs should be seen in the light of their application in shell analyses. Plane stress membrane elements are commonly combined with plate elements to form flat shell elements. The membrane and plate (bending) constituents of such a flat shell element are depicted separately in Figure 2.1. The element possesses nodal displacements u_x, u_y and u_z and rotations θ_x, θ_y and θ_z, and can be subjected to both in-plane membrane and bending actions at each node i.

As explained for example in Zienkiewicz and Taylor [22], for in-plane actions, the states of stress and strain can be uniquely defined in terms of the two in-plane displacements. The

relation between in-plane forces and displacements is given by:

$$\boldsymbol{k}^{\mathrm{m}}\boldsymbol{q}^{\mathrm{m}} = \boldsymbol{f}^{\mathrm{m}}, \tag{2.1}$$

where $\boldsymbol{q}^{\mathrm{m}} = [\boldsymbol{u}_{xi} \;\; \boldsymbol{u}_{yi}]^T$, represents the in-plane displacements in the x and y directions, with corresponding forces $\boldsymbol{f}^{\mathrm{m}} = \left[\boldsymbol{f}_{xi} \;\; \boldsymbol{f}_{yi}\right]^T$. The components of displacement are comprised of the displacements at each node. For the 4-node element depicted in Figure 2.1, we have $\boldsymbol{u}_{xi} = [u_{x1} \;\; u_{x2} \;\; u_{x3} \;\; u_{x4}]^T$, $\boldsymbol{u}_{yi} = [u_{y1} \;\; u_{y2} \;\; u_{y3} \;\; u_{y4}]^T$, with the forces expanded similarly. The superscript 'm' denotes these as in-plane membrane components. $\boldsymbol{k}^{\mathrm{m}}$ is the membrane stiffness matrix.

Similarly, the bending components can be expressed uniquely in terms of the out-of-plane displacement and two rotations at each node as

$$\boldsymbol{k}^{\mathrm{b}}\boldsymbol{q}^{\mathrm{b}} = \boldsymbol{f}^{\mathrm{b}}, \tag{2.2}$$

where $\boldsymbol{q}^{\mathrm{b}} = [\boldsymbol{u}_{zi} \;\; \boldsymbol{\theta}_{xi} \;\; \boldsymbol{\theta}_{yi}]^T$, with the forces and moments given by $\boldsymbol{f}^{\mathrm{b}} = [\boldsymbol{f}_{zi} \;\; \boldsymbol{m}_{xi} \;\; \boldsymbol{m}_{yi}]^T$. In this case, the superscript 'b' indicates that these terms are bending-related, and $\boldsymbol{k}^{\mathrm{b}}$ is the plate bending stiffness matrix.

In this simple illustrative example, there is no coupling between in-plane and bending actions. What is more, up to this point it has not been necessary, at least in terms of the description of the problem mechanics, to include the in-plane rotations ($\boldsymbol{\theta}_{zi}$).

All six degrees of freedom at each node can now be assembled as

$$\boldsymbol{k}\boldsymbol{q} = \boldsymbol{f}, \tag{2.3}$$

where, at each node, displacements and rotations are given as $\boldsymbol{q}_i = [\boldsymbol{q}_i^{\mathrm{m}} \;\; \boldsymbol{q}_i^{\mathrm{b}} \;\; \boldsymbol{\theta}_{zi}]^T$ and the forces and moments are assembled as $\boldsymbol{f}_i = [\boldsymbol{f}_i^{\mathrm{m}} \;\; \boldsymbol{f}_i^{\mathrm{b}} \;\; \boldsymbol{m}_{zi}]^T$. The stiffness matrix is in turn, made up of the following submatrices for a 4-node element

$$\boldsymbol{k} = \left[\begin{array}{c|c|c} \boldsymbol{k}^{\mathrm{m}}_{8\times 8} & \mathbf{0}_{8\times 12} & \mathbf{0}_{20\times 4} \\ \hline \mathbf{0}_{12\times 8} & \boldsymbol{k}^{\mathrm{b}}_{12\times 12} & \\ \hline \multicolumn{2}{c|}{\mathbf{0}_{4\times 20}} & \mathbf{0}_{4\times 4} \end{array}\right], \tag{2.4}$$

where no stiffness is associated with the rotational degree of freedom.

Difficulties arise if any number of flat shell elements employing this formulation, connected at a node, are co-planar (or nearly so) [22]. Examples of this type of assemblage include flat shell segments, as well as straight boundaries of singly curved shells. When the local coordinate directions of these elements happen to coincide with the global coordinates, the equilibrium equations corresponding to terms with $\boldsymbol{\theta}_{zi}$ reduce to 0=0, which does not present special difficulties. However, if the local and global coordinates differ the global stiffness matrix becomes singular, and detection of this singularity could present difficulties. If it is not possible to assemble stiffness matrices in local coordinates (and simply delete all 0=0 equations), an arbitrary stiffness k'_{θ_z}, can be inserted at these points only. Both of these procedures lead to programming difficulties in general codes, due to the subjective nature of 'nearly co-planar' detection.

There are several problems (apart from the rank deficiency) associated with this type of element. The ordinary membrane part of the stiffness matrix employing an isoparametric formulation is usually very stiff, especially in bending. This problem can be alleviated by employing a mixed or hybrid element, or an element with an enhanced strain formulation. A more serious problem is that of possible incompatible in-plane rotation which could occur in an assembly, for example in beam-slab connections, or at the intersection of a folded plate.

These issues can be addressed if suitable membrane elements with drilling degrees of freedom (DOFs) are formulated, implemented and superimposed on an appropriate plate element to form a shell element with 6 DOFs per node. Since most general and commercial finite element codes make provision for 6 DOFs per node in any case, this improvement is largely cost free in terms of computational and implementational effort [22]. Furthermore, the resulting membrane elements are generally more accurate due to an enrichment of the displacement field [21, 23, 24].

2.3 Historical development of elements with drilling DOFs

In this section a brief history of the development of elements with drilling DOFs is presented. Distinction will be made between *vertex* (or ω) rotations which need not be directly related to the continuum mechanics definition of in-plane rotation, and *drilling* (or Ω) rotations that are. In a finite element setting, the Ω drilling degree of freedom may be physically interpreted as a true rotation of the vertex bisecting the angle between adjacent edges of the finite element. The continuum mechanics definition of the in-plane rotation field Ω_z is

$$\Omega_z = \frac{1}{2}\left(\frac{\partial u_y}{\partial x} - \frac{\partial u_x}{\partial y}\right), \tag{2.5}$$

where u_x and u_y are the components of the in-plane displacement field in the x and y directions, respectively.

Compilations of early (unsuccessful) efforts to develop elements with drilling DOFs are presented by Frey [25] and Bergan and Felippa [26] as well as, among others, [27, 28]. Several early attempts to develop membrane elements with drilling DOFs failed, for example [29, 30]. These repeated failures prompted Irons and Ahmad [31] to view as futile the task of constructing elements with drilling degrees of freedom.[1]

However in the mid-80's, Allman [32] and Bergan and Felippa [26] achieved a previously unattained level of success. Instead of the cubic functions previously used, they employed a quadratic displacement function for the normal component of displacement.

The interpolation used by Allman (referred to as Allman interpolations) is depicted in Figure 2.2. Specifically the interpolation consists of a quadratic function for the component of displacement normal to the element side, and a linear form for the tangential component of displacement.

[1] To be fair though, some of the theory used to develop current elements was not known to them at the time [26].

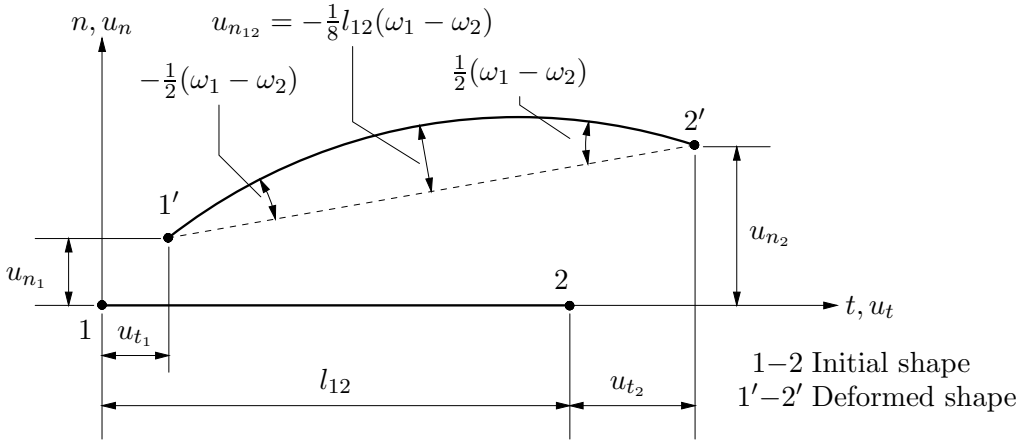

Figure 2.2: Displacement of an element side 1−2.

According to Allman [32] (who introduced the term 'vertex rotations'), the relation between vertex rotation, ω, and normal displacement is given by

$$-\omega_2 + \omega_1 = \frac{\partial u_n}{\partial s}|_l - \frac{\partial u_n}{\partial s}|_0, \tag{2.6}$$

where ω_1 and ω_2 are the vertex rotations at nodes 1 and 2, respectively. It can be shown that this reduces to

$$\omega_1 - \omega_2 = -\frac{8}{l_{12}} u_{n_{12}}. \tag{2.7}$$

The interpolation of u_n can therefore be written in terms of nodal vertex rotations as

$$u_n = (1 - \frac{s}{l_{12}})u_{n_1} + \frac{s}{l_{12}} u_{n_2} - \frac{s}{2}(1 - \frac{s}{l_{12}})(\omega_1 - \omega_2). \tag{2.8}$$

Clearly, these vertex rotations are not the same as the true rotations for plane elasticity, defined in (2.5), but related to them in an indeterminate way only [25].

Since then, many papers on the subject have appeared. Cook [33] showed that the Allman element can be obtained by applying a coordinate transformation to a higher order element with mid-side nodes. This technique was extended to elements other than triangles, resulting in rank deficient quadrilateral elements. MacNeal and Harder [24] refined this element by developing a method to suppress the rank deficiency.

Other noteworthy developments are credited to Jetteur, Jaamei and Frey [25, 34, 35, 36] and to Taylor and Simo *et al.* [37, 38, 39].

More recently, Hughes and Brezzi [18], presented a rigorous mathematical framework in which to formulate elements with independent rotational interpolations. They argue that, utilising the formulation of Reissner [40], formulations employing 'convenient' displacement, rotation and stress interpolations are doomed to failure. Instead, they propose a modified variational principle, with improved stability properties in the discrete form.

Early finite element interpolations employing the formulation of Hughes and Brezzi were presented by Hughes *et al.* [41] and Ibrahimbegovic *et al.* [21, 42]. These elements depend

on a problem-dependent penalty parameter γ, which relates the in-plane translations to the in-plane rotations. The value of γ has been the topic of a number of studies [18, 21, 43, 44, 44]. For linear elastic isotropic Dirichlet problems, the formulation is reported to be relatively insensitive to the value of γ [18, 21, 45], and it was proposed that $\gamma = \mu$, with μ the shear modulus. For different conditions (e.g. orthotropy or elastodynamics), a greater sensitivity to the value of γ is to be expected. For dynamic problems, for example, Hughes *et al.* [44] propose $\gamma = \mu/10$.

Independent from work on drilling degrees of freedom, the developments in mixed/hybrid membrane finite elements have been equally important during recent years. Since the assumed stress finite element presented by Pian [46], numerous formulations have been proposed. A compilation is presented by Pian [47]. Eventually, assumed stress formulations were combined with drilling degrees of freedom in a single element formulation, e.g. see Aminpour [48, 49], Sze and Ghali [50], and Geyer and Groenwold for quadrilateral 8β and 9β drill families [43].

Since then, the development of membrane finite elements with drilling DOFs has been significant. Sze and co-workers [51, 50] developed elements with in-plane rotations and assumed stress fields. Groenwold and Stander [52, 53] applied the 5-point quadrature presented by Dovey [54] to drilling degree of freedom membranes, which improved the element behaviour through the introduction of a 'soft' higher order deformation mode. Later Geyer and Groenwold [43] also developed assumed stress finite elements with drilling DOFs. Recently Pimpinelli developed an assumed strain quadrilateral element with drilling degrees of freedom [20].

In this chapter the effect of the parameter γ, which relates the in-plane translations and rotations, is numerically investigated. The chapter is set out as follows: Firstly in Section 2.4, the framework developed by Hughes and Brezzi [18], within which elements with drilling DOFs are formulated, is presented. The finite element interpolations employed are then detailed in Section 2.5. Next, stability requirements for the Dirichlet elastostatic problem due to Hughes and Brezzi are briefly discussed in Section 2.6. In Section 2.7, stability and consistency requirements are numerically verified for constant stress states. Numerical results are presented in Section 2.8, while concluding remarks are presented in Section 2.9.

2.4 Variational formulation of elements with drilling DOFs

The focus of this chapter is the element sensitivity to the problem dependant parameter γ, and not the variational formulation of the elements. It would therefore not be appropriate to present details of the variational formulation of elements with drilling DOFs here, especially since that information can be found in the references presented in Section 2.3. Instead, only the functionals from which the elements used in this study are derived (as introduced in [18]), are presented.

This presentation is merely to illustrate the framework wherein these elements are formulated, as well as to act as an introduction to show how this framework for the elastostatic

problem was extended for piezoelectricity in Chapter 3.

We proceed, as in [20], by defining $\bar{\Omega}$ as a closed and bounded domain occupied by a body in three dimensional space. The interior part of $\bar{\Omega}$ is denoted by Ω and it's boundary by $\partial\Omega$, $\Omega \cup \partial\Omega = \bar{\Omega}$. The measure of Ω is V and the measure of $\partial\Omega$ is S. $\mathcal{V}$ is the vector space associated with the Euclidean point space and $\mathcal{L}$ the space of all linear applications of $\mathcal{V}$ into $\mathcal{V}$, which possesses inner product $\boldsymbol{A} \cdot \boldsymbol{B} = \mathrm{tr}(\boldsymbol{A}^t\boldsymbol{B})$, $\boldsymbol{A}, \boldsymbol{B} \in \mathcal{L}$ and $\boldsymbol{A}^t$ the transpose of $\boldsymbol{A}$ (see [20]). Reference will also be made to subsets of $\mathcal{L}$, namely $\mathcal{S}$ and $\mathcal{W}$ which contain, respectively symmetric and skew-symmetric tensors in $\mathcal{L}$.

The boundary $\partial\Omega$, is split into two parts, $\partial\Omega_u$ and $\partial\Omega_t$ such that $\partial\Omega_u \cup \partial\Omega_t = \partial\Omega$ and $\partial\Omega_u \cap \partial\Omega_t = \emptyset$. On $\partial\Omega_u$ displacements $\bar{\boldsymbol{u}}$ are prescribed, while on $\partial\Omega_t$ the traction $\bar{\boldsymbol{t}}$ is prescribed.[2] The discussion is limited to linear elastic problems and discussion of boundary conditions is omitted.[3]

In the most general case, the stress tensor, $\boldsymbol{\sigma} \in \mathcal{L}$ (which is not *a priori* assumed to be symmetric), the displacement vector field $\boldsymbol{u}$, the skew-symmetric infinitesimal rotational tensor, $\boldsymbol{\psi} \in \mathcal{W}$, and the strain tensor $\boldsymbol{\epsilon} \in \mathcal{S}$ are taken as dependent variables. The variational formulation requires the rotations $\boldsymbol{\psi}$, strains $\boldsymbol{\epsilon}$ and stresses $\boldsymbol{\sigma}$, together with the displacement generalised derivatives $\boldsymbol{\nabla u}$, belong to the space of square-integrable functions over the region Ω.

The Euclidean decomposition of a second-rank tensor is used, e.g.,

$$\boldsymbol{\sigma} \;=\; \mathrm{symm}\;\boldsymbol{\sigma} + \mathrm{skew}\;\boldsymbol{\sigma}, \tag{2.9}$$

where

$$\mathrm{symm}\;\boldsymbol{\sigma} = \frac{1}{2}(\boldsymbol{\sigma} + \boldsymbol{\sigma}^t), \tag{2.10}$$

$$\mathrm{skew}\;\boldsymbol{\sigma} = \frac{1}{2}(\boldsymbol{\sigma} - \boldsymbol{\sigma}^t). \tag{2.11}$$

The problem under consideration is now constructed as follows: Given $\boldsymbol{f}$, the body force vector, find $\boldsymbol{u}$, $\boldsymbol{\psi}$, $\boldsymbol{\sigma}$ and $\boldsymbol{\epsilon}$ such that:

$$\mathrm{div}\;\boldsymbol{\sigma} + \boldsymbol{f} = \boldsymbol{0}, \tag{2.12}$$

$$\mathrm{skew}\;\boldsymbol{\sigma} = \boldsymbol{0}, \tag{2.13}$$

$$\boldsymbol{\psi} = \mathrm{skew}\boldsymbol{\nabla u}, \tag{2.14}$$

$$\boldsymbol{\epsilon} = \mathrm{symm}\boldsymbol{\nabla u}, \tag{2.15}$$

$$\mathrm{symm}\;\boldsymbol{\sigma} = \boldsymbol{c}\;\boldsymbol{\epsilon}, \tag{2.16}$$

for all $\boldsymbol{x} \in \Omega$. Equations (2.12) through (2.16) represent respectively, the linear and rotational momentum balance equations, the definition of rotation in terms of displacement

[2] It is of course possible to have part of the boundary with both displacements and tractions prescribed, as often used to simulate symmetry boundary conditions [55]. However, at no point are both forces and displacements in coincident directions prescribed.

[3] Boundary conditions may be incorporated in the standard manner, e.g. see [16, 21, 56, 57], and will be dealt with in more detail in Chapter 3.

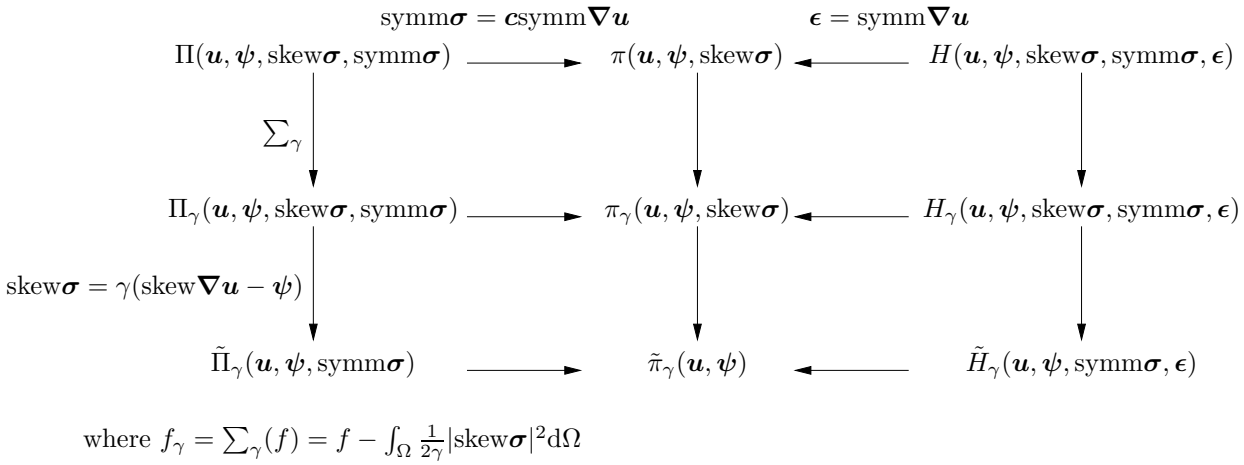

Figure 2.3: Relationship among functionals. (Figure from [18].)

gradient, the compatibility condition for strain in terms of displacement gradient and the constitutive equations. The tensor of elastic stiffness is represented by $\boldsymbol{c}$.

Reissner [40] presented a variational formulation for the boundary value problem reflected in (2.12) to (2.16). However, this formulation is inappropriate for numerical applications. The problems associated with Reissner's formulation are summarised, and addressed in the ground-breaking paper of Hughes and Brezzi [18]. Upon concluding their paper, a graphical illustration of the relationships between the various functionals employed in their study is given. These relations are repeated in Figure 2.3.

The functionals denoted H are used as a basis for Hu-Washizu type variational formulations, while those denoted Π are used to construct Hellinger-Reissner like formulations. The simplest functionals which ultimately result in 'irreducible' displacement-based formulations are denoted π.

In particular, the functional denoted H is given explicitly by Hughes and Brezzi [18] as

$$H(\boldsymbol{u}, \boldsymbol{\psi}, \text{skew}\boldsymbol{\sigma}, \text{symm}\boldsymbol{\sigma}, \boldsymbol{\epsilon}) = \frac{1}{2}\int_\Omega \boldsymbol{c\epsilon} \cdot \boldsymbol{\epsilon} \text{d}V + \int_\Omega (\text{symm}\boldsymbol{\nabla u} - \boldsymbol{\epsilon}) \cdot \text{symm}\boldsymbol{\sigma} \text{d}V + \int_\Omega (\text{skew}\boldsymbol{\nabla u} - \boldsymbol{\psi}) \cdot \text{skew}\boldsymbol{\sigma} \text{d}V - \int_\Omega \boldsymbol{f} \cdot \boldsymbol{u} \text{d}V + \text{Boundary Terms}, \quad (2.17)$$

where symm$\boldsymbol{\sigma}$ acts as a Lagrange multiplier enforcing the compatibility conditions and skew$\boldsymbol{\sigma}$ enforces the relationship between $\boldsymbol{\psi}$ and $\boldsymbol{u}$.

It can be shown that the functional H can be used to derive a Hellinger-Reissner like functional Π by substituting $\boldsymbol{\epsilon} = \boldsymbol{s}\ \boldsymbol{\sigma}$ into (2.17), where $\boldsymbol{s} = \boldsymbol{c}^{-1}$ is the compliance tensor. Since $\boldsymbol{\epsilon}$ does not appear in the functional, the compatibility conditions are enforced in a strong sense *a priori*. This connection is not illustrated in the original figure, see Figure 2.3. The

functional Π is now given as

$$\Pi(\boldsymbol{u},\boldsymbol{\psi},\text{skew}\boldsymbol{\sigma},\text{symm}\boldsymbol{\sigma}) = -\frac{1}{2}\int_\Omega \boldsymbol{s}\text{symm}\boldsymbol{\sigma}\cdot\text{symm}\boldsymbol{\sigma}\text{d}V + \int_\Omega \text{symm}\boldsymbol{\nabla u}\cdot\text{symm}\boldsymbol{\sigma}\text{d}V + \int_\Omega(\text{skew}\boldsymbol{\nabla u}-\boldsymbol{\psi})\cdot\text{skew}\boldsymbol{\sigma}\text{d}V - \int_\Omega \boldsymbol{f}\cdot\boldsymbol{u}\text{d}V + \text{Boundary Terms}. \quad (2.18)$$

A similar Π functional to that found in, for example [43, 58], is presented. This functional is slightly different to the one suggested by Reissner [40] and used by Hughes and Brezzi as a basis for their theory [18]. However, it results in the same Euler-Lagrange equations as the one suggested by Reissner and Hughes and Brezzi.

Finally, as shown in Figure 2.3, the functional π can be derived by either substituting the compatibility conditions into H or by substituting $\text{symm}\boldsymbol{\sigma} = \boldsymbol{c}\,\text{symm}\boldsymbol{\nabla u}$ into Π. The π functional can then be trivially shown to be

$$\pi(\boldsymbol{u},\boldsymbol{\psi},\text{skew}\boldsymbol{\sigma}) = \frac{1}{2}\int_\Omega \boldsymbol{c}\text{symm}\boldsymbol{\nabla u}\cdot\text{symm}\boldsymbol{\nabla u}\text{d}V + \int_\Omega(\text{skew}\boldsymbol{\nabla u}-\boldsymbol{\psi})\cdot\text{skew}\boldsymbol{\sigma}\text{d}V - \int_\Omega \boldsymbol{f}\cdot\boldsymbol{u}\text{d}V + \text{Boundary Terms}. \quad (2.19)$$

The functionals which have been presented thus far are not appropriate for numerical implementation. The Π functional suggested by Reissner in particular, was shown to have stability problems in the discrete form [18]. The variational problem of Reissner was modified in order to preserve the stability of the discrete problem by the addition of the term $\frac{1}{2\gamma}\int_\Omega |\text{skew}\boldsymbol{\sigma}|^2\,\text{d}V$ [18], as depicted in Figure 2.3. The resulting Hu-Washizu type functional H_γ, after the modification is thus given by

$$H_\gamma(\boldsymbol{u},\boldsymbol{\psi},\text{skew}\boldsymbol{\sigma},\text{symm}\boldsymbol{\sigma},\boldsymbol{\epsilon}) = \frac{1}{2}\int_\Omega \boldsymbol{c}\boldsymbol{\epsilon}\cdot\boldsymbol{\epsilon}\text{d}V + \int_\Omega(\text{symm}\boldsymbol{\nabla u}-\boldsymbol{\epsilon})\cdot\text{symm}\boldsymbol{\sigma}\text{d}V + \int_\Omega(\text{skew}\boldsymbol{\nabla u}-\boldsymbol{\psi})\cdot\text{skew}\boldsymbol{\sigma}\text{d}V - \frac{1}{2\gamma}\int_\Omega |\text{skew}\boldsymbol{\sigma}|^2\text{d}V - \int_\Omega \boldsymbol{f}\cdot\boldsymbol{u}\text{d}V + \text{Boundary Terms}. \quad (2.20)$$

The corresponding Hellinger-Reissner-like functional Π_γ can be shown to be

$$\Pi_\gamma(\boldsymbol{u},\boldsymbol{\psi},\text{skew}\boldsymbol{\sigma},\text{symm}\boldsymbol{\sigma}) = -\frac{1}{2}\int_\Omega \boldsymbol{s}\text{symm}\boldsymbol{\sigma}\cdot\text{symm}\boldsymbol{\sigma}\text{d}V + \int_\Omega \text{symm}\boldsymbol{\nabla u}\cdot\text{symm}\boldsymbol{\sigma}\text{d}V + \int_\Omega(\text{skew}\boldsymbol{\nabla u}-\boldsymbol{\psi})\cdot\text{skew}\boldsymbol{\sigma}\text{d}V - \frac{1}{2\gamma}\int_\Omega |\text{skew}\boldsymbol{\sigma}|^2\text{d}V - \int_\Omega \boldsymbol{f}\cdot\boldsymbol{u}\text{d}V + \text{Boundary Terms}, \quad (2.21)$$

and the equivalent π functional including $\text{skew}\boldsymbol{\sigma}$ can be written as

$$\pi_\gamma(\boldsymbol{u},\boldsymbol{\psi},\text{skew}\boldsymbol{\sigma}) = \frac{1}{2}\int_\Omega \boldsymbol{c}\text{symm}\boldsymbol{\nabla u}\cdot\text{symm}\boldsymbol{\nabla u}\text{d}V + \int_\Omega(\text{skew}\boldsymbol{\nabla u}-\boldsymbol{\psi})\cdot\text{skew}\boldsymbol{\sigma}\text{d}V - \frac{1}{2\gamma}\int_\Omega |\text{skew}\boldsymbol{\sigma}|^2\text{d}V - \int_\Omega \boldsymbol{f}\cdot\boldsymbol{u}\text{d}V + \text{Boundary Terms}. \quad (2.22)$$

Finally, it is possible, and indeed attractive for the skew-symmetric part of the stress tensor to be eliminated from the functionals by substituting $\text{skew}\boldsymbol{\sigma} = \gamma(\text{skew}\boldsymbol{\nabla u} - \boldsymbol{\psi})$, which appears as one of the Euler-Lagrange equations in the foregoing three functionals. The resulting Hu-Washizu like functional can be shown to be

$$\tilde{H}_\gamma(\boldsymbol{u}, \boldsymbol{\psi}, \text{symm}\boldsymbol{\sigma}, \boldsymbol{\epsilon}) = \frac{1}{2}\int_\Omega \boldsymbol{c\epsilon} \cdot \boldsymbol{\epsilon} \text{d}V + \int_\Omega (\text{symm}\boldsymbol{\nabla u} - \boldsymbol{\epsilon}) \cdot \text{symm}\boldsymbol{\sigma} \text{d}V + \frac{\gamma}{2}\int_\Omega |\text{skew}\boldsymbol{\nabla u} - \boldsymbol{\psi}|^2 \text{d}V - \int_\Omega \boldsymbol{f} \cdot \boldsymbol{u} \text{d}V + \text{Boundary Terms}. \quad (2.23)$$

Pimpinelli [20] used a slightly modified version of the $\tilde{H}_\gamma$ functional to derive a numerical model based on the minimisation of his modified Hu-Washizu like functional. His element is based in the framework of the assumed strain method of Simo and Rifai [59]. The Hellinger-Reissner like equivalent, using the base functional Π_γ is found to be

$$\tilde{\Pi}_\gamma(\boldsymbol{u}, \boldsymbol{\psi}, \text{symm}\boldsymbol{\sigma}) = -\frac{1}{2}\int_\Omega \boldsymbol{s}\text{symm}\boldsymbol{\sigma} \cdot \text{symm}\boldsymbol{\sigma} \text{d}V + \int_\Omega \text{symm}\boldsymbol{\nabla u} \cdot \text{symm}\boldsymbol{\sigma} \text{d}V + \frac{\gamma}{2}\int_\Omega |\text{skew}\boldsymbol{\nabla u} - \boldsymbol{\psi}|^2 \text{d}V - \int_\Omega \boldsymbol{f} \cdot \boldsymbol{u} \text{d}V + \text{Boundary Terms}. \quad (2.24)$$

Finally, the resulting 'irreducible' functional with only displacement and in-plane rotations as independent variables is

$$\tilde{\pi}_\gamma(\boldsymbol{u}, \boldsymbol{\psi}) = \frac{1}{2}\int_\Omega \boldsymbol{c}\text{symm}\boldsymbol{\nabla u} \cdot \text{symm}\boldsymbol{\nabla u} \text{d}V + \frac{\gamma}{2}\int_\Omega |\text{skew}\boldsymbol{\nabla u} - \boldsymbol{\psi}|^2 \text{d}V - \int_\Omega \boldsymbol{f} \cdot \boldsymbol{u} \text{d}V + \text{Boundary Terms}. \quad (2.25)$$

It can be shown that for each of the elements implemented in this chapter, the patch test is passed for any $\gamma > 0$ [18]. However, the parameter γ is problem dependent [18, 21], and its sensitivity is detailed in this chapter.

Since not all of the elements resulting from the formulations just highlighted are implemented here, Figure 2.4 depicts the links between the various functionals in relation to this study. The functionals contained in the top row are those based on Reissner's work [40], and were shown to have stability issues in discrete form. They therefore do not form part of this investigation. Also, although recently Pimpinelli [20] proposed an assumed strain quadrilateral element with drilling degrees of freedom, based on a functional similar to $\tilde{H}_\gamma$, elements based on Hu-Washizu like functionals are beyond the scope of this study. The elements considered in this study are based on the functionals enclosed by the solid line. Details of the variational formulations and numerical implementations of these elements can be found in many references, including [18, 21, 43] and are therefore not repeated here.

2.5 Finite element interpolation

In this section, the finite element interpolations employed in the elements arising from the variational formulations pointed out in the foregoing are presented. For the sake of brevity,

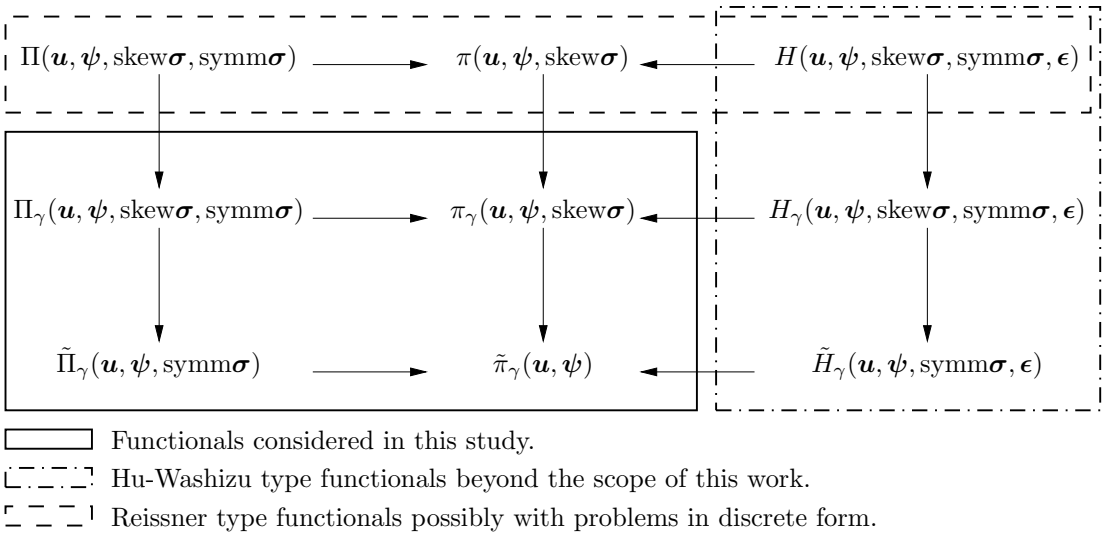

Figure 2.4: Applications of functionals proposed by Hughes and Brezzi in discrete form.

we refrain from giving the elemental stiffness matrices here, as they are easily derived through application of stationary principles to the functionals presented in the previous section.[4]

It is required that the three distinct independent interpolation fields arising from the translations, rotations and the assumed stress field are interpolated.[5] The standard element displacement gradient operators follow [43, 53].

Consider a 4-node quadrilateral element with degrees of freedom as depicted in Figure 2.5. The reference surface of the element is defined by

$$\boldsymbol{x} \;=\; \sum_{I=1}^{4} N_I^e(r,s)\boldsymbol{x}_I, \tag{2.26}$$

where $\boldsymbol{x}$ represents coordinates (x, y) and $N_I(r, s)$ are the isoparametric shape functions [60]

$$N_I^e(r,s) \;=\; \frac{1}{4}(1+r_I r)(1+s_I s)\;;\; I=1,2,3,4. \tag{2.27}$$

The independent rotation field is interpolated as a standard bilinear field over each element:

$$\theta_z \;\equiv\; \psi^h \;=\; \sum_e \sum_{I=1}^{4} N_I^e(r,s)\psi_i. \tag{2.28}$$

The in-plane displacement approximation is taken as an Allman-type interpolation

$$\begin{pmatrix} u_x \\ u_y \end{pmatrix} \;=\; \boldsymbol{u}^h \;=\; \sum_e \sum_{I=1}^{4} N_I^e(r,s)\boldsymbol{u}_I \;+\; \sum_e \sum_{I=5}^{8} NS_I^e(r,s)\frac{l_{JK}}{8}(\psi_K-\psi_J)\boldsymbol{n}_{JK}, \tag{2.29}$$

[4] Once again, these can be found in many references, including [21, 43, 52, 53].

[5] Since Hu-Washizu functionals are not considered, interpolation of strain or enhanced strain is not necessary.

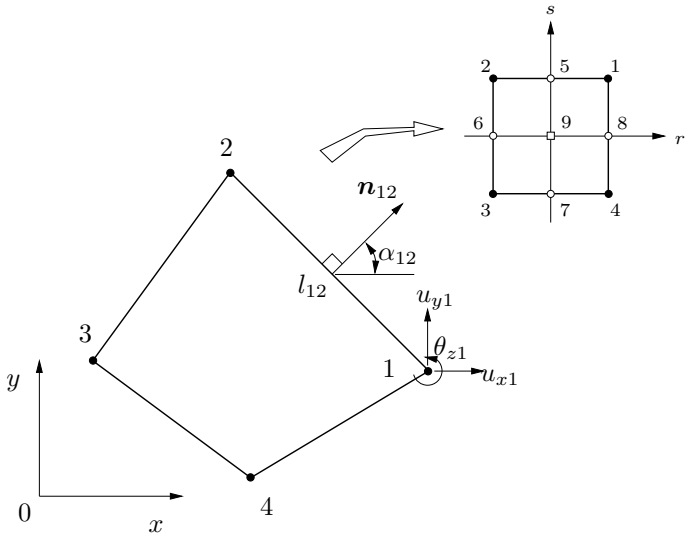

Figure 2.5: Four node element with drilling degrees of freedom.

where l_{JK} and $\boldsymbol{n}_{JK}$ are the length and the outward unit normal vector on the element side associated with the corner nodes J and K, i.e.

$$\boldsymbol{n}_{JK} \;=\; \left\{ \begin{array}{c} n_1 \\ n_2 \end{array} \right\} \;=\; \left\{ \begin{array}{c} \cos\alpha_{JK} \\ \sin\alpha_{JK} \end{array} \right\}, \tag{2.30}$$

and

$$l_{JK} \;=\; ((x_K - x_J)^2 + (y_K - y_J)^2)^{1/2}. \tag{2.31}$$

In the above, a FORTRAN-like definition of adjacent corner nodes is employed:

$$J \;=\; I - 4 \;;\quad K \;= \mathrm{mod}(I, 4) + 1. \tag{2.32}$$

In Equation (2.29) the serendipity shape functions are defined by

$$NS^e_I(r,s) \;=\; \frac{1}{2}(1 - r^2)(1 + s_I s) \;;\; I = 5, 7, \tag{2.33}$$

$$NS^e_I(r,s) \;=\; \frac{1}{2}(1 + r_I r)(1 - s^2) \;;\; I = 6, 8. \tag{2.34}$$

Employing matrix notation and defining

$$\mathrm{symm}\ \boldsymbol{\nabla} \boldsymbol{u}^e \;=\; \boldsymbol{B}^e_I \boldsymbol{u}_I \;+\; \boldsymbol{G}^e_I \psi_I, \tag{2.35}$$

where $\boldsymbol{u}_I$ and ψ_I are nodal values of the displacement and the rotation fields, respectively. The $\boldsymbol{B}^e_I$ matrix in Equation (2.35) has the standard form

$$\boldsymbol{B}^e_I \;=\; \left[\begin{array}{cc} N^e_{I,x} & 0 \\ 0 & N^e_{I,y} \\ N^e_{I,y} & N^e_{I,x} \end{array} \right] \;;\; I = 1, 2, 3, 4, \tag{2.36}$$

where $N_{I,x} = \frac{\partial N_I}{\partial x}$. The part of the displacement interpolation associated with the rotation defines

$$\boldsymbol{G}_I^e = \frac{1}{8}\begin{bmatrix} \left(l_{IJ}\cos\alpha_{IJ}NS^e_{L,x} - l_{IK}\cos\alpha_{IK}NS^e_{M,x}\right) \\ \left(l_{IJ}\sin\alpha_{IJ}NS^e_{L,y} - l_{IK}\sin\alpha_{IK}NS^e_{M,y}\right) \\ \left\{ \begin{array}{c} l_{IJ}\cos\alpha_{IJ}NS^e_{L,y} - l_{IK}\cos\alpha_{IK}NS^e_{M,y} \\ + \\ l_{IJ}\sin\alpha_{IJ}NS^e_{L,x} - l_{IK}\sin\alpha_{IK}NS^e_{M,x} \end{array} \right\} \end{bmatrix}, \tag{2.37}$$

where

$$I = 1,2,3,4;\ \ M = I+4;\ \ L = M - 1 + 4\text{int}(1/I);$$
$$K = \text{mod}(M,4) + 1;\ \ J = L - 4, \tag{2.38}$$

and

$$NS_{L,x} = \frac{\partial NS_L}{\partial x}.$$

Terms associated with the skew-symmetric part of the displacement gradient are now considered. Denoting

$$\text{skew}\ \boldsymbol{\nabla u}^e - \psi^e = \boldsymbol{b}_I^e \boldsymbol{u}_I + g_I^e \psi_I, \tag{2.39}$$

where

$$\boldsymbol{b}_I^e = < -\frac{1}{2}N^e_{I,y} \quad \frac{1}{2}N^e_{I,x} > ; \quad I = 1,2,3,4, \tag{2.40}$$

and

$$g_I^e = [-\frac{1}{16}(l_{IJ}\cos\alpha_{IJ}NS^e_{L,y} l_{IK}\cos\alpha_{IK}NS^e_{M,y})$$
$$+\frac{1}{16}(l_{IJ}\sin\alpha_{IJ}NS^e_{L,x} l_{IK}\sin\alpha_{IK}NS^e_{M,x}) - N_I^e] ; \quad I = 1,2,3,4, \tag{2.41}$$

with indices J, K, L, M again defined by (2.38)

For the assumed stress field, the global stresses are directly interpolated by the stress parameters β_i, i.e.

$$\text{symm}\ \boldsymbol{\sigma}^h = \sum_e \boldsymbol{P}^e \boldsymbol{\beta}^e, \tag{2.42}$$

where $\boldsymbol{P}^e$ is the interpolation matrix in terms of the local coordinates and $\boldsymbol{\beta}^e$ is the stress parameter vector. The stress field assumed in (2.42) may, without loss of generality, be expressed for an individual element as:

$$\text{symm}\ \boldsymbol{\sigma}^e = \boldsymbol{P\beta} = \text{symm}\ \boldsymbol{\sigma}_c^e + \text{symm}\ \boldsymbol{\sigma}_h^e = [\boldsymbol{I}_c\ \boldsymbol{P}_h]\left\{ \begin{array}{c} \boldsymbol{\beta}_c \\ \boldsymbol{\beta}_h \end{array} \right\}, \tag{2.43}$$

where the superscript e is dropped on $\boldsymbol{P}_*$ and $\boldsymbol{\beta}_*$ for reasons of clarity. In (2.43), $\boldsymbol{I}_c$ allows for the accommodation of constant stress states required to pass the patch test. The higher order stress field is represented by

$$\text{symm}\ \boldsymbol{\sigma}_h^e = \boldsymbol{P}_h\boldsymbol{\beta}_h = \boldsymbol{P}_{h2}\boldsymbol{\beta}_{h2} + \boldsymbol{P}_{h3}\boldsymbol{\beta}_{h3}, \tag{2.44}$$

where $\boldsymbol{P}_{h2}\boldsymbol{\beta}_{h2}$ and $\boldsymbol{P}_{h3}\boldsymbol{\beta}_{h3}$ are introduced for reasons of clarity. We select

$$\boldsymbol{P}_{h2}\boldsymbol{\beta}_{h2}+\boldsymbol{P}_{h3}\boldsymbol{\beta}_{h3} = \begin{bmatrix} \eta & 0 \\ 0 & \xi \\ 0 & 0 \end{bmatrix} \begin{Bmatrix} \beta_4 \\ \beta_5 \end{Bmatrix} + \begin{bmatrix} -\xi & 0 & \eta^2 \\ 0 & -\eta & -\xi^2 \\ \eta & \xi & 0 \end{bmatrix} \begin{Bmatrix} \beta_6 \\ \beta_7 \\ \beta_8 \end{Bmatrix}. \tag{2.45}$$

Combined with $\boldsymbol{I}_c$, $\boldsymbol{P}_{h2}$ yields the usual formulation for a 5-parameter stress field, as was for instance also used by Di and Ramm [61], for their 5β elements. $\boldsymbol{P}_{h3}$ represents the additional terms required for elements with drilling degrees of freedom. This formulation is similar to the unconstrained field used by Sze and Ghali [50]. However, (2.42) represents an unconstrained interpolation field, which is not necessarily optimal. Constraints may be enforced by a suitable transformation matrix (e.g. see [61]). Here, the rational constraints proposed by Pian and Sumihara [62] are opted for, viz.

$$\text{symm}\,\boldsymbol{\sigma}_h^e = \boldsymbol{P}_h\boldsymbol{\beta}_h = \boldsymbol{T}_0\boldsymbol{P}_{h2}\boldsymbol{\beta}_{h2}+\boldsymbol{T}_0\boldsymbol{P}_{h3}\boldsymbol{\beta}_{h3}, \tag{2.46}$$

with

$$\boldsymbol{T}_0 = \begin{bmatrix} a_1^2 & a_3^2 & 2a_1a_3 \\ b_1^2 & b_3^2 & 2b_1b_3 \\ a_1b_1 & a_3b_3 & a_1b_3+a_3b_1 \end{bmatrix}, \tag{2.47}$$

and

$$\begin{bmatrix} a_1 & b_1 \\ a_2 & b_2 \\ a_3 & b_3 \end{bmatrix} = \frac{1}{4}\begin{bmatrix} -1 & 1 & 1 & -1 \\ 1 & -1 & 1 & -1 \\ -1 & -1 & 1 & 1 \end{bmatrix} \begin{bmatrix} x_1 & y_1 \\ x_2 & y_2 \\ x_3 & y_3 \\ x_4 & y_4 \end{bmatrix}. \tag{2.48}$$

While normalized transformation of the higher order part of the stress field is probably more accurate [43], the rational approach of Pian and Sumihara is simpler, in particular if element equilibrium is enforced.

Finally, 9 stress parameters may also be used, even though this is one more than the optimal number of stress parameters. In this case, the higher order stress field becomes

$$\boldsymbol{P}_{h3}\boldsymbol{\beta}_{h3} = \begin{bmatrix} -\xi & 0 & \eta^2 & 0 \\ 0 & -\eta & 0 & -\xi^2 \\ \eta & \xi & 0 & 0 \end{bmatrix} \begin{Bmatrix} \beta_6 \\ \beta_7 \\ \beta_8 \\ \beta_9 \end{Bmatrix}. \tag{2.49}$$

2.6 Stability analysis

After Hughes and Brezzi, the simplest form of the functionals considered in Section 2.4, namely functional $\tilde{\pi}_\gamma(\boldsymbol{u},\boldsymbol{\psi})$ given by (2.25) is considered. The variational equation which results from variations on (2.25) is

$$\begin{aligned} 0 = \delta\tilde{\pi}_\gamma = &\int_\Omega \boldsymbol{c}\,\text{symm}\boldsymbol{\nabla}\boldsymbol{u}\cdot\text{symm}\boldsymbol{\nabla}\delta\boldsymbol{u}\mathrm{d}V \\ &+\gamma\int_\Omega(\text{skew}\boldsymbol{\nabla}\boldsymbol{u}-\boldsymbol{\psi})\cdot(\text{skew}\boldsymbol{\nabla}\delta\boldsymbol{u}-\delta\boldsymbol{\psi})\mathrm{d}V-\int_\Omega\boldsymbol{f}\cdot\delta\boldsymbol{u}\mathrm{d}V. \end{aligned} \tag{2.50}$$

Hughes and Brezzi then rewrite (2.50) as follows: Find $\{\boldsymbol{u}, \boldsymbol{\psi}\}$ such that

$$\boldsymbol{B}_\gamma(\boldsymbol{u}, \boldsymbol{\psi}; \delta\boldsymbol{u}, \delta\boldsymbol{\psi}) = \boldsymbol{f}(\{\delta\boldsymbol{u}, \delta\boldsymbol{\psi}\}), \tag{2.51}$$

for arbitrary variations $\delta\boldsymbol{u}$ and $\delta\boldsymbol{\psi}$, where $\boldsymbol{B}_\gamma(\boldsymbol{u}, \boldsymbol{\psi}; \delta\boldsymbol{u}, \delta\boldsymbol{\psi})$ is in symmetric bilinear form, and where $\boldsymbol{f}(\{\boldsymbol{v}, \boldsymbol{\omega}\})$ is continuous. It is now possible to prove that $\boldsymbol{B}_\gamma$ is U-elliptic [18], viz. there exists a constant $\eta_U > 0$, such that

$$\boldsymbol{B}_\gamma(\boldsymbol{u}, \boldsymbol{\psi}; \delta\boldsymbol{u}, \delta\boldsymbol{\psi}) \geq \eta_U ||\{\delta\boldsymbol{u}, \delta\boldsymbol{\psi}\}||_U^2, \ \forall \ \{\delta\boldsymbol{u}, \delta\boldsymbol{\psi}\} \in U, \tag{2.52}$$

where $U \equiv V \times W$, and V and W are appropriate spaces of displacement and rotation functions. For the Dirichlet problem and isotropy (see Hughes and Brezzi [18] for details), this results in

$$\gamma \leq \mu, \tag{2.53}$$

with μ the shear modulus. The equality or upper bound represented by (2.53) was selected by a number of authors. In Section 2.8, this bound is further reflected on from a numerical point of view. Incidentally, the numerical approach was already suggested by Hughes and Brezzi, who remark that 'numerical experimentation will be useful in finding optimal values for γ.'

2.7 Consistency and stability

It is well known that the elements with drilling DOFs considered herein all pass the patch test; they are also of adequate rank. Hence they are unconditionally convergent. This is true for any value of $\gamma > 0$ [18, 52].

This leads to the observation that the symmetry condition of the stress tensor should exactly be achieved for problems characterized by constant states of strain, viz. skew $\boldsymbol{\nabla u} - \boldsymbol{\psi} = 0$. Numerical experimentation reveals that this is, to machine precision, indeed the case for pure extension and pure shear patch tests, as well as the modified pure shear patch depicted in Figure 2.6.

2.8 Numerical experiments

In this section, numerical results for the elements highlighted in the foregoing are presented. The integration schemes employed on individual partition matrices are as given in [63]. The penalty matrix, relating displacements and in-plane rotations, is evaluated using a 1 point integration rule. The remaining partition stiffness terms are calculated using a 3×3 integration rule, although a reduced order (5 or 8 point) scheme could also be used. The following denotation is used:

- Q4X denotes drill elements without assumed stress interpolation. Unless otherwise stated, the mixed formulation, with functional represented by (2.22), is used.

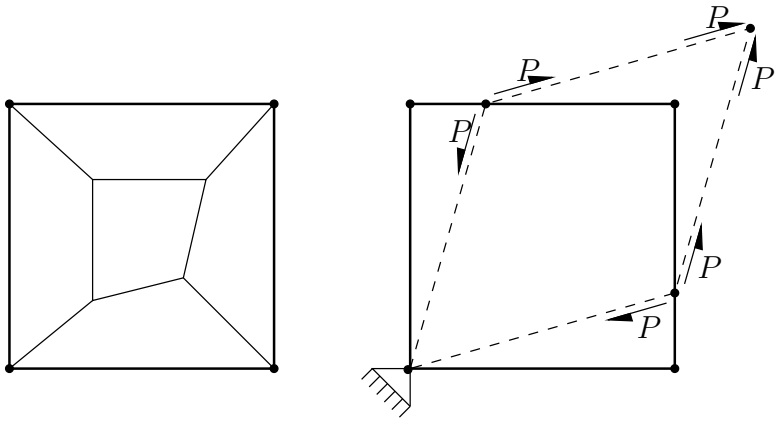

Figure 2.6: Modified shear patch test

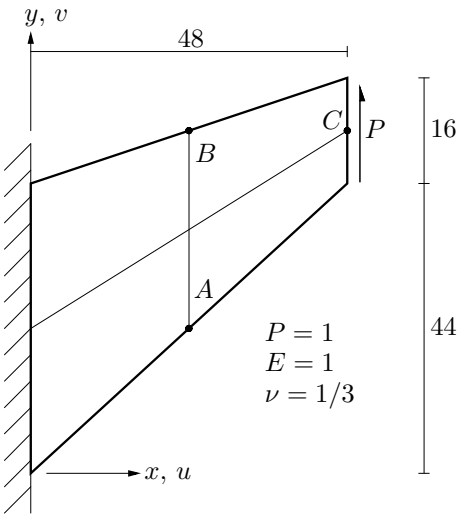

Figure 2.7: Cook's membrane

- 8β and 9β respectively indicates assumed stress drill elements with 8 and 9 stress interpolation parameters (see (2.45) and (2.49)). Unless otherwise stated, results are presented for the displacement formulation, this time represented by (2.24).

2.8.1 Cook's membrane

The popular swept and tapered cantilever beam subjected to a uniformly distributed tip load, as originally proposed by Cook, is depicted in Figure 2.7. Results as a function of parameter γ, are depicted in Figures 2.8 and 2.9, for respectively a 4×4 and a 32×32 mesh. At $\gamma = \mu$ there is a distinct change in slope of the beam tip displacement and rotation curves. The maximum value of skew$\boldsymbol{\sigma}$ over all elements, denoted τ_0 in the figures, is also reported (normalized with respect to it's value at $\gamma = \mu$). The value of τ_0 clearly increases sharply as γ increases above μ, and it is obvious that $\gamma \leq \mu$ is required. However, the equality is not necessarily optimal, $\gamma = \mu/10$, $\mu/100$, or even $\mu/1000$, may be more accurate.

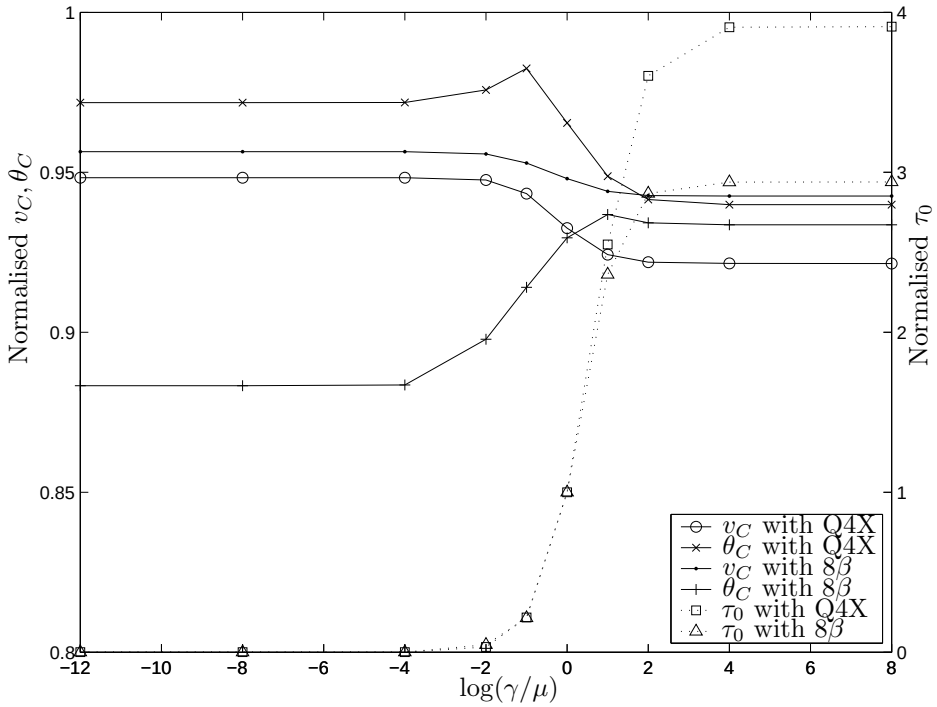

Figure 2.8: Cook's membrane: Effect of γ on displacement, rotation and skew $\boldsymbol{\sigma}$ for the 4×4 mesh

2.8.2 Cantilever beam subjected to end shear

A further popular test problem is the shear loaded cantilever beam depicted in Figure 2.10. For the penalty γ, a similar trend is observed to that of Cook's membrane above (Figure 2.11). Again the effect of γ is not nearly as pronounced on rotation and displacement as on the skew part of the stress tensor, and values of $\gamma < \mu$ seem suitable, rather than $\gamma = \mu$.

2.8.3 Orthotropic membrane cantilever

Next the orthotropic cantilever, depicted in Figure 2.12, is considered. Even though only one layer is considered, the strain variation becomes quite complex for non-zero ply angle arrangements [43].

Numerical results for the parameter γ are presented in Figures 2.13 and 2.14, for a ply arrangement of respectively 0 and 30 degrees. The displacement and rotation results are normalized with respect to solutions computed using a refined finite element mesh. For 0 degrees, the displacement based and stress based elements are almost identical (which is not surprising, since the mesh is regular).

For the 30 degrees orientation, the displacement and rotation prediction of the stress based element is superior, while this element also predicts a lower value of skew$\boldsymbol{\sigma}$. On the scale of the graphs, it is not very obvious how sensitive the displacement results are to the value of γ, however, results may differ by some 5% as a result of different values of γ. For this

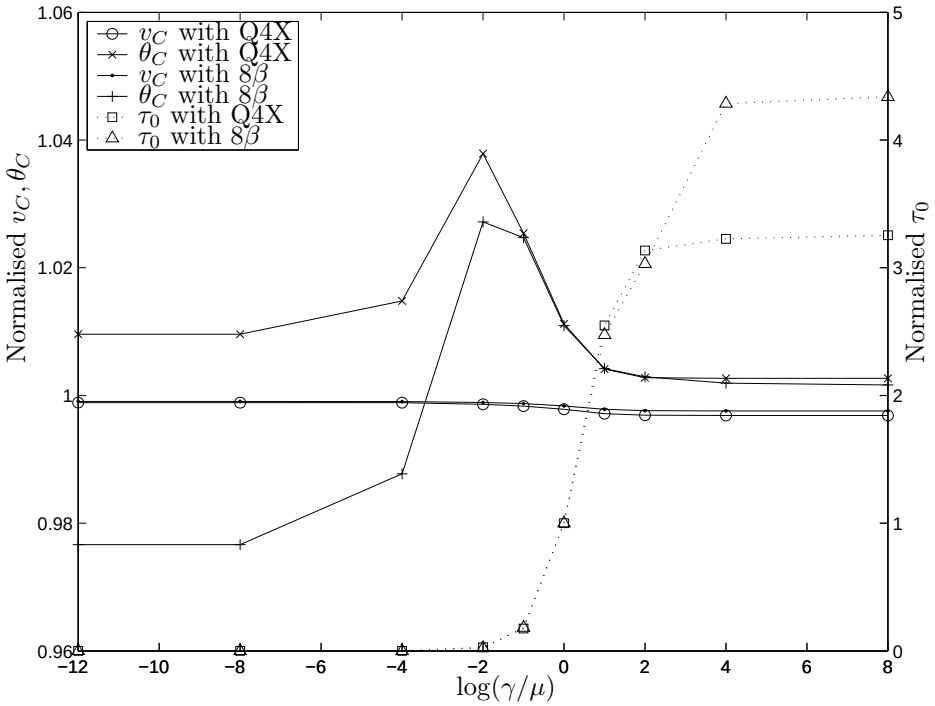

Figure 2.9: Cook's membrane: Effect of γ on displacement, rotation and skew $\boldsymbol{\sigma}$ for the 32×32 mesh

problem, it is clear that $\gamma = \mu_{12}$ is no longer ideal; values of $\gamma = \mu_{12}/10^3$ or even $\mu_{12}/10^4$ seem superior.

For the irregular distorted mesh, results are depicted in Figure 2.15. While the mesh distortion is probably a bit extreme, the effect of γ is illustrated clearly. Element performance starts to degrade from roughly $\gamma = \mu/10000$, and the degradation is quite pronounced. For this problem, the loss in accuracy of displacements, rotations as well as skew$\boldsymbol{\sigma}$ due to high values of γ is significant.

2.9 Conclusions

In this chapter, the formulation of finite elements with drilling DOFs has briefly been outlined. Thereafter, a numerical investigation into the effect of the penalty parameter in elements with drilling degrees of freedom, for which the stress tensor $\boldsymbol{\sigma}$ is not *a priori* assumed to be symmetric, has been presented. The parameter under investigation is γ, which relates the in-plane translations to the rotations.

Rather than only reporting on the quantitative influence of the penalty parameter γ on measures like displacement, rotation and stress, the skewness of the nonsymmetric part of the stress tensor $\boldsymbol{\sigma}$, is directly assessed. Results are presented for both isotropic and orthotropic constitutive relationships.

It is shown that, in general, values smaller than $\gamma = \mu$, with μ the shear modulus, are

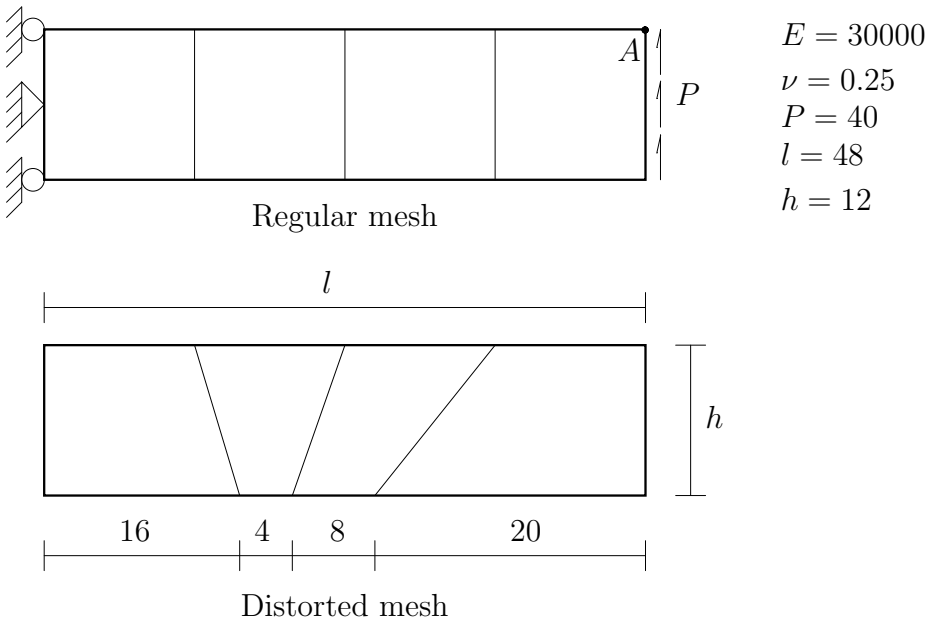

Figure 2.10: Cantilever beam under shear load

desirable, even though the formulation is convergent for all values of γ. Values of $\gamma/\mu = 10^{-1}$ or 10^{-2} seem to result in accurate solutions. However, in implementing elements with drilling degrees of freedom based on the procedure suggested by Hughes and Brezzi [18], the skewness of the nonsymmetric part of the stress tensor $\boldsymbol{\sigma}$, may directly be used to quantitatively assess the validity of selected values of γ.

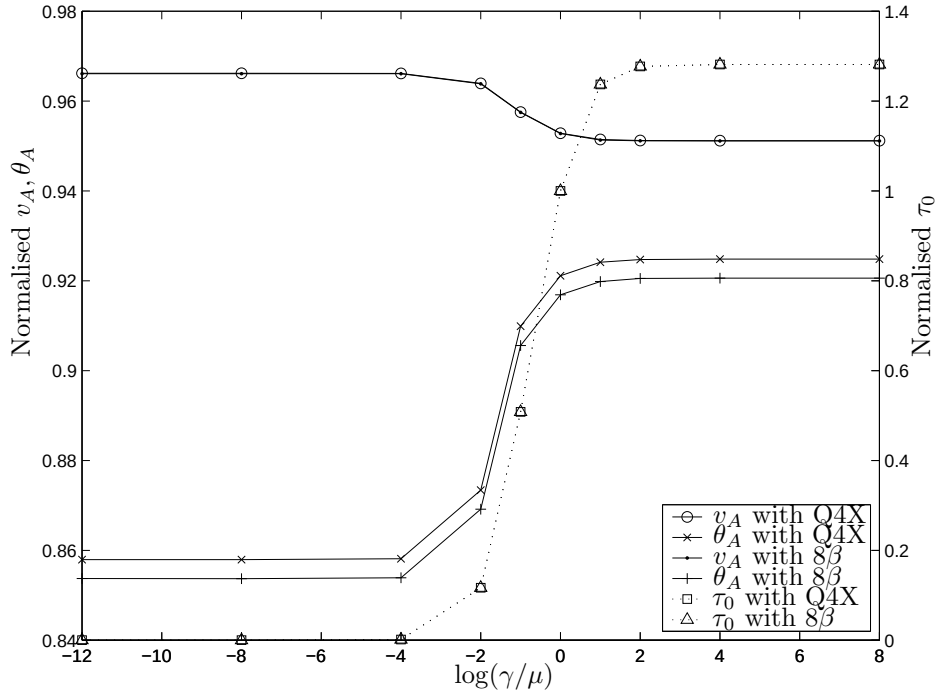

Figure 2.11: Cantilever beam: Effect of γ on tip displacement and skew $\boldsymbol{\sigma}$

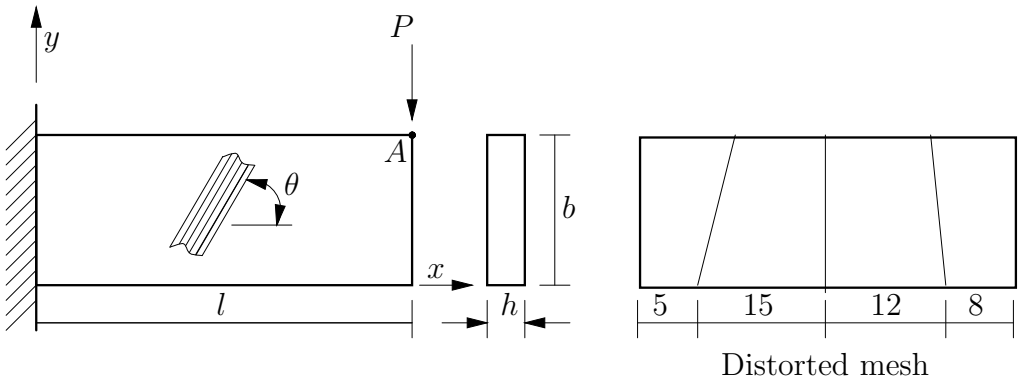

Figure 2.12: Orthotropic membrane cantilever

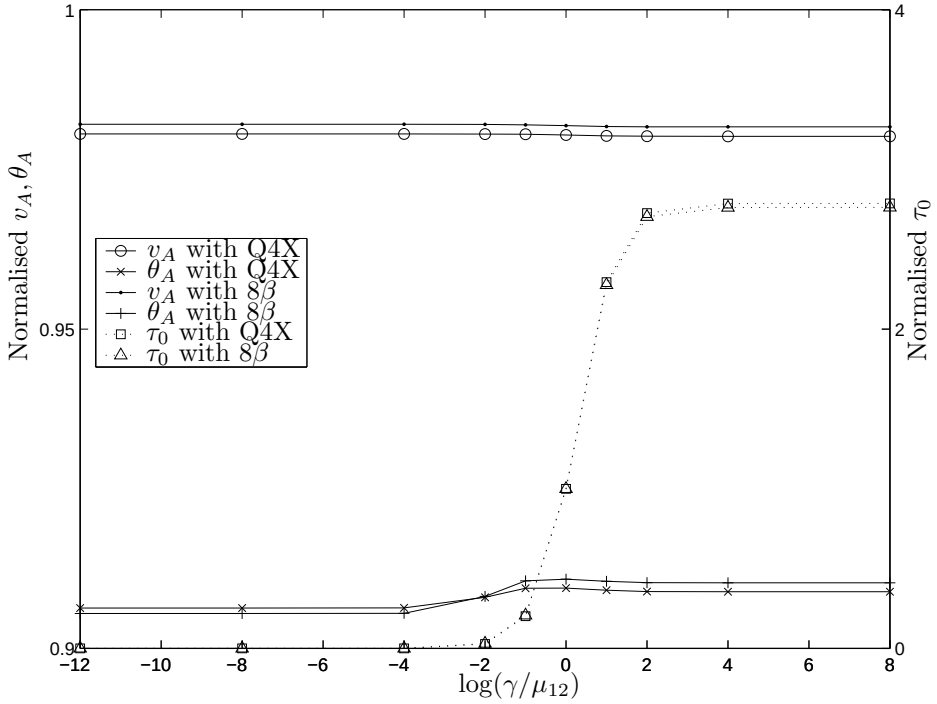

Figure 2.13: Orthotropic membrane cantilever: Effect of γ for a 0 degree ply arrangement (regular mesh)

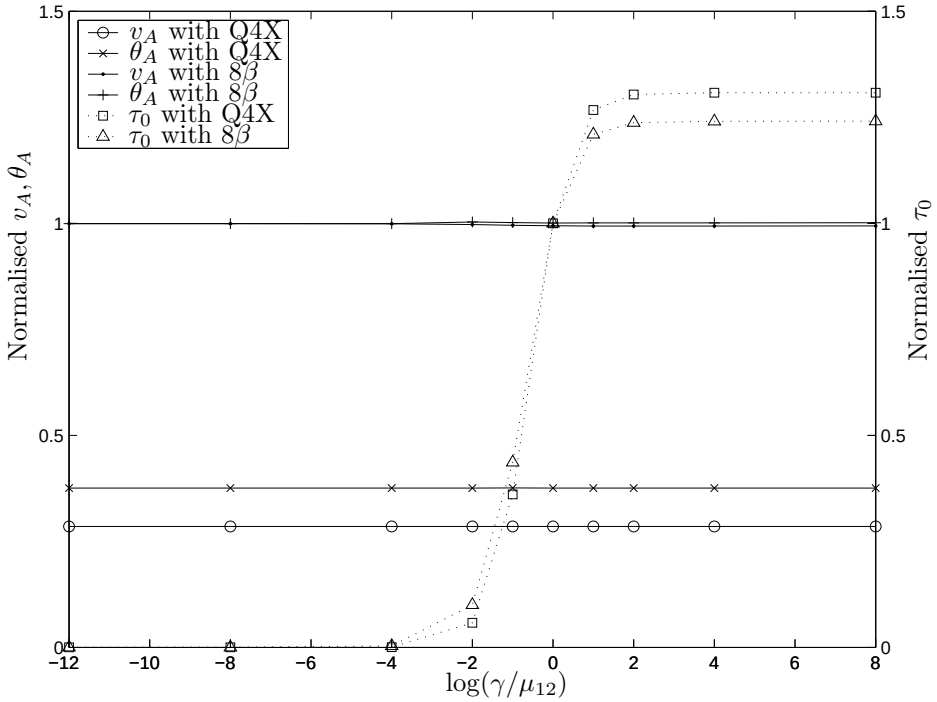

Figure 2.14: Orthotropic membrane cantilever: Effect of γ for a 30 degree ply arrangement (regular mesh)

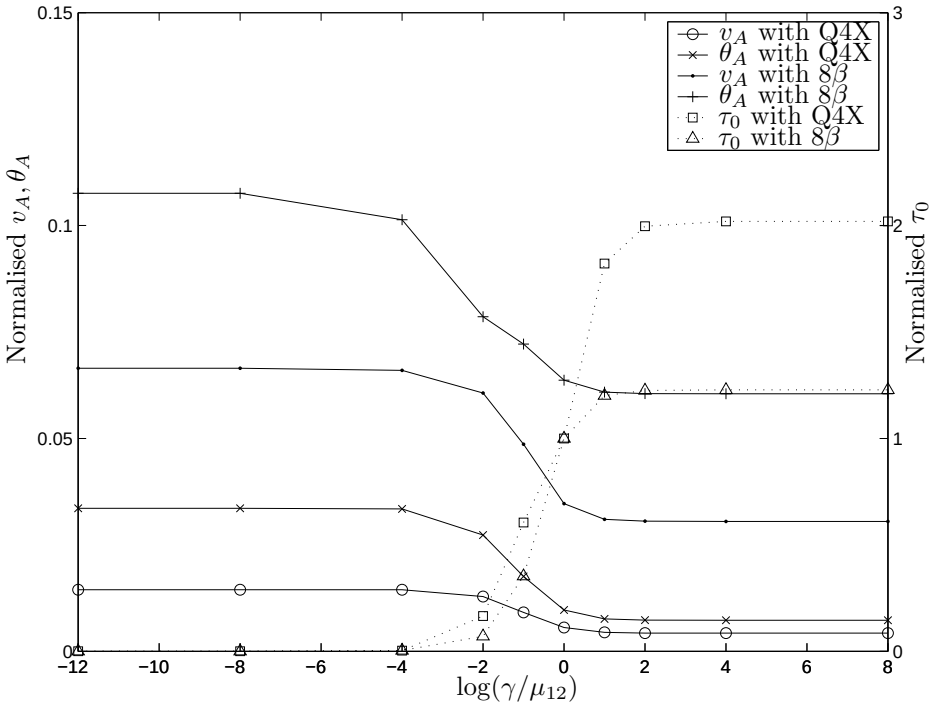

Figure 2.15: Orthotropic membrane cantilever: Effect of γ for a 30 degree ply arrangement (distorted mesh)

Chapter 3

Piezoelectric elements with drilling degrees of freedom

3.1 Summary

In this chapter, several new planar four node piezoelectric elements with drilling degrees of freedom are presented. Firstly, two families of variational formulations accounting for piezoelectricity and in-plane rotations are derived. The first family retains the skew-symmetric part of the stress tensor, while in the second, the skew part of stress is eliminated from the functional. The performance of the finite elements derived from the variational formulations presented in this chapter are then investigated. The resulting new elements are shown to be accurate and robust in comparison with a number of existing elements, for several benchmark test problems.

3.1.1 Another brief word on notation

As explained in Section 2.1.1, the symbolic designation traditionally used by researchers working in piezoelectric finite element development, e.g. see [64, 65, 66] is now reverted to. In particular, the symbols used to denote mechanical quantities and properties are different to those employed in Chapter 2. Once again, the symbols are defined during the course of the chapter.

We continue to employ the same tensor notation as that introduced in Chapter 2, which is similar to that employed by, for example, Pimpinelli [20] and Cannarozzi and Ubertini [66].

3.2 Introduction

In recent years, the use of smart materials has become widespread and almost commonplace. The technology employed in piezoelectric applications in particular, has reached a mature level, and piezoelectric materials are frequently used in engineering applications.

Piezoelectric materials transfer electric energy to mechanical energy and *vice versa*, and can therefore be used as either actuators or sensors, or both. Applications include ultrasonic transducers for sonar and medical purposes, compact ultrasonic piezoelectric motors, structural monitoring and/or active damping elements, and even ignition systems.

Analytical closed-form solutions to problems involving piezoelectric materials are often difficult to compute, unless geometries and boundary conditions are relatively simple, see for example Heyliger [67] and Kapuria *et al.* [68]. A general numerical method for the solution of piezoelectric problems is therefore essential. (Analytical solutions are, however, very useful as benchmark problems.)

The finite element method has become a standard modelling utility for various physical processes, including piezoelectricity. Development of piezoelectric finite elements has progressed significantly since the early paper of Allik and Hughes [69]. In fact, Benjeddou [70] presented a survey article in which over 100 recent papers from the open literature are reviewed, indicating the research interest in the field.

The original implementation of Allik and Hughes, and many of the finite elements since, (see Benjeddou for examples), have been based on formulations interpolating for only kinematic–like variables, i.e. displacement and electric potential. These elements are often stiff, inaccurate and sensitive to mesh distortion. To alleviate these problems, mixed and hybrid variational formulations have been developed (see for example Yang [71]), with original contributions in variational formulations for piezoelectric media credited to EerNisse and Holland [72, 73]. Various hybrid and mixed finite elements have since been developed, with notable contributions by Cannarozzi and Ubertini [66] and Sze and co-workers [64, 65, 74, 75, 76].

Independent of the development of piezoelectric finite elements, many advances have been made in the development of elastic finite elements. One of the significant contributions has been the addition of in-plane rotations, or drilling degrees of freedom (DOFs). Drilling DOFs are particularly important in shell elements, since the result is a shell element with six DOFs per node, which allows for the modelling of beam-slab connections and folded plates. An introduction into, and a brief history of, elements with drilling DOFs and their variational formulation can be found in Chapter 2, and will therefore not be repeated here.

The aim of this chapter is to combine the theory, developed for elastic elements with drilling DOFs, with some recent advances in piezoelectric finite element technology. The result is two new families of accurate, piezoelectric finite elements with drilling DOFs.

We endeavour to, not only improve on element accuracy, but importantly, improve on the modelling capabilities of existing piezoelectric finite elements. In fact, the piezoelectric elements developed herein are used in a topology optimization environment, together with elastic elements possessing drilling DOFs, see Chapter 5 and [77]. Their accuracy can also be exploited in fracture analyses. Aside from the improved accuracy, these elements can be employed to calculate through-thickness phenomena in thick piezoelectric shells. The variational formulations can also be used to generate three dimensional solid elements with drilling DOFs. These solid elements would possess three displacement, three rotational and one potential DOF per node.

The remainder of this chapter is set out as follows. In Section 3.3, the equations governing the linear electroelastic problem are presented. Section 3.4 introduces a number of new

variational formulations accounting for piezoelectricity and in-plane rotations. In Section 3.5 the interpolations used in the finite element implementations are briefly highlighted. Section 3.6 details the finite element implementation of our variational formulations. The partitioned submatrices arising from the finite element implementations are presented in Section 3.7. Section 3.8 contains the results of a numerical evaluation of the new elements. Finally, in Section 3.9 some closing remarks are offered.

3.3 Governing equations

In this section, the equations governing the linear electroelastic problem are presented in strong form. Let $\bar{\Omega}$ be a closed and bounded domain occupied by a body in three dimensional space. The interior part of $\bar{\Omega}$ is denoted by Ω and it's boundary by $\partial\Omega$, $\Omega \cup \partial\Omega = \bar{\Omega}$. The measure of Ω is V and the measure of $\partial\Omega$ is S. $\mathcal{V}$ is the vector space associated with the Euclidean point space and $\mathcal{L}$ the space of all linear applications of $\mathcal{V}$ into $\mathcal{V}$, which possesses inner product $\boldsymbol{A} \cdot \boldsymbol{B} = \mathrm{tr}(\boldsymbol{A}^t\boldsymbol{B})$, $\boldsymbol{A}, \boldsymbol{B} \in \mathcal{L}$ and $\boldsymbol{A}^t$ the transpose of $\boldsymbol{A}$ (see Pimpinelli [20]). Reference will also be made to subsets of $\mathcal{L}$, namely $\mathcal{S}$ and $\mathcal{W}$ which contain, respectively symmetric and skew-symmetric tensors in $\mathcal{L}$.

The boundary $\partial\Omega$, is split into four parts, $\partial\Omega_u$, $\partial\Omega_t$, $\partial\Omega_\phi$ and $\partial\Omega_d$ such that $\partial\Omega_u \cup \partial\Omega_t = \partial\Omega_\phi \cup \partial\Omega_d = \partial\Omega$ and $\partial\Omega_u \cap \partial\Omega_t = \partial\Omega_\phi \cap \partial\Omega_d = \emptyset$. On $\partial\Omega_u$ displacements $\bar{\boldsymbol{u}}$ are prescribed, while on $\partial\Omega_t$ the traction $\bar{\boldsymbol{t}}$ is prescribed. Similarly, on $\partial\Omega_\phi$ the prescribed potentials are $\bar{\phi}$ and on $\partial\Omega_d$ the density of the electric charge $\bar{d}$ is prescribed.

The Euclidean decomposition of second-rank tensors is frequently employed, e.g.

$$\boldsymbol{T} = \mathrm{symm}\boldsymbol{T} + \mathrm{skew}\boldsymbol{T}, \tag{3.1}$$

where

$$\mathrm{symm}\boldsymbol{T} = \frac{1}{2}(\boldsymbol{T} + \boldsymbol{T}^t), \tag{3.2}$$

$$\mathrm{skew}\boldsymbol{T} = \frac{1}{2}(\boldsymbol{T} - \boldsymbol{T}^t). \tag{3.3}$$

The linear electroelastic problem is governed by the following conditions at all points $\boldsymbol{x} \in \bar{\Omega}$.

3.3.1 Constitutive equations

There exist four equivalent versions of the electroelastic constitutive equations, depending on the choice of independent variables (see for example Ikeda [78]). The constitutive equations, in terms of strain and electric field are:

$$\begin{aligned} \boldsymbol{T} &= \boldsymbol{c}_E\boldsymbol{S} - \boldsymbol{e}^t\boldsymbol{E}, \\ \boldsymbol{D} &= \boldsymbol{e}\boldsymbol{S} + \boldsymbol{\epsilon}_S\boldsymbol{E}, \end{aligned} \tag{3.4}$$

where $\boldsymbol{T}$ and $\boldsymbol{S}$ are the stress and strain tensors, $\boldsymbol{D}$ is the electric flux density, also referred to as electric displacement (see for example Wu *et al.* [65]), and $\boldsymbol{E}$ denotes the electric

field. Furthermore, $\boldsymbol{c}_E$ is a fourth order tensor of elastic stiffness, measured at constant electric field as indicated by the subscript 'E'. $\boldsymbol{\epsilon}_S$ is the second order permittivity tensor at constant strain, and $\boldsymbol{e}$ is a third order electroelastic, or piezoelectric, coupling tensor. Both $\boldsymbol{c}_E$ and $\boldsymbol{\epsilon}_S$ are symmetric and positive definite. As described by Cannarozzi and Ubertini [66], $\boldsymbol{e}$ is such that the product $\boldsymbol{e}^t\boldsymbol{a}$ is a second order symmetric tensor for each vector $\boldsymbol{a}$, with $\boldsymbol{e}^t$ defined as $\boldsymbol{A}\cdot\boldsymbol{e}^t\boldsymbol{a} = \boldsymbol{e}\boldsymbol{A}\cdot\boldsymbol{a}$, and $\boldsymbol{A}$ a symmetric second order tensor. Incidentally, the constitutive relations in terms of strain and electric field were used in the original finite element implementations [69].

Since the derivation of the other forms of the constitutive equations, through Legendre transformation, are well known (see for example [66, 78]) they will simply be stated here without further elaboration.

In terms of strain $\boldsymbol{S}$ and electric flux density $\boldsymbol{D}$, the relations are

$$\begin{aligned} \boldsymbol{T} &= \boldsymbol{c}_D\boldsymbol{S} - \boldsymbol{h}^t\boldsymbol{D}, \\ \boldsymbol{E} &= -\boldsymbol{h}\boldsymbol{S} + \boldsymbol{\chi}_S\boldsymbol{D}, \end{aligned} \tag{3.5}$$

and the constitutive terms are computed as

$$\boldsymbol{c}_D = \boldsymbol{c}_E + \boldsymbol{e}^t\boldsymbol{\epsilon}_S^{-1}\boldsymbol{e}, \quad \boldsymbol{h} = \boldsymbol{\epsilon}_S^{-1}\boldsymbol{e}, \quad \boldsymbol{\chi}_S = \boldsymbol{\epsilon}_S^{-1}. \tag{3.6}$$

Rewriting in terms of stress $\boldsymbol{T}$ and electric field $\boldsymbol{E}$, get

$$\begin{aligned} \boldsymbol{S} &= \boldsymbol{s}_E\boldsymbol{T} + \boldsymbol{d}^t\boldsymbol{E}, \\ \boldsymbol{D} &= \boldsymbol{d}\boldsymbol{T} + \boldsymbol{\epsilon}_T\boldsymbol{E}, \end{aligned} \tag{3.7}$$

with

$$\boldsymbol{s}_E = \boldsymbol{c}_E^{-1}, \quad \boldsymbol{d} = \boldsymbol{e}\boldsymbol{c}_E^{-1}, \quad \boldsymbol{\epsilon}_T = \boldsymbol{\epsilon}_S + \boldsymbol{e}\boldsymbol{c}_E^{-1}\boldsymbol{e}^t. \tag{3.8}$$

Finally, with stress $\boldsymbol{T}$ and electric flux density $\boldsymbol{D}$ selected as independent variables, the result is

$$\begin{aligned} \boldsymbol{S} &= \boldsymbol{s}_D\boldsymbol{T} + \boldsymbol{g}^t\boldsymbol{D}, \\ \boldsymbol{E} &= -\boldsymbol{g}\boldsymbol{T} + \boldsymbol{\chi}_T\boldsymbol{D}, \end{aligned} \tag{3.9}$$

with

$$\boldsymbol{s}_D = (\boldsymbol{c}_E + \boldsymbol{e}^t\boldsymbol{\epsilon}_S^{-1}\boldsymbol{e})^{-1}, \quad \boldsymbol{g} = \boldsymbol{\epsilon}_S^{-1}\boldsymbol{e}\boldsymbol{s}_D, \quad \boldsymbol{\chi}_T = \boldsymbol{\epsilon}_S^{-1} - \boldsymbol{\epsilon}_S^{-1}\boldsymbol{e}\boldsymbol{s}_D\boldsymbol{e}^t\boldsymbol{\epsilon}_S^{-1}. \tag{3.10}$$

The tensors $\boldsymbol{c}_D$, $\boldsymbol{s}_E$, $\boldsymbol{s}_D$, $\boldsymbol{\chi}_S$, $\boldsymbol{\chi}_T$ and $\boldsymbol{\epsilon}_T$ are all symmetric and positive definite, and $\boldsymbol{h}$, $\boldsymbol{d}$ and $\boldsymbol{g}$ are third order tensors with the same properties as $\boldsymbol{e}$. In the presentation of the constitutive equations a condensed notation, assuming symmetric stress and strain tensors is used for the sake of clarity. That is to say, in (3.4), (3.5), (3.7) and (3.9), $\boldsymbol{T} \equiv \text{symm}\boldsymbol{T}$ and $\boldsymbol{S} \equiv \text{symm}\boldsymbol{S}$. This is of importance, since the stress tensor in the formulations to follow are not *a priori* assumed to be symmetric.

3.3.2 Compatibility conditions

The strain-displacement and electric field-potential relationships, together with the displacement and electric potential boundary conditions are, respectively

$$\boldsymbol{S} = \text{symm}\boldsymbol{\nabla u} \quad \text{in } \Omega, \tag{3.11}$$
$$\boldsymbol{E} = -\nabla\phi \quad \text{in } \Omega, \tag{3.12}$$
$$\boldsymbol{u} = \bar{\boldsymbol{u}} \quad \text{on } \partial\Omega_u, \tag{3.13}$$
$$\phi = \bar{\phi} \quad \text{on } \partial\Omega_\phi, \tag{3.14}$$

where $\boldsymbol{u}$ is the displacement vector field, and ϕ represents the scalar electric potential field.

3.3.3 Equilibrium conditions

The static force equilibrium equations and Gauss's Law in differential form, together with the boundary conditions, are given by:

$$\text{div}\boldsymbol{T} + \boldsymbol{f} = \boldsymbol{0} \quad \text{in } \Omega, \tag{3.15}$$
$$\text{div}\boldsymbol{D} - q = 0 \quad \text{in } \Omega, \tag{3.16}$$
$$\text{symm}\boldsymbol{T}\,\boldsymbol{n} = \bar{\boldsymbol{t}} \quad \text{on } \partial\Omega_t, \tag{3.17}$$
$$\boldsymbol{D}\cdot\boldsymbol{n} = -\bar{d} \quad \text{on } \partial\Omega_d, \tag{3.18}$$

where $\boldsymbol{f}$ is a distributed body force, q is a distributed electric charge in Ω, and $\boldsymbol{n}$ is the unit outward normal vector on $\partial\Omega$. Usually q is taken as zero [71], but for completeness it will be included in the presentation to follow.

3.3.4 Rotational momentum balance conditions and definition of infinitesimal rotation

In the current formulation, the stress tensor $\boldsymbol{T}$ is not *a priori* assumed to be symmetric, and in-plane rotations are included. The following two additional conditions need to be satisfied:

$$\text{skew}\boldsymbol{T} = \boldsymbol{0} \quad \text{in } \Omega, \tag{3.19}$$
$$\boldsymbol{\psi} = \text{skew}\boldsymbol{\nabla u} \quad \text{in } \Omega, \tag{3.20}$$

where (3.19) represents the rotational momentum balance conditions and (3.20) is the definition of infinitesimal rotations in terms of displacement gradient.

3.4 Variational formulation

Hughes and Brezzi [18] presented a general framework within which to construct variational formulations for problems which include rotational freedom. This framework is outlined in

Section 2.4. The most general type is their Hu-Washizu-like variational formulation accounting for rotations and nonsymmetric stress tensors. The variational framework of Hughes and Brezzi is now generalised to account for the piezoelectric effect.

In the functionals to follow, unless otherwise stated, $\boldsymbol{u}, \phi, \boldsymbol{E}$ and $\boldsymbol{D}$ are the displacement, electric potential, electric field and electric flux density fields, respectively. The nonsymmetric stress tensor is denoted $\boldsymbol{T} \in \mathcal{L}$. The skew-symmetric infinitesimal spin or rotation tensor is $\boldsymbol{\psi} \in \mathcal{W}$, and $\boldsymbol{S} \in \mathcal{S}$ is the symmetric strain tensor. Where applicable, they are sufficiently regular and square integrable functions of $\boldsymbol{x}$. In particular, the rotations $\boldsymbol{\psi}$, strains $\boldsymbol{S}$, stresses $\boldsymbol{T}$, electric field $\boldsymbol{E}$, electric flux density $\boldsymbol{D}$, as well as the generalised derivatives $\boldsymbol{\nabla u}$ and $\boldsymbol{\nabla}\phi$ belong to the space of square integrable functions over Ω.

3.4.1 Hu-Washizu-like variational formulations

A Hu-Washizu-like variational formulation is now proposed. It is also shown how this leads to a Hellinger-Reissner-like functional, as well as functionals in an irreducible form. The aim is not to present a rigorous mathematical study of the presented formulations. Rather, in the latter part of this chapter, a numerical study of the discrete finite element implementation is presented.

Two formulation families are proposed. The first, designated here as M-Type, retains the skew-symmetric part of the stress tensor. Since part of the stress tensor is always retained, even in its simplest or irreducible form, M-Type functionals will result in a *mixed* formulation, even in the 'irreducible' form. In the second family, denoted K-Type, the skew-symmetric part of stress is eliminated. The result is an irreducible form which requires only *kinematic*–like interpolations, i.e. displacement and electric potential.

M-Type formulation based on functional Π^H_M

The following Hu-Washizu-like functional is proposed:

$$\begin{aligned}\Pi^H_M(\boldsymbol{u}, \boldsymbol{\psi}, \mathrm{symm}\boldsymbol{T}, \mathrm{skew}\boldsymbol{T}, \boldsymbol{S}, \phi, \boldsymbol{D}, \boldsymbol{E}) = \frac{1}{2}\int_\Omega \boldsymbol{c}_E\ \boldsymbol{S}\cdot\boldsymbol{S}\,\mathrm{d}V - \int_\Omega \boldsymbol{e}\ \boldsymbol{S}\cdot\boldsymbol{E}\,\mathrm{d}V \\ - \frac{1}{2}\int_\Omega \boldsymbol{\epsilon}_S\ \boldsymbol{E}\cdot\boldsymbol{E}\,\mathrm{d}V + \int_\Omega (\mathrm{symm}\boldsymbol{\nabla u} - \boldsymbol{S})\cdot\mathrm{symm}\boldsymbol{T}\,\mathrm{d}V + \int_\Omega (\mathrm{skew}\boldsymbol{\nabla u} - \boldsymbol{\psi})\cdot\mathrm{skew}\boldsymbol{T}\,\mathrm{d}V \\ + \int_\Omega (\boldsymbol{\nabla}\phi + \boldsymbol{E})\cdot\boldsymbol{D}\,\mathrm{d}V - \frac{1}{2}\gamma^{-1}\int_\Omega |\mathrm{skew}\boldsymbol{T}|^2\,\mathrm{d}V - \int_\Omega \boldsymbol{f}\cdot\boldsymbol{u}\,\mathrm{d}V + \int_\Omega q\,\phi\,\mathrm{d}V \\ - \int_{\partial\Omega_t} \bar{\boldsymbol{t}}\cdot\boldsymbol{u}\,\mathrm{d}S + \int_{\partial\Omega_d} \bar{d}\,\phi\,\mathrm{d}S - \int_{\partial\Omega_u} (\boldsymbol{u}-\bar{\boldsymbol{u}})\cdot(\boldsymbol{T}\,\boldsymbol{n})\,\mathrm{d}S - \int_{\partial\Omega_\phi} (\phi-\bar{\phi})(\boldsymbol{D}\cdot\boldsymbol{n})\,\mathrm{d}S,\end{aligned} \tag{3.21}$$

where the subscript 'M' emphasises that the functional is of M-type and the superscript 'H' that it is a Hu-Washizu-like functional. The term $\frac{1}{2}\gamma^{-1}\int_\Omega |\mathrm{skew}\boldsymbol{T}|^2\,\mathrm{d}V$ was shown to preserve the ellipticity of the discrete problem in linear elastostatics [18]. In (3.21), the term $\boldsymbol{Tn}$ in the boundary term on $\partial\Omega_u$ was found to be the Lagrange multiplier which enforces

the prescribed displacements, where $\boldsymbol{T} \equiv \text{symm}\boldsymbol{T} + \text{skew}\boldsymbol{T}$. The condition of stationarity gives rise to the following variational equation:

$$\begin{aligned}
\delta\Pi_M^H = 0 = &\int_\Omega \boldsymbol{c}_E\boldsymbol{S}\cdot\delta\boldsymbol{S}\,\mathrm{d}V - \int_\Omega \boldsymbol{e}\boldsymbol{S}\cdot\delta\boldsymbol{E}\,\mathrm{d}V - \int_\Omega \boldsymbol{e}^t\boldsymbol{E}\cdot\delta\boldsymbol{S}\,\mathrm{d}V - \int_\Omega \boldsymbol{\epsilon}_S\boldsymbol{E}\cdot\delta\boldsymbol{E}\,\mathrm{d}V \\
&+ \int_\Omega (\text{symm}\boldsymbol{\nabla}\boldsymbol{u} - \boldsymbol{S})\cdot\text{symm}\delta\boldsymbol{T}\,\mathrm{d}V + \int_\Omega \text{symm}\boldsymbol{T}\cdot\text{symm}\boldsymbol{\nabla}\delta\boldsymbol{u} - \text{symm}\boldsymbol{T}\cdot\delta\boldsymbol{S}\,\mathrm{d}V \\
&+ \int_\Omega (\text{skew}\boldsymbol{\nabla}\boldsymbol{u} - \boldsymbol{\psi})\cdot\text{skew}\delta\boldsymbol{T}\,\mathrm{d}V + \int_\Omega \text{skew}\boldsymbol{T}\cdot\text{skew}\boldsymbol{\nabla}\delta\boldsymbol{u} - \text{skew}\boldsymbol{T}\cdot\delta\boldsymbol{\psi}\,\mathrm{d}V \\
&+ \int_\Omega (\boldsymbol{\nabla}\phi + \boldsymbol{E})\cdot\delta\boldsymbol{D}\,\mathrm{d}V + \int_\Omega \boldsymbol{D}\cdot\boldsymbol{\nabla}\delta\phi + \boldsymbol{D}\cdot\delta\boldsymbol{E}\,\mathrm{d}V - \int_\Omega \gamma^{-1}\text{skew}\boldsymbol{T}\cdot\text{skew}\delta\boldsymbol{T}\,\mathrm{d}V \\
&- \int_\Omega \boldsymbol{f}\cdot\delta\boldsymbol{u}\,\mathrm{d}V + \int_\Omega q\delta\phi\,\mathrm{d}V - \int_{\partial\Omega_t} \bar{\boldsymbol{t}}\cdot\delta\boldsymbol{u}\,\mathrm{dS} + \int_{\partial\Omega_d} \bar{d}\delta\phi\,\mathrm{dS} \\
&- \int_{\partial\Omega_u} [(\boldsymbol{u} - \bar{\boldsymbol{u}})\cdot(\delta\boldsymbol{T}\boldsymbol{n}) - (\boldsymbol{T}\boldsymbol{n})\cdot\delta\boldsymbol{u}]\,\mathrm{dS} \\
&- \int_{\partial\Omega_\phi} \left[(\phi - \bar{\phi})(\delta\boldsymbol{D}\cdot\boldsymbol{n}) - (\boldsymbol{D}\cdot\boldsymbol{n})\delta\phi\right]\,\mathrm{dS}.
\end{aligned} \tag{3.22}$$

Applying the Gauss-Green identities, given by

$$\int_\Omega \boldsymbol{u}\cdot\text{div}\boldsymbol{T}\,\mathrm{d}V = -\int_\Omega \boldsymbol{T}\cdot\boldsymbol{\nabla}\boldsymbol{u}\,\mathrm{d}V + \int_{\partial\Omega} \boldsymbol{u}\cdot\boldsymbol{T}\boldsymbol{n}\,\mathrm{dS} \tag{3.23}$$

$$\int_\Omega \phi\,\text{div}\boldsymbol{D}\,\mathrm{d}V = -\int_\Omega \boldsymbol{D}\cdot\boldsymbol{\nabla}\phi\,\mathrm{d}V + \int_{\partial\Omega} \phi(\boldsymbol{D}\cdot\boldsymbol{n})\,\mathrm{dS}, \tag{3.24}$$

and gathering like terms results in

$$\begin{aligned}
0 = \delta\Pi_M^H = &\int_\Omega (\boldsymbol{c}_E\,\boldsymbol{S} - \boldsymbol{e}^t\,\boldsymbol{E} - \text{symm}\boldsymbol{T})\cdot\delta\boldsymbol{S}\,\mathrm{d}V - \int_\Omega (\boldsymbol{e}\,\boldsymbol{S} + \boldsymbol{\epsilon}_S\,\boldsymbol{E} - \boldsymbol{D})\cdot\delta\boldsymbol{E}\,\mathrm{d}V \\
&+ \int_\Omega (\text{symm}\boldsymbol{\nabla}\boldsymbol{u} - \boldsymbol{S})\cdot\text{symm}\delta\boldsymbol{T}\,\mathrm{d}V + \int_\Omega (\text{skew}\boldsymbol{\nabla}\boldsymbol{u} - \boldsymbol{\psi} - \gamma^{-1}\text{skew}\boldsymbol{T})\cdot\text{skew}\delta\boldsymbol{T}\,\mathrm{d}V \\
&- \int_\Omega \text{skew}\boldsymbol{T}\cdot\delta\boldsymbol{\psi}\,\mathrm{d}V + \int_\Omega (\boldsymbol{\nabla}\phi + \boldsymbol{E})\cdot\delta\boldsymbol{D}\,\mathrm{d}V - \int_\Omega (\text{div}\boldsymbol{T} + \boldsymbol{f})\cdot\delta\boldsymbol{u}\,\mathrm{d}V \\
&- \int_\Omega (\text{div}\boldsymbol{D} - q)\delta\phi\,\mathrm{d}V + \int_{\partial\Omega_t} (\boldsymbol{T}\,\boldsymbol{n} - \bar{\boldsymbol{t}})\cdot\delta\boldsymbol{u}\,\mathrm{dS} + \int_{\partial\Omega_d} (\boldsymbol{D}\cdot\boldsymbol{n} + \bar{d})\delta\phi\,\mathrm{dS} \\
&- \int_{\partial\Omega_u} (\boldsymbol{u} - \bar{\boldsymbol{u}})\cdot(\delta\boldsymbol{T}\,\boldsymbol{n})\,\mathrm{dS} - \int_{\partial\Omega_\phi} (\phi - \bar{\phi})(\delta\boldsymbol{D}\cdot\boldsymbol{n})\,\mathrm{dS}.
\end{aligned} \tag{3.25}$$

All of the necessary Euler-Lagrange equations appear in (3.25). The variation $\delta\boldsymbol{\psi}$ enforces $\text{skew}\boldsymbol{T} = \boldsymbol{0}$ in Ω, while $\text{skew}\delta\boldsymbol{T}$ enforces compatibility between rotations and the skew part of the displacement gradient.

K-Type formulation based on functional Π_K^H

The skew-symmetric part of the stress tensor can be eliminated using the Euler-Lagrange equation $\gamma^{-1}\text{skew}\boldsymbol{T} = \text{skew}\boldsymbol{\nabla u} - \boldsymbol{\psi}$ in Ω, which appears in (3.25) as demonstrated by Hughes and Brezzi [18], to obtain the K-type Hu-Washizu-like functional:

$$\begin{aligned}\Pi_K^H(\boldsymbol{u},\boldsymbol{\psi},\text{symm}\boldsymbol{T},\boldsymbol{S},\phi,\boldsymbol{D},\boldsymbol{E}) &= \frac{1}{2}\int_\Omega \boldsymbol{c}_E\ \boldsymbol{S}\cdot\boldsymbol{S}\,\mathrm{d}V - \int_\Omega \boldsymbol{e}\ \boldsymbol{S}\cdot\boldsymbol{E}\,\mathrm{d}V \\ &- \frac{1}{2}\int_\Omega \boldsymbol{\epsilon}_S\ \boldsymbol{E}\cdot\boldsymbol{E}\,\mathrm{d}V + \int_\Omega(\text{symm}\boldsymbol{\nabla u}-\boldsymbol{S})\cdot\text{symm}\boldsymbol{T}\,\mathrm{d}V + \int_\Omega(\boldsymbol{\nabla}\phi+\boldsymbol{E})\cdot\boldsymbol{D}\,\mathrm{d}V \\ &+ \frac{1}{2}\gamma\int_\Omega|\text{skew}\boldsymbol{\nabla u}-\boldsymbol{\psi}|^2\,\mathrm{d}V - \int_\Omega \boldsymbol{f}\cdot\boldsymbol{u}\,\mathrm{d}V - \int_\Omega q\,\phi\,\mathrm{d}V - \int_{\partial\Omega_t}\bar{\boldsymbol{t}}\cdot\boldsymbol{u}\,\mathrm{dS} \\ &+ \int_{\partial\Omega_d}\bar{d}\,\phi\,\mathrm{dS} - \int_{\partial\Omega_u}(\boldsymbol{u}-\bar{\boldsymbol{u}})\cdot(\boldsymbol{T}\,\boldsymbol{n})\,\mathrm{dS} - \int_{\partial\Omega_\phi}(\phi-\bar{\phi})(\boldsymbol{D}\cdot\boldsymbol{n})\,\mathrm{dS}.\end{aligned} \tag{3.26}$$

Note that in this case, the stress term $\boldsymbol{T}$, in the Lagrange multiplier enforcing the displacement boundary conditions on $\partial\Omega_u$ is calculated as $\boldsymbol{T} = \text{symm}\boldsymbol{T} + \text{skew}\boldsymbol{T}$, where $\text{skew}\boldsymbol{T} = \gamma(\text{skew}\boldsymbol{\nabla u} - \boldsymbol{\psi})$. The first variation (and gathering like terms) results in

$$\begin{aligned}\delta\Pi_K^H = 0 = &\int_\Omega(\boldsymbol{c}_E\boldsymbol{S} - \boldsymbol{e}^t\boldsymbol{E} - \text{symm}\boldsymbol{T})\cdot\delta\boldsymbol{S}\,\mathrm{d}V - \int_\Omega(\boldsymbol{e}\boldsymbol{S} + \boldsymbol{\epsilon}_S\boldsymbol{E} - \boldsymbol{D})\cdot\delta\boldsymbol{S}\,\mathrm{d}V \\ &+ \int_\Omega(\text{symm}\boldsymbol{\nabla u}-\boldsymbol{S})\cdot\text{symm}\delta\boldsymbol{T}\,\mathrm{d}V - \int_\Omega(\gamma(\text{skew}\boldsymbol{\nabla u}-\boldsymbol{\psi}))\cdot\delta\boldsymbol{\psi}\,\mathrm{d}V \\ &+ \int_\Omega(\boldsymbol{\nabla}\psi+\boldsymbol{E})\cdot\delta\boldsymbol{D}\,\mathrm{d}V - \int_\Omega -(\text{symm}\boldsymbol{T}+\gamma(\text{skew}\boldsymbol{\nabla u}-\boldsymbol{\psi}))\cdot(\boldsymbol{\nabla}\delta\boldsymbol{u}) + \boldsymbol{f}\cdot\delta\boldsymbol{u}\,\mathrm{d}V \\ &- \int_\Omega -\boldsymbol{D}\cdot\boldsymbol{\nabla}\delta\phi - q\delta\phi\,\mathrm{d}V - \int_{\partial\Omega_t}\bar{\boldsymbol{t}}\cdot\delta\boldsymbol{u}\,\mathrm{dS} + \int_{\partial\Omega_d}\bar{d}\delta\phi\,\mathrm{dS} \\ &- \int_{\partial\Omega_u}\left[(\boldsymbol{u}-\bar{\boldsymbol{u}})\cdot(\delta\boldsymbol{T}\boldsymbol{n}) - (\boldsymbol{T}\boldsymbol{n})\cdot\delta\boldsymbol{u}\right]\,\mathrm{dS} - \int_{\partial\Omega_\phi}\left[(\phi-\bar{\phi})(\delta\boldsymbol{D}\cdot\boldsymbol{n}) - (\boldsymbol{D}\cdot\boldsymbol{n})\delta\phi\right]\,\mathrm{dS}.\end{aligned} \tag{3.27}$$

After applying the Gauss-Green identities, the following result is achieved:

$$\begin{aligned}\delta\Pi_K^H = 0 = &\int_\Omega(\boldsymbol{c}_E\ \boldsymbol{S} - \boldsymbol{e}^t\ \boldsymbol{E} - \text{symm}\boldsymbol{T})\cdot\delta\boldsymbol{S}\,\mathrm{d}V - \int_\Omega(\boldsymbol{e}\ \boldsymbol{S} + \boldsymbol{\epsilon}_S\ \boldsymbol{E} - \boldsymbol{D})\cdot\delta\boldsymbol{E}\,\mathrm{d}V \\ &+ \int_\Omega(\text{symm}\boldsymbol{\nabla u}-\boldsymbol{S})\cdot\text{symm}\delta\boldsymbol{T}\,\mathrm{d}V - \int_\Omega(\gamma(\text{skew}\boldsymbol{\nabla u}-\boldsymbol{\psi}))\cdot\delta\boldsymbol{\psi}\,\mathrm{d}V \\ &+ \int_\Omega(\boldsymbol{\nabla}\phi+\boldsymbol{E})\cdot\delta\boldsymbol{D}\,\mathrm{d}V - \int_\Omega(\text{div}\boldsymbol{T}+\boldsymbol{f})\cdot\delta\boldsymbol{u}\,\mathrm{d}V - \int_\Omega(\text{div}\boldsymbol{D}-q)\delta\phi\,\mathrm{d}V \\ &+ \int_{\partial\Omega_t}(\boldsymbol{T}\,\boldsymbol{n}-\bar{\boldsymbol{t}})\cdot\delta\boldsymbol{u}\,\mathrm{dS} + \int_{\partial\Omega_d}(\boldsymbol{D}\cdot\boldsymbol{n}+\bar{d})\delta\phi\,\mathrm{dS} \\ &- \int_{\partial\Omega_u}(\boldsymbol{u}-\bar{\boldsymbol{u}})\cdot(\delta\boldsymbol{T}\,\boldsymbol{n})\,\mathrm{dS} - \int_{\partial\Omega_\phi}(\phi-\bar{\phi})(\delta\boldsymbol{D}\cdot\boldsymbol{n})\,\mathrm{dS},\end{aligned} \tag{3.28}$$

which again contains all the necessary Euler equations. Here, the variation $\delta\boldsymbol{\psi}$ simultaneously enforces $\text{skew}\boldsymbol{T} = \boldsymbol{0}$ in Ω and compatibility between rotations and the skew part of displacement gradient.

In the remainder of this section, it is demonstrated how these two Hu-Washizu like functionals can be used to derive (two) irreducible functionals, (two) fully mixed Hellinger-Reissner like functionals and (four) degenerate Hellinger-Reissner like functionals.

The two preceding formulations were presented in some detail. For brevity, the presentation of the variational formulations of the remaining proposed functionals will be abbreviated. Only the functional and the final resulting variational equations containing the Euler-Lagrange equations will be presented.

3.4.2 Irreducible formulations

In order to simplify the formulation for finite element implementation, the irreducible forms emanating from Π_M^H and Π_K^H are now derived. In the context of this work, by 'irreducible' it is implied that the fewest independent variables for a given functional family are used. Of course, $\boldsymbol{u}$ and ϕ are the only independent variables required to fully describe the electroelastic problem since all other variables can be derived from these.[1] However, the 'irreducible' finite elements with drilling DOFs presented herein also require the in-plane rotation field $\boldsymbol{\psi}$ to be included as an independent variable. Furthermore, the M-type functionals intentionally retain skew$\boldsymbol{T}$, even in irreducible form.

M-Type formulation based on functional Π_M

The irreducible form resulting from Π_M^H can be derived by substituting the mechanical and electrical compatibilities (3.11) and (3.12) respectively into Π_M^H. Therefore, $\boldsymbol{S} = \text{symm}\boldsymbol{\nabla u}$, and $\boldsymbol{E} = -\boldsymbol{\nabla}\phi$ are substituted into (3.21).

The resulting functional, which retains the skew-symmetric part of stress as an independent variable, together with displacements, electric potentials and in-plane rotations, is:

$$\begin{aligned}\Pi_M(\boldsymbol{u},\boldsymbol{\psi},\text{skew}\boldsymbol{T},\phi) = \frac{1}{2}\int_\Omega \boldsymbol{c}_E\ \text{symm}\boldsymbol{\nabla u}\cdot\text{symm}\boldsymbol{\nabla u}\,\mathrm{d}V + \int_\Omega \boldsymbol{e}\ \text{symm}\boldsymbol{\nabla u}\cdot\boldsymbol{\nabla}\phi\,\mathrm{d}V \\ -\frac{1}{2}\int_\Omega \boldsymbol{\epsilon}_S\ \boldsymbol{\nabla}\phi\cdot\boldsymbol{\nabla}\phi\,\mathrm{d}V + \int_\Omega(\text{skew}\boldsymbol{\nabla u}-\boldsymbol{\psi})\cdot\text{skew}\boldsymbol{T}\,\mathrm{d}V - \frac{1}{2}\gamma^{-1}\int_\Omega|\text{skew}\boldsymbol{T}|^2\,\mathrm{d}V \\ -\int_\Omega \boldsymbol{f}\cdot\boldsymbol{u}\,\mathrm{d}V + \int_\Omega q\,\phi\,\mathrm{d}V - \int_{\partial\Omega_t}\bar{\boldsymbol{t}}\cdot\boldsymbol{u}\,\mathrm{dS} + \int_{\partial\Omega_d}\bar{d}\,\phi\,\mathrm{dS},\end{aligned} \tag{3.29}$$

where both $\boldsymbol{u}$ and ϕ are admissible, and therefore satisfy the essential boundary conditions. Since the aforementioned substitution effectively eliminates strain and electric field as independent variables, the compatibility between strain and displacement gradient and electric field and potential gradient are enforced in a strong sense. Furthermore the symmetric part of stress as well as electric flux density are also eliminated from the functional upon this substitution. Therefore the constitutive relations in (3.4) are also assumed to hold in a strong

[1] Not the fully story, stress and electric flux density or strain and electric field (or combinations) could also theoretically be used as the independent variables.

sense [16, 55]. After some algebra, the first variation of Π_M reduces to

$$\begin{aligned}\delta\Pi_M = 0 = &\int_\Omega (\text{skew}\boldsymbol{\nabla u} - \boldsymbol{\psi} - \gamma^{-1}\text{skew}\boldsymbol{T}) \cdot \text{skew}\delta\boldsymbol{T}\, \text{d}V - \int_\Omega \text{skew}\boldsymbol{T} \cdot \delta\boldsymbol{\psi}\, \text{d}V \\ &- \int_\Omega (\text{div}\boldsymbol{T} + \boldsymbol{f}) \cdot \delta\boldsymbol{u}\, \text{d}V - \int_\Omega (\text{div}\boldsymbol{D} - q)\delta\phi\, \text{d}V + \int_{\partial\Omega_t} (\boldsymbol{T}\,\boldsymbol{n} - \bar{\boldsymbol{t}}) \cdot \delta\boldsymbol{u}\, \text{dS} \\ &+ \int_{\partial\Omega_d} (\boldsymbol{D} \cdot \boldsymbol{n} + \bar{d})\delta\phi\, \text{dS},\end{aligned} \tag{3.30}$$

which again contains all the necessary Euler-Lagrange equations.

K-Type formulation: Functional Π_K

The K-type equivalent irreducible functional is derived using similar substitutions of the compatibility conditions, this time into Π_K^H. The emerging functional, with only displacements, in-plane rotations and electric potential as independent variables, can be shown to be:

$$\begin{aligned}\Pi_K(\boldsymbol{u}, \boldsymbol{\psi}, \phi) = &\frac{1}{2}\int_\Omega \boldsymbol{c}_E \text{symm}\boldsymbol{\nabla u} \cdot \text{symm}\boldsymbol{\nabla u}\, \text{d}V + \int_\Omega \boldsymbol{e}\text{symm}\boldsymbol{\nabla u} \cdot \boldsymbol{\nabla}\phi\, \text{d}V \\ &- \frac{1}{2}\int_\Omega \boldsymbol{\epsilon}_S \boldsymbol{\nabla}\phi \cdot \boldsymbol{\nabla}\phi\, \text{d}V + \frac{1}{2}\gamma\int_\Omega |\text{skew}\boldsymbol{\nabla u} - \boldsymbol{\psi}|^2\, \text{d}V - \int_\Omega \boldsymbol{f} \cdot \boldsymbol{u}\, \text{d}V \\ &+ \int_\Omega q\phi\, \text{d}V - \int_{\partial\Omega_t} \bar{\boldsymbol{t}} \cdot \boldsymbol{u}\, \text{dS} + \int_{\partial\Omega_d} \bar{d}\phi\, \text{dS},\end{aligned} \tag{3.31}$$

where both $\boldsymbol{u}$ and ϕ are again admissible functions. Once again, the constitutive and compatibility conditions are enforced in a strong sense. After applying the Gauss-Green identities and grouping like terms, the resulting variational equation is given by:

$$\begin{aligned}\delta\Pi_K = 0 = &-\int_\Omega \gamma(\text{skew}\boldsymbol{\nabla u} - \boldsymbol{\psi}) \cdot \delta\boldsymbol{\psi}\, \text{d}V - \int_\Omega (\text{div}\boldsymbol{T} + \boldsymbol{f}) \cdot \delta\boldsymbol{u}\, \text{d}V - \int_\Omega (\text{div}\boldsymbol{D} - q)\delta\phi\, \text{d}V \\ &+ \int_{\partial\Omega_t} (\boldsymbol{T}\boldsymbol{n} - \bar{\boldsymbol{t}}) \cdot \delta\boldsymbol{u}\, \text{dS} + \int_{\partial\Omega_d} (\boldsymbol{D} \cdot \boldsymbol{n} + \bar{d})\delta\phi\, \text{dS}.\end{aligned} \tag{3.32}$$

Recognising $\gamma(\text{skew}\boldsymbol{\nabla u} - \boldsymbol{\psi})$ as the skew-symmetric part of stress, once again all the necessary Euler equations are contained in (3.32).

3.4.3 Fully mixed Hellinger-Reissner-like formulations

Strain $\boldsymbol{S}$ and electric field $\boldsymbol{E}$ can both be eliminated from the Hu-Washizu-like functionals by substituting the constitutive relations in (3.9) into functionals Π_M^H and Π_K^H, resulting in fully mixed Hellinger-Reissner-like functionals. Of course, since strain and electric field are eliminated from the functional, their compatibility conditions are assumed *a priori*.

M-Type formulation based on functional Π_M^{TD}

The constitutive relations in terms of stress $\boldsymbol{T}$ and electric flux density $\boldsymbol{D}$ are substituted into Π_M^H, and the functional Π_M^{TD} is introduced. The superscripts 'T' and 'D' represent the additional independent variables (supplemental to the kinematic variables):

$$\begin{aligned}\Pi_M^{TD}(\boldsymbol{u},\boldsymbol{\psi},\text{symm}\boldsymbol{T},\text{skew}\boldsymbol{T},\phi,\boldsymbol{D}) = &-\frac{1}{2}\int_\Omega \boldsymbol{s}_D\ \text{symm}\boldsymbol{T}\cdot\text{symm}\boldsymbol{T}\,\mathrm{d}V - \int_\Omega \boldsymbol{g}\ \text{symm}\boldsymbol{T}\cdot\boldsymbol{D}\,\mathrm{d}V\\ &+\frac{1}{2}\int_\Omega \boldsymbol{\chi}_T\ \boldsymbol{D}\cdot\boldsymbol{D}\,\mathrm{d}V + \int_\Omega \text{symm}\boldsymbol{\nabla u}\cdot\text{symm}\boldsymbol{T}\,\mathrm{d}V + \int_\Omega \boldsymbol{\nabla}\phi\cdot\boldsymbol{D}\,\mathrm{d}V\\ &+\int_\Omega(\text{skew}\boldsymbol{\nabla u}-\boldsymbol{\psi})\cdot\text{skew}\boldsymbol{T}\,\mathrm{d}V - \frac{1}{2}\gamma^{-1}\int_\Omega|\text{skew}\boldsymbol{T}|^2\,\mathrm{d}V - \int_\Omega \boldsymbol{f}\cdot\boldsymbol{u}\,\mathrm{d}V\\ &+\int_\Omega q\,\phi\,\mathrm{d}V - \int_{\partial\Omega_t}\bar{\boldsymbol{t}}\cdot\boldsymbol{u}\,\mathrm{dS} + \int_{\partial\Omega_d}\bar{d}\,\phi\,\mathrm{dS} - \int_{\partial\Omega_u}(\boldsymbol{u}-\bar{\boldsymbol{u}})\cdot(\boldsymbol{T}\,\boldsymbol{n})\,\mathrm{dS}\\ &-\int_{\partial\Omega_\phi}(\phi-\bar{\phi})(\boldsymbol{D}\cdot\boldsymbol{n})\,\mathrm{dS}.\end{aligned} \tag{3.33}$$

After applying the Gauss-Green identities, the result of the first variation is

$$\begin{aligned}\delta\Pi_M^{TD} = 0 = &-\int_\Omega(\boldsymbol{s}_D\ \text{symm}\boldsymbol{T} + \boldsymbol{g}^t\ \boldsymbol{D} - \text{symm}\boldsymbol{\nabla u})\cdot\text{symm}\delta\boldsymbol{T}\,\mathrm{d}V\\ &+\int_\Omega(\text{skew}\boldsymbol{\nabla u}-\boldsymbol{\psi}-\gamma^{-1}\text{skew}\boldsymbol{T})\cdot\text{skew}\delta\boldsymbol{T}\,\mathrm{d}V\\ &+\int_\Omega(-\boldsymbol{g}\ \text{symm}\boldsymbol{T} + \boldsymbol{\chi}_T\ \boldsymbol{D} + \boldsymbol{\nabla}\phi)\cdot\delta\boldsymbol{D}\,\mathrm{d}V - \int_\Omega \text{skew}\boldsymbol{T}\cdot\delta\boldsymbol{\psi}\,\mathrm{d}V\\ &-\int_\Omega(\text{div}\boldsymbol{T}+\boldsymbol{f})\cdot\delta\boldsymbol{u}\,\mathrm{d}V - \int_\Omega(\text{div}\boldsymbol{D}-q)\delta\phi\,\mathrm{d}V + \int_{\partial\Omega_t}(\boldsymbol{T}\,\boldsymbol{n}-\bar{\boldsymbol{t}})\cdot\delta\boldsymbol{u}\,\mathrm{dS}\\ &+\int_{\partial\Omega_d}(\boldsymbol{D}\cdot\boldsymbol{n}+\bar{d})\delta\phi\,\mathrm{dS} - \int_{\partial\Omega_u}(\boldsymbol{u}-\bar{\boldsymbol{u}})\cdot(\delta\boldsymbol{T}\,\boldsymbol{n})\,\mathrm{dS} - \int_{\partial\Omega_\phi}(\phi-\bar{\phi})(\delta\boldsymbol{D}\cdot\boldsymbol{n})\,\mathrm{dS},\end{aligned} \tag{3.34}$$

where the Euler equation $\boldsymbol{s}_D\ \text{symm}\boldsymbol{T} + \boldsymbol{g}^t\ \boldsymbol{D} = \text{symm}\boldsymbol{\nabla u}$ weakly enforces the relationship between strain derived from compatibility conditions (3.11), and strain based on stress and electric flux density from constitutive equations (3.9). Similarly, $-\boldsymbol{g}\ \text{symm}\boldsymbol{T}+\boldsymbol{\chi}_T\ \boldsymbol{D} = -\boldsymbol{\nabla}\phi$ enforces weakly the relationship between compatibility (3.12) and constitutive equations (3.9) for electric field.

K-Type formulation: Functional Π_K^{TD}

The corresponding K-type fully-mixed functional can be derived by either making the substitutions of constitutive equations described previously to arrive at the Π_M^{TD} functional, or through elimination of the skew-symmetric part of stress by substitution of $\text{skew}\boldsymbol{T} = \gamma(\text{skew}\boldsymbol{\nabla u}-\boldsymbol{\psi})$ which appears as one of the Euler equations in (3.34) into Π_M^{TD}. In either

case, the resulting functional is

$$\begin{aligned}\Pi_K^{TD}(\boldsymbol{u},\boldsymbol{\psi},\text{symm}\boldsymbol{T},\phi,\boldsymbol{D}) = &-\frac{1}{2}\int_\Omega \boldsymbol{s}_D\text{symm}\boldsymbol{T}\cdot\text{symm}\boldsymbol{T}\,\mathrm{d}V - \int_\Omega \boldsymbol{g}\text{symm}\boldsymbol{T}\cdot\boldsymbol{D}\,\mathrm{d}V\\ &+\frac{1}{2}\int_\Omega \boldsymbol{\chi}_T\boldsymbol{D}\cdot\boldsymbol{D}\,\mathrm{d}V + \int_\Omega \text{symm}\boldsymbol{\nabla u}\cdot\text{symm}\boldsymbol{T}\,\mathrm{d}V + \int_\Omega \boldsymbol{\nabla}\phi\cdot\boldsymbol{D}\,\mathrm{d}V\\ &+\frac{1}{2}\gamma\int_\Omega |\text{skew}\boldsymbol{\nabla u}-\boldsymbol{\psi}|^2\,\mathrm{d}V - \int_\Omega \boldsymbol{f}\cdot\boldsymbol{u}\,\mathrm{d}V + \int_\Omega q\phi\,\mathrm{d}V\\ &-\int_{\partial\Omega_t}\bar{\boldsymbol{t}}\cdot\boldsymbol{u}\,\mathrm{dS} + \int_{\partial\Omega_d}\bar{d}\phi\,\mathrm{dS} - \int_{\partial\Omega_u}(\boldsymbol{u}-\bar{\boldsymbol{u}})\cdot(\boldsymbol{T}\boldsymbol{n})\,\mathrm{dS}\\ &-\int_{\partial\Omega_\phi}(\phi-\bar{\phi})(\boldsymbol{D}\cdot\boldsymbol{n})\,\mathrm{dS}.\end{aligned} \tag{3.35}$$

Once again, like terms are collected after taking the first variation, and apply the Gauss-Green identities to arrive at the variational equation:

$$\begin{aligned}\delta\Pi_K^{TD} = 0 = &-\int_\Omega(\boldsymbol{s}_D\text{symm}\boldsymbol{T} + \boldsymbol{g}^t\boldsymbol{D} - \text{symm}\boldsymbol{\nabla u})\cdot\text{symm}\delta\boldsymbol{T}\,\mathrm{d}V\\ &+(-\boldsymbol{g}\text{symm}\boldsymbol{T} + \boldsymbol{\chi}_T\boldsymbol{D} + \boldsymbol{\nabla}\phi)\cdot\delta\boldsymbol{D}\,\mathrm{d}V - \int_\Omega\gamma(\text{skew}\boldsymbol{\nabla u}-\boldsymbol{\psi})\cdot\delta\boldsymbol{\psi}\,\mathrm{d}V\\ &-\int_\Omega(\text{div}\boldsymbol{T}+\boldsymbol{f})\cdot\delta\boldsymbol{u}\,\mathrm{d}V - \int_\Omega(\text{div}\boldsymbol{D}-q)\delta\phi\,\mathrm{d}V + \int_{\partial\Omega_t}(\boldsymbol{T}\boldsymbol{n}-\bar{\boldsymbol{t}})\cdot\delta\boldsymbol{u}\,\mathrm{dS}\\ &+\int_{\partial\Omega_d}(\boldsymbol{D}\cdot\boldsymbol{n}+\bar{d})\delta\phi\,\mathrm{dS} - \int_{\partial\Omega_u}(\boldsymbol{u}-\bar{\boldsymbol{u}})\cdot(\delta\boldsymbol{T}\boldsymbol{n})\,\mathrm{dS} - \int_{\partial\Omega_\phi}(\phi-\bar{\phi})(\delta\boldsymbol{D}\cdot\boldsymbol{n})\,\mathrm{dS}.\end{aligned} \tag{3.36}$$

Again, the variation on $\boldsymbol{\psi}$ simultaneously enforces compatibility between the skew-symmetric part of the displacement gradient and the rotation field, and the symmetry conditions for stress. Once again all weak relationships necessary, are contained in (3.36).

3.4.4 Degenerate Hellinger-Reissner-like formulations

It is also possible to derive functionals with only stress $\boldsymbol{T}$ *or* electric flux density $\boldsymbol{D}$ assumed, additionally to $\boldsymbol{u}$ and ϕ, using the remaining forms of the constitutive equations, given in (3.5) and (3.7). Since only stress or electric flux density are assumed, these functionals will be referred to as degenerate.

M-Type formulation: Functional Π_M^D

If strain (and the symmetric part of stress) are eliminated from Π_M^H by substituting $\boldsymbol{S} = \text{symm}\boldsymbol{\nabla u}$, and if electric field is eliminated by substituting the second equation of (3.5) into Π_M^H, the M-type Hellinger-Reissner like functional which results is:

$$\begin{aligned}\Pi_M^D(\boldsymbol{u},\boldsymbol{\psi},\text{skew}\boldsymbol{T},\phi,\boldsymbol{D}) = \frac{1}{2}\int_\Omega \boldsymbol{c}_D\,\text{symm}\boldsymbol{\nabla u}\cdot\text{symm}\boldsymbol{\nabla u}\,\text{d}V - \int_\Omega \boldsymbol{h}\,\text{symm}\boldsymbol{\nabla u}\cdot\boldsymbol{D}\,\text{d}V\\ + \frac{1}{2}\int_\Omega \boldsymbol{\chi}_S\,\boldsymbol{D}\cdot\boldsymbol{D}\,\text{d}V + \int_\Omega(\text{skew}\boldsymbol{\nabla u}-\boldsymbol{\psi})\cdot\text{skew}\boldsymbol{T}\,\text{d}V + \int_\Omega \boldsymbol{\nabla}\phi\cdot\boldsymbol{D}\,\text{d}V\\ - \frac{1}{2}\gamma^{-1}\int_\Omega|\text{skew}\boldsymbol{T}|^2\,\text{d}V - \int_\Omega \boldsymbol{f}\cdot\boldsymbol{u}\,\text{d}V + \int_\Omega q\,\phi\,\text{d}V - \int_{\partial\Omega_t}\bar{\boldsymbol{t}}\cdot\boldsymbol{u}\,\text{dS}\\ + \int_{\partial\Omega_d}\bar{d}\,\phi\,\text{dS} - \int_{\partial\Omega_\phi}(\phi-\bar{\phi})(\boldsymbol{D}\cdot\boldsymbol{n})\,\text{dS},\end{aligned} \tag{3.37}$$

where the displacement field $\boldsymbol{u}$ is admissible. In this case, the compatibility between strain and displacement gradient $\boldsymbol{S} = \text{symm}\boldsymbol{\nabla u}$, as well as the constitutive relationship between stress and stain and electric flux density, $\text{symm}\boldsymbol{T} = \boldsymbol{c}_D\boldsymbol{S} - \boldsymbol{h}^t\boldsymbol{D}$ are assumed to be enforced in a strong sense.

Yet again, the first variation is computed, and after applying integration by parts, the resulting variational statement is

$$\begin{aligned}\delta\Pi_M^D = 0 = \int_\Omega(\text{skew}\boldsymbol{\nabla u}-\boldsymbol{\psi}-\gamma^{-1}\text{skew}\boldsymbol{T})\cdot\text{skew}\delta\boldsymbol{T}\,\text{d}V\\ - \int_\Omega(\boldsymbol{h}\text{symm}\boldsymbol{\nabla u}-\boldsymbol{\chi}_S\boldsymbol{D}-\boldsymbol{\nabla}\phi)\cdot\delta\boldsymbol{D}\,\text{d}V - \int_\Omega\text{skew}\boldsymbol{T}\cdot\delta\boldsymbol{\psi}\,\text{d}V\\ - \int_\Omega(\text{div}\boldsymbol{T}+\boldsymbol{f})\cdot\delta\boldsymbol{u}\,\text{d}V - \int_\Omega(\text{div}\boldsymbol{D}-q)\delta\phi\,\text{d}V + \int_{\partial\Omega_t}(\boldsymbol{T}\boldsymbol{n}-\bar{\boldsymbol{t}})\cdot\delta\boldsymbol{u}\,\text{dS}\\ + \int_{\partial\Omega_d}(\boldsymbol{D}\cdot\boldsymbol{n}+\bar{d})\delta\phi\,\text{dS} - \int_{\partial\Omega_\phi}(\phi-\bar{\phi})(\delta\boldsymbol{D}\cdot\boldsymbol{n})\,\text{dS}.\end{aligned} \tag{3.38}$$

Once again (3.38) enforces all the necessary relations in a weak sense. In particular the arbitrary variation on $\boldsymbol{D}$ weakly enforces the relationship between electric field in terms of potential gradient and electric field in terms of its constitutive definition in (3.5).

K-Type formulation: Functional Π_K^D

Once again, the skew-symmetric part of stress can be eliminated from Π_M^D by substituting the Euler equation in terms of the skew-stress, which appears in (3.38), to produce Π_K^D. Alternatively, Π_K^D can be derived from Π_K^H by making the appropriate substitutions, described in the derivation of Π_M^D. The K-type functional with displacement, electric potential, in-plane rotations and electric flux density as independent variables is found to be:

$$\begin{aligned}\Pi_K^D(\boldsymbol{u},\boldsymbol{\psi},\phi,\boldsymbol{D}) =& \frac{1}{2}\int_\Omega \boldsymbol{c}_D\text{symm}\boldsymbol{\nabla u}\cdot\text{symm}\boldsymbol{\nabla u}\,\mathrm{d}V - \int_\Omega \boldsymbol{h}\text{symm}\boldsymbol{\nabla u}\cdot\boldsymbol{D}\,\mathrm{d}V \\ &+\frac{1}{2}\int_\Omega \boldsymbol{\chi}_S\boldsymbol{D}\cdot\boldsymbol{D}\,\mathrm{d}V + \int_\Omega \boldsymbol{\nabla}\phi\cdot\boldsymbol{D}\,\mathrm{d}V + \frac{1}{2}\gamma\int_\Omega |\text{skew}\boldsymbol{\nabla u}-\boldsymbol{\psi}|^2\,\mathrm{d}V \\ &-\int_\Omega \boldsymbol{f}\cdot\boldsymbol{u}\,\mathrm{d}V + \int_\Omega q\phi\,\mathrm{d}V - \int_{\partial\Omega_t}\bar{\boldsymbol{t}}\cdot\boldsymbol{u}\,\mathrm{dS} + \int_{\partial\Omega_d}\bar{d}\phi\,\mathrm{dS} \\ &-\int_{\partial\Omega_\phi}(\phi-\bar{\phi})(\boldsymbol{D}\cdot\boldsymbol{n})\,\mathrm{dS},\end{aligned} \tag{3.39}$$

where $\boldsymbol{u}$ is again admissible. Following the same process as previously, after taking the first variation, applying the Gauss-Green identities, and collecting like terms, the resulting variational statement is given by

$$\begin{aligned}\delta\Pi_K^D = 0 =& -\int_\Omega(\boldsymbol{h}\text{symm}\boldsymbol{\nabla u}-\boldsymbol{\chi}_S\boldsymbol{D}-\boldsymbol{\nabla}\phi)\cdot\delta\boldsymbol{D}\,\mathrm{d}V - \int_\Omega\gamma(\text{skew}\boldsymbol{\nabla u}-\boldsymbol{\psi})\cdot\delta\boldsymbol{\psi}\,\mathrm{d}V \\ &-\int_\Omega(\text{div}\boldsymbol{T}+\boldsymbol{f})\cdot\delta\boldsymbol{u}\,\mathrm{d}V - \int_\Omega(\text{div}\boldsymbol{D}-q)\delta\phi\,\mathrm{d}V + \int_{\partial\Omega_t}(\boldsymbol{T}\boldsymbol{n}-\bar{\boldsymbol{t}})\cdot\delta\boldsymbol{u}\,\mathrm{dS} \\ &+\int_{\partial\Omega_d}(\boldsymbol{D}\cdot\boldsymbol{n}+\bar{d})\delta\phi\,\mathrm{dS} - \int_{\partial\Omega_\phi}(\phi-\bar{\phi})(\delta\boldsymbol{D}\cdot\boldsymbol{n})\,\mathrm{dS},\end{aligned} \tag{3.40}$$

which yet again contains all the necessary Euler-Lagrange equations.

M-Type formulation: Functional Π_M^T

If on the other hand, electric field (and electric flux density) are eliminated from Π_M^H by substituting $\boldsymbol{E}=-\boldsymbol{\nabla}\phi$, and if strain is eliminated by substituting the first equation of (3.7) into Π_M^H, a functional with symm$\boldsymbol{T}$ assumed is achieved.

$$\begin{aligned}\Pi_M^T(\boldsymbol{u},\boldsymbol{\psi},\text{symm}\boldsymbol{T},\text{skew}\boldsymbol{T},\phi) =& -\frac{1}{2}\int_\Omega \boldsymbol{s}_E\,\text{symm}\boldsymbol{T}\cdot\text{symm}\boldsymbol{T}\,\mathrm{d}V + \int_\Omega \boldsymbol{d}\,\text{symm}\boldsymbol{T}\cdot\boldsymbol{\nabla}\phi\,\mathrm{d}V \\ &-\frac{1}{2}\int_\Omega \boldsymbol{\epsilon}_T\,\boldsymbol{\nabla}\phi\cdot\boldsymbol{\nabla}\phi\,\mathrm{d}V + \int_\Omega \text{symm}\boldsymbol{\nabla u}\cdot\text{symm}\boldsymbol{T}\,\mathrm{d}V + \int_\Omega(\text{skew}\boldsymbol{\nabla u}-\boldsymbol{\psi})\cdot\text{skew}\boldsymbol{T}\,\mathrm{d}V \\ &-\frac{1}{2}\gamma^{-1}\int_\Omega|\text{skew}\boldsymbol{T}|^2\,\mathrm{d}V - \int_\Omega \boldsymbol{f}\cdot\boldsymbol{u}\,\mathrm{d}V + \int_\Omega q\,\phi\,\mathrm{d}V - \int_{\partial\Omega_t}\bar{\boldsymbol{t}}\cdot\boldsymbol{u}\,\mathrm{dS} \\ &+\int_{\partial\Omega_d}\bar{d}\,\phi\,\mathrm{dS} - \int_{\partial\Omega_u}(\boldsymbol{u}-\bar{\boldsymbol{u}})\cdot(\boldsymbol{T}\,\boldsymbol{n})\,\mathrm{dS},\end{aligned} \tag{3.41}$$

where ϕ is admissible. In this instance, the constitutive equation $\boldsymbol{D}=\boldsymbol{d}\text{symm}+\boldsymbol{\epsilon}_T\boldsymbol{E}$ and compatibility condition $\boldsymbol{E}=-\boldsymbol{\nabla}\phi$ require enforcement in a strong sense. Yet again, after some calculations, the first variation ultimately results in

$$\begin{aligned}\delta\Pi_M^T = 0 = &\int_\Omega -(\boldsymbol{s}_E\text{symm}\boldsymbol{T} - \boldsymbol{d}^t\boldsymbol{\nabla}\phi - \text{symm}\boldsymbol{\nabla}\boldsymbol{u})\cdot\text{symm}\delta\boldsymbol{T}\,\text{d}V - \int_\Omega \text{skew}\boldsymbol{T}\delta\boldsymbol{\psi}\,\text{d}V\\ &+\int_\Omega(\text{skew}\boldsymbol{\nabla}\boldsymbol{u} - \boldsymbol{\psi} - \gamma^{-1}\text{skew}\boldsymbol{T})\cdot\text{skew}\delta\boldsymbol{T} - \int_\Omega(\text{div}\boldsymbol{T}+\boldsymbol{f})\cdot\delta\boldsymbol{u}\,\text{d}V\\ &-\int_\Omega(\text{div}\boldsymbol{D}-q)\delta\phi\,\text{d}V + \int_{\partial\Omega_t}(\boldsymbol{T}\boldsymbol{n}-\bar{\boldsymbol{t}})\cdot\delta\boldsymbol{u}\,\text{dS} + \int_{\partial\Omega_d}(\boldsymbol{D}\cdot\boldsymbol{n}+\bar{d})\delta\phi\,\text{dS}\\ &-\int_{\partial\Omega_u}(\boldsymbol{u}-\bar{\boldsymbol{u}})\cdot(\delta\boldsymbol{T}\boldsymbol{n})\,\text{dS}.\end{aligned} \tag{3.42}$$

The variational statement in (3.42) once yet again weakly enforces all necessary relationships. In this instance, variations on symm$\boldsymbol{T}$ weakly enforces the relationship between strain derived from displacement gradient and strain contained in the constitutive equations in (3.7).

K-Type formulation: Functional Π_K^T

Finally, the K-type counterpart of (3.41) can be constructed by either eliminating the skew symmetric part of stress from Π_M^T or by making the appropriate substitutions in Π_K^H (see Figure 3.1 and Section 3.4.5 for details).

$$\begin{aligned}\Pi_K^T(\boldsymbol{u},\boldsymbol{\psi},\text{symm}\boldsymbol{T},\phi) = &-\frac{1}{2}\int_\Omega \boldsymbol{s}_E\text{symm}\boldsymbol{T}\cdot\text{symm}\boldsymbol{T}\,\text{d}V + \int_\Omega \boldsymbol{d}\text{symm}\boldsymbol{T}\cdot\boldsymbol{\nabla}\phi\,\text{d}V\\ &-\frac{1}{2}\int_\Omega \boldsymbol{\epsilon}_T\boldsymbol{\nabla}\phi\cdot\boldsymbol{\nabla}\phi\,\text{d}V + \int_\Omega \text{symm}\boldsymbol{\nabla}\boldsymbol{u}\cdot\text{symm}\boldsymbol{T}\,\text{d}V\\ &+\frac{1}{2}\gamma\int_\Omega|\text{skew}\boldsymbol{\nabla}\boldsymbol{u}-\boldsymbol{\psi}|^2\,\text{d}V - \int_\Omega \boldsymbol{f}\cdot\boldsymbol{u}\,\text{d}V + \int_\Omega q\phi\,\text{d}V\\ &-\int_{\partial\Omega_t}\bar{\boldsymbol{t}}\cdot\boldsymbol{u}\,\text{dS} + \int_{\partial\Omega_d}\bar{d}\phi\,\text{dS} - \int_{\partial\Omega_u}(\boldsymbol{u}-\bar{\boldsymbol{u}})\cdot(\boldsymbol{T}\boldsymbol{n})\,\text{dS},\end{aligned} \tag{3.43}$$

where ϕ is admissible. Following the same process as before, the first variation can be shown to reduce to

$$\begin{aligned}\delta\Pi_K^T = 0 = &\int_\Omega -(\boldsymbol{s}_E\text{symm}\boldsymbol{T} - \boldsymbol{d}^t\boldsymbol{\nabla}\phi - \text{symm}\boldsymbol{\nabla}\boldsymbol{u})\cdot\text{symm}\delta\boldsymbol{T}\,\text{d}V\\ &-\int_\Omega\gamma(\text{skew}\boldsymbol{\nabla}\boldsymbol{u}-\boldsymbol{\psi})\cdot\delta\boldsymbol{\psi}\,\text{d}V - \int_\Omega(\text{div}\boldsymbol{T}+\boldsymbol{f})\cdot\delta\boldsymbol{u}\,\text{d}V\\ &-\int_\Omega(\text{div}\boldsymbol{D}-q)\delta\phi\,\text{d}V + \int_{\partial\Omega_t}(\boldsymbol{T}\boldsymbol{n}-\bar{\boldsymbol{t}})\cdot\delta\boldsymbol{u}\,\text{dS} + \int_{\partial\Omega_d}(\boldsymbol{D}\cdot\boldsymbol{n}+\bar{d})\delta\phi\,\text{dS}\\ &-\int_{\partial\Omega_u}(\boldsymbol{u}-\bar{\boldsymbol{u}})\cdot(\delta\boldsymbol{T}\boldsymbol{n})\,\text{dS},\end{aligned} \tag{3.44}$$

which once yet again weakly enforces all necessary conditions.

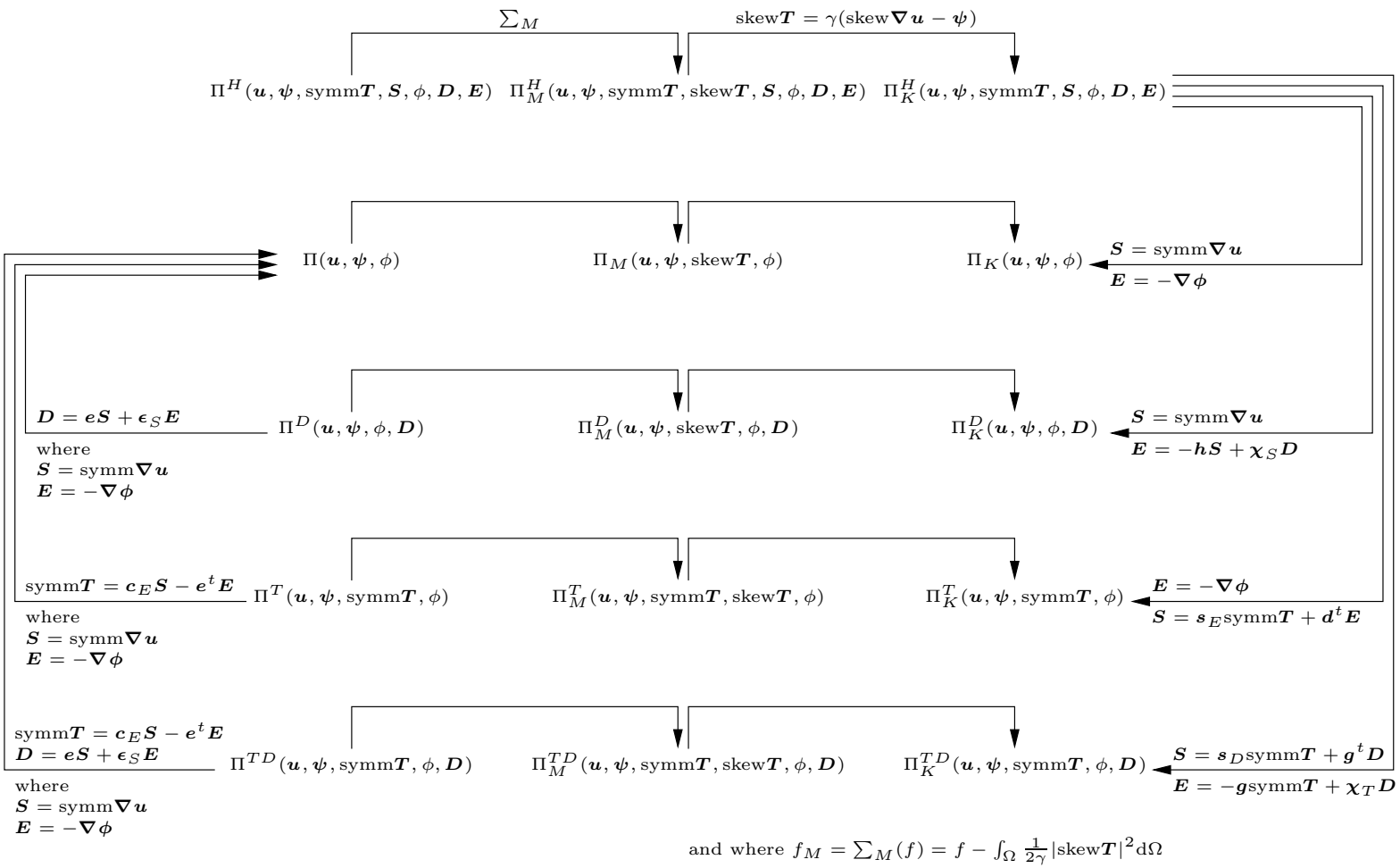

Figure 3.1: Relationships between the functionals.

In all, ten new functionals have been introduced in this section. At this point, a summary of the relationships between the functionals is appropriate, since not all of the relationships have explicitly been detailed in the foregoing.

3.4.5 Relationships between the functionals

In Figure 3.1 the relations between the various functionals are graphically depicted for the piezoelectricity problem. This figure is similar to Figure 2.3 presented in Section 2.4 for the elastostatic problem.

In total, 15 functionals are represented in Figure 3.1 arranged in five rows and three columns. The top row contains the Hu-Washizu like functionals while the irreducible functionals are represented in the second row. Rows three and four contain the degenerate Hellinger-Reissner like functionals. Finally, the fully mixed functionals are presented in the fifth row from the top (see Figure 3.2). The three families of functionals are contained in different columns. The Reissner like functionals (not explicitly presented in this chapter) are contained in the first column (from the left), the middle column contains the M-type functional while the K-type functionals are represented in the column on the right hand side.

As indicated in Figure 3.1, the only difference between the Reissner like functionals and the M-type functionals is the additional term $\int_\Omega \frac{1}{2\gamma}|\text{skew}\boldsymbol{T}|^2 \, \mathrm{d}V$. Furthermore, K-Type functionals can be derived from M-Type functionals by making the substitution $\text{skew}\boldsymbol{T} = \gamma(\text{skew}\boldsymbol{\nabla u} - \boldsymbol{\psi})$. These relations are indicated by the arrows above the respective columns.

In the preceding text, it has been shown that the irreducible, degenerate Hellinger-Reissner and fully mixed Hellinger-Reissner functionals can be derived from the Hu-Washizu like functional by making the substitutions as indicated by the arrows on the far right of Figure 3.2.

Finally it can also be shown that, within any of the three families (columns), both the degenerate and fully mixed Hellinger-Reissner like functionals can be used as a basis to derive the irreducible functionals. Specifically, if $\text{symm}\boldsymbol{T} = \boldsymbol{c}_E \ \text{symm}\boldsymbol{\nabla u} + \boldsymbol{e}^t \ \boldsymbol{\nabla\phi}$ and $\boldsymbol{D} = \boldsymbol{e} \ \text{symm}\boldsymbol{\nabla u} - \boldsymbol{\epsilon}_S \ \boldsymbol{\nabla\phi}$ are substituted into the fully mixed functionals, the corresponding irreducible functionals result. Similarly, if $\text{symm}\boldsymbol{T} = \boldsymbol{c}_E \ \text{symm}\boldsymbol{\nabla u} + \boldsymbol{e}^t \ \boldsymbol{\nabla\phi}$ is substituted into the degenerate functionals including stress, or if $\boldsymbol{D} = \boldsymbol{e} \ \text{symm}\boldsymbol{\nabla u} - \boldsymbol{\epsilon}_S \ \boldsymbol{\nabla\phi}$ is substituted into the degenerate functionals including electric flux density, the irreducible functionals also result. These relations are shown on the far left of Figure 3.1.

In this work, not all of the finite elements resulting from variational formulations of the 15 functionals depicted in Figure 3.1 have been implemented numerically. Figure 3.2 depicts the relations between the functionals in terms of their finite element implementation in this study.

As explained in Chapter 2, elastostatic formulations resulting from the functional of Reissner [40] are not suitable for implementation in discrete form, due to stability issues [18]. Numerical experiments confirmed that this is also the case for the piezoelectric problem. Furthermore, assumed strain (and electric field) finite elements are beyond the scope of this study. The Hu-Washizu like functionals in the top row of Figure 3.2 are therefore not implemented. The eight elements based on the remaining functionals are all implemented, and

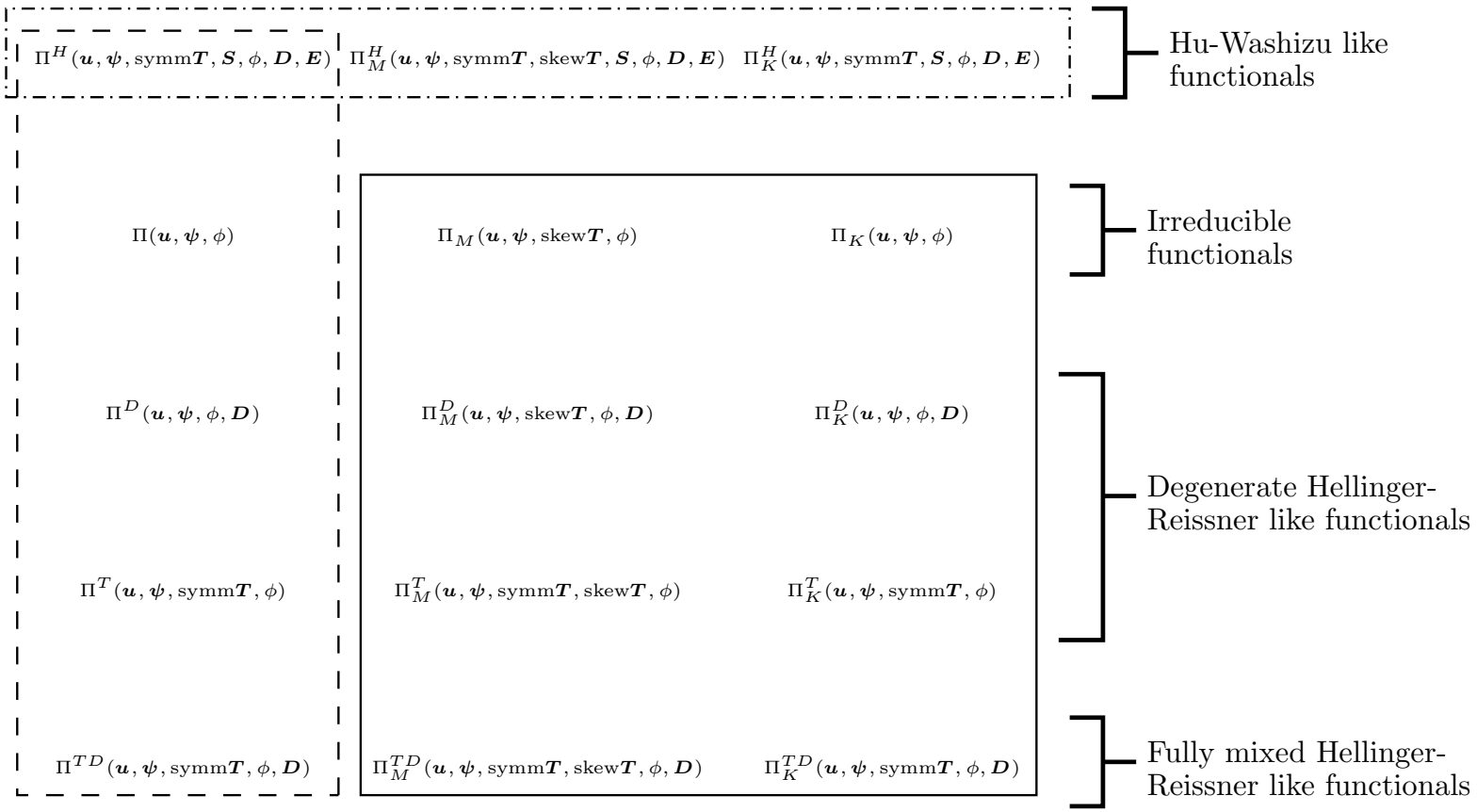

Figure 3.2: Relationships between the functionals in terms of their finite element implementation.

will be the focus of the remainder of this chapter.

3.5 Finite element interpolations

In this section the interpolations, used in the finite element implementation arising from the functionals presented in Section 3.4, are briefly discussed. The scalar potential and the independent rotation fields are interpolated as

$$\phi^h = \sum_e \sum_{i=1}^{4} N_i^e(\xi,\eta)\phi_i, \tag{3.45}$$

$$\psi^h = \sum_e \sum_{i=1}^{4} N_i^e(\xi,\eta)\psi_i, \tag{3.46}$$

respectively, with N_i^e the standard bilinear shape functions. The in-plane displacement approximation is taken as an Allman-type interpolation field, after Ibrahimbegovic *et al.* [21]

$$\left\{ \begin{array}{c} u_1 \\ u_2 \end{array} \right\} = \boldsymbol{u}^h = \sum_e \sum_{i=1}^{4} N_i^e(\xi,\eta)\boldsymbol{u}_i + \frac{l_{jk}}{8} \sum_e \sum_{i=5}^{8} NS_i^e(\xi,\eta)(\psi_k - \psi_j)\boldsymbol{n}_{jk}, \tag{3.47}$$

with NS_i the Serendipity shape functions. The hierarchical bubble shape function is not included. Furthermore, l_{jk} and $\boldsymbol{n}_{jk}$ denote the length and the outward unit normal vector on the element side associated with the corner nodes j and k (see Figure 3.3), i.e.

$$\boldsymbol{n}_{jk} = \left\{ \begin{array}{c} n_1 \\ n_2 \end{array} \right\} = \left\{ \begin{array}{c} \cos\alpha_{jk} \\ \sin\alpha_{jk} \end{array} \right\}, \tag{3.48}$$

and

$$l_{jk} = ((x_k - x_j)^2 + (y_k - y_j)^2)^{1/2}. \tag{3.49}$$

The indices in the above are explicitly given in Section 2.5.

The skew-symmetric stress field is chosen constant over the element, i.e.

$$\text{skew}\, \boldsymbol{T}^h = \sum_e T_0^e. \tag{3.50}$$

Using matrix notation, $\text{symm}\boldsymbol{\nabla}\boldsymbol{u}^e$ and $\text{skew}\boldsymbol{\nabla}\boldsymbol{u}^e$ are respectively given by

$$\text{symm}\boldsymbol{\nabla}\boldsymbol{u}^e = \boldsymbol{B}_i^e\boldsymbol{u}_i + \boldsymbol{G}_i^e\boldsymbol{\psi}_i, \tag{3.51}$$

and

$$\text{skew}\boldsymbol{\nabla}\boldsymbol{u}^e = \boldsymbol{b}_i^e\boldsymbol{u}_i + \boldsymbol{g}_i^e\boldsymbol{\psi}_i. \tag{3.52}$$

The operators arising from this interpolation are also summarised in Section 2.5, and are therefore not repeated here. The 'membrane locking correction', due to Taylor [38] is used, i.e. element strains are modified to become

$$\text{symm}\boldsymbol{\nabla}\tilde{\boldsymbol{u}}^e = \boldsymbol{B}_i^e\boldsymbol{u}_i + \left(\boldsymbol{G}_i^e - \frac{1}{\Omega^e} \int_{\Omega^e} \boldsymbol{G}_i^e \, \mathrm{d}V \right) \boldsymbol{\psi}_i. \tag{3.53}$$

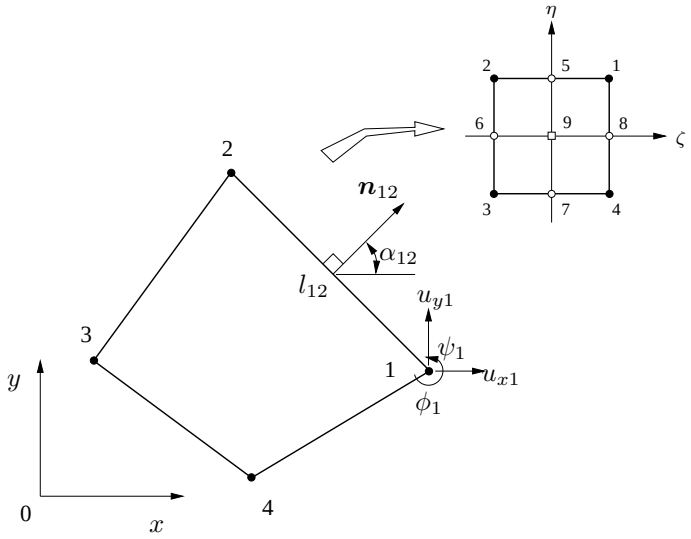

Figure 3.3: A planar 4-node piezoelectric element with drilling rotations.

For interpolations of stress and electric flux density, the necessary (but not sufficient) conditions for element stability are:

$$n_{\beta T} \geq n_u - m_u, \tag{3.54}$$

$$n_{\beta D} \geq n_\phi - m_\phi, \tag{3.55}$$

where $n_{\beta T}$ and $n_{\beta D}$ are the number of assumed stress and electric flux density modes, respectively. Furthermore, n_u and n_ϕ are the number of displacement and potential modes, respectively. The number of rigid body displacement modes is m_u, and m_ϕ represents the single (constant potential) distribution resulting in zero field. The equality conditions in (3.54) and (3.55) represent the optimal number of parameters in both cases.

For our planar elements with drilling degrees of freedom (DOFs), $n_u = 12$, and $n_\phi = 4$. The single potential distribution resulting in zero field means $m_\phi = 1$, and usually membrane elements possess three rigid body modes ($m_u = 3$). The optimal number of parameters required is therefore $n_{\beta T} = 9$ for stress and $n_{\beta D} = 3$ for flux density. One more than optimal, i.e. $n_{\beta D} = 4$, parameters are required for interpolation of the electric flux density in order to ensure the element is invariant [65]. Stability is achieved if no spurious zero energy modes appear, viz. if rank sufficiency of the mechanical stiffness and dielectric stiffness matrices is maintained [66].

Sze *et al.* [50, 51] presented a rank sufficient elastic element with drilling DOFs using only 8 interpolating stress modes, which appears to be one less than the optimal prescribed in (3.54). However, $n_{\beta T} = 8$ seems adequate, since m_u in (3.54) is in fact equal to 4 and not 3. The additional so-called θ_1–mode (in which rotations at each node are equal) is intrinsic to the reduced displacement interpolation. The strain corresponding to this state is zero.

Geyer and Groenwold [43] also presented a family of membrane elements with drilling DOFs, some of which employ only 8 stress modes for interpolation and retain stability. Elements with both 8 and 9 stress interpolating modes are tested.

The assumed electric flux density vector is interpolated using

$$\boldsymbol{D}^h = \sum_e \left[\begin{array}{cc} \boldsymbol{I}^e_{Dc} & \boldsymbol{A}^e_D \boldsymbol{P}^e_{Dh} \end{array} \right] \left\{ \begin{array}{c} \boldsymbol{\beta}^e_{Dc} \\ \boldsymbol{\beta}^e_{Dh} \end{array} \right\}, \tag{3.56}$$

where $\boldsymbol{I}^e_{Dc}$ is a 2×2 identity matrix to account for the constant flux density case and $\boldsymbol{\beta}^e_{Dc}$ are the corresponding parameters. $\boldsymbol{A}^e_D$ is a transformation matrix [65, 76, 79], and $\boldsymbol{P}^e_{Dh}$ represents the interpolation of the higher order part of charge density with $\boldsymbol{\beta}^e_{Dh}$ the corresponding parameters. $\boldsymbol{A}^e_D$ and $\boldsymbol{P}^e_{Dh}$ are given explicitly as

$$\boldsymbol{A}^e_D = \left[\begin{array}{cc} a_1 & a_3 \\ b_1 & b_3 \end{array} \right], \tag{3.57}$$

where for each element, a_i and b_i are based on the nodal coordinates x and y and are given by

$$\left[\begin{array}{cc} a_1 & b_1 \\ a_2 & b_2 \\ a_3 & b_3 \end{array} \right] = \frac{1}{4} \left[\begin{array}{cccc} -1 & 1 & 1 & -1 \\ 1 & -1 & 1 & -1 \\ -1 & -1 & 1 & 1 \end{array} \right] \left[\begin{array}{cc} x_1 & y_1 \\ x_2 & y_2 \\ x_3 & y_3 \\ x_4 & y_4 \end{array} \right]. \tag{3.58}$$

The interpolation based on the local $\xi - \eta$ coordinates is given by

$$\boldsymbol{P}^e_{Dh} = \left[\begin{array}{cc} \eta & 0 \\ 0 & \xi \end{array} \right]. \tag{3.59}$$

The interpolation for electric flux density $\boldsymbol{D}^h$ can therefore be given explicitly by

$$\boldsymbol{D}^h = \sum_e \left[\begin{array}{cccc} 1 & 0 & a_1\eta & a_3\xi \\ 0 & 1 & b_1\eta & b_3\xi \end{array} \right] \left\{ \begin{array}{c} \boldsymbol{\beta}^e_{Dc} \\ \boldsymbol{\beta}^e_{Dh} \end{array} \right\}. \tag{3.60}$$

The assumed symmetric part of stress is similarly interpolated as

$$\text{symm}\boldsymbol{T}^h = \sum_e \left[\begin{array}{cc} \boldsymbol{I}^e_{Tc} & \boldsymbol{A}^e_T \boldsymbol{P}^e_{Thn} \end{array} \right] \left\{ \begin{array}{c} \boldsymbol{\beta}^e_{Tc} \\ \boldsymbol{\beta}^e_{Th} \end{array} \right\}, \tag{3.61}$$

where $\boldsymbol{I}^e_{Tc}$ is a 3×3 identity matrix accounting for a constant stress state, with corresponding stress parameters $\boldsymbol{\beta}^e_{Tc}$. $\boldsymbol{A}^e_T$ is a transformation matrix given by

$$\boldsymbol{A}^e_T = \left[\begin{array}{ccc} a_1^2 & a_3^2 & 2a_1a_3 \\ b_1^2 & b_3^2 & 2b_1b_3 \\ a_1b_1 & a_3b_3 & a_1b_3 + a_3b_1 \end{array} \right]. \tag{3.62}$$

There are many other constraint matrices, (see for example Di and Ramm [61]), which can be used, but are not considered here for the sake of brevity. Two different higher order stress interpolations are implemented. The first has 8 (i.e. 5 non-constant) $\boldsymbol{\beta}_T$–parameters and the other 9 (6 non-constant). The element with the 8 $\boldsymbol{\beta}_T$–parameters has a higher order interpolation matrix given by

$$\boldsymbol{P}^e_{Th5} = \left[\begin{array}{ccccc} \eta & 0 & -\xi & 0 & \eta^2 \\ 0 & \xi & 0 & -\eta & -\xi^2 \\ 0 & 0 & \eta & \xi & 0 \end{array} \right], \tag{3.63}$$

which is similar to the field used by Sze and Ghali [50]. The element containing 9 $\boldsymbol{\beta}_T$–parameters has a matrix given by

$$\boldsymbol{P}^e_{Th6} = \begin{bmatrix} \eta & 0 & -\xi & 0 & \eta^2 & 0 \\ 0 & \xi & 0 & -\eta & 0 & \xi^2 \\ 0 & 0 & \eta & \xi & 0 & 0 \end{bmatrix}. \tag{3.64}$$

Alternative interpolations are given by Geyer and Groenwold [43].

3.6 Finite element implementation

For simplicity, in this section the boundary terms are neglected, but may be included in the usual manner. The body charge, q, terms are also neglected, as is usually done [71]. In what is to follow, $\boldsymbol{u}^h, \text{symm}\boldsymbol{T}^h, \text{skew}\boldsymbol{T}^h, \phi^h, \boldsymbol{D}^h$ represent the interpolations for displacement, symmetric and skew-symmetric stress, electric potential and electric flux density, respectively. The fields $\boldsymbol{u}^h$ and ϕ^h satisfy the necessary boundary conditions, and $\boldsymbol{\psi}^h$ denotes the interpolated rotation field.

In our paper [80], due to space considerations, only two elements derived from the foregoing variational formulations are presented. In this section however, all of eight new elements are presented.

3.6.1 Irreducible piezoelectric elements with drilling DOFs

Firstly the two simplest (irreducible) finite elements are presented. The element originating from the functional Π_M is denoted P4dM, while the K-type element derived from Π_K is denoted P4dK.

P4dM element based on Π_M

We proceed by writing the discrete form of the first variation of Π_M in a matrix-like form, similar to the notation used in [18, 21], as

$$\begin{aligned} 0 = &\int_{\Omega^h} (\text{symm}\boldsymbol{\nabla}\delta\boldsymbol{u}^h)^t \cdot \boldsymbol{c}_E \cdot (\text{symm}\boldsymbol{\nabla}\boldsymbol{u}^h)\, \mathrm{d}V + \int_{\Omega^h} (\boldsymbol{\nabla}\delta\phi^h)^t \cdot \boldsymbol{e} \cdot (\text{symm}\boldsymbol{\nabla}\boldsymbol{u}^h)\, \mathrm{d}V \\ &+ \int_{\Omega^h} (\text{symm}\boldsymbol{\nabla}\delta\boldsymbol{u}^h)^t \cdot \boldsymbol{e}^t \cdot (\boldsymbol{\nabla}\phi^h)\, \mathrm{d}V - \int_{\Omega^h} (\boldsymbol{\nabla}\delta\phi^h)^t \cdot \boldsymbol{\epsilon}_S \cdot (\boldsymbol{\nabla}\phi^h)\, \mathrm{d}V \\ &+ \int_{\Omega^h} (\text{skew}\delta\boldsymbol{T}^h)^t \cdot (\text{skew}\boldsymbol{\nabla}\boldsymbol{u}^h - \boldsymbol{\psi}^h)\, \mathrm{d}V + \int_{\Omega^h} (\text{skew}\boldsymbol{\nabla}\delta\boldsymbol{u}^h)^t \cdot \text{skew}\boldsymbol{T}^h \\ &- (\delta\boldsymbol{\psi}^h)^t \cdot \text{skew}\boldsymbol{T}^h\, \mathrm{d}V - \gamma^{-1} \int_{\Omega^h} (\text{skew}\delta\boldsymbol{T}^h)^t \cdot \text{skew}\boldsymbol{T}^h\, \mathrm{d}V - \int_{\Omega^h} (\delta\boldsymbol{u}^h)^t \cdot \boldsymbol{f}\, \mathrm{d}V. \end{aligned} \tag{3.65}$$

Employing the interpolations and operators presented in Section 3.5, (3.65) can be written in matrix notation, as:

$$\begin{bmatrix} \boldsymbol{K}^e_{uu} & \boldsymbol{K}^e_{u\phi} & \boldsymbol{h}^e \\ [\boldsymbol{K}^e_{u\phi}]^t & -\boldsymbol{K}^e_{\phi\phi} & \boldsymbol{0} \\ [\boldsymbol{h}^e]^t & \boldsymbol{0} & -\gamma^{-1}\Omega^e \end{bmatrix} \begin{Bmatrix} \boldsymbol{a} \\ \boldsymbol{\phi} \\ T^e_0 \end{Bmatrix} = \begin{Bmatrix} \boldsymbol{f} \\ \boldsymbol{0} \\ 0 \end{Bmatrix}; \quad \boldsymbol{a} = \begin{Bmatrix} \boldsymbol{u} \\ \boldsymbol{\psi} \end{Bmatrix}. \tag{3.66}$$

The skew symmetric part of the stress tensor can be eliminated on the element level using static condensation, so that the system of equations necessary to solve the problem are

$$\begin{bmatrix} \boldsymbol{K}^e_M \end{bmatrix} \begin{Bmatrix} \boldsymbol{a} \\ \boldsymbol{\phi} \end{Bmatrix} = \begin{Bmatrix} \boldsymbol{f} \\ \boldsymbol{0} \end{Bmatrix}, \tag{3.67}$$

where

$$\boldsymbol{K}^e_M = \begin{bmatrix} \boldsymbol{K}^e_{uu} + \frac{\gamma}{\Omega^e}\boldsymbol{h}^e[\boldsymbol{h}^e]^t & \boldsymbol{K}^e_{u\phi} \\ [\boldsymbol{K}^e_{u\phi}]^t & -\boldsymbol{K}^e_{\phi\phi} \end{bmatrix}. \tag{3.68}$$

Individual partitioned stiffness matrix terms are given in Section 3.7. Both $\boldsymbol{K}^e_{uu}$ and $\boldsymbol{K}^e_{u\phi}$ are evaluated using a 5-point numerical integration scheme, while $\boldsymbol{h}^e$ and $\boldsymbol{K}^e_{\phi\phi}$ employ a standard 4-point scheme. The top left (12×12) portion of the stiffness matrix represents the mechanical part. The 12×4 partition, denoted $\boldsymbol{K}^e_{u\phi}$, represents the piezoelectric part, and the bottom right portion, $-\boldsymbol{K}^e_{\phi\phi}$, the 4×4 dielectric part of the stiffness matrix.

The skew part of the stress tensor (constant over each element) can be recovered as a post-processing step, and is given by

$$T^e_0 = \gamma \frac{[\boldsymbol{h}^e]^t \boldsymbol{a}}{\Omega^e}. \tag{3.69}$$

P4dK element based on Π_K

The element arising from the irreducible K-type functional is now derived. To this end, the discrete form of $\delta\Pi_K$ can be written using the same notation as

$$\begin{aligned} 0 = &\int_{\Omega^h} (\text{symm}\boldsymbol{\nabla}\delta\boldsymbol{u}^h)^t \cdot \boldsymbol{c}_E \cdot (\text{symm}\boldsymbol{\nabla}\boldsymbol{u}^h)\, \mathrm{d}V + \int_{\Omega^h} (\boldsymbol{\nabla}\delta\phi^h)^t \cdot \boldsymbol{e} \cdot (\text{symm}\boldsymbol{\nabla}\boldsymbol{u}^h)\, \mathrm{d}V \\ &+ \int_{\Omega^h} (\text{symm}\boldsymbol{\nabla}\delta\boldsymbol{u}^h)^t \cdot \boldsymbol{e}^t \cdot (\boldsymbol{\nabla}\phi^h)\, \mathrm{d}V - \int_{\Omega^h} (\boldsymbol{\nabla}\delta\phi^h)^t \cdot \boldsymbol{\epsilon}_S \cdot (\boldsymbol{\nabla}\phi^h)\, \mathrm{d}V \\ &+ \gamma \int_{\Omega^h} (\text{skew}\boldsymbol{\nabla}\delta\boldsymbol{u}^h - \delta\boldsymbol{\psi}^h)^t \cdot (\text{skew}\boldsymbol{\nabla}\boldsymbol{u}^h - \boldsymbol{\psi}^h)\, \mathrm{d}V - \int_{\Omega^h} (\delta\boldsymbol{u}^h)^t \cdot \boldsymbol{f}\, \mathrm{d}V. \end{aligned} \tag{3.70}$$

The condensed matrix form of (3.70) can be directly written as:

$$\begin{bmatrix} \boldsymbol{K}^e_K \end{bmatrix} \begin{Bmatrix} \boldsymbol{a} \\ \boldsymbol{\phi} \end{Bmatrix} = \begin{Bmatrix} \boldsymbol{f} \\ \boldsymbol{0} \end{Bmatrix}, \tag{3.71}$$

where the expanded stiffness matrix is explicitly given by:

$$\begin{bmatrix} \boldsymbol{K}^e_K \end{bmatrix} = \begin{bmatrix} \boldsymbol{K}^e_{uu} + \boldsymbol{P}^e & \boldsymbol{K}^e_{u\phi} \\ [\boldsymbol{K}^e_{u\phi}]^t & -\boldsymbol{K}^e_{\phi\phi} \end{bmatrix}. \tag{3.72}$$

The individual partitioned stiffness matrices are again given in Section 3.7. In particular, the matrix $\boldsymbol{P}^e$, which represents the second last term in (3.70), is evaluated using a single point integration scheme.

3.6.2 Fully mixed piezoelectric element with drilling DOFs

The matrix form of the two fully-mixed finite elements can be derived similarly. The two elements are denoted P4dMnTD and P4dKnTD, originating from the M- and K-type fully mixed functionals, respectively. The n in the element denotation reflects the number of stress β parameters.

P4dMnTD element based on Π_M^{TD}

Considering first the M-type element based on Π_M^{TD}, the discrete form of the first variation of the functional can be written as:

$$\begin{aligned}
0 = &- \int_{\Omega^h} (\text{symm}\delta\boldsymbol{T}^h)^t \cdot \boldsymbol{s}_D \cdot (\text{symm}\boldsymbol{T}^h)\, \mathrm{d}V - \int_{\Omega^h} (\delta\boldsymbol{D}^h)^t \cdot \boldsymbol{g} \cdot (\text{symm}\boldsymbol{T}^h)\, \mathrm{d}V \\
&- \int_{\Omega^h} (\text{symm}\delta\boldsymbol{T}^h)^t \cdot \boldsymbol{g}^t \cdot (\boldsymbol{D}^h)\, \mathrm{d}V + \int_{\Omega^h} (\delta\boldsymbol{D}^h)^t \cdot \boldsymbol{\chi}_T \cdot (\boldsymbol{D}^h)\, \mathrm{d}V \\
&+ \int_{\Omega^h} (\text{symm}\delta\boldsymbol{T}^h)^t \cdot (\text{symm}\boldsymbol{\nabla}\boldsymbol{u}^h)\, \mathrm{d}V + \int_{\Omega^h} (\text{symm}\boldsymbol{\nabla}\delta\boldsymbol{u}^h)^t \cdot (\text{symm}\boldsymbol{T}^h)\, \mathrm{d}V \\
&+ \int_{\Omega^h} (\delta\boldsymbol{D}^h)^t \cdot (\boldsymbol{\nabla}\phi^h)\, \mathrm{d}V + \int_{\Omega^h} (\boldsymbol{\nabla}\delta\phi^h)^t \cdot (\delta\boldsymbol{D}^h)\, \mathrm{d}V \\
&+ \int_{\Omega^h} (\text{skew}\delta\boldsymbol{T}^h)^t \cdot (\text{skew}\boldsymbol{\nabla}\boldsymbol{u}^h - \boldsymbol{\psi}^h)\, \mathrm{d}V \\
&+ \int_{\Omega^h} (\text{skew}\boldsymbol{\nabla}\delta\boldsymbol{u}^h)^t \cdot \text{skew}\boldsymbol{T}^h - (\delta\boldsymbol{\psi}^h)^t \cdot \text{skew}\boldsymbol{T}^h\, \mathrm{d}V \\
&- \gamma^{-1} \int_{\Omega^h} (\text{skew}\delta\boldsymbol{T}^h)^t \cdot \text{skew}\boldsymbol{T}^h\, \mathrm{d}V - \int_{\Omega^h} (\delta\boldsymbol{u}^h)^t \cdot \boldsymbol{f}\, \mathrm{d}V.
\end{aligned} \tag{3.73}$$

The discrete version of the formulation can again be rewritten in matrix form as

$$\begin{bmatrix}
\boldsymbol{0} & \boldsymbol{0} & \boldsymbol{h}^e & \boldsymbol{K}^e_{uT} & \boldsymbol{0} \\
\boldsymbol{0} & \boldsymbol{0} & \boldsymbol{0} & \boldsymbol{0} & \boldsymbol{K}^e_{\phi D} \\
[\boldsymbol{h}^e]^t & \boldsymbol{0} & -\gamma^{-1}\Omega^e & \boldsymbol{0} & \boldsymbol{0} \\
[\boldsymbol{K}^e_{uT}]^t & \boldsymbol{0} & \boldsymbol{0} & -\boldsymbol{K}^{TDe}_{TT} & -\boldsymbol{K}^{TDe}_{TD} \\
\boldsymbol{0} & [\boldsymbol{K}^e_{\phi D}]^t & \boldsymbol{0} & -[\boldsymbol{K}^{TDe}_{TD}]^t & \boldsymbol{K}^{TDe}_{DD}
\end{bmatrix}
\begin{Bmatrix} \boldsymbol{a} \\ \boldsymbol{\phi} \\ T^e_0 \\ \boldsymbol{\beta}^{TDe}_T \\ \boldsymbol{\beta}^{TDe}_D \end{Bmatrix}
= \begin{Bmatrix} \boldsymbol{f} \\ \boldsymbol{0} \\ 0 \\ \boldsymbol{0} \\ \boldsymbol{0} \end{Bmatrix}. \tag{3.74}$$

This matrix form can be further condensed by eliminating T^e_0, $\boldsymbol{\beta}^{TDe}_T$ and $\boldsymbol{\beta}^{TDe}_D$ using static condensation to arrive at:

$$\begin{bmatrix} \boldsymbol{K}^{TDe}_M \end{bmatrix} \begin{Bmatrix} \boldsymbol{a} \\ \boldsymbol{\phi} \end{Bmatrix} = \begin{Bmatrix} \boldsymbol{f} \\ \boldsymbol{0} \end{Bmatrix}, \tag{3.75}$$

where the stress and electric flux density β-parameters can be shown to be

$$\left\{ \begin{array}{c} \boldsymbol{\beta}_T^{TDe} \\ \boldsymbol{\beta}_D^{TDe} \end{array} \right\} = \left[\begin{array}{cc} \boldsymbol{K}_{TT}^{TDe} & \boldsymbol{K}_{TD}^{TDe} \\ [\boldsymbol{K}_{TD}^{TDe}]^t & -\boldsymbol{K}_{DD}^{TDe} \end{array} \right]^{-1} \left[\begin{array}{cc} [\boldsymbol{K}_{uT}^{e}]^t & \boldsymbol{0} \\ \boldsymbol{0} & [\boldsymbol{K}_{\phi D}^{e}]^t \end{array} \right] \left\{ \begin{array}{c} \boldsymbol{a} \\ \boldsymbol{\phi} \end{array} \right\}, \tag{3.76}$$

T_0^e is again given by (3.69), and the stiffness matrix for this element can be written as

$$\boldsymbol{K}_M^{TDe} = \left[\begin{array}{cc} \frac{\gamma}{\Omega^e} \boldsymbol{h}^e [\boldsymbol{h}^e]^t & \boldsymbol{0} \\ \boldsymbol{0} & \boldsymbol{0} \end{array} \right] + \left[\begin{array}{cc} \boldsymbol{K}_{uT}^{e} & \boldsymbol{0} \\ \boldsymbol{0} & \boldsymbol{K}_{\phi D}^{e} \end{array} \right] \left[\begin{array}{cc} \boldsymbol{K}_{TT}^{TDe} & \boldsymbol{K}_{TD}^{TDe} \\ [\boldsymbol{K}_{TD}^{TDe}]^t & -\boldsymbol{K}_{DD}^{TDe} \end{array} \right]^{-1} \left[\begin{array}{cc} [\boldsymbol{K}_{uT}^{e}]^t & \boldsymbol{0} \\ \boldsymbol{0} & [\boldsymbol{K}_{\phi D}^{e}]^t \end{array} \right]. \tag{3.77}$$

Again, individual partitioned stiffness matrix terms are given in Section 3.7. The partitioned submatrices $\boldsymbol{K}_{uT}^e$, $\boldsymbol{K}_{TT}^{TDe}$ and $\boldsymbol{K}_{TD}^{TDe}$ are calculated using a 5-point integration scheme, while $\boldsymbol{K}_{\phi D}^e$ and $\boldsymbol{K}_{DD}^{TDe}$ are evaluated using a 4-point scheme. The number of stress parameters in $\boldsymbol{\beta}_T^e$ (either 8 or 9) is denoted n in the element designation P4dMnTD.

P4dKnTD element based on Π_K^{TD}

Focusing now on the K-type fully mixed element, the discrete form of the variational equation derived from Π_K^{TD} can be derived as:

$$\begin{aligned} 0 = &- \int_{\Omega^h} (\text{symm}\delta\boldsymbol{T}^h)^t \cdot \boldsymbol{s}_D \cdot (\text{symm}\boldsymbol{T}^h)\, \text{d}V - \int_{\Omega^h} (\delta\boldsymbol{D}^h)^t \cdot \boldsymbol{g} \cdot (\text{symm}\boldsymbol{T}^h)\, \text{d}V \\ &- \int_{\Omega^h} (\text{symm}\delta\boldsymbol{T}^h)^t \cdot \boldsymbol{g}^t \cdot (\boldsymbol{D}^h)\, \text{d}V + \int_{\Omega^h} (\delta\boldsymbol{D}^h)^t \cdot \boldsymbol{\chi}_T \cdot (\boldsymbol{D}^h)\, \text{d}V \\ &+ \int_{\Omega^h} (\text{symm}\delta\boldsymbol{T}^h)^t \cdot (\text{symm}\boldsymbol{\nabla}\boldsymbol{u}^h)\, \text{d}V + \int_{\Omega^h} (\text{symm}\boldsymbol{\nabla}\delta\boldsymbol{u}^h)^t \cdot (\text{symm}\boldsymbol{T}^h)\, \text{d}V \\ &+ \int_{\Omega^h} (\delta\boldsymbol{D}^h)^t \cdot (\boldsymbol{\nabla}\phi^h)\, \text{d}V + \int_{\Omega^h} (\boldsymbol{\nabla}\delta\phi^h)^t \cdot (\delta\boldsymbol{D}^h)\, \text{d}V \\ &+ \gamma \int_{\Omega^h} (\text{skew}\boldsymbol{\nabla}\delta\boldsymbol{u}^h - \delta\boldsymbol{\psi}^h)^t \cdot (\text{skew}\boldsymbol{\nabla}\boldsymbol{u}^h - \boldsymbol{\psi}^h)\, \text{d}V - \int_{\Omega^h} (\delta\boldsymbol{u}^h)^t \cdot \boldsymbol{f}\, \text{d}V. \end{aligned} \tag{3.78}$$

The matrix form of the discrete variational equation becomes

$$\left[\begin{array}{cccc} \boldsymbol{P}^e & \boldsymbol{0} & \boldsymbol{K}_{uT}^e & \boldsymbol{0} \\ \boldsymbol{0} & \boldsymbol{0} & \boldsymbol{0} & \boldsymbol{K}_{\phi D}^e \\ [\boldsymbol{K}_{uT}^e]^t & \boldsymbol{0} & -\boldsymbol{K}_{TT}^{TDe} & -\boldsymbol{K}_{TD}^{TDe} \\ \boldsymbol{0} & [\boldsymbol{K}_{\phi D}^e]^t & -[\boldsymbol{K}_{TD}^{TDe}]^t & \boldsymbol{K}_{DD}^{TDe} \end{array} \right] \left[\begin{array}{c} \boldsymbol{a} \\ \boldsymbol{\phi} \\ \boldsymbol{\beta}_T^{TDe} \\ \boldsymbol{\beta}_D^{TDe} \end{array} \right] = \left[\begin{array}{c} \boldsymbol{f} \\ \boldsymbol{0} \\ \boldsymbol{0} \\ \boldsymbol{0} \end{array} \right]. \tag{3.79}$$

The stiffness matrix can be compacted by condensing $\boldsymbol{\beta}_T^{TDe}$ and $\boldsymbol{\beta}_D^{TDe}$ out on the element level, resulting in:

$$\left[\boldsymbol{K}_K^{TDe} \right] \left\{ \begin{array}{c} \boldsymbol{a} \\ \boldsymbol{\phi} \end{array} \right\} = \left\{ \begin{array}{c} \boldsymbol{f} \\ \boldsymbol{0} \end{array} \right\}, \tag{3.80}$$

with the β-parameters, given by (3.76) and the stiffness matrix given by

$$\boldsymbol{K}_K^{TDe} = \begin{bmatrix} \boldsymbol{P}^e & \boldsymbol{0} \\ \boldsymbol{0} & \boldsymbol{0} \end{bmatrix} + \begin{bmatrix} \boldsymbol{K}_{uT}^e & \boldsymbol{0} \\ \boldsymbol{0} & \boldsymbol{K}_{\phi D}^e \end{bmatrix} \begin{bmatrix} \boldsymbol{K}_{TT}^{TDe} & \boldsymbol{K}_{TD}^{TDe} \\ (\boldsymbol{K}_{TD}^{TDe})^t & -\boldsymbol{K}_{DD}^{TDe} \end{bmatrix}^{-1} \begin{bmatrix} [\boldsymbol{K}_{uT}^e]^t & \boldsymbol{0} \\ \boldsymbol{0} & [\boldsymbol{K}_{\phi D}^e]^t \end{bmatrix}. \tag{3.81}$$

Once again, individual stiffness sub-matrices are given explicitly in Section 3.7. The integration schemes used are as given previously, and again the number of stress β-parameters n, is included in the element designation.

3.6.3 Degenerate assumed flux density piezoelectric element with drilling DOFs

The degenerate assumed flux density piezoelectric elements with drilling DOFs, emanating from functions Π_M^D and Π_K^D, denoted P4dMD and P4dKD, respectively are now detailed.

P4dMD element based on Π_M^D

Considering the M-type degenerate element formulation with assumed electric flux density, the discrete version of the resulting variational equation can be written as

$$\begin{aligned} 0 = &\int_{\Omega^h} (\text{symm}\boldsymbol{\nabla}\delta\boldsymbol{u}^h)^t \cdot \boldsymbol{c}_D \cdot (\text{symm}\boldsymbol{\nabla}\boldsymbol{u}^h)\,\mathrm{d}V - \int_{\Omega^h} (\delta\boldsymbol{D}^h)^t \cdot \boldsymbol{h} \cdot (\text{symm}\boldsymbol{\nabla}\boldsymbol{u}^h)\,\mathrm{d}V \\ &- \int_{\Omega^h} (\text{symm}\boldsymbol{\nabla}\delta\boldsymbol{u}^h)^t \cdot \boldsymbol{h}^t \cdot (\boldsymbol{D}^h)\,\mathrm{d}V + \int_{\Omega^h} (\delta\boldsymbol{D}^h)^t \cdot \boldsymbol{\chi}_S \cdot (\boldsymbol{D}^h)\,\mathrm{d}V \\ &+ \int_{\Omega^h} (\delta\boldsymbol{D}^h)^t \cdot (\boldsymbol{\nabla}\phi^h)\,\mathrm{d}V + \int_{\Omega^h} (\boldsymbol{\nabla}\delta\phi^h)^t \cdot (\boldsymbol{D}^h)\,\mathrm{d}V \\ &+ \int_{\Omega^h} (\text{skew}\delta\boldsymbol{T}^h)^t \cdot (\text{skew}\boldsymbol{\nabla}\boldsymbol{u}^h - \boldsymbol{\psi}^h)\,\mathrm{d}V + \int_{\Omega^h} (\text{skew}\boldsymbol{\nabla}\delta\boldsymbol{u}^h)^t \cdot \text{skew}\boldsymbol{T}^h \\ &- (\delta\boldsymbol{\psi}^h)^t \cdot \text{skew}\boldsymbol{T}^h\,\mathrm{d}V - \gamma^{-1}\int_{\Omega^h} (\text{skew}\delta\boldsymbol{T}^h)^t \cdot \text{skew}\boldsymbol{T}^h\,\mathrm{d}V - \int_{\Omega^h} (\delta\boldsymbol{u}^h)^t \cdot \boldsymbol{f}\,\mathrm{d}V. \end{aligned} \tag{3.82}$$

This equation can once again be rewritten in matrix form using the element operators, detailed in Section 3.4.4, as

$$\begin{bmatrix} \boldsymbol{K}_{uu}^{De} & \boldsymbol{0} & \boldsymbol{h}^e & -\boldsymbol{K}_{uD}^e \\ \boldsymbol{0} & \boldsymbol{0} & \boldsymbol{0} & \boldsymbol{K}_{\phi D}^e \\ [\boldsymbol{h}^e]^t & \boldsymbol{0} & -\gamma^{-1}\Omega^e & \boldsymbol{0} \\ -[\boldsymbol{K}_{uD}^e]^t & [\boldsymbol{K}_{\phi D}^e]^t & \boldsymbol{0} & \boldsymbol{K}_{DD}^{De} \end{bmatrix} \begin{Bmatrix} \boldsymbol{a} \\ \boldsymbol{\phi} \\ T_0^e \\ \boldsymbol{\beta}_D^{De} \end{Bmatrix} = \begin{Bmatrix} \boldsymbol{f} \\ \boldsymbol{0} \\ 0 \\ \boldsymbol{0} \end{Bmatrix}. \tag{3.83}$$

The expanded matrix form given in (3.83) can be written in terms of only kinematic-like variables by condensing out all additional terms as

$$\left[\ \boldsymbol{K}_M^{De}\ \right]\left\{\begin{array}{c}\boldsymbol{a}\\ \boldsymbol{\phi}\end{array}\right\}=\left\{\begin{array}{c}\boldsymbol{f}\\ \boldsymbol{0}\end{array}\right\}, \tag{3.84}$$

where the electric flux density β-parameters are

$$\boldsymbol{\beta}_D^{De}=[\boldsymbol{K}_{DD}^{De}]^{-1}[(\boldsymbol{K}_{uD}^{e})^t-(\boldsymbol{K}_{\phi D}^{e})^t]\left\{\begin{array}{c}\boldsymbol{a}\\ \boldsymbol{\phi}\end{array}\right\}, \tag{3.85}$$

and the condensed stiffness matrix is given by

$$\boldsymbol{K}_M^{De}=\left[\begin{array}{cc}\boldsymbol{K}_{uu}^{De}+\frac{\gamma}{\Omega^e}\boldsymbol{h}^e[\boldsymbol{h}^e]^t & \boldsymbol{0}\\ \boldsymbol{0} & \boldsymbol{0}\end{array}\right]-\left[\begin{array}{c}\boldsymbol{K}_{uD}^{e}\\ -\boldsymbol{K}_{\phi D}^{e}\end{array}\right][\boldsymbol{K}_{DD}^{De}]^{-1}\left[\ (\boldsymbol{K}_{uD}^{e})^t-(\boldsymbol{K}_{\phi D}^{e})^t\ \right]. \tag{3.86}$$

The sub-matrices $\boldsymbol{K}_{uu}^{De}$ and $\boldsymbol{K}_{uD}^{e}$ are both evaluated using a 5-point integration scheme, while $\boldsymbol{K}_{DD}^{De}$ is computed using a standard 4-point scheme. Expressions for these matrices are explicitly given in Section 3.7.

P4dKD element based on Π_K^D

The K-type equivalent variational equation with assumed electric flux density can be calculated as

$$\begin{aligned}0=&\int_{\Omega^h}(\mathrm{symm}\boldsymbol{\nabla}\delta\boldsymbol{u}^h)^t\cdot\boldsymbol{c}_D\cdot(\mathrm{symm}\boldsymbol{\nabla}\boldsymbol{u}^h)\,\mathrm{d}V-\int_{\Omega^h}(\delta\boldsymbol{D}^h)^t\cdot\boldsymbol{h}\cdot(\mathrm{symm}\boldsymbol{\nabla}\boldsymbol{u}^h)\,\mathrm{d}V\\&-\int_{\Omega^h}(\mathrm{symm}\boldsymbol{\nabla}\delta\boldsymbol{u}^h)^t\cdot\boldsymbol{h}^t\cdot(\boldsymbol{D}^h)\,\mathrm{d}V+\int_{\Omega^h}(\delta\boldsymbol{D}^h)^t\cdot\boldsymbol{\chi}_S\cdot(\boldsymbol{D}^h)\,\mathrm{d}V\\&+\int_{\Omega^h}(\delta\boldsymbol{D}^h)^t\cdot(\boldsymbol{\nabla}\phi^h)\,\mathrm{d}V+\int_{\Omega^h}(\boldsymbol{\nabla}\delta\phi^h)^t\cdot(\boldsymbol{D}^h)\,\mathrm{d}V\\&+\gamma\int_{\Omega^h}(\mathrm{skew}\boldsymbol{\nabla}\delta\boldsymbol{u}^h-\delta\boldsymbol{\psi}^h)^t\cdot(\mathrm{skew}\boldsymbol{\nabla}\boldsymbol{u}^h-\boldsymbol{\psi}^h)\,\mathrm{d}V-\int_{\Omega^h}(\delta\boldsymbol{u}^h)^t\cdot\boldsymbol{f}\,\mathrm{d}V.\end{aligned} \tag{3.87}$$

The matrix form of (3.87) becomes

$$\left[\begin{array}{ccc}\boldsymbol{K}_{uu}^{De}+\boldsymbol{P}^e & \boldsymbol{0} & -\boldsymbol{K}_{uD}^{e}\\ \boldsymbol{0} & \boldsymbol{0} & \boldsymbol{K}_{\phi D}^{e}\\ -[\boldsymbol{K}_{uD}^{e}]^t & [\boldsymbol{K}_{\phi D}^{e}]^t & \boldsymbol{K}_{DD}^{De}\end{array}\right]\left\{\begin{array}{c}\boldsymbol{a}\\ \boldsymbol{\phi}\\ \boldsymbol{\beta}_D^{De}\end{array}\right\}=\left\{\begin{array}{c}\boldsymbol{f}\\ \boldsymbol{0}\\ \boldsymbol{0}\end{array}\right\}. \tag{3.88}$$

Again, the matrix form in (3.88) is simplified to include only kinematic variables as

$$\left[\ \boldsymbol{K}_K^{De}\ \right]\left\{\begin{array}{c}\boldsymbol{a}\\ \boldsymbol{\phi}\end{array}\right\}=\left\{\begin{array}{c}\boldsymbol{f}\\ \boldsymbol{0}\end{array}\right\}, \tag{3.89}$$

where the same electric flux density β-parameters as (3.85) result. In this case, the simplified stiffness matrix is

$$\boldsymbol{K}_K^{De} = \begin{bmatrix} \boldsymbol{K}_{uu}^{De} + \boldsymbol{P}^e & \boldsymbol{0} \\ \boldsymbol{0} & \boldsymbol{0} \end{bmatrix} - \begin{bmatrix} \boldsymbol{K}_{uD}^e \\ -\boldsymbol{K}_{\phi D}^e \end{bmatrix} [\boldsymbol{K}_{DD}^{De}]^{-1} \begin{bmatrix} (\boldsymbol{K}_{uD}^e)^t - (\boldsymbol{K}_{\phi D}^e)^t \end{bmatrix}, \tag{3.90}$$

with individual stiffness matrix terms presented in Section 3.7. The same integration schemes as used previously are again employed here to evaluate individual sub-matrices.

3.6.4 Degenerate assumed stress piezoelectric elements with drilling DOFs

Finally, the assumed stress degenerate mixed elements are presented. These elements are denoted P4dMnT and P4dKnT, and arise from Π_M^T and Π_K^T, respectively. Again, the n in the element designation denotes the number of stress parameters employed. Of course 'assumed stress' refers specifically to the assumed symmetric part of stress since all M-type elements contain an assumed skew-symmetric stress.

P4dMnT element based on Π_M^T

The assumed stress degenerate Hellinger-Reissner like variational equation in discrete form is given by

$$\begin{aligned} 0 = &- \int_{\Omega^h} (\text{symm}\delta\boldsymbol{T}^h)^t \cdot \boldsymbol{s}_E \cdot (\text{symm}\boldsymbol{T}^h)\, \text{d}V + \int_{\Omega^h} (\boldsymbol{\nabla}\delta\phi^h)^t \cdot \boldsymbol{d} \cdot (\text{symm}\boldsymbol{T}^h)\, \text{d}V \\ &+ \int_{\Omega^h} (\text{symm}\delta\boldsymbol{T}^h)^t \cdot \boldsymbol{d}^t \cdot (\boldsymbol{\nabla}\phi^h)\, \text{d}V - \int_{\Omega^h} (\boldsymbol{\nabla}\delta\phi^h)^t \cdot \boldsymbol{\epsilon}_T \cdot (\boldsymbol{\nabla}\phi^h)\, \text{d}V \\ &+ \int_{\Omega^h} (\text{symm}\delta\boldsymbol{T}^h)^t \cdot (\text{symm}\boldsymbol{\nabla}\boldsymbol{u}^h)\, \text{d}V + \int_{\Omega^h} (\text{symm}\boldsymbol{\nabla}\delta\boldsymbol{u}^h)^t \cdot (\text{symm}\boldsymbol{T}^h)\, \text{d}V \\ &+ \int_{\Omega^h} (\text{skew}\delta\boldsymbol{T}^h)^t \cdot (\text{skew}\boldsymbol{\nabla}\boldsymbol{u}^h - \boldsymbol{\psi}^h)\, \text{d}V + \int_{\Omega^h} (\text{skew}\boldsymbol{\nabla}\delta\boldsymbol{u}^h)^t \cdot \text{skew}\boldsymbol{T}^h \\ &- (\delta\boldsymbol{\psi}^h)^t \cdot \text{skew}\boldsymbol{T}^h\, \text{d}V - \gamma^{-1} \int_{\Omega^h} (\text{skew}\delta\boldsymbol{T}^h)^t \cdot \text{skew}\boldsymbol{T}^h\, \text{d}V - \int_{\Omega^h} (\delta\boldsymbol{u}^h)^t \cdot \boldsymbol{f}\, \text{d}V. \end{aligned} \tag{3.91}$$

Yet again, the expression in (3.91) can be rewritten in matrix form as

$$\begin{bmatrix} \boldsymbol{0} & \boldsymbol{0} & \boldsymbol{h}^e & \boldsymbol{K}_{uT}^e \\ \boldsymbol{0} & -\boldsymbol{K}_{\phi\phi}^{Te} & \boldsymbol{0} & \boldsymbol{K}_{\phi T}^e \\ [\boldsymbol{h}^e]^t & \boldsymbol{0} & -\gamma^{-1}\Omega^e & \boldsymbol{0} \\ [\boldsymbol{K}_{uT}^e]^t & [\boldsymbol{K}_{\phi T}^e]^t & \boldsymbol{0} & -\boldsymbol{K}_{TT}^{Te} \end{bmatrix} \begin{Bmatrix} \boldsymbol{a} \\ \boldsymbol{\phi} \\ T_0^e \\ \boldsymbol{\beta}_T^{Te} \end{Bmatrix} = \begin{Bmatrix} \boldsymbol{f} \\ \boldsymbol{0} \\ 0 \\ \boldsymbol{0} \end{Bmatrix}. \tag{3.92}$$

The matrix form in (3.92) is again rewritten in simplified form as

$$\left[\ \boldsymbol{K}_M^{Te}\ \right]\left\{\begin{array}{c}\boldsymbol{a}\\ \boldsymbol{\phi}\end{array}\right\}=\left\{\begin{array}{c}\boldsymbol{f}\\ \boldsymbol{0}\end{array}\right\}, \tag{3.93}$$

where the stress β-parameters are found to be

$$\boldsymbol{\beta}_M^T=[\boldsymbol{K}_{TT}^{Te}]^{-1}[(\boldsymbol{K}_{uT}^e)^t+(\boldsymbol{K}_{\phi T}^e)^t]\left\{\begin{array}{c}\boldsymbol{a}\\ \boldsymbol{\phi}\end{array}\right\}. \tag{3.94}$$

Finally, the condensed stiffness matrix is written as

$$\boldsymbol{K}_M^{Te}=\left[\begin{array}{cc}\frac{\gamma}{\Omega^e}\boldsymbol{h}^e[\boldsymbol{h}^e]^t & \boldsymbol{0}\\ \boldsymbol{0} & -\boldsymbol{K}_{\phi\phi}^{Te}\end{array}\right]+\left[\begin{array}{c}\boldsymbol{K}_{uT}^e\\ \boldsymbol{K}_{\phi T}^e\end{array}\right][\boldsymbol{K}_{TT}^{Te}]^{-1}\left[\begin{array}{cc}(\boldsymbol{K}_{uT}^e)^t & (\boldsymbol{K}_{\phi T}^e)^t\end{array}\right]. \tag{3.95}$$

The submatrices $\boldsymbol{K}_{TT}^{Te}$ and $\boldsymbol{K}_{\phi T}^e$ are evaluated with a 5-point integration scheme, while the term $\boldsymbol{K}_{\phi\phi}^{Te}$ employs a 4-point scheme. Expressions for these terms are contained in Section 3.7.

P4dKnT element based on Π_K^T

The last element implementation is based on the assumed stress K-type Hellinger-Reissner like functional. The first variation of Π_K^T can be expressed in discrete form as

$$\begin{aligned}0=&-\int_{\Omega^h}(\mathrm{symm}\delta\boldsymbol{T}^h)^t\cdot\boldsymbol{s}_E\cdot(\mathrm{symm}\boldsymbol{T}^h)\,\mathrm{d}V+\int_{\Omega^h}(\boldsymbol{\nabla}\delta\phi^h)^t\cdot\boldsymbol{d}\cdot(\mathrm{symm}\boldsymbol{T}^h)\,\mathrm{d}V\\&+\int_{\Omega^h}(\mathrm{symm}\delta\boldsymbol{T}^h)^t\cdot\boldsymbol{d}^t\cdot(\boldsymbol{\nabla}\phi^h)\,\mathrm{d}V-\int_{\Omega^h}(\boldsymbol{\nabla}\delta\phi^h)^t\cdot\boldsymbol{\epsilon}_T\cdot(\boldsymbol{\nabla}\phi^h)\,\mathrm{d}V\\&+\int_{\Omega^h}(\mathrm{symm}\delta\boldsymbol{T}^h)^t\cdot(\mathrm{symm}\boldsymbol{\nabla}\boldsymbol{u}^h)\,\mathrm{d}V+\int_{\Omega^h}(\mathrm{symm}\boldsymbol{\nabla}\delta\boldsymbol{u}^h)^t\cdot(\mathrm{symm}\boldsymbol{T}^h)\,\mathrm{d}V\\&+\gamma\int_{\Omega^h}(\mathrm{skew}\boldsymbol{\nabla}\delta\boldsymbol{u}^h-\delta\boldsymbol{\psi}^h)^t\cdot(\mathrm{skew}\boldsymbol{\nabla}\boldsymbol{u}^h-\boldsymbol{\psi}^h)\,\mathrm{d}V-\int_{\Omega^h}(\delta\boldsymbol{u}^h)^t\cdot\boldsymbol{f}\,\mathrm{d}V.\end{aligned} \tag{3.96}$$

This expression can once yet again be written in matrix form as

$$\left[\begin{array}{ccc}\boldsymbol{P}^e & \boldsymbol{0} & \boldsymbol{K}_{uT}^e\\ \boldsymbol{0} & -\boldsymbol{K}_{\phi\phi}^{Te} & \boldsymbol{K}_{\phi T}^e\\ [\boldsymbol{K}_{uT}^e]^t & [\boldsymbol{K}_{\phi T}^e]^t & -\boldsymbol{K}_{TT}^{Te}\end{array}\right]\left\{\begin{array}{c}\boldsymbol{a}\\ \boldsymbol{\phi}\\ \boldsymbol{\beta}_T^{Te}\end{array}\right\}=\left\{\begin{array}{c}\boldsymbol{f}\\ \boldsymbol{0}\\ \boldsymbol{0}\end{array}\right\}. \tag{3.97}$$

The matrix form of (3.97) is finally simplified to

$$\left[\ \boldsymbol{K}_K^{Te}\ \right]\left\{\begin{array}{c}\boldsymbol{a}\\ \boldsymbol{\phi}\end{array}\right\}=\left\{\begin{array}{c}\boldsymbol{f}\\ \boldsymbol{0}\end{array}\right\}, \tag{3.98}$$

where the condensed stress β-parameters are given by (3.94), and the simplified element stiffness matrix is given by

$$\boldsymbol{K}_K^{Te} = \begin{bmatrix} \boldsymbol{P}^e & \boldsymbol{0} \\ \boldsymbol{0} & -\boldsymbol{K}_{\phi\phi}^{Te} \end{bmatrix} + \begin{bmatrix} \boldsymbol{K}_{uT}^e \\ \boldsymbol{K}_{\phi T}^e \end{bmatrix} [\boldsymbol{K}_{TT}^{Te}]^{-1} \begin{bmatrix} (\boldsymbol{K}_{uT}^e)^t & (\boldsymbol{K}_{\phi T}^e)^t \end{bmatrix}. \tag{3.99}$$

The components of the stiffness matrix are yet again presented in Section 3.7.

3.7 Partitioned stiffness matrices

In Section 3.6 expressions for the individual partitioned sub-matrices were omitted. For the convenience of the reader, it was chosen instead to present all partitioned sub-matrices together for easier reference. The partitioned stiffness matrices are therefore all given here in matrix form by:

$$\boldsymbol{K}_{uu}^{e\ (5)} = \int_{\Omega^e} [\boldsymbol{B}_u^e \quad \boldsymbol{G}_u^e]^t \boldsymbol{c}_E [\boldsymbol{B}_u^e \quad \boldsymbol{G}_u^e]\, \mathrm{d}V, \tag{3.100}$$

$$\boldsymbol{K}_{u\phi}^{e\ (5)} = \int_{\Omega^e} [\boldsymbol{B}_u^e \quad \boldsymbol{G}_u^e]^t \boldsymbol{e}^t [\boldsymbol{B}_\phi^e]\, \mathrm{d}V, \tag{3.101}$$

$$\boldsymbol{K}_{\phi\phi}^{e\ (4)} = \int_{\Omega^e} [\boldsymbol{B}_\phi^e]^t \boldsymbol{\epsilon}_S [\boldsymbol{B}_\phi^e]\, \mathrm{d}V, \tag{3.102}$$

$$\boldsymbol{h}^{e\ (4)} = \int_{\Omega^e} [\boldsymbol{b}^e \quad \boldsymbol{g}^e]^t\, \mathrm{d}V, \tag{3.103}$$

$$\boldsymbol{K}_{uu}^{De\ (5)} = \int_{\Omega^e} [\boldsymbol{B}_u^e \quad \boldsymbol{G}_u^e]^t \boldsymbol{c}_D [\boldsymbol{B}_u^e \quad \boldsymbol{G}_u^e]\, \mathrm{d}V, \tag{3.104}$$

$$\boldsymbol{K}_{uD}^{e\ (5)} = \int_{\Omega^e} [\boldsymbol{B}_u^e \quad \boldsymbol{G}_u^e]^t \boldsymbol{h}^t [\boldsymbol{P}_D^e]\, \mathrm{d}V, \tag{3.105}$$

$$\boldsymbol{K}_{\phi D}^{e\ (4)} = \int_{\Omega^e} [\boldsymbol{B}_\phi^e]^t [\boldsymbol{P}_D^e]\, \mathrm{d}V, \tag{3.106}$$

$$\boldsymbol{K}_{DD}^{De\ (4)} = \int_{\Omega^e} [\boldsymbol{P}_D^e]^t \boldsymbol{\chi}_S [\boldsymbol{P}_D^e]\, \mathrm{d}V, \tag{3.107}$$

$$\boldsymbol{K}_{\phi T}^{e\ (5)} = \int_{\Omega^e} [\boldsymbol{B}_\phi^e]^t \boldsymbol{d} [\boldsymbol{P}_T^e]\, \mathrm{d}V, \tag{3.108}$$

$$\boldsymbol{K}_{\phi\phi}^{Te\ (4)} = \int_{\Omega^e} [\boldsymbol{B}_\phi^e]^t \boldsymbol{\epsilon}_T [\boldsymbol{B}_\phi^e]\, \mathrm{d}V, \tag{3.109}$$

$$\boldsymbol{K}_{uT}^{e\ (5)} = \int_{\Omega^e} [\boldsymbol{B}_u^e \quad \boldsymbol{G}_u^e]^t [\boldsymbol{P}_T^e]\, \mathrm{d}V, \tag{3.110}$$

$$\boldsymbol{K}_{TT}^{Te\ (5)} = \int_{\Omega^e} [\boldsymbol{P}_T^e]^t \boldsymbol{s}_E [\boldsymbol{P}_T^e]\, \mathrm{d}V, \tag{3.111}$$

$$\boldsymbol{K}_{TD}^{TDe\ (5)} = \int_{\Omega^e} [\boldsymbol{P}_T^e]^t \boldsymbol{g}^t [\boldsymbol{P}_D^e]\, \mathrm{d}V, \tag{3.112}$$

$$\boldsymbol{K}_{TT}^{TDe\ (5)} = \int_{\Omega^e} [\boldsymbol{P}_T^e]^t \boldsymbol{s}_D [\boldsymbol{P}_T^e]\, \mathrm{d}V, \tag{3.113}$$

$$\boldsymbol{K}_{DD}^{TDe\ (4)} = \int_{\Omega^e} [\boldsymbol{P}_D^e]^t \boldsymbol{\chi}_T [\boldsymbol{P}_D^e]\, \mathrm{d}V, \tag{3.114}$$

and finally,

$$\boldsymbol{P}^{e\ (1)} = \gamma \int_{\Omega^e} [\boldsymbol{b}^e \quad \boldsymbol{g}^e]^t [\boldsymbol{b}^e \quad \boldsymbol{g}^e]\, \mathrm{d}V. \tag{3.115}$$

The superscript in parentheses $^{(\cdot)}$ represents the number of integration points used to perform the numerical integration over the element area. (The elements are assumed to be homogeneous and have constant area profile through the thickness. Analytical through thickness integration is thus employed.)

3.8 Numerical evaluation

In this section, the developed piezoelectric finite elements are assessed numerically and compared with existing elements. The effect of selected parameters are also quantified. Unlike in our paper where, for brevity, only the two elements were reported on, in this section the performance of all eight new elements is evaluated. The elements used in the comparison are denoted as follows:

Elements without drilling DOFs

Existing elements from literature were implemented, against which our new elements are benchmarked. These existing elements are denoted as follows:

- P4 – A standard, planar 4 node, quadrilateral piezoelectric element without drilling DOFs. Only the displacement $\boldsymbol{u}$ and the potential ϕ interpolated for, see for example [69].
- P4D – A mixed 4 node element with only electric flux density $\boldsymbol{D}$ assumed additionally to displacement and electric potential, as proposed in [76]. The same electric flux density interpolation (with four β-parameters) as in Section 3.5 is employed.
- P4T – A mixed 4 node element with only stress $\boldsymbol{T}$ assumed additionally to displacement and electric potential, as proposed in [76]. In this case, an interpolation with only five stress β-parameters is required. The standard stress interpolation of, for instance Di and Ramm [61] is employed.
- P4TD – A mixed 4 node element with both stress $\boldsymbol{T}$ and electric flux density $\boldsymbol{D}$ assumed additionally to displacement and electric potential, as proposed in [65]. An interpolation for electric flux density with four β parameters and five stress β-parameters is employed.

'Irreducible' elements with drilling DOFs:

- P4dM – A 4 node element with drilling DOFs, derived from functional Π_M in (3.29), and with stiffness matrix given by (3.68).

- P4dK – A 4 node element with drilling DOFs, derived from functional Π_K in (3.31), and with stiffness matrix given by (3.72).

'Degenerate' Hellinger-Reissner like elements:

- P4dMD – A 4 node assumed electric flux density element with drilling DOFs, derived from functional Π_M^D in (3.37), and with stiffness matrix given by (3.86).
- P4dKD – A 4 node assumed electric flux density element with drilling DOFs, derived from functional Π_K^D in (3.39), and with stiffness matrix given by (3.90).
- P4dMnT – A 4 node assumed stress element with drilling DOFs, derived from functional Π_M^T in (3.41), and with stiffness matrix given by (3.95), and number of stress parameters given by n.
- P4dKnT – A 4 node assumed stress element with drilling DOFs, derived from functional Π_K^T in (3.43), and with stiffness matrix given by (3.99), and number of stress parameters given by n.

Fully mixed Hellinger-Reissner like elements:

- P4dMnTD – A fully mixed 4 node element, based on functional Π_M^{TD} given in (3.33), with stiffness matrix given in (3.77). The number of stress interpolation parameters is given by n.
- P4dKnTD – A fully mixed 4 node element, based on functional Π_M^{TD} given in (3.35), with stiffness matrix given in (3.81). The number of stress interpolation parameters is given by n.

In the test problems to follow, unless otherwise stated, the material constants of PZT-4 given by Sze *et al.* [64] are employed so that our piezoelectric elements may be compared to theirs. To this end, the following material constants are used:

$$c_{11} = 139 \times 10^3, \quad c_{33} = 113 \times 10^3, \quad c_{13} = 74.3 \times 10^3, \quad c_{55} = 25.6 \times 10^3 \text{ (in N/mm}^2\text{)}$$
$$e_{15} = 13.44 \times 10^6, \quad e_{31} = -6.98 \times 10^6, \quad e_{33} = 13.84 \times 10^6 \text{ (in pC/mm}^2\text{)}$$
$$\epsilon_{11} = 6.00 \times 10^9, \quad \epsilon_{33} = 5.47 \times 10^9 \text{ (in pC/(GVmm))}.$$

The units of length, force, stress, charge, electric displacement and electric potential, respectively, are taken as mm, N, N/mm^2, pC, pC/mm^2 and GV. This unusual unit choice alleviates the ill effects resulting from the poor scaling of the global stiffness matrix. The poling direction in the test problems to follow, unless otherwise stated, is taken as the global y–direction. The constitutive equations which result are

$$\begin{Bmatrix} T_{xx} \\ T_{yy} \\ T_{xy} \\ D_x \\ D_y \end{Bmatrix} = \begin{bmatrix} c_{11} & c_{13} & 0 & 0 & -e_{31} \\ c_{13} & c_{33} & 0 & 0 & -e_{33} \\ 0 & 0 & c_{55} & -e_{15} & 0 \\ 0 & 0 & e_{15} & \epsilon_{11} & 0 \\ e_{31} & e_{33} & 0 & 0 & \epsilon_{33} \end{bmatrix} \begin{Bmatrix} S_{xx} \\ S_{yy} \\ S_{xy} \\ E_x \\ E_y \end{Bmatrix}. \tag{3.116}$$

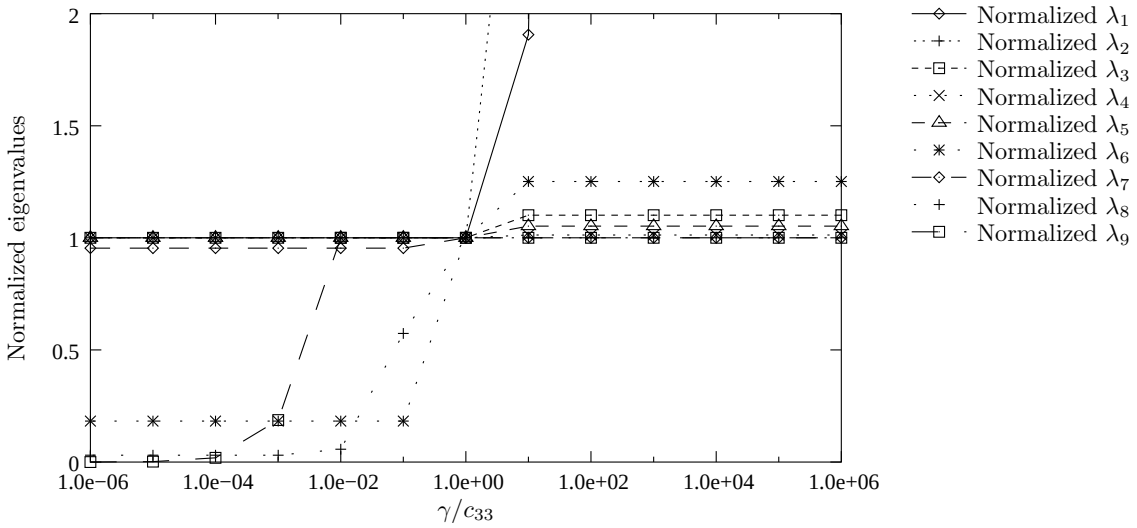

Figure 3.4: Effect of γ on eigenvalues (normalised with respect to their values at $\gamma/c_{33} = 1$).

Constants used in the analytical solutions of some of the tests to follow, are given by

$$\begin{bmatrix} s_{11} & s_{13} & g_{31} \\ s_{13} & s_{33} & g_{33} \\ -g_{31} & -g_{33} & \beta_{33} \end{bmatrix} = \begin{bmatrix} c_{11} & c_{13} & -e_{31} \\ c_{13} & c_{33} & -e_{33} \\ e_{31} & e_{33} & \epsilon_{33} \end{bmatrix}^{-1} . \tag{3.117}$$

3.8.1 Effect of γ

The elements developed in the foregoing are dependant on the problem-dependent penalty parameter γ. The effect of γ has been the focus of a number of recent studies, see Chapter 2 and [43, 58, 81] for examples. For linear elastic isotropic Dirichlet problems, the formulation is reported to be relatively insensitive to the value of γ [18, 21, 45], and it was proposed that $\gamma = \mu$, the shear modulus. Under different conditions, e.g. orthotropy (as in the case of piezoelectric materials) or dynamic problems, a greater sensitivity to γ is expected. For dynamic problems, for example, Hughes *et al.* [82] propose a value of $\gamma = \mu/10$.

To determine an appropriate value for γ, an eigenvalue analysis of an undistorted (square) P4dM element is performed. Although results are only reported for the P4dM element, the trends depicted in Figures 3.4 and 3.5 are typical for all of our new elements. Figure 3.4 depicts the effect of γ on the non-zero eigenvalues, arranged in descending order. The eigenvalues are normalised with respect to their values at $\gamma = c_{33}$. It is clear that the 'softer' modes are most sensitive to γ at values of $\gamma/c_{33} < 1$. For values of $\gamma/c_{33} > 1$, on the other hand, the 'harder' modes are significantly more sensitive, in particular λ_1 and λ_2, indicative of a locking-like phenomena. This results from the terms in the stiffness matrix containing γ dominating the response.

In order to determine the effect of γ on the accuracy of the current formulations, a representative test problem is studied for an array of γ values. The 10 element cantilever, depicted

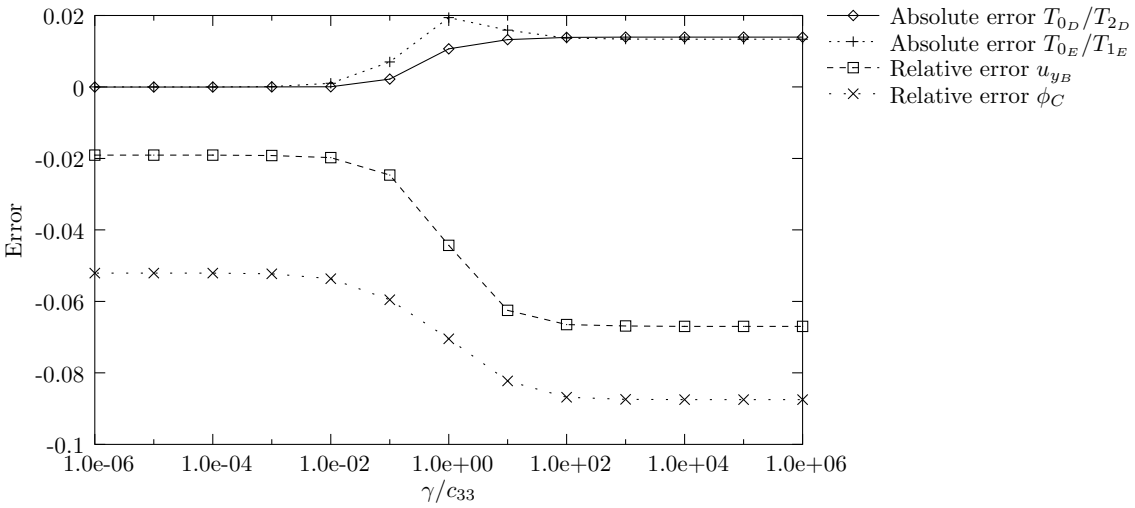

Figure 3.5: Effect of γ on skew part of stress and other accuracy measures.

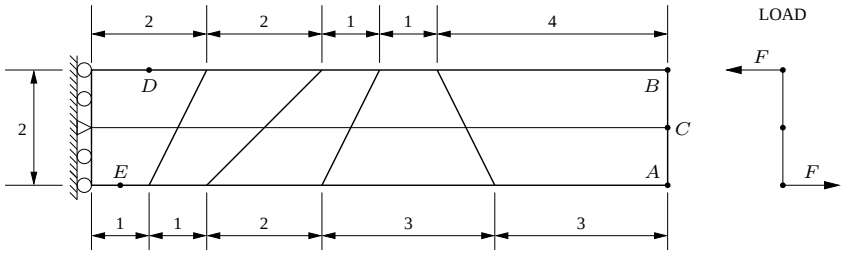

Figure 3.6: Ten element piezoelectric cantilever beam subjected to pure bending.

Figure 3.6, is selected for this study. In Figure 3.5 some accuracy measures are plotted as a function of γ/c_{33}.

Figure 3.5 shows how the accuracy of u_{yB}, the y–displacement at point B and of ϕ_C, the electric potential at C (see Figure 3.6), decrease at values of $\gamma/c_{33} > 1$. Also plotted is an indication of the error on the skew-symmetric part of stress, T_0 as suggested in Chapter 2 and [58]. The plotted values are normalised with respect to principle stresses at points D and E. T_{0D} and T_{0E} are the constant skew-symmetric part of stress in the elements containing points D and E, respectively. T_{2D} is the second (compressive) principle stress calculated at D and T_{1E} is the first principle stress at E. Since the skew-symmetric part of stress should be zero, both T_{0D}/T_{2D} and T_{0E}/T_{1E} should in turn be zero. Notably, the error on the skew-symmetric stress increases with larger values of γ/c_{33}. To avoid operating in the regime where the gradient change of the accuracy measures occurs, it is suggested that a value of $\gamma/c_{33} = 10^{-2}$ be used.

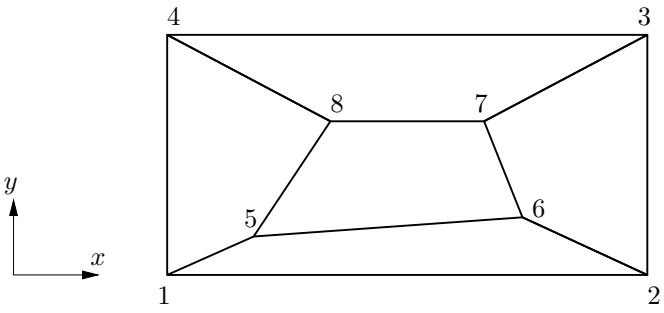

Coordinates:

Vertex	x	y
1	0.2	0.
2	0.44	0.
3	0.44	0.12
4	0.2	0.12
5	0.24	0.02
6	0.38	0.03
7	0.36	0.08
8	0.28	0.08

Figure 3.7: Mesh for piezoelectric patch test.

3.8.2 Eigenvalue analysis

Since a reduced order integration scheme is employed during stiffness calculations and a nonstandard γ value is used, element rank sufficiency needs to be verified by means of an eigenvalue analysis. The eigenvalues of 2×2, undistorted (square) elements are computed. (Eigenvalue analyses should in general be carried out on undistorted elements, since distortion may actually suppress zero energy modes due to the inaccuracies of an approximate integration scheme.)

In the case of planar piezoelectric elements, the mechanical partition of the stiffness matrix should contain only 3 zero eigenvalues corresponding to the 3 rigid body modes. An eigenvalue analysis of the dielectric part of the element stiffness matrix should reveal a single zero eigenvalue, corresponding to the constant potential distribution resulting in zero electric field. For the sake of brevity, the eigenvalues are not reported here. It was, however verified that each element possesses the proper number of non-zero eigenvalues.

3.8.3 Patch test

The patch test is a standard method to test for element convergence, as well as any possible implementation or programming errors. The test is performed with the geometry and mesh suggested by Sze *et al.* [64], as shown in Figure 3.7. Kinematic (displacement and potential) terms on the boundary are prescribed, corresponding to:

$$u_x = s_{11}\sigma_0 x, \qquad u_y = s_{13}\sigma_0 y, \qquad \phi = g_{31}\sigma_0 y, \tag{3.118}$$

with σ_0 a stress parameter. The corresponding stress and electric displacement can be shown to be constant, and are given by

$$T_{xx} = \sigma_0, \qquad T_{yy} = T_{xy} = D_x = D_y = 0. \tag{3.119}$$

Compliance with the conditions above was verified for each of the elements used in this study. A force patch test, with prescribed boundary forces corresponding to (3.119), was also conducted.

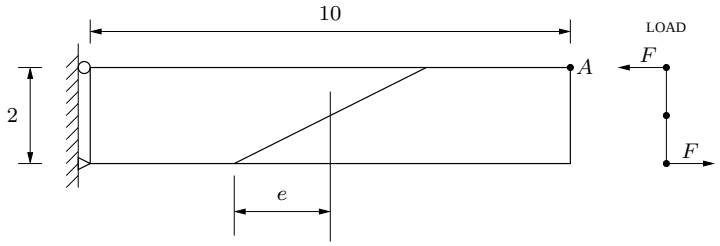

Figure 3.8: Two element piezoelectric cantilever beam subjected to pure bending.

3.8.4 Two element beam

The two element beam bending test is used to quantify the effect of distortion on element accuracy. Figure 3.8 depicts a cantilever beam of length L=10 and height h=2, modelled using two elements with a common distortion e. The electric potential of all nodes at $y = -1$ is prescribed to be zero. The exact solution for this problem was presented by Sze *et al.* [64]. The analytical solutions to this problem include:

$$u_x = -s_{11}\sigma_0 xy, \quad u_y = \frac{s_{13}\sigma_0}{2}\left(\frac{h^2}{4} - y^2\right) + \frac{s_{11}}{2}\sigma_0 x^2, \quad \phi = \frac{g_{31}\sigma_0}{2}\left(\frac{h^2}{4} - y^2\right), \quad T_x = -\sigma_0 y,$$

$$T_y = T_{xy} = D_x = D_y = 0, \qquad M = \int_{-h/2}^{h/2} yT_x \mathrm{d}y = -\frac{h^3\sigma_0}{12} = -hF.$$

Figure 3.9 depicts the relative error of the y–displacement at point A, i.e. $u_{y_A}/u_{y\text{Exact}} - 1$, for the various elements being tested. Considering the irreducible elements, the superior accuracy and stability of the P4dM and P4dK elements over the standard P4 elements is clear. The displacement accuracy of the assumed flux density elements are similar to that of the irreducible, and are actually slightly less accurate than the irreducible elements. Although the elements with 8 β-parameters perform slightly better than the elements with 9 β-parameters, the assumed stress elements surprisingly severely overestimate the tip displacements for the non-distorted mesh. The P4TD fully mixed elements without drilling degrees of freedom achieve an accuracy comparable to the elements developed by Sze *et al.* [64]. It is also demonstrated that the P4dM8TD and P4dK8TD elements are accurate and stable, even at extreme mesh distortions. In fact, for this problem these elements perform slightly better than the stabilised plane element developed by Sze *et al.* [64], as shown in Figure 3.9.

Figure 3.10 depicts the absolute error on the electric potential at point A, ϕ_A. In contrast to the displacement results, the elements without drilling DOFs all achieve a better accuracy on electric potential than the elements of the same family with drilling DOFs. However, considering the irreducible elements (which are the least numerically expensive and are the easiest to implement) the accuracy gained on the displacement is far more significant than that lost on electric potential. Unfortunately Sze *et al.* [64] did not report on this quantity, so comparison with their element was not possible. Having said than, the parabolic 'through-thickness' potential distribution of the exact solution can, of course, not be captured using

bilinear potential interpolations with the current mesh. The result is that for a regular mesh, zero electric field is predicted and therefore relatively large errors on displacement accrue due to the inherent coupling (as is apparent with the assumed stress elements).

This test is therefore repeated with a mesh consisting of two elements along the length (as before), but this time with two elements through the thickness (four elements in total). Although the effects of the mesh distortion are more pronounced for the aspect ratio of the elements in this test, this in our opinion, is a more reasonable mesh for this problem, since the physics of the problem can be approximated by all elements used in the comparison. That is to say, the parabolic potential distribution can be approximated using the bilinear potential interpolations of the aforementioned elements.

The displacement results are depicted in Figure 3.11. A significant improvement is achieved for the assumed stress degenerate elements, especially at zero distortion. All the elements with assumed stress (degenerate and full-mixed) perform similarly well. Once again the superior accuracy of our new irreducible elements with drilling DOFs over the standard P4 elements is noted. Our new elements also perform better than the existing P4D assumed flux density elements.

Figure 3.12 depicts the absolute error on ϕ_A for our four element beam problem. For this measure, a marked improvement is once again noted for the degenerate assumed stress elements with drilling DOFs. For this mesh, the standard P4T element only out-performs our new elements at extreme mesh distortions ($e > 2$). The electric potential of all fully mixed elements (with and without drilling DOFs) achieve similar accuracy. Although the irreducible and assumed flux density exhibit a slightly superior accuracy on electric potential when compared to the assumed stress and fully mixed elements, this slight accuracy improvement comes at the expense of a significant loss of accuracy on displacement accuracy.

3.8.5 Ten element beam

The same beam geometry as used in the two and four element test (with identical boundary conditions) is modelled, but this time with ten irregular elements as shown in Figure 3.6. Displacements and electric potentials are evaluated at points A, B and C and stresses and electric flux densities are calculated directly at points D and E. This problem was used by Wu *et al.* [65] to verify the accuracy of their P4TD element. Results are presented in Table 3.1.

Again, considering the irreducible elements used in this comparison, the the superior accuracy with respect most fields of the elements with drilling DOFs relative to P4 is evident. Our assumed flux density degenerate elements significantly out-perform the standard P4D elements on almost all measures. The performance of the assumed stress elements with and without drilling DOFs is similar, as is the performance of the fully mixed elements. In fact, the performance of the assumed stress family of elements is similar to the family of fully mixed elements with the notable exception of electric flux density accuracy. The inclusion of the independent interpolation for electric flux density therefore appears to significantly improve the accuracy of electrical quantities (potential and electric flux density).

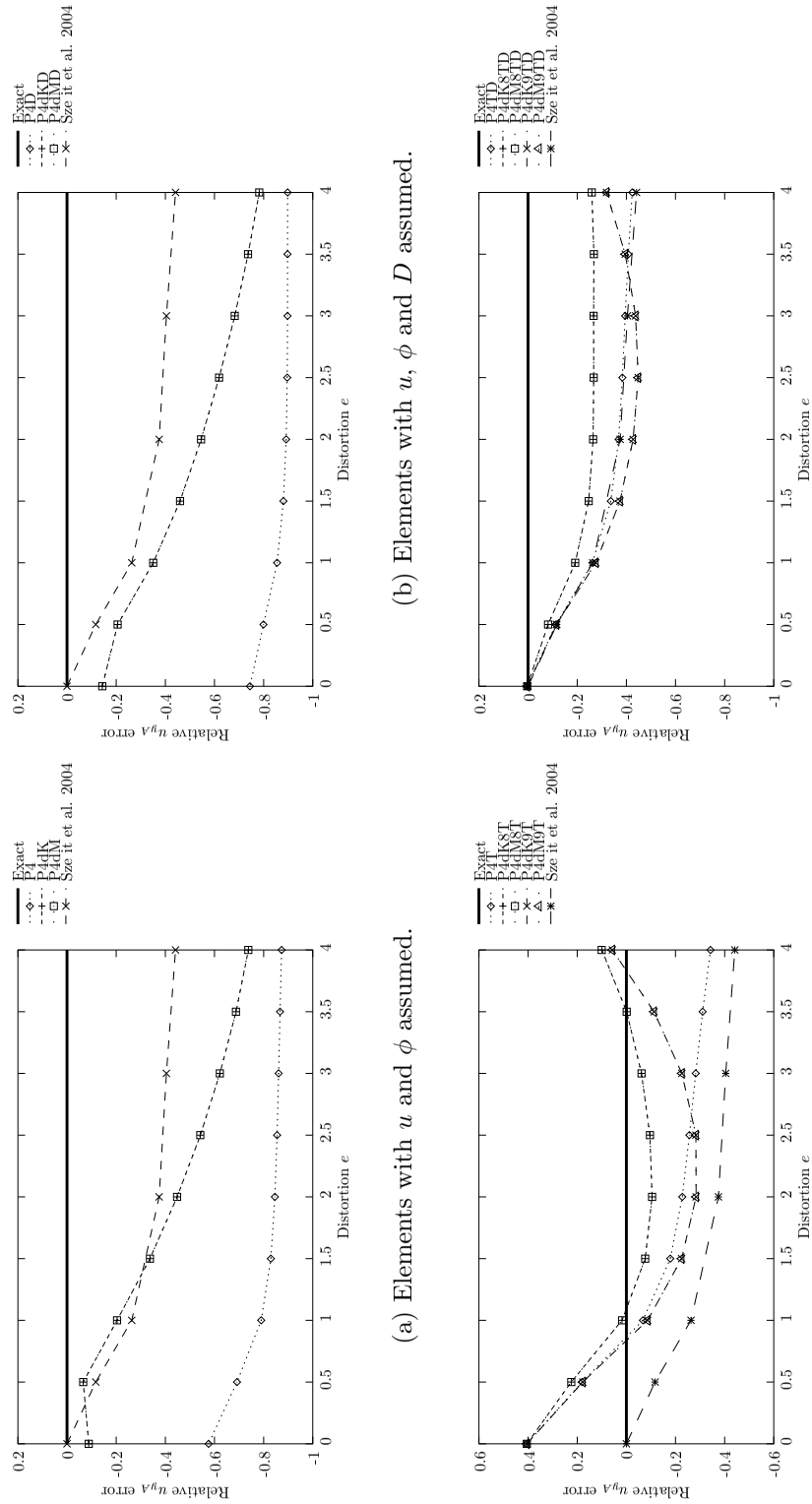

(a) Elements with u and ϕ assumed.

(b) Elements with u, ϕ and D assumed.

(c) Elements with u, ϕ and T assumed.

(d) Elements with u, ϕ, D and T assumed.

Figure 3.9: Two element piezoelectric beam subjected to pure bending: Effect of distortion on v_A.

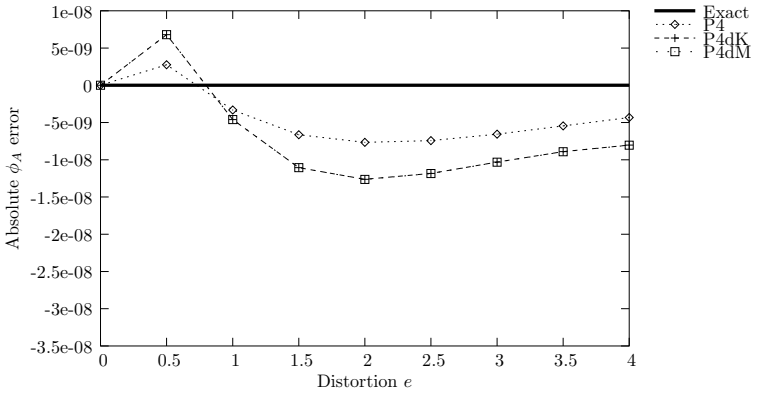

(a) Elements with u and ϕ assumed.

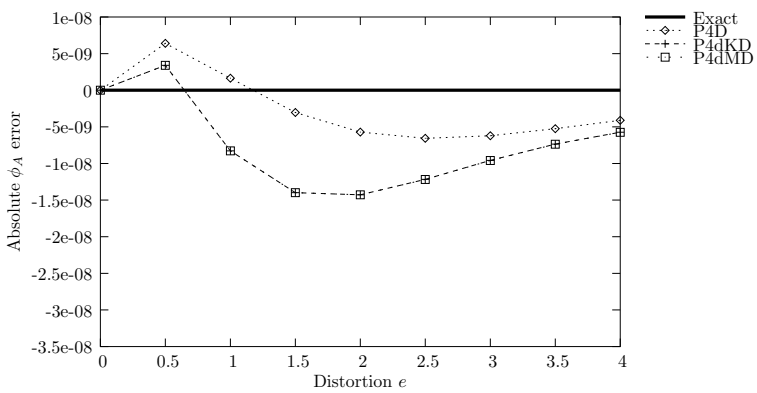

(b) Elements with u, ϕ and D assumed.

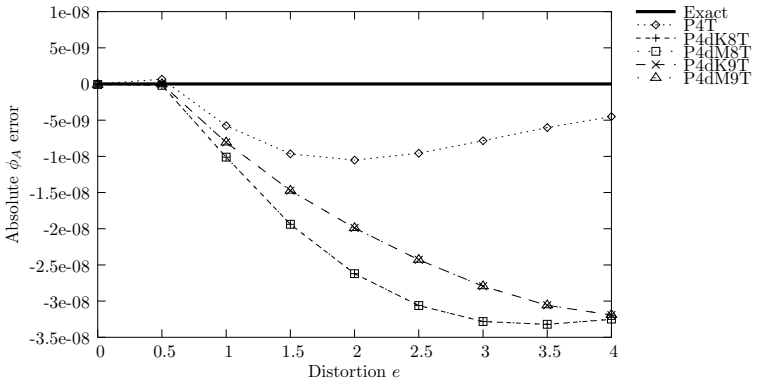

(c) Elements with u, ϕ and T assumed.

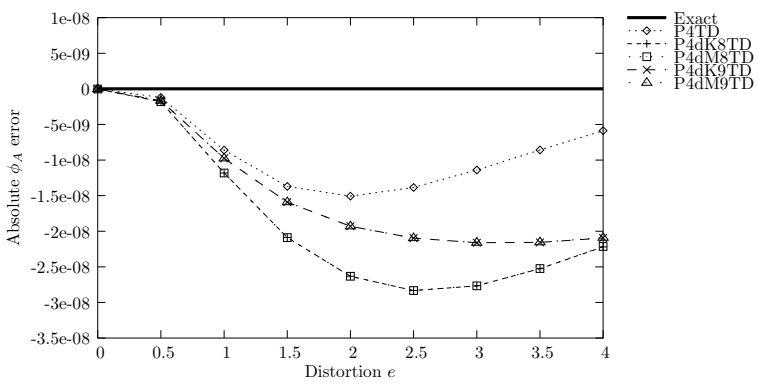

(d) Elements with u, ϕ, D and T assumed.

Figure 3.10: Two element piezoelectric beam subjected to pure bending: Effect of distortion on ϕ_A.

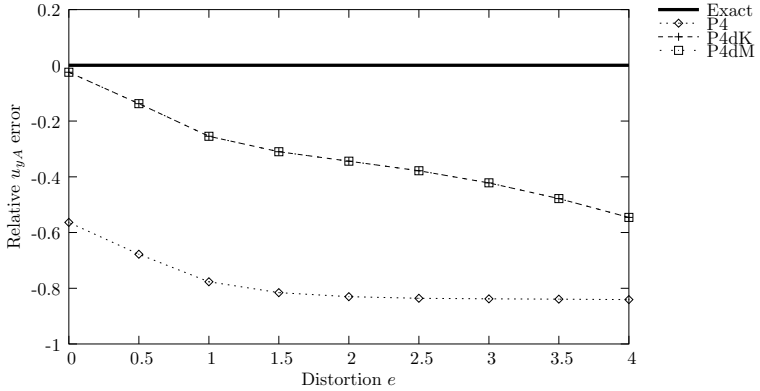

(a) Elements with u and ϕ assumed.

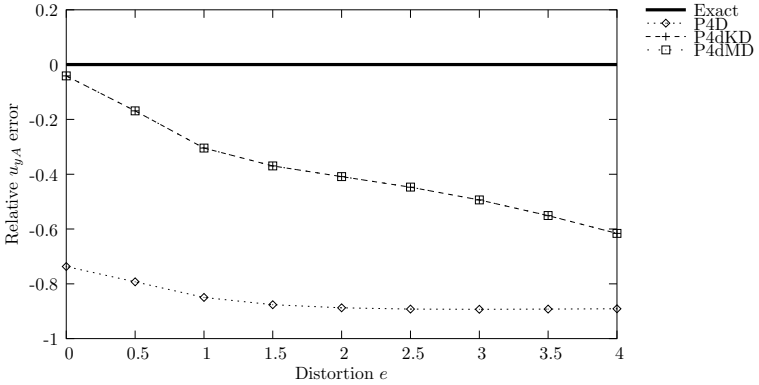

(b) Elements with u, ϕ and D assumed.

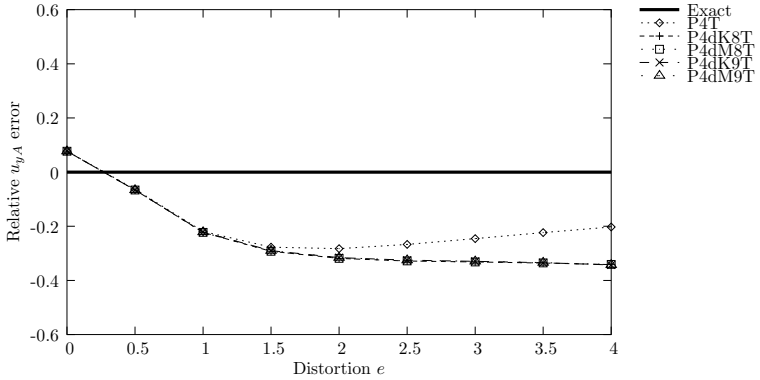

(c) Elements with u, ϕ and T assumed.

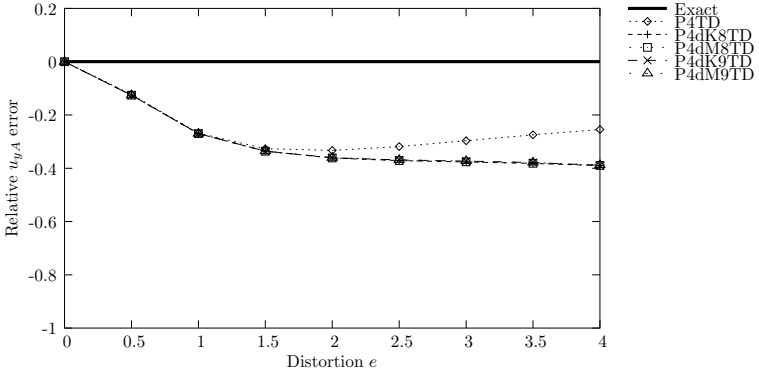

(d) Elements with u, ϕ, D and T assumed.

Figure 3.11: Four element piezoelectric beam subjected to pure bending: Effect of distortion on v_A.

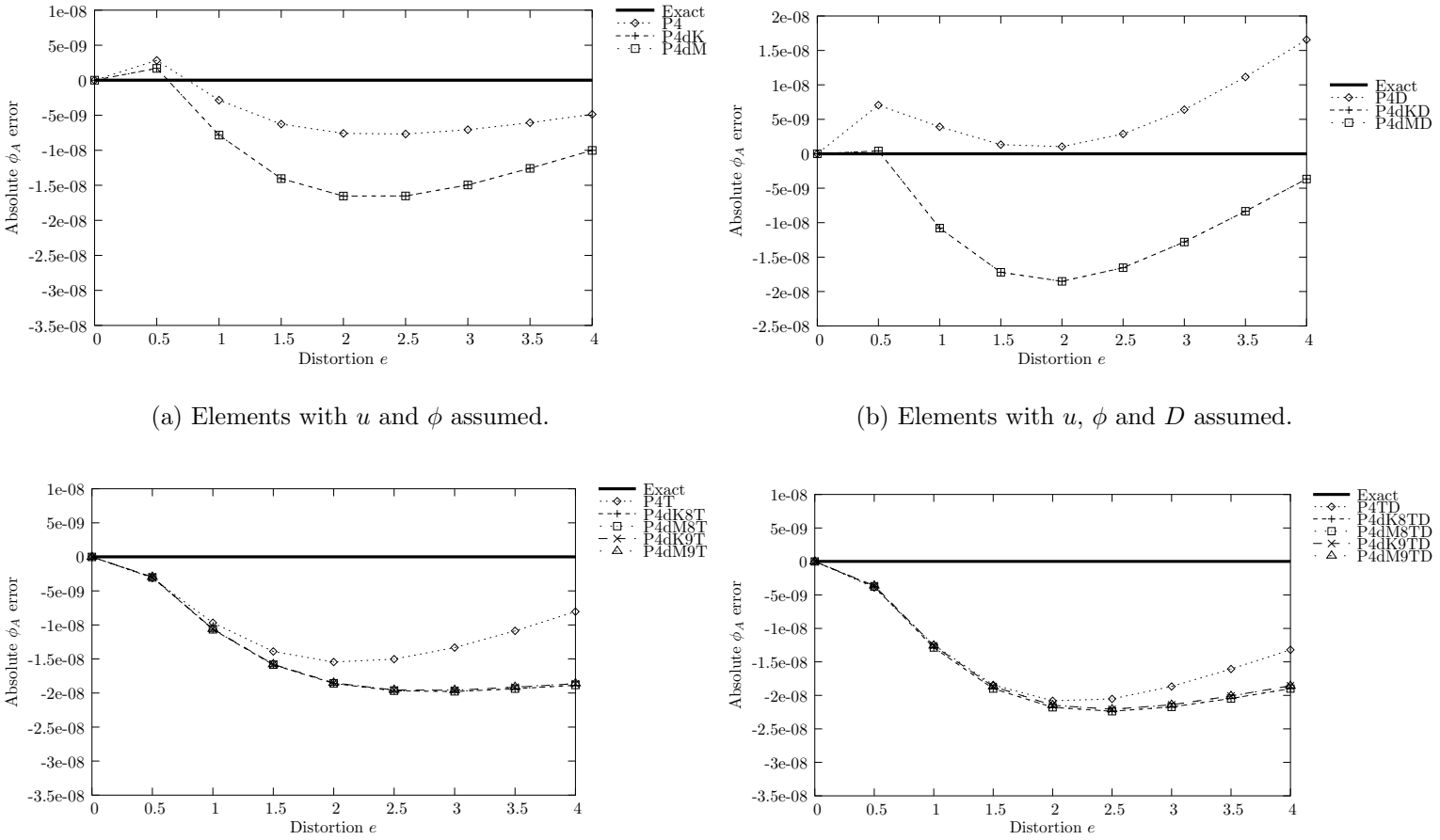

(a) Elements with u and ϕ assumed.

(b) Elements with u, ϕ and D assumed.

(c) Elements with u, ϕ and T assumed.

(d) Elements with u, ϕ, D and T assumed.

Figure 3.12: Four element piezoelectric beam subjected to pure bending: Effect of distortion on ϕ_A.

Table 3.1: Ten element piezoelectric cantilever subject to pure bending.

	Relative % error u_{xB}	Relative % error u_{yB}	Relative % error ϕ_C	Relative % error T_{xD}	Relative % error T_{xE}	Absolute error D_{yD}	Absolute error D_{yE}
P4	-40.4175	-36.1072	-48.1191	-21.3819	-5.2331	90.1438	-10.0964
P4dM	-3.4094	-1.3680	-5.3626	9.2982	18.1271	97.7308	-102.4166
P4dK	-3.4102	-1.3691	-5.3643	9.2977	18.1313	97.7287	-102.3594
P4D	-50.1581	-44.4320	-68.7544	-28.2890	-14.1054	32.5175	67.5230
P4dMD	-8.5244	-6.7333	-6.7703	7.5064	18.6191	-5.0939	7.6408
P4dKD	-8.5248	-6.7340	-6.7723	7.5049	18.6171	-5.0934	7.6520
P4T	1.0322	2.9902	7.5749	-7.1865	-6.9662	174.6776	-218.2058
P4dM8T	0.4151	2.2293	7.2564	-5.5496	-2.1303	183.0845	-231.3944
P4dK8T	0.4148	2.2295	7.2527	-5.5553	-2.1301	183.0898	-231.3809
P4dM9T	0.4814	2.2079	7.1959	-10.0337	-2.0298	130.5465	-225.8105
P4dK9T	0.4812	2.2082	7.1938	-10.0357	-2.0308	130.6023	-225.7964
P4TD	-5.7885	-4.0462	1.7121	0.7077	0.4331	-6.6586	7.4355
P4dM8TD	-6.4972	-4.8806	1.2997	1.9039	7.1635	-4.7693	8.3963
P4dK8TD	-6.4976	-4.8809	1.2964	1.8987	7.1609	-4.7642	8.4026
P4dM9TD	-6.4364	-4.8969	1.0597	-0.9267	7.1655	-4.3515	8.4282
P4dK9TD	-6.4368	-4.8971	1.0582	-0.9300	7.1626	-4.3471	8.4343

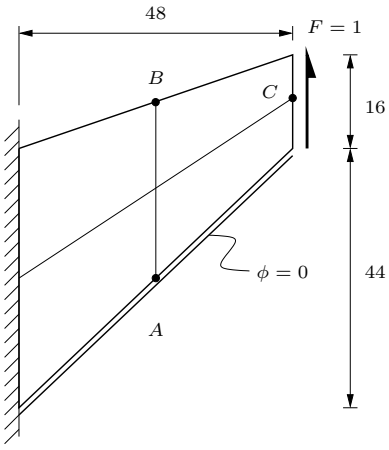

Figure 3.13: Piezoelectric Cook's membrane.

3.8.6 Cook's membrane

The final pathological test of element accuracy under mechanical actuation is depicted in Figure 3.13. The geometry and loading is similar to the popular Cook's membrane consisting of a swept and tapered beam with distributed tip load. The lower surface is prescribed to have a voltage of 0V. Since no analytical solution exists for this problem, the predicted solutions are compared to a finite element approximation with a sufficiently fine mesh. The best known values of u_{yC} and ϕ_C, computed by performing a detailed finite element analysis with a refined mesh, are 2.109×10^{-4}mm and 1.732×10^{-8}GV, respectively. Figure 3.14 depicts the magnitude of the relative error on u_{yC}, the y–displacement of point C, for different mesh refinements on a log scale. The accuracy of the irreducible and assumed flux density elements with drilling DOFs compared to their standard P4 and P4D counterparts is once again illustrated. In this case, the assumed stress elements achieve a far greater accuracy than the other elements, with the P4T element achieving the best displacement accuracy of all elements. All of the fully mixed elements with and without drilling DOFs perform similarly well.

Figure 3.15 depicts the magnitude of the relative error on ϕ_C, the electric potential at point C. The accuracy of electric potential within the four individual element families is similar, and a far less marked distinction between elements with and without drilling DOFs is apparent. Invariably upon comparing Figures 3.14 and 3.15, elements with superior displacement accuracy exhibit poorer potential accuracy and vice versa. Furthermore, the respective elements' loss of accuracy on electric potential appears to be less substantial than the accuracy gained on displacement accuracy.

Table 3.2 presents the relative percentage errors on the first principle stress at point A, T_{1A} and the magnitude of the electric flux density at B, $|D_B|$. The best known values for T_{1A} and $|D_B|$ are 0.21613 N/mm^2 and 22.409 pC/mm^2, respectively. In this case, the irreducible elements with drilling DOFs achieve the best approximations for both T_{1A} and $|D_B|$ with the exception of $|D_B|$ for the 2×2 discretisation. Again, the accuracy of the elements with drilling DOFs within the irreducible and assumed flux density families is illustrated.

Furthermore, as before the assumed stress and fully mixed families achieve similar accuracies regardless of whether drilling DOFs are included or not. Our new elements with 9 stress β-parameters appear to perform very well.

Table 3.2: Relative percentage error on stress and electric displacement for Cook's membrane.

	2×2 mesh		4×4 mesh		8×8 mesh	
	T_{1A}	$\lvert D_B \rvert$	T_{1A}	$\lvert D_B \rvert$	T_{1A}	$\lvert D_B \rvert$
P4	-44.6706	-80.3136	-19.8108	-68.3021	-3.7775	-33.9002
P4dM	-9.2049	-38.4155	-0.7867	-9.7136	-0.7298	-6.7096
P4dK	-9.1978	-38.4299	-0.7834	-9.7162	-0.7291	-6.7099
P4D	-50.8613	-77.1129	-20.2323	-86.1091	-3.8591	-38.5268
P4dMD	-19.7603	-42.8530	-3.7775	-19.5042	-1.2428	-8.9451
P4dKD	-19.7569	-42.8726	-3.7756	-19.5085	-1.2423	-8.9457
P4T	-21.4767	1.0435	-6.9101	-17.2497	-2.1175	-10.3702
P4dM8T	-28.7225	-4.0746	-8.2523	-24.1994	-2.3955	-12.9287
P4dK8T	-28.7176	-4.0162	-8.2527	-24.1880	-2.3958	-12.9280
P4dM9T	-19.8624	-1.8967	-6.2470	-25.8652	-1.8419	-11.9210
P4dK9T	-19.8634	-1.8251	-6.2477	-25.8541	-1.8422	-11.9204
P4TD	-20.9579	-45.4065	-6.0842	-23.5878	-1.6060	-10.6112
P4dM8TD	-35.3104	-48.9795	-7.3783	-25.3382	-2.1842	-11.6869
P4dK8TD	-35.3060	-48.9936	-7.3791	-25.3460	-2.1843	-11.6889
P4dM9TD	-18.2960	-47.2924	-4.7375	-25.4509	-1.3131	-11.6292
P4dK9TD	-18.2993	-47.3067	-4.7382	-25.4583	-1.3132	-11.6312

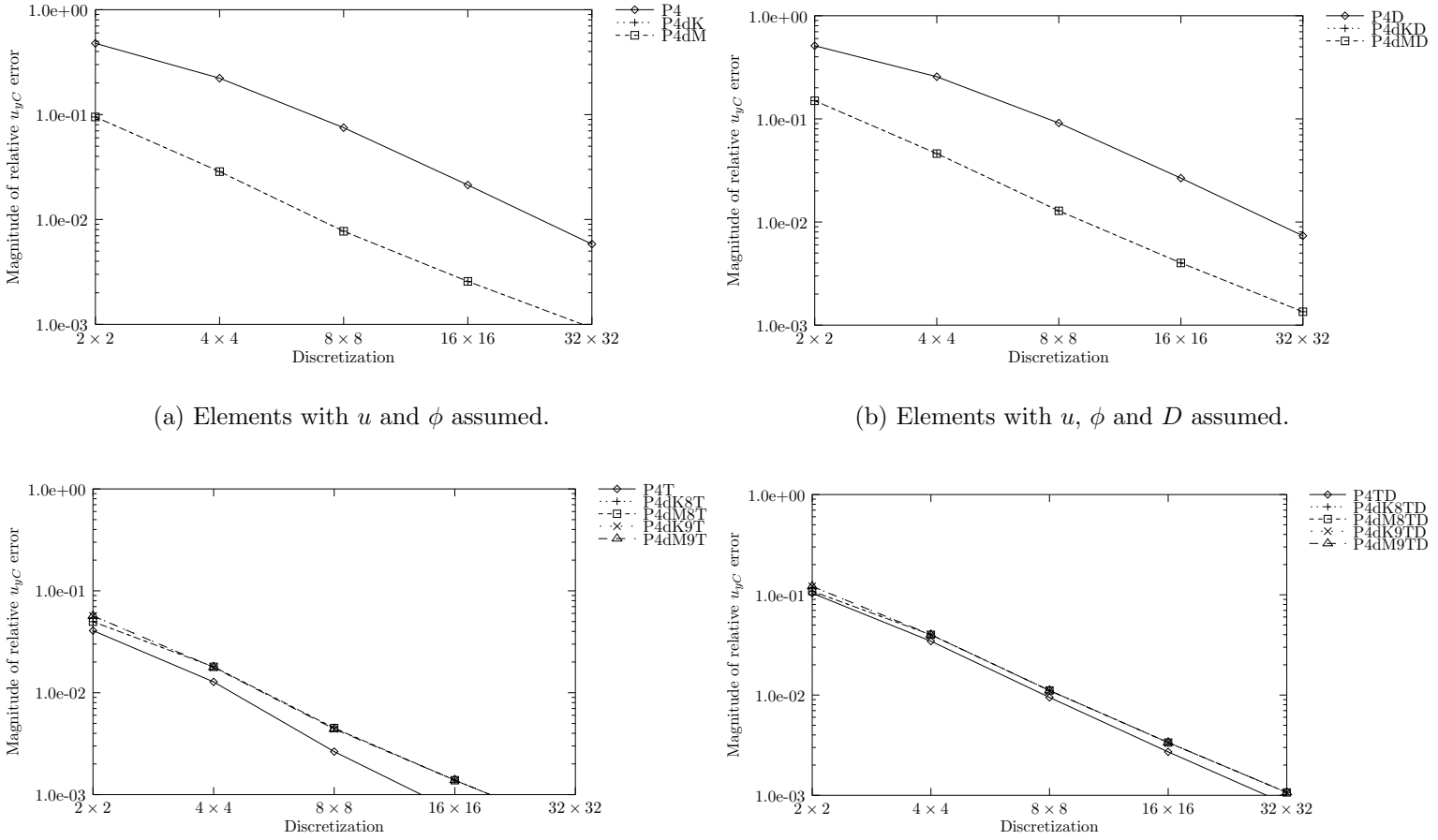

(a) Elements with u and ϕ assumed.

(b) Elements with u, ϕ and D assumed.

(c) Elements with u, ϕ and T assumed.

(d) Elements with u, ϕ, D and T assumed.

Figure 3.14: Cook's membrane: y–displacement at C (u_{yC}).

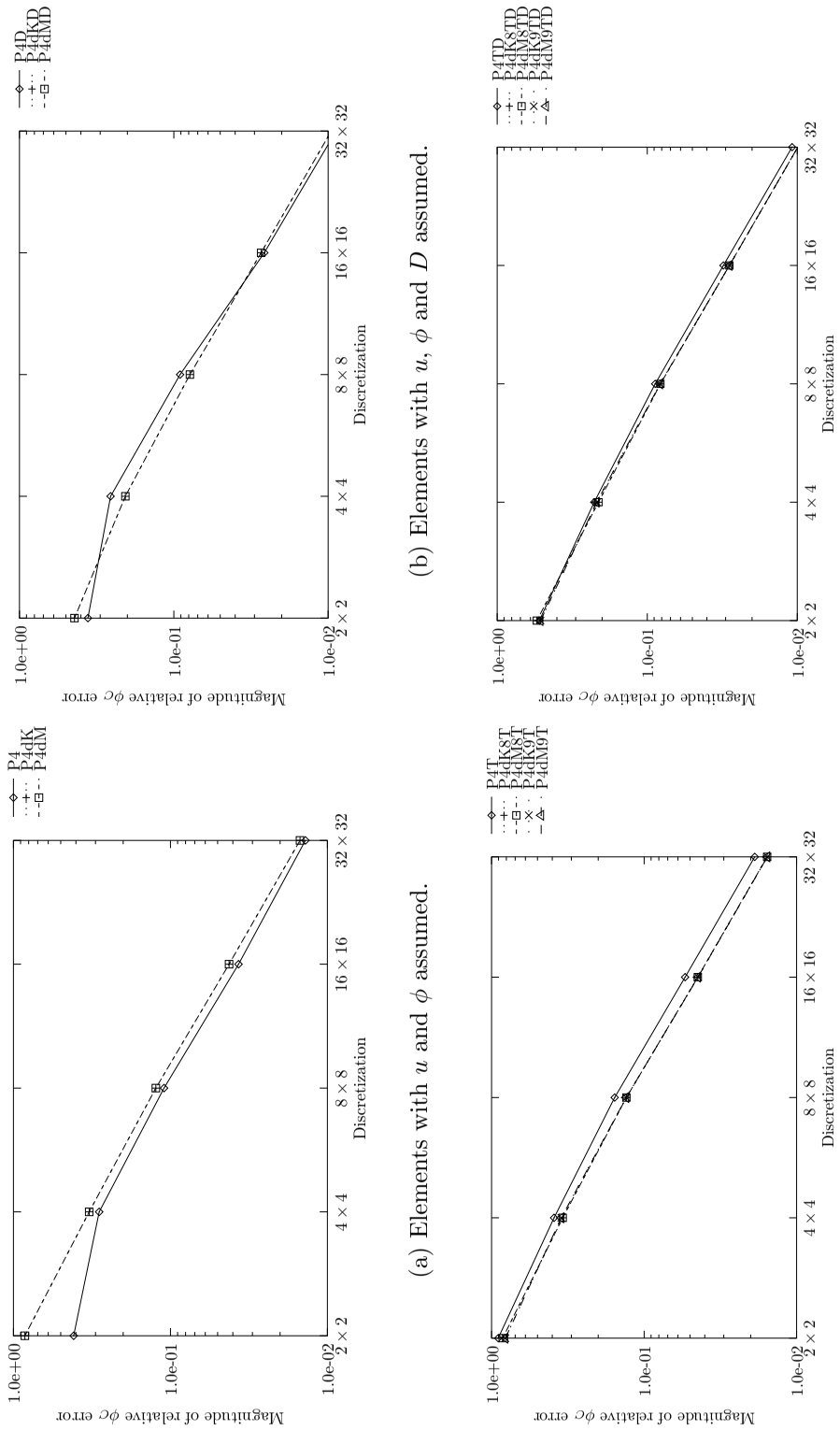

(a) Elements with u and ϕ assumed.

(b) Elements with u, ϕ and D assumed.

(c) Elements with u, ϕ and T assumed.

(d) Elements with u, ϕ, D and T assumed.

Figure 3.15: Cook's membrane: Electric potential at C (ϕ_{yC}).

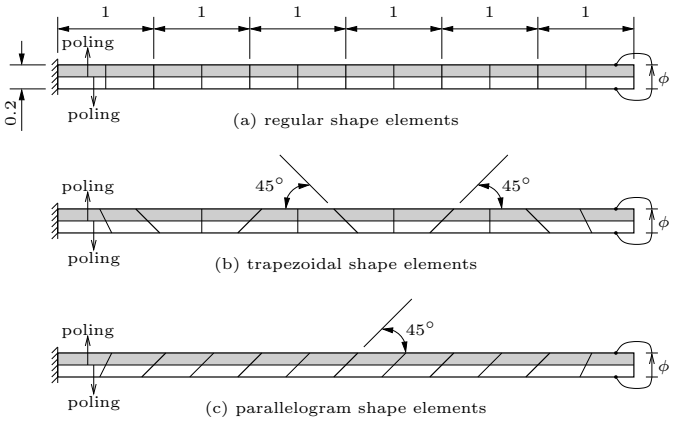

Figure 3.16: Bimorph based on MacNeal's elongated beam.

3.8.7 Piezoelectric bimorph beam

The final problem, evaluating element accuracy under electrical actuation, takes the form of a piezoelectric bimorph beam. The physical problem consists of two identical layers of piezoelectric material with opposite polarities, as indicated in Figure 3.16. Upon application of an electric field in the through-thickness direction, the bimorph bends as a result of moments caused by the layers' opposing polarities.

This problem is often solved using PVDF material constants and compared to the solution of Tzou [83]. For the purpose of the current study, tests are conducted using two different materials. To assess the element accuracy by beam solution, the Poisson's ratio is set to zero. Therefore the material properties for the PVDF material are [84] $E_1 = E_2 = E_3 = 2\times10^3$ (N/mm^2), $\nu_{12} = \nu_{13} = \nu_{23}=0$, $e_{31} = e_{32}=$-0.046$\times10^6$ (pC/mm^2) and $\epsilon_{11} = \epsilon_{33} = \epsilon_{33}=0.1062\times10^9$ (pC/GVmm). The e_{33} coefficient is assumed to be zero [84]. In the second case, the material properties of PZT-4, as used in the preceding problems, are used and the solution is compared to a refined finite element solution.

Since at least two elements are required through the thickness, the meshes used here represents a bisection of the discretisation suggested by MacNeal and Harder [85]. The top surface of the beam is subjected to 1V, and the bottom surface to -1V. The relative percentage error on the tip displacement is reported for the two different materials and the three meshes in Table 3.3. The beam solution for the PVDF material is 6.2100×10^{-5} mm, while the best known solution for the PZT-4 material is 4.3622×10^{-4} mm.

The over-stiff response of the P4 and P4D elements are once again highlighted for both regular and distorted elements. The significant improvement in performance upon addition of the drilling DOFs within these two element families is also once again apparent.

The results for both the assumed stress and fully mixed families employing the PVDF material are similar. Notably, elements with drilling DOFs and no assumed flux density interpolation predict the exact (beam) solution for the undistorted mesh. Meanwhile the same slight displacement error results for undistorted assumed flux density and fully mixed elements with drilling DOFs.

Table 3.3: Relative percentage error on vertical tip displacement of piezoelectric bimorph.

	PVDF			PZT-4		
	Regular	Trapezoidal	Parallel	Regular	Trapezoidal	Parallel
P4	-75.7576	-85.7547	-88.7211	-63.2273	-80.9720	-87.5199
P4dM	0	-35.4700	-10.4663	-6.3609	-27.7086	1.9377
P4dK	0	-35.4711	-10.4666	-6.3609	-27.7102	1.9372
P4D	-75.7722	-85.7599	-88.7247	-78.6452	-86.8639	-91.3582
P4dMD	-0.2484	-35.5802	-10.6666	-8.3357	-32.5815	-7.8569
P4dKD	-0.2484	-35.5813	-10.6669	-8.3357	-32.5825	-7.8572
P4T	0	-29.2346	-4.2227	7.0048	-19.7686	4.1441
P4dM8T	0	-33.8712	-5.0015	6.6919	-22.8712	3.8611
P4dK8T	0	-33.8721	-5.0020	6.6919	-22.8717	3.8604
P4dM9T	0	-33.8995	-5.0448	6.3358	-23.3704	3.5463
P4dK9T	0	-33.9004	-5.0453	6.3358	-23.3711	3.5457
P4TD	-0.2484	-29.3670	-4.4527	-2.6514	-26.4455	-5.2251
P4dM8TD	-0.2484	-33.9872	-5.2288	-2.9145	-29.0260	-5.5317
P4dK8TD	-0.2484	-33.9881	-5.2292	-2.9145	-29.0263	-5.5321
P4dM9TD	-0.2484	-34.0154	-5.2717	-3.2111	-29.4803	-5.8180
P4dK9TD	-0.2484	-34.0163	-5.2722	-3.2111	-29.4807	-5.8184

For this problem, the assumed stress elements perform slightly better than the fully mixed elements for the PZT-4 material and distorted meshes, with our assumed stress elements with drilling DOFs performing marginally better than the standard P4T element. The excellent performance of the irreducible elements for the PZT-4 bimorph is also noted.

3.9 Conclusions

A number of variational formulations accounting for piezoelectricity and in-plane rotations have been presented. Two new families of functionals, namely M-type, which retains the skew-symmetric part of the stress tensor, and K-Type, in which the skew part of stress is eliminated, are introduced.

From the M-Type Hu-Washizu-like functional an irreducible formulation with only 'kinematic' independent variables, i.e. displacement and electric potential, was developed. It has also been shown how a 'fully' mixed formulation, with stress and electric flux density assumed, can be generated. Two M-Type 'degenerate' Hellinger-Reissner-like functionals with either stress or electric flux density assumed, are also given. It was also demonstrated how the K-Type counterparts of our M-type functionals can be constructed.

Furthermore, numerical implementations of the M- and K-Type formulations are presented. The accuracy and robustness of our elements on a number of benchmark problems was demonstrated. The addition of drilling degrees of freedom enriches the interpolated displacement field, resulting in improved element performance. This is borne out by the improved accuracy and robustness of the P4dM and P4dK elements over the standard P4 piezoelectric element. The improved performance of our mixed elements with drilling degrees of freedom is generally less marked when compared to existing mixed piezoelectric elements. In fact, it is difficult to conclusively state that any one of the elements used in this study is better in terms of accuracy than all the others. This is so since none of the elements herein consistently outperforms all the other elements on all reported accuracy measures. Our 'fully mixed' elements, however, are shown to be accurate and stable, even at extreme element distortions. They also allow for improved modelling capabilities due to the additional rotational degree of freedom, e.g. compatibility with elastic elements with drilling degrees of freedom is ensured. The results presented herein, therefore indicate that the P4dMnTD and P4dKnTD elements are useful for modelling engineering applications.

What is more, the variational formulations constructed in this work can be used to establish three dimensional solid piezoelectric elements with drilling degrees of freedom. Furthermore, the planar elements derived here, when combined with piezoelectric plate elements, can be used to calculate through-thickness phenomena in thick piezoelectric shell elements.

Chapter 4

Modified reduced order quadratures for quadratic membrane elements

4.1 Summary

Reduced integration is frequently used in evaluating the element stiffness matrix of quadratically interpolated finite elements. Typical examples are the serendipity (Q8) and Lagrangian (Q9) membrane finite elements, for which a reduced 2×2 Gauss-Legendre integration rule is frequently used, as opposed to full 3×3 Gauss-Legendre integration. This 'softens' these element, thereby increasing accuracy, albeit at the introduction of spurious zero energy modes on the element level. This is in general not considered problematic for the "hourglass" mode common to Q8 and Q9 elements, since this spurious mode is non-communicable. The remaining two zero energy modes occurring in the Q9 element are indeed communicable. However, in topology optimization for instance, conditions may arise where the spurious mode associated with the Q8 element becomes activated. To effectively suppress these modes altogether in elements employing quadratic interpolation fields, two modified quadratures are employed herein. For the Q8 and Q9 membrane elements, the respective rules are a five and an eight point rule. As compared to fully integrated elements, the new rules enhance element accuracy due to the introduction of soft, higher-order deformation modes. A number of standard test problems reveal that element accuracy remains comparable to that of the under-integrated counterparts.

4.2 Introduction

In the earlier days of the development of the finite element method, numerical integration schemes attracted significant attention (e.g. see [54, 86, 87, 88]), possibly due to the limitations of the computing devices available at the time.

More recently, reduced integration schemes have frequently been used in combination with stabilization methods and explicit integration in the time domain, so as to increase computational efficiency when simulating computationally demanding models, e.g. nonlinear

crash analysis, metal forming, etc. The contributions of Belytschko and others (e.g. see [89, 90, 91, 92, 93]) are notable here. In essence they employ reduced integration schemes in conjunction with stabilization methods to prevent spurious modes that arise as a result of these schemes. On this subject the paper of Hughes *et al.* [94] is informative.

While the need for reduced integration is obvious in explicitly integrated, computationally demanding analyses, reduced integration is also frequently employed in implicitly integrated elastostatic or -dynamic analyses. This is normally done to alleviate locking in membrane, plate or shell elements, or merely to improve the behavior or these elements. Typical examples are the serendipity and Lagrangian membrane elements, which are over-stiff when full integration is used.

In the finite element method the equilibrium equations involve integration over the element volume. This is also true for the expressions for consistent nodal loads, mass matrices, penalty matrices, etc. For simple elements the integrand may be formed explicitly, resulting in *exact* integration. However, numerical integration schemes are necessary when element geometries are distorted, of which the Gaussian rules are possibly the best known and most frequently employed. The effects of numerical integration schemes are summarized in a clear manner by Cook *et al.* [17]:

For numerically integrated elements, full integration indicates a quadrature rule sufficient to provide the exact integrals of all terms in the element stiffness matrix $\boldsymbol{K}^e$ if the element geometry is undistorted. The same 'full integration' rule will not exactly integrate $\boldsymbol{K}^e$ if the element is distorted, or if the center nodes are offset from the element midpoints, since the Jacobian $\boldsymbol{J}$ is no longer constant throughout the element domain.

In this work, reduced order integration refers an integration scheme of lower order (fewer points and lower order of accuracy) than the lowest order rule which results in the exact integration of elemental matrices for an undistorted element.

A lower-order quadrature rule, called reduced integration, may be desirable for two reasons. Firstly, since the expense of generating the matrix $\boldsymbol{K}^e$ by numerical integration is proportional to the number of sampling points, fewer points results in lower computational cost. Secondly, a low order rule tends to soften an element, thus countering the overly-stiff behavior associated with assumed displacement fields. (The displacement based finite element method is monotonically convergent from below.) Softening comes about because certain higher-order polynomial terms happen to vanish at Gauss points of a low-order rule. Simply stated, with fewer sampling points, some of the more complicated displacement modes offer less resistance to deformation.

We pertinently differentiate between (a) the accuracy of an integration scheme, and (b) the numerical accuracy of finite elements. The former indicates the error of an approximate integration scheme as compared to the exact integral, while the latter indicates the performance of finite elements employing these approximate numerical schemes. It is reiterated that the numerical accuracy or performance of finite elements frequently increases when the accuracy of the integration scheme itself decreases. This is due to the fact that some limiting behavior (e.g. locking) is rendered negligible, or almost so, when reduced as opposed to full integration is employed. While accuracy of integration of $\boldsymbol{K}^e$ decreases with reduced integration, the element accuracy may actually increase.

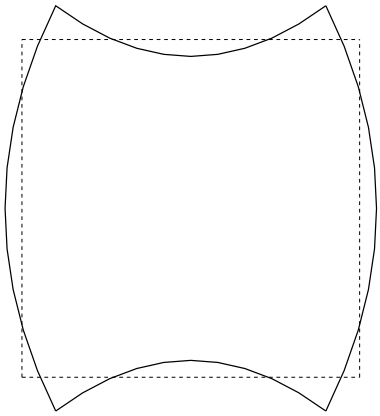

Figure 4.1: Typical spurious mode of Q8 employing a 4 point Gauss-Legendre scheme.

In summary, reduced integration may be able to simultaneously reduce cost, reduce accuracy in the evaluation of integration expressions, and increase the accuracy of the finite element analysis. Barring extremely expensive analyses, it is however noted that most authors agree that reduced integration should in general not be used if reduced cost is the sole motivation.

Numerical testing of any proposed rule is mandatory. Even though solution accuracy may be mesh dependent and problem dependent, one quadrature rule is usually superior to others. For bilinear (Q4) and eight-node plane elements (Q8), and for eight node linear solid elements, an order 2 Gauss rule is favored over an order 3 rule (four and eight points for plane and solid elements, respectively).

For Q4, the order 2 Gauss rule is problem free (at least as far as spurious modes are concerned). For Q8, the order 2 Gauss rule introduces a spurious mode on the element level. For Q9 (the Lagrangian 'bubble' counterpart of Q8), the order 2 Gauss rule introduces 3 spurious modes on the element level. The "hourglass" spurious mode common to the Q8 and Q9 elements, depicted in Figure 4.1, is in general not considered problematic since it is non-communicable, viz. the spurious mode is unable to propagate in a mesh consisting of more than one element. However, in some practical situations, conditions may arise where this spurious mode becomes activated. One example is the SIMP (Solid Isotropic Material with Penalization) material description, frequently used in topology optimization (e.g. see [4]), where the elasticity tensor in adjacent elements may vary considerably. The remaining two zero energy modes associated with the Q9 element are, however, communicable.

For illustrative purposes the general expression for the stiffness matrix $\boldsymbol{K}^e$ of a single three-dimensional finite element is considered, and can be written as (e.g. see [60])

$$\boldsymbol{K}^e = \int_\Omega \boldsymbol{B}^T \boldsymbol{C} \boldsymbol{B} \, d\Omega, \tag{4.1}$$

where $\boldsymbol{B}$ is the strain-displacement operator, $\boldsymbol{C}$ the matrix that defines the constitutive relationship, and Ω the element volume. Also, $d\Omega = dx\, dy\, dz$ in the Cartesian coordinate system, which is transformed to the natural coordinate system as $d\Omega = dr\, ds\, dt\, |\boldsymbol{J}|$, with $|\boldsymbol{J}|$ the determinant of the Jacobian matrix $\boldsymbol{J}$ of the transformation. In the natural coordinate

system,

$$\boldsymbol{K}^e = \int_{-1}^{1}\int_{-1}^{1}\int_{-1}^{1} \boldsymbol{B}^T\boldsymbol{C}\boldsymbol{B}\,|\boldsymbol{J}|\;dr\,ds\,dt. \tag{4.2}$$

During numerical integration, (4.2) is written as

$$\boldsymbol{K}^e = \sum_{n=1}^{N} W_n \boldsymbol{B}^T(r_n,s_n,t_n)\,\boldsymbol{C}\,\boldsymbol{B}(r_n,s_n,t_n)\,|\boldsymbol{J}(r_n,s_n,t_n)|, \tag{4.3}$$

where (r_n, s_n, t_n) is the n^{th} position of the integration point, associated with weight W_n, of any suitable integration scheme using N integration points. In (4.3) it is assumed that the constitutive relation defined by $\boldsymbol{C}$ is not a function of the global coordinates (x, y, z). It is desirable that (4.3) is problem free in terms of locking, (element) accuracy and spurious modes.

For 2-D planar elements the through-thickness component is usually constant, (4.3) therefore reduces to

$$\boldsymbol{K}^e = h\sum_{n=1}^{N} W_n \boldsymbol{B}^T(r_n,s_n)\,\boldsymbol{C}\,\boldsymbol{B}(r_n,s_n)\,|\boldsymbol{J}(r_n,s_n)|, \tag{4.4}$$

where h represents the constant element thickness and where the Jacobian, $\boldsymbol{J}$, is of reduced size compared to (4.3).

In this study it is attempted to effectively suppress spurious modes in quadratic finite elements altogether, using two modified quadratures proposed by Dovey [54].

This chapter is laid out as follows: Firstly, a summary of the formulation presented by Dovey is presented since his work on reduced order integration is probably not widely known. Numerical experiments are then performed for several well known test problems using the modified quadrature rules, as well as the standard order 2 and order 3 Gauss-Legendre rules. Finally, conclusions are drawn, based on the results of our numerical experiments.

For the sake of brevity, we restrict ourselves to the 2-D problem. However, the development for quadratically interpolated 3-D brick elements is similar. In 2-D, the standard order 2 and order 3 Gauss-Legendre rules will be referred to as the 4 and 9 point Gauss-Legendre rules.

4.3 Derivation of numerical integration schemes

In this section the work of Dovey [54] is closely followed. The same notation is used. Consider the area integral given by

$$I = \int_{-1}^{1}\int_{-1}^{1} F(r,s)\;\;dr\,ds, \tag{4.5}$$

where $F(r, s)$ is any polynomial function of r and s. Any polynomial expression of two variables can be expressed in the form

$$F(r,s) = \sum_{i,j} A_{ij} r^i s^j. \tag{4.6}$$

No limits are placed on the summation indices i and j as any arbitrary polynomial is being considered.

Let any N-point rule be written as

$$I^* = \sum_{n=1}^{N} W_n F(r_n, s_n), \tag{4.7}$$

where I^* represents the numerical approximation to I. Integration point n is given by (r_n, s_n) and the associated weight is given as W_n.

Each term of (4.6) may be trivially integrated as follows:

$$\int_{-1}^{1}\int_{-1}^{1} A_{ij} r^i s^j \, drds = \begin{cases} \frac{2^2 A_{ij}}{(i+1)(j+1)} & i, j \text{ both even,} \\ 0 & \text{otherwise.} \end{cases} \tag{4.8}$$

Application of the quadrature rule of (4.7) to the function $F(r, s)$ in the form of (4.6) gives the following result, which is expressed in terms of the coefficients A_{ij} as

$$I^* = A_{00}\sum_{n=1}^{N}(W_n) + A_{10}\sum_{n=1}^{N}(W_n r_n) + A_{01}\sum_{n=1}^{N}(W_n s_n) + A_{20}\sum_{n=1}^{N}\left(W_n r_n^2\right) + \cdots \tag{4.9}$$

Two points are to be noted:

- Symmetry of the rule in each coordinate implies that the coefficients corresponding to all odd powers will vanish in (4.9). This of course corresponds to the vanishing of the integral of odd powers over this region.
- Symmetry with respect to both coordinates is required to ensure invariance of the rule.

Equating the coefficients of A_{ij} between (4.8) and (4.9) gives a series of equations in the weights W_n and the coordinates r_n and s_n. Evidently the number of equations that are satisfied for a particular set of weights and coordinates indicate which polynomial terms are integrated exactly by that particular rule. Also, the degree to which each remaining equation is not satisfied gives the error in that polynomial term. Each equation has the form

$$\sum_{n=1}^{N} W_n r_n^i s_n^j = \frac{2^2}{(i+1)(j+1)}, \tag{4.10}$$

for the coefficient A_{ij}. Clearly all equations containing odd values for either i or j are satisfied identically for symmetric rules.

The maximum number of equations needed from (4.10) is determined by the order of the function $F(r, s)$ which is to be integrated. If the maximum number of equations possible is satisfied for a particular configuration, then an optimal scheme for that configuration is obtained. However, if less than the maximum number are satisfied, a less accurate rule is obtained, but freedom is available for arbitrary selection of some values of weights or coordinates. The foregoing was used by Dovey to derive a symmetrical 5 and 8 point rule, as is briefly presented in the following.

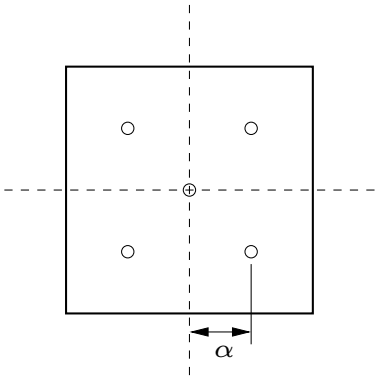

Figure 4.2: 5 Point integration scheme.

4.3.1 A five point rule

The 5-point rule is depicted in Figure 4.2. Due to symmetry, the weights W_α are identical. The rule is indicated by

$$I^* \;=\; W_0 F(0,0) + W_\alpha F(\pm\alpha, \pm\alpha). \tag{4.11}$$

The second term of (4.11) indicates four points when all combinations of positive and negative signs are taken.

Employing (4.10) the first four equations are obtained for the appropriate terms A_{ij} as

$$\begin{array}{lcl} A_{00} & : & W_0 + 4W_\alpha = 4, \\ A_{20}, A_{02} & : & 4W_\alpha\alpha^2 = 4/3, \\ A_{22} & : & 4W_\alpha\alpha^4 = 4/9, \\ A_{40}, A_{04} & : & 4W_\alpha\alpha^4 = 4/5. \end{array} \tag{4.12}$$

The last two of these equations are directly inconsistent and so the last is discarded. Also, however, the first three are inconsistent if the center point is retained.

Solving the first three expressions of (4.12) leads to

$$\alpha \;=\; 1/\sqrt{3};\;\; W_\alpha \;=\; 1 \;\text{ and }\; W_0 \;=\; 0, \tag{4.13}$$

which is the 2×2 Gaussian product rule. The leading error term is defined by the last of equations (4.12) and gives the error $(I^* - I)$, corresponding to the fourth power terms, r^4 and s^4, as

$$E_{40} \;=\; (4W_\alpha\alpha^4 - 4/5)A_{40},\;\; E_{04} \;=\; (4W_\alpha\alpha^4 - 4/5)A_{04}. \tag{4.14}$$

However, the center point may be retained by selecting a value for W_0, computing W_α and α from the first two relationships in (4.12). This implies an error in the A_{22} term. The scheme is now defined by

$$W_\alpha \;=\; 1 - W_0/4, \tag{4.15}$$

$$\alpha \;=\; \left(\frac{1}{3W_\alpha}\right)^{\frac{1}{2}}. \tag{4.16}$$

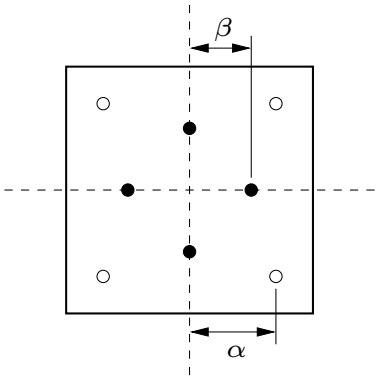

Figure 4.3: 8 Point integration scheme.

The scheme only has physical meaning while $0 \leq W_0 < 4$. The error in the A_{22} term is minimized as $W_0 \rightarrow 0$. In practice this implies that the 5-point scheme converges to the 2×2 Gaussian scheme as $W_0 \rightarrow 0$. This rule was previously used by Groenwold and Stander for their 4-node thick shell finite element with 6 d.o.f. per node [52].

It is noted that as $W_0 \rightarrow 4$, $W_\alpha \rightarrow 0$ and from (4.16), $\alpha \rightarrow \infty$. Even though, for a polynomial being integrated between -1 and 1, function evaluations outside of this region may be permitted, it is preferable that for applications in the finite element method this situation be avoided. The value of α is therefore limited to the defined region $0 \leq \alpha \leq 1$. This implies from (4.15) and (4.16) that W_0 be chosen such that $0 \leq W_0 \leq \frac{8}{3}$.

4.3.2 An eight point rule

The 8-point rule is depicted in Figure 4.3. This rule was previously employed for membrane elements with in-plane rotational degrees of freedom by Stander and Wilson [95] in the QC9(8) element, and also by Ibrahimbegovic *et al.* [21] in their drilling degree of freedom membrane element. The rule is described by

$$I^* = W_\alpha F(\pm\alpha, \pm\alpha) + W_\beta \left[F(\pm\beta, 0) + F(0, \pm\beta)\right]. \tag{4.17}$$

Due to symmetry, the weights W_α are identical, as are the weights W_β. The governing equations are given by

$$\begin{array}{lcl} A_{00} & : & 4W_\alpha + 4W_\beta = 4, \\ A_{20}, A_{02} & : & 4W_\alpha\alpha^2 + 2W_\beta\beta^2 = 4/3, \\ A_{22} & : & 4W_\alpha\alpha^4 = 4/9, \\ A_{40}, A_{04} & : & 4W_\alpha\alpha^4 + 2W_\beta\beta^4 = 4/5. \end{array} \tag{4.18}$$

All four equations may be satisfied and the solution is

$$\alpha = \sqrt{7/9}; \quad W_\alpha = 9/49; \quad \beta = \sqrt{7/15}; \quad W_\beta = 40/49. \tag{4.19}$$

This rule gives comparable accuracy to the 3×3 Gaussian rule. However unlike the 3×3 Gauss rule, this 8-point rule possesses leading error terms are given by:

$$E_{42} = (4W_\alpha\alpha^6 - 4/15)A_{42},\ E_{24} = (4W_\alpha\alpha^6 - 4/15)A_{24},\ \text{and} \tag{4.20}$$

$$E_{44} = (4W_\alpha\alpha^8 - 4/25)A_{44}. \tag{4.21}$$

A scheme of lower accuracy, neglecting the last term of (4.18), is defined by

$$W_\alpha = 1 - W_\beta, \tag{4.22}$$

$$\alpha = (\frac{1}{9W_\alpha})^{\frac{1}{4}}, \tag{4.23}$$

$$\beta = \left(\frac{2/3 - 2W_\alpha\alpha^2}{W_\beta}\right)^{\frac{1}{2}}. \tag{4.24}$$

In this case both α and β are restricted to be between 0 and 1. This implies that W_β be chosen such that $0 < W_\beta < \frac{8}{9}$.

4.4 Numerical evaluation

For the purpose of determining accuracy, approximate area integration schemes should be evaluated numerically [54]. Without numerical evaluation the effect of reduced integration on for instance locking, higher order deformation modes, etc., cannot be determined.

Moreover, such evaluations should include an investigation into element eigenvalues to determine element rank. In general, it is of the utmost importance to prevent any spurious modes or rank deficiencies [96], which could lead to unstable mechanisms on the structural level. Even if no mechanisms appear in an assembled structure, element rank deficiency should always be accepted cautiously. The basis for this reasoning is that no extent of numerical testing can fully characterize an element with inherent mechanisms, and no guarantee for well-defined behavior under all conditions can be given. (Again, computationally demanding models may be considered an exception. However, one does of course *not* expect elements with quadratic interpolations in these models.)

The derived modified quadratures, as well as the standard 4 and 9 point quadrature rules, are now applied to various test problems in order to obtain estimates for appropriate values of the weights W_0 and W_β.

4.4.1 Eigenvalue analysis

The results of an eigenvalue analysis of a single (square) Q8 element are tabulated in Table 4.1. (Eigenvalue analyses should in general be done for regular, undistorted elements, since distortion may actually suppress zero energy modes due to the inaccuracies of an approximate integration scheme.) In Table 4.1, the 9 point scheme represents full and exact integration. As is well known, the 4 point scheme introduces a superfluous zero energy mode or mechanism ($\lambda_{13} \approx 0$). The mode associated with λ_{13} is depicted in Figure 4.1. With the 5 and 8 point

λ_i	4 pt. scheme –	5 pt. scheme $W_0 = 0.01$	5 pt. scheme $W_0 = 0.1(8/3)$	8 pt. scheme $W_\beta = 0.01$	8 pt. scheme $W_\beta = 0.1(8/9)$	9 pt. scheme –
1	4.82388e+00	4.82388e+00	4.82388e+00	4.82388e+00	4.82388e+00	4.82388e+00
2	4.82388e+00	4.82388e+00	4.82388e+00	4.82388e+00	4.82388e+00	4.82388e+00
3	2.31873e+00	2.32416e+00	2.47404e+00	2.31933e+00	2.32434e+00	2.41527e+00
4	2.00000e+00	2.00251e+00	2.07309e+00	2.00126e+00	2.01168e+00	2.21240e+00
5	1.37447e+00	1.37447e+00	1.37447e+00	1.37447e+00	1.37447e+00	1.37447e+00
6	1.37447e+00	1.37447e+00	1.37447e+00	1.37447e+00	1.37447e+00	1.37447e+00
7	1.00000e+00	1.00251e+00	1.07143e+00	1.00063e+00	1.00582e+00	1.10000e+00
8	7.50000e-01	7.50209e-01	7.56048e-01	7.50629e-01	7.55908e-01	8.79436e-01
9	5.00000e-01	5.01251e-01	5.34055e-01	5.00628e-01	5.05772e-01	5.87596e-01
10	4.31271e-01	4.31475e-01	4.36678e-01	4.31294e-01	4.31482e-01	4.34735e-01
11	3.01646e-01	3.01646e-01	3.01646e-01	3.01646e-01	3.01646e-01	3.01646e-01
12	3.01646e-01	3.01646e-01	3.01646e-01	3.01646e-01	3.01646e-01	3.01646e-01
13	$<$ 1.0e-15	4.17595e-04	1.18095e-02	1.25524e-03	1.15433e-02	1.70564e-01
14	$<$ 1.0e-15	$<$ 1.0e-15	$<$ 1.0e-15	$<$ 1.0e-15	$<$ 1.0e-15	$<$ 1.0e-15
15	$<$ 1.0e-15	$<$ 1.0e-15	$<$ 1.0e-15	$<$ 1.0e-15	$<$ 1.0e-15	$<$ 1.0e-15
16	$<$ 1.0e-15	$<$ 1.0e-15	$<$ 1.0e-15	$<$ 1.0e-15	$<$ 1.0e-15	$<$ 1.0e-15

Table 4.1: Eigenvalues of a square Q8 serendipity element for different integration schemes (plane stress, $|\boldsymbol{J}| = 1$, $E = 1$, $\nu = 1/3$).

schemes, the mechanism is replaced by a 'soft' higher order deformation mode, as borne out by the low value for λ_{13}. Hence a low strain energy is associated with this particular mode.

Figure 4.4 depicts the effect of the weights W_0 and W_β on the value of λ_{13}, for respectively the 5 and 8 point schemes. If the soft higher order mode is desired, a low value of weight should be used, typically in the region of 10% of the maximum weight for both W_0 and W_β, viz. $W_0 = 0.1(8/3)$ and $W_\beta = 0.1(8/9)$. Furthermore, if W_β is chosen in the region of $40/49$ for the 8 point scheme, similar values to the 9 point scheme are obtained.

For the Q9 element, a similar analysis is carried out with results tabulated in Table 4.2. As is well known, e.g. see [17], reduced integration of this element with an order 2 Gauss rule induces 3 zero energy modes ($\lambda_{13,14,15} \approx 0$). For this element the 5 point scheme only eliminates one of the spurious modes, and the resulting element remains rank deficient by 2.

Figure 4.5 depicts the effect of integration rule weight on λ_{15} for both the 5 and 8 point schemes. For the 5 point scheme, W_0 has no effect on λ_{15} as illustrated in Figure 4.5, or on λ_{14} (not shown). For λ_{13}, however, the weight of the 5 point rule has an effect similar to that experienced by the Q8 element.

4.4.2 Effect of element aspect ratio

For both Q8 and Q9, the effect of element aspect ratio on the λ_{13} is now studied. For this test, a single rectangular element of unit height, with variable length, and constant material

λ_i	4 pt. scheme –	5 pt. scheme $W_0 = 0.1(8/3)$	8 pt. scheme $W_\beta = 0.01$	8 pt. scheme $W_\beta = 0.1(8/9)$	8 pt. scheme $W_\beta = 40/49$	9 pt. scheme –
1	4.82388e+00	4.81443e+00	4.82783e+00	4.86165e+00	6.25205e+00	5.58912e+00
2	4.82388e+00	4.81443e+00	4.82783e+00	4.86165e+00	6.25205e+00	5.58912e+00
3	2.31873e+00	2.32416e+00	2.31933e+00	2.32434e+00	2.41527e+00	2.41527e+00
4	2.00000e+00	2.00251e+00	2.00126e+00	2.01168e+00	2.21240e+00	2.21240e+00
5	1.37447e+00	1.37396e+00	1.37522e+00	1.38171e+00	1.75566e+00	1.56065e+00
6	1.37447e+00	1.37396e+00	1.37522e+00	1.38171e+00	1.75566e+00	1.56065e+00
7	1.00000e+00	1.00251e+00	1.00063e+00	1.00582e+00	1.10000e+00	1.10000e+00
8	7.50000e-01	7.50209e-01	7.50629e-01	7.55908e-01	8.84191e-01	8.79436e-01
9	5.00000e-01	5.01251e-01	5.00628e-01	5.05772e-01	8.84191e-01	6.80792e-01
10	4.31271e-01	4.31475e-01	4.31294e-01	4.31482e-01	8.79436e-01	6.80792e-01
11	3.01646e-01	3.01593e-01	3.02001e-01	3.05498e-01	5.87596e-01	5.87596e-01
12	3.01646e-01	3.01593e-01	3.02001e-01	3.05498e-01	4.34735e-01	4.34735e-01
13	$<$ 1.0e-15	4.17595e-04	5.02504e-03	4.64348e-02	2.74764e-01	2.69437e-01
14	$<$ 1.0e-15	$<$ 1.0e-15	5.02504e-03	4.64348e-02	2.74764e-01	2.69437e-01
15	$<$ 1.0e-15	$<$ 1.0e-15	1.25524e-03	1.15433e-02	1.70564e-01	1.70564e-01
16	$<$ 1.0e-15	$<$ 1.0e-15	$<$ 1.0e-15	$<$ 1.0e-15	$<$ 1.0e-15	$<$ 1.0e-15
17	$<$ 1.0e-15	$<$ 1.0e-15	$<$ 1.0e-15	$<$ 1.0e-15	$<$ 1.0e-15	$<$ 1.0e-15
18	$<$ 1.0e-15	$<$ 1.0e-15	$<$ 1.0e-15	$<$ 1.0e-15	$<$ 1.0e-15	$<$ 1.0e-15

Table 4.2: Eigenvalues of a square Q9 Lagrange element for different integration schemes (plane stress, $|\boldsymbol{J}| = 1$, $E = 1$, $\nu = 1/3$).

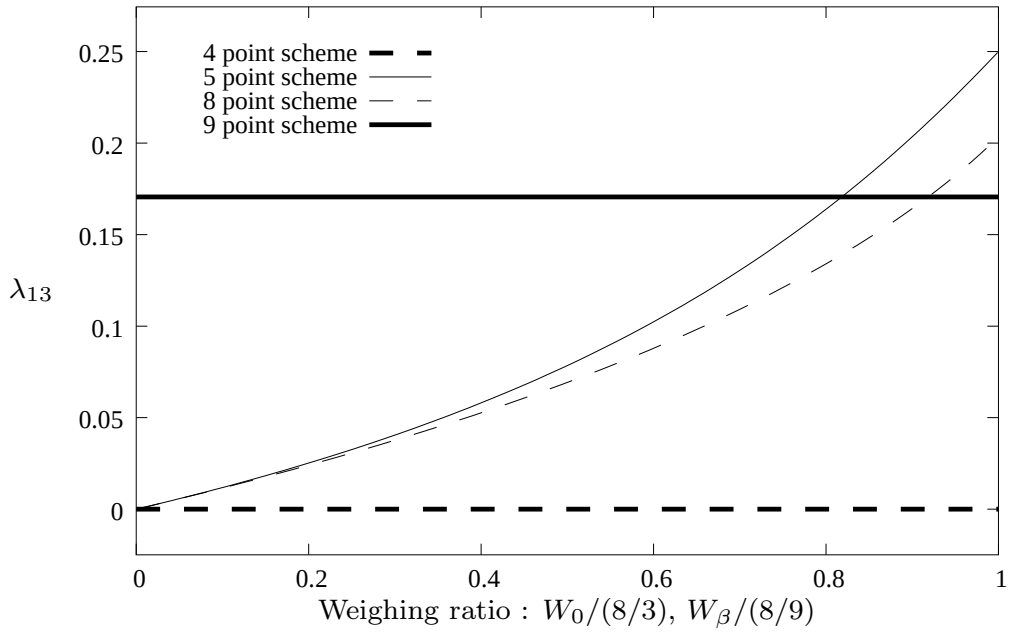

Figure 4.4: λ_{13} of Q8 with different integration schemes (plane stress, $|\boldsymbol{J}| = 1$, $E = 1$, $\nu = 1/3$).

properties $E = 1$ and $\nu = 1/3$ is used. Results are depicted in Figures 4.6 and 4.7 for Q8 and Q9 respectively.

For Q8, λ_{13} obtained with all of the 5 and 8 point rules converge to the eigenvalue obtained using full 3×3 Gauss-Legendre integration. (While this value decreases as the aspect ratio increases, it never reaches zero.) For Q9, similar results are obtained, although the results reiterate that Q9 is to be integrated using the 8 point scheme. For this element, the results for λ_{14} and λ_{15} are similar (not shown).

The foregoing illustrates that, for both Q8 and Q9, the modified integration schemes do not induce mechanisms as element aspect ratio is increased.

4.4.3 Cantilever beam in pure bending

Figure 4.8 depicts a cantilever beam modeled using two elements with a common distortion d. The vertical displacements v_A and v_B, and horizontal displacement u_B are reported for the Q8 and Q9 elements, using different integration schemes. The results are tabulated in Table 4.3. Since the Q9 element stiffness matrix becomes singular when 4 and 5 point schemes are used, these results are not reported. For $d = 0$, both elements predict the exact solutions for displacements. In addition, the Q9 element is completely insensitive to distortion using both the 8 and 9 point schemes and predicts the exact solution in all cases. Even for the extreme case of $d = 5$, the exact solution is recovered.

For the Q8 element, Figure 4.9 depicts the effect of distortion on the vertical displacement v_B for the various integration schemes. With the 4 and 5 point schemes (the latter with

d	Element	Scheme	Weight	v_A	u_B	v_B
1.0	Q8	4	–	7.50000	1.50000	7.51000
		5	0.01	7.50000	1.50000	7.51002
			0.1(8/3)	7.50000	1.50000	7.51045
		8	0.01	7.49961	1.49992	7.50958
			0.1(8/9)	7.49648	1.49929	7.50621
			40/49	7.41490	1.48277	7.42211
		9	–	7.44849	1.48962	7.45721
	Q9	8	0.01	7.50000	1.50000	7.52250
			0.1(8/9)	7.50000	1.50000	7.52250
			40/49	7.50000	1.50000	7.52250
		9	–	7.50000	1.50000	7.52250
2.0	Q8	4	–	7.50000	1.50000	7.47250
		5	0.01	7.50000	1.50000	7.47256
			0.1(8/3)	7.50000	1.50000	7.47429
		8	0.01	7.49187	1.49849	7.46381
			0.1(8/9)	7.43244	1.48708	7.40160
			40/49	6.27595	1.25407	6.23790
		9	–	6.66839	1.33307	6.63637
	Q9	8	0.01	7.50000	1.50000	7.52250
			0.1(8/9)	7.50000	1.50000	7.52250
			40/49	7.50000	1.50000	7.52250
		9	–	7.50000	1.50000	7.52250
Exact				7.50000	1.50000	7.52250

Table 4.3: Displacement results for distorted cantilever beam.

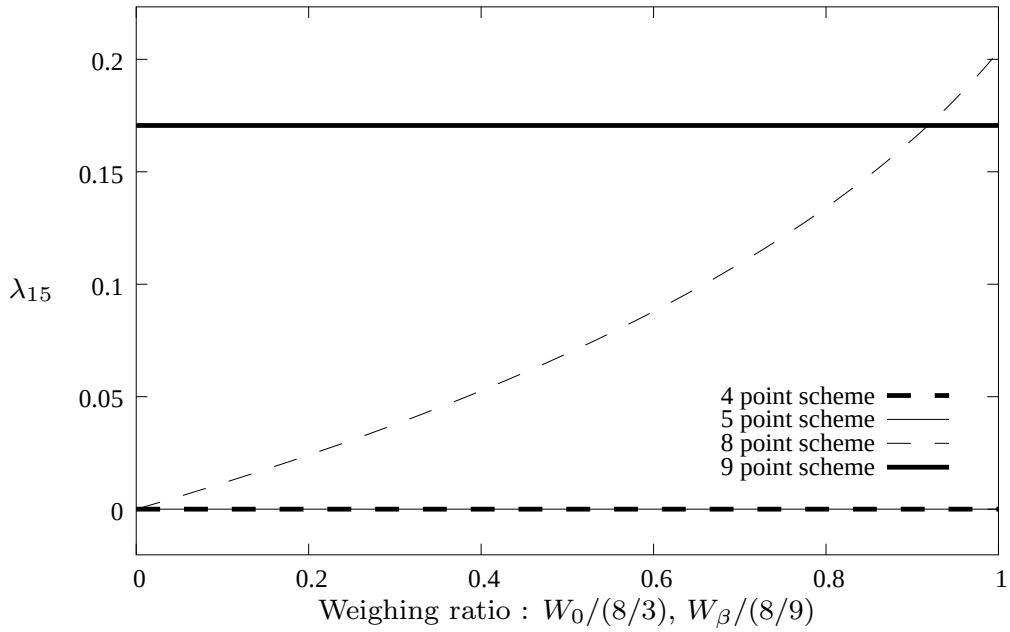

Figure 4.5: λ_{15} of Q9 element for different integration schemes (plane stress, $|\boldsymbol{J}| = 1$, $E = 1$, $\nu = 1/3$).

low value of W_0), this element is notably less sensitive to the severity of the distortion as compared to the 8 and 9 point schemes. Again, $W_0 = 0.1(8/3)$ and $W_\beta = 0.1(8/9)$ seem suitable.

4.4.4 A near mechanism

Again, Cook *at al.* [17] are cited: A structure that appears to be adequately constrained may have an instability that makes the assembled structural stiffness matrix $\boldsymbol{K}$ singular, or near-singular. Or, unstable elements may combine to form a structure that is stable, but unduly susceptible to certain load patterns, so that computed displacements are excessive. Again, this situation may occur in topology optimization problems.

The situation is depicted in Figure 4.10. A 2×2 Gauss rule is used to integrate $\boldsymbol{K}^e$ in each element. The stiff element, shown shaded, is weakly restrained by soft elements connected to the fixed boundary allowing a singular mode to become pronounced.

Figure 4.11 depicts the incremental displacement $\hat{v}$ at point A, as illustrated in Figure 4.10. The 5 and 8 point schemes yield comparable results (their respective curves are not distinguishable on the scale of the figure. Again, suitable weights are roughly 10% of the maximum permissible weights (viz. $0.1(8/3)$ for the 5 point rule and $0.1(8/9)$ for the 8 point rule).

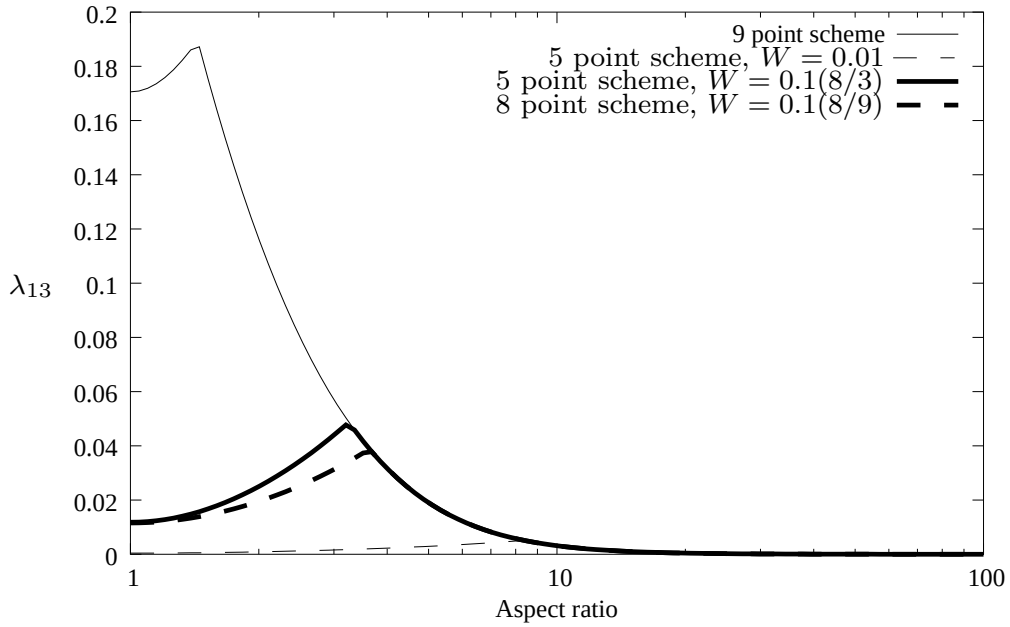

Figure 4.6: Effect of aspect ratio on λ_{13} of Q8 for different integration schemes.

4.4.5 Highly constrained square plate

In this test, a highly constrained mesh is used to demonstrate that spurious modes are not confined to meshes with few constraints, as illustrated by Bićanić and Hinton [97]. A square 6×6 mesh is completely constrained on the boundary, and an eigenvalue analysis is carried out on the global stiffness matrix. In Figures 4.12, 4.13 and 4.14 the lowest six eigenvectors are depicted together with the corresponding eigenvalue, for the 4, 8 ($W_\beta = 0.1(8/9)$) and 9 point schemes, respectively.

Modes 5 and 6 of the 4 point scheme in Figure 4.12 are spurious and are due to instabilities caused by the reduced integration scheme. (These modes are also known as Escher modes.) In Figure 4.13, it is shown that these spurious modes are not present when a 9 point integration scheme is used. What is more, it is shown that if the 8 point scheme is used with $W_\beta = 0.1(8/9)$, the spurious modes are eliminated, as demonstrated in Figure 4.14.

4.4.6 Cook's membrane

This popular test problem has been used by many authors and is depicted in Figure 4.15. The center displacement v_C for the various integration schemes is tabulated in Table 4.4, while stresses $(\sigma_{\min})_B$ and $(\sigma_{\max})_A$ are presented in Table 4.5.

The displacement results reveal the over-stiff behavior of the Q8 element with a 9 point rule and an 8 point scheme with $W_\beta = 40/49$. All other integration schemes predict displacement values close to the best known solution. Although the four point scheme is the most accurate, this high accuracy of course comes at the expense of a mechanism. Figure 4.16 depicts the effect of different values of weight on the center displacement v_C for a single Q8 element.

Element	Scheme	Weight	1×1	2×2	4×4
Q8	4	-	20.00	23.17	23.73
	5	0.01	19.98	23.17	23.73
		$0.1(\frac{8}{3})$	19.52	23.09	23.72
	8	0.01	19.95	23.17	23.73
		$0.1(\frac{8}{9})$	19.58	23.14	23.73
		40/49	17.16	22.71	23.71
	9	-	17.22	22.72	23.71
Q9	4	-	26.97	24.15	24.00
	5	0.01	26.97	24.15	24.00
		$0.1(\frac{8}{3})$	26.75	24.11	23.99
	8	0.01	26.74	24.10	23.97
		$0.1(\frac{8}{9})$	25.25	23.91	23.94
		40/49	19.09	23.20	23.82
	9	-	19.64	23.29	23.84
Best known				23.95	

Table 4.4: Cook's membrane: Center displacement v_C.

			1×1		2×2		4×4	
Element	Scheme	Weight	$(\sigma_{max})_A$	$(\sigma_{min})_B$	$(\sigma_{max})_A$	$(\sigma_{min})_B$	$(\sigma_{max})_A$	$(\sigma_{min})_B$
Q8	4	-	0.12530	-0.26746	0.26210	-0.23356	0.24439	-0.20198
	5	0.01	0.12536	-0.26700	0.26198	-0.23354	0.24438	-0.20196
		$0.1(\frac{8}{3})$	0.12678	-0.25577	0.25881	-0.23313	0.24408	-0.20156
	8	0.01	0.12553	-0.26589	0.26197	-0.23351	0.24439	-0.20196
		$0.1(\frac{8}{9})$	0.12726	-0.25437	0.26090	-0.23312	0.24425	-0.20182
		40/49	0.13451	-0.18594	0.24722	-0.22750	0.24212	-0.20075
	9	-	0.13446	-0.18623	0.24727	-0.22741	0.24212	-0.20075
Q9	4	-	0.18776	-0.15703	0.27176	-0.33457	0.24523	-0.33042
	5	0.01	0.18745	-0.15732	0.27178	-0.33436	0.24532	-0.33029
		$0.1(\frac{8}{3})$	0.17950	-0.16401	0.27184	-0.32621	0.24675	-0.32073
	8	0.01	0.18476	-0.15786	0.26984	-0.30335	0.24484	-0.26768
		$0.1(\frac{8}{9})$	0.16806	-0.16181	0.26437	-0.22257	0.24657	-0.21771
		40/49	0.13613	-0.16055	0.25023	-0.21037	0.24374	-0.20539
	9	-	0.13736	-0.15334	0.25015	-0.20845	0.24362	-0.20633
Best known			0.2360	-0.2010	0.2360	-0.2010	0.2360	-0.2010

Table 4.5: Cook's membrane: Stress analysis.

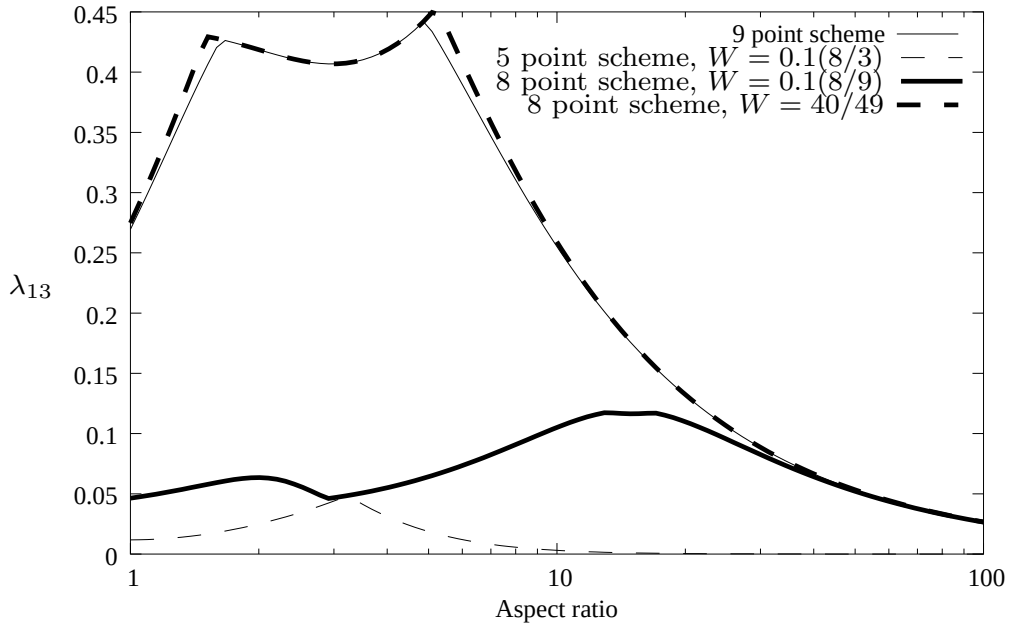

Figure 4.7: Effect of aspect ratio on λ_{13} of Q9 for different integration schemes.

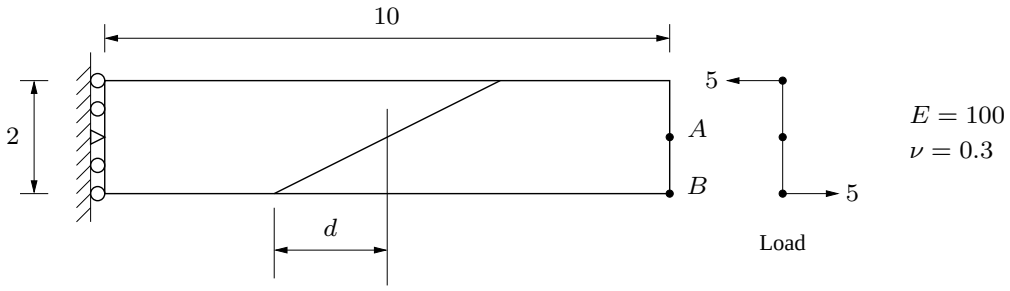

Figure 4.8: Distorted cantilever beam.

In contrast to the Q8 element, for the Q9 element the lower order integration schemes overestimate the displacement, while the 9 and 8 point schemes with $W_\beta = 40/49$ still lock. The best scheme for the Q9 element is the 8 point scheme with $W_\beta = 0.1(8/9)$. Figure 4.17 depicts the effect of different values of weight on the center displacement u_C for a Q9 element. As expected, locking of the Q9 element is to a great extent alleviated by low values of W_β.

The stress results generally reveal the same trend. It should be noted that for the 1×1 mesh, a single value of stress is calculated at points A and B, whereas in the case of the 2×2 and 4×4 meshes, the average of the stresses over the two relevant elements is calculated and reported. This explains the non-monotonic convergence behavior between the three mesh densities (although monotonic convergence on displacement does of course not imply that the stresses converge monotonically over the whole domain).

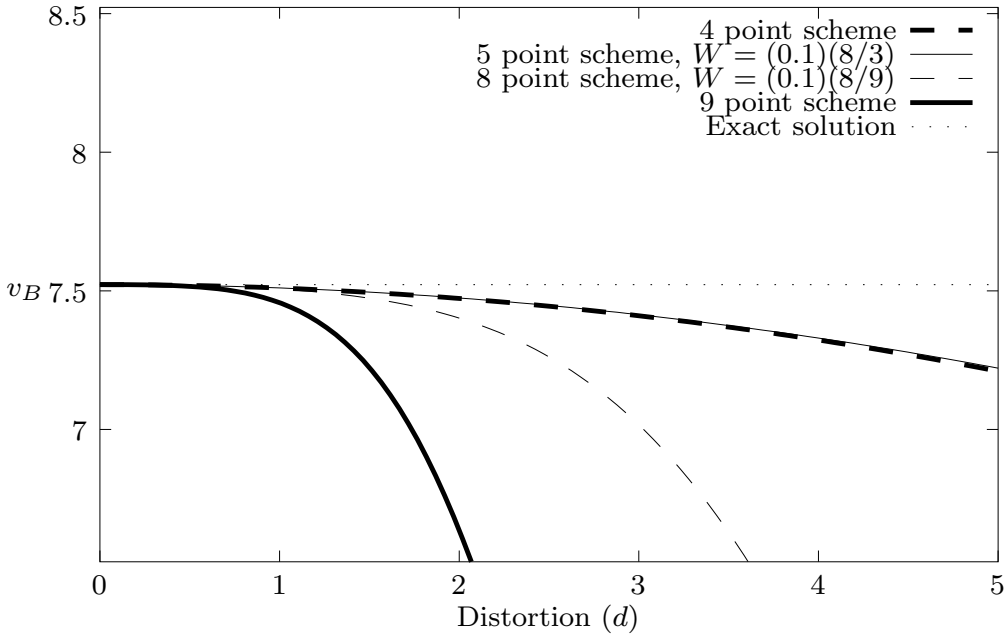

Figure 4.9: Distorted cantilever beam: Effect of distortion d on v_B for various integration schemes with Q8 elements.

4.5 Conclusion

The effect of modified reduced order quadrature rules on the presence of spurious modes in the stiffness matrices of the Q8 serendipity and Q9 Lagrange membrane finite elements has been investigated. For these elements, modified reduced order quadratures present an alternative to full integration using order 3 Gauss rules, (which results in excessively stiff behavior), and reduced integration using an order 2 Gauss rule, (which results in the introduction of spurious modes on the element level). Even though the spurious mode associated with the Q8 element is non-communicable, it remains undesirable, and may influence results in a number of situations of practical importance, e.g. topology optimization.

The alternative 5 and 8 point schemes proposed for respectively Q8 and Q9, allow for the elimination of spurious modes, while element accuracy is enhanced as compared to order 3 Gauss rules, through the introduction of soft higher order deformation modes. For the respective elements, the following considerations are pointed out:

For the Q8 element, both the 5 and 8 point rules can be used for integrating the element stiffness matrix. In each case the spurious mode is eliminated. If the weights W_0 and W_β are both chosen to be in the order of 10% of the maximum allowable weight, a highly accurate element is obtained. The numerical cost of the 8 point scheme is higher than the 5 point scheme, with no obvious benefits. Hence it is recommended that the Q8 element be integrated using the 5 point rule, with $W_0 = 0.1(8/3) = 8/30$.

For the Q9 element, the 5 point rule is inadequate since only one of the three spurious modes is eliminated. The 8 point rule (with $W_\beta = 0.1(8/9) = 8/90$) results in a rank

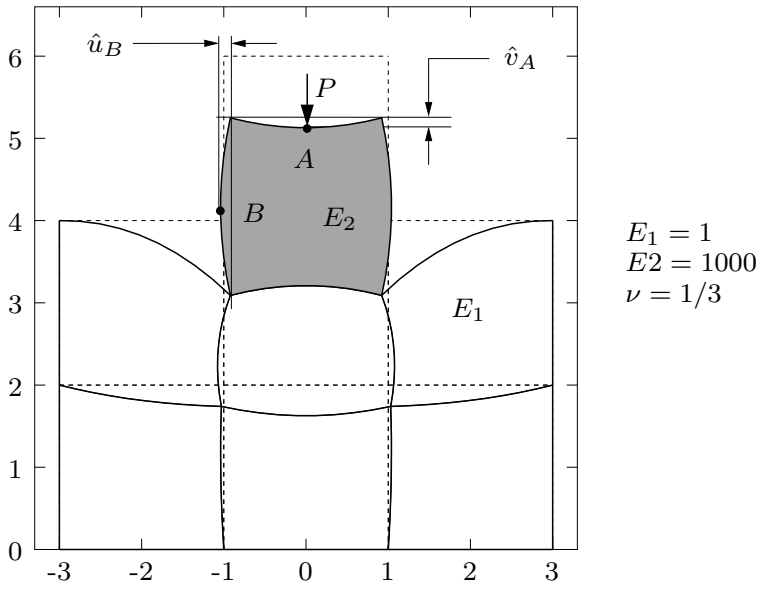

Figure 4.10: Near mechanism with point load.

sufficient element of increased accuracy as compared to the fully integrated counterpart.

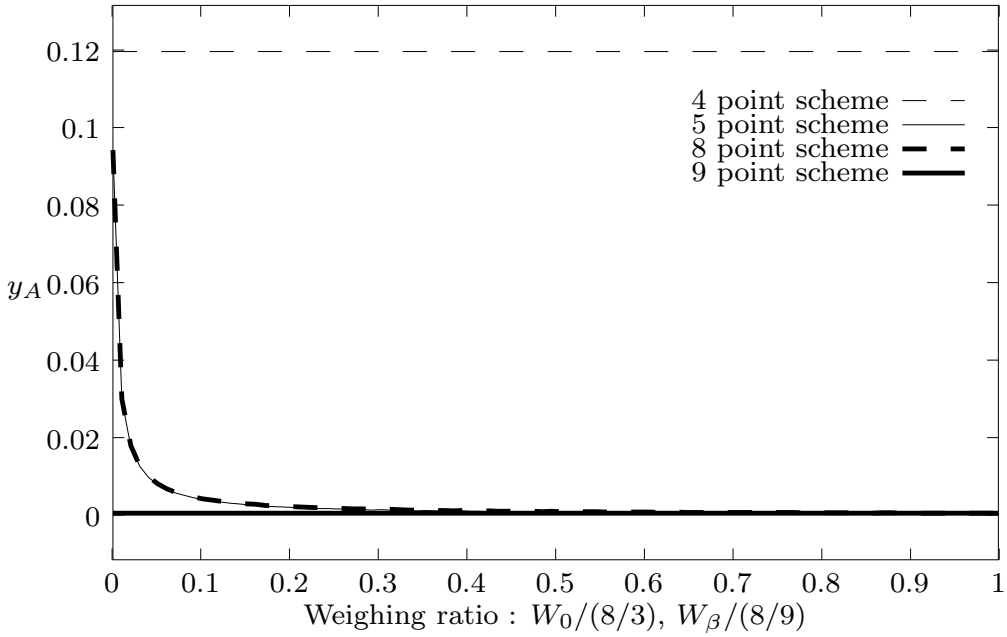

Figure 4.11: Incremental displacement $\hat{v}$ at A.

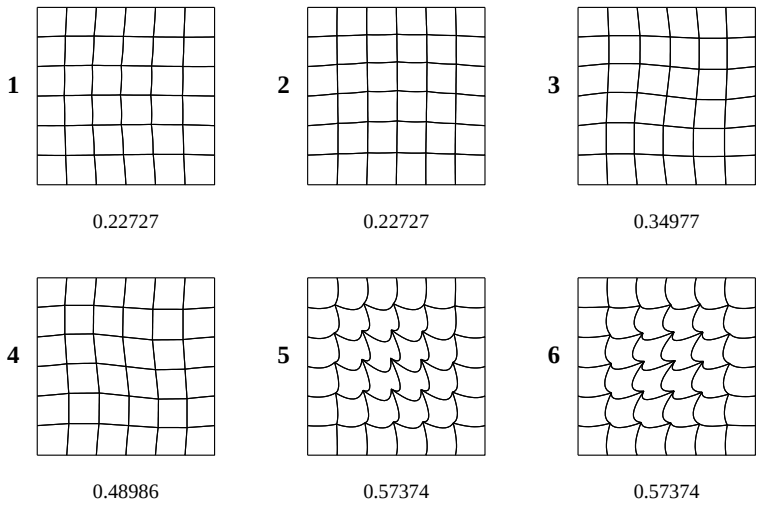

Figure 4.12: Lowest six eigenvalues and eigenvectors (Escher modes) for constrained mesh with Q9 elements and 4 point integration scheme (mesh size 6×6, $E = 2.4$, $\nu = 0.2$).

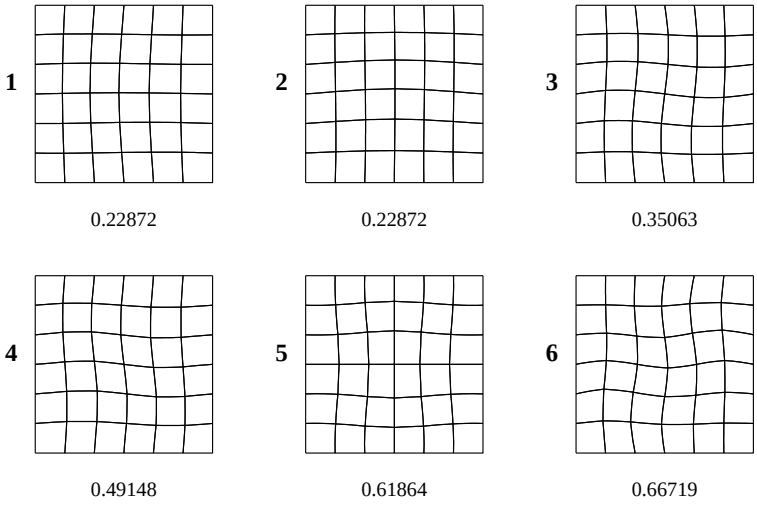

Figure 4.13: Lowest six eigenvalues and eigenvectors for constrained mesh with Q9 elements and 9 point integration scheme (mesh size 6×6, $E = 2.4$, $\nu = 0.2$).

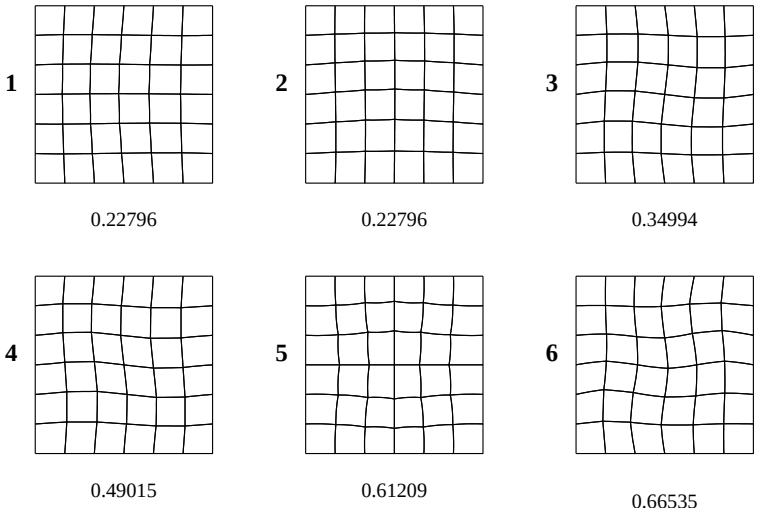

Figure 4.14: Lowest six eigenvalues and eigenvectors for constrained mesh with Q9 elements and 8 point integration scheme, $W_\beta = 0.1(8/9)$ (mesh size 6×6, $E = 2.4$, $\nu = 0.2$).

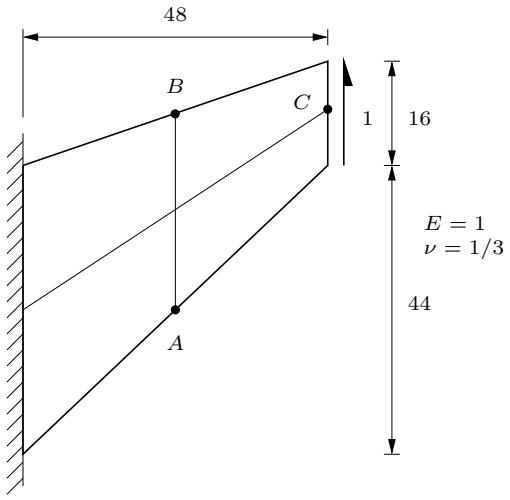

Figure 4.15: Cook's membrane

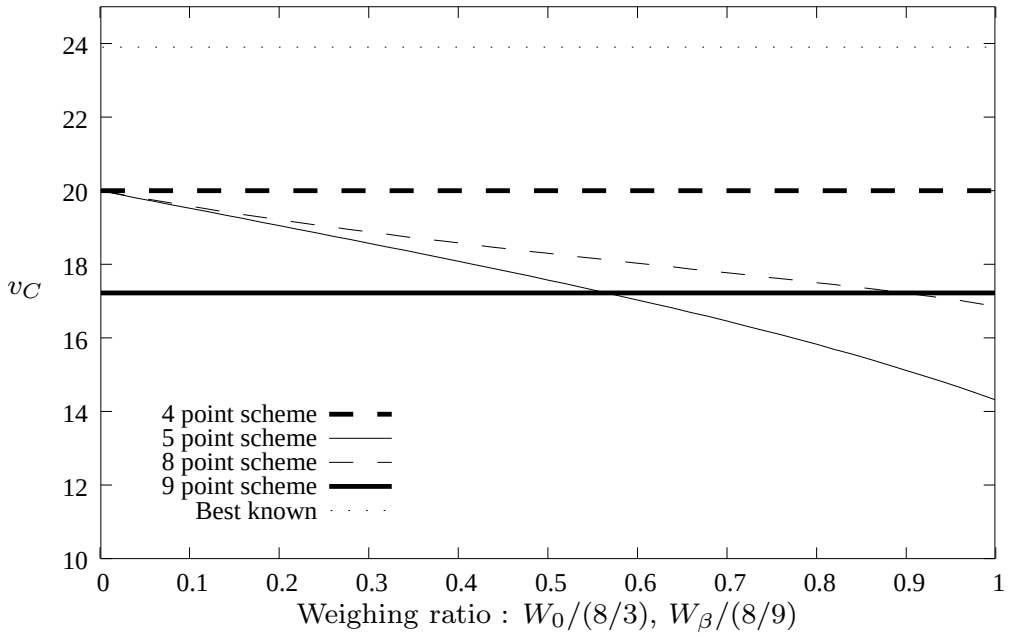

Figure 4.16: Effect of weight on v_C for Cook's membrane (Q8, 1×1 mesh).

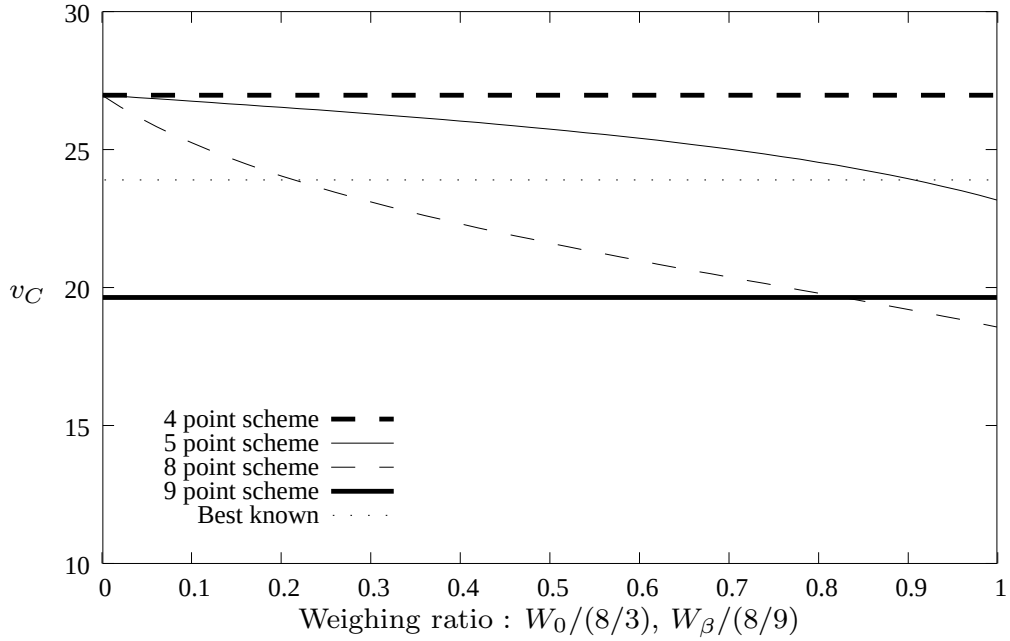

Figure 4.17: Effect of weight on v_C for Cook's membrane (Q9, 1×1 mesh).

Part 2:

Application of Finite Element Technology to Topology Optimization

Chapter 5

New schemes to deal with problematic material layouts exploiting elements with drilling degrees of freedom

5.1 Summary

In this chapter, the use of membrane finite elements with drilling degrees of freedom (to be denoted Q4X) in topology optimization is investigated. Special attention is paid to their use in schemes to treat problematic material layouts resulting from numerical instabilities, e.g. checkerboarding and one-node connected hinges. A treatment for a less prominent problem, termed the diagonal member herein, is also suggested.

Firstly it is shown that the severity of checkerboarding is significantly reduced when employing elements with drilling degrees of freedom (DOFs), as compared to results obtained using standard Q4 elements. The salient features of elements with drilling DOFs are further exploited in the development of new methods to treat one-node hinges and diagonal members.

As an application, topology optimization is applied in the design of a piezoelectrically driven micropositioner. Typically, such devices are designed on an inefficient trial-and-error basis, whereas in this study topology optimization is applied as a design tool, to somewhat automate the process. The mechanism employs two piezoelectric stack actuators in a push-pull configuration to provide the input displacement. Various objective and constraint functions, including simply maximizing output rotation, as well as maximizing stiffness measures subject to a required rotation being maintained, are investigated. In each case, unsuitable results are achieved due to the presence of one-node connected hinges in 'optimal' designs. Finally, the most promising of the two proposed schemes is successfully applied to improve upon designs achieved using conventional Q4 elements and filter strategies.

5.2 Introduction

In membrane and shell elements, drilling degrees of freedom (DOFs) are highly desirable. They allow for the modeling of, for instance, folded plates and beam-slab intersections. Due to the enriched displacement field, these elements are also significantly more accurate than their counterparts with translational DOFs only [21]. For bending dominated problems for example, drilling DOFs enhance the accuracy of 4-node elements to a level comparable to that of 8- or 9-node elements, while the 4-node element with only translational DOFs (Q4) is notoriously inaccurate. The computational effort associated with elements with drilling DOFs is low, since the connectivity of the assembled structural stiffness matrix is comparable to that of Q4.

While most commercial finite element codes include elements with an in-plane rotational DOFs, in some cases these 'vertex' rotations are artificial. In contrast, the membrane finite elements with drilling rotations used in the problems herein, are based on the continuum mechanics definition of in-plane rotations. In Chapter 2 a brief overview of these elements was presented in an elastostatics setting, and some accuracy and stability issues were addressed. In Chapter 3 the focus was on elements with drilling DOFs in the context of the piezoelectricity problem.

In this chapter, the use of the elements developed in Chapters 2 and 3 are employed in a topology optimization environment. A reasonably detailed introduction to topology optimization using the SIMP (Simple Isotropic Material with Penalization) material parameterization is presented in Appendix A. Also discussed are common numerical instabilities, as well as previously proposed methods to deal with them.

Specifically, the utility of elements with drilling DOFs to deal with checkerboarding, one-node hinges and diagonal members is investigated. Checkerboarding is characterized by material being distributed in alternating solid and void elements in a checkerboard-like pattern, as depicted in Figure 5.1(a). A one-node connected hinge occurs when two diagonally opposite elements are solid while the other two surrounding elements are void as illustrated in Figure 5.1(b). Finally, diagonal members (which have received far less attention than either checkerboarding or one-node hinges[1]) are formed by multiple diagonally connected elements as depicted in Figure 5.1(c). In each case, the numerical model of these layouts is poor, the checkerboard being over-stiff and the one-node hinge representing a perfect (impractical) hinge with zero rotational stiffness. On the other hand, the numerical model of a diagonal member subjected to axial loads is acceptable, while in bending it is unacceptably flexible.

Firstly, it is shown, by numerical example, that simply employing elements with drilling DOFs, instead of standard Q4 elements, results in a significant reduction in checkerboarding severity. Additionally, two new schemes to treat specifically one-node connected hinges and diagonal structural members, are suggested. In principle, the first scheme uses the rotations computed at interior nodes to detect excessive rotations at suspect nodes. The second scheme essentially replaces planar elements forming a one-node hinge, where appropriate,

[1] In fairness, many of the methods to deal with checkerboarding and one-node hinges will also prevent diagonal members. However some do not, see for example [98].

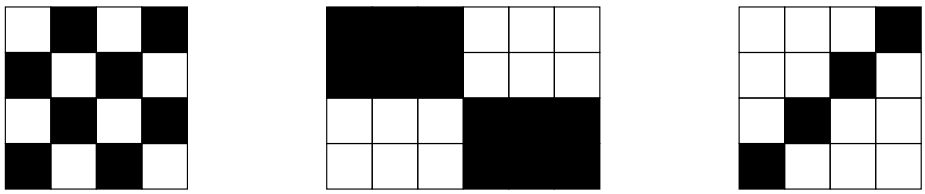

(a) (b) (c)

Figure 5.1: Checkerboard, diagonal member and one node hinge material layouts: (a) checkerboard. (b) one node hinge, (c) diagonal member.

with a more realistic beam model of the material layout while other elements in the mesh are modelled using planar elements as usual. Instead of only evaluating these new schemes on popular test problems, such as the MBB beam or the force inverter, their application is extended to the practical design of a compliant mechanism for micropositioning applications. The device under investigation is a prototype, designed to demonstrate capability for an infrared optical system.

In infrared detectors in particular, the detector elements need to be relatively large and sufficiently isolated from one another. The result is therefore a relatively sparse detector array often with insufficient density to prevent image aliasing. A possible method to improve resolution is to mount the detector array on a piezoelectric actuator, to collect the lost part of the image. To be feasible however, this would need to be accommodated in the design phase of the optical system. A further possibility (the one considered here) is to retro-fit existing infrared cameras with an actuator that manipulates other optical devices, such as lenses or mirrors, in order to recover lost parts of the image.

The design problem is formulated using three different optimization statements. The first requires only that the rotation of a mirror be maximised. In the other two formulations, a measure of mechanism stiffness is maximised, subject to a mirror rotation requirement being met. Upon inspection of the designs resulting from this optimization process, using Q4 elements and standard filter techniques, unsatisfactory one-node hinges are found at points where significant bending is required. Therefore, the most promising of the two newly developed schemes is applied to improve on these results.

This chapter is set out as follows: In Section 5.3 elements with drilling DOFs are briefly re-capped, while in Section 5.4 the topology optimization problem formulations, for all examples evaluated in this chapter, are presented. In Section 5.4.2 the effect of element formulation on checkerboarding is briefly considered. Two new schemes to deal with one-node hinges and diagonal members are presented in Section 5.5. Numerical results are presented in Section 5.6 and finally concluding remarks are related in Section 5.7.

5.3 Elements with drilling degrees of freedom

For completeness, in this section a very short introduction to elements with drilling DOFs is presented in no detail whatsoever. Further details regarding elastic elements can be found in, for instance [18, 21] and in the other references in Chapter 2. This formulation has also been extended to piezoelectric materials and the resulting planar piezoelectric elements with drilling DOFs can be found in Chapter 3 and Long *et al.* [80].

Usually planar elements possess only two (translational) DOFs per node. Formulations with a third (in-plane rotational) degree of freedom result in elements with superior accuracy, and modelling capabilities. For example, planar configurations such as beam-slab connections can be modelled, and when the planar elements are combined with plate elements, folded plates can be modelled properly.

In this work, the standard 4-node bilinear quadrilateral elements *without* drilling DOFs will be denoted Q4, while the corresponding elements *with* drilling DOFs will be denoted Q4X. Finally, 9-node Lagrangian elements (*without* drilling DOFs) are labeled Q9.

5.4 Problem formulations

In this chapter, a number of different topology optimization problems, all using the SIMP material model, are considered. For convenience and ease of reference, in this section details of *all* test problem formulations are given. The first (and simplest) is the minimum compliance problem. This problem is often used to benchmark newly proposed procedures since reference solutions[2] exist for many problems, including the MBB beam problem. Minimum compliance problems will be used to numerically determine the effect of element formulation on checkerboarding.

Since one-node connected hinges are more common in compliant mechanism design problems than in minimum compliance problems, the efficacy of our new schemes will be evaluated on popular compliant mechanism topology optimization problems[3].

Finally, a topology optimization procedure is employed in the design of a practical compliant mechanism. The device under consideration is a demonstrator mirror scanning device for optical applications. For comparison, the problem is posed using three different formulations. In the remainder of this section, the afforementioned problems are described in more detail.

Unless otherwise specified, a penalty value of $p = 3$ is employed throughout.

[2] At least qualitative solutions are known [99]. Generally authors do not publish objective function values, or only present normalised values making quantitative comparisons difficult.

[3] Once again, only qualitative comparisons will be made with results for problems such as the force inverter.

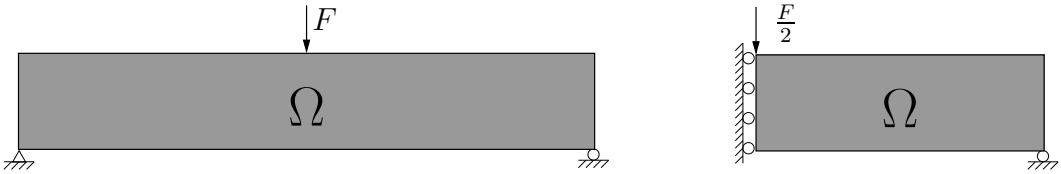

(a) (b)

Figure 5.2: The minimum compliance problem for the MMB beam: (a) Full model, (b) symmetric model.

5.4.1 The minimum compliance topology optimization problem using SIMP

The minimum compliance problem seeks to find the material distribution which maximizes the global stiffness, subject to a bound on the available material. The discrete form of the minimum compliance problem employing the SIMP material model can be written as:

$$\min_{\boldsymbol{\rho}} \; c(\boldsymbol{\rho}) \tag{5.1}$$

$$\text{such that} \; : v(\boldsymbol{\rho}) = \frac{1}{v_\Omega}\left(\sum_{i=1}^{Nel} \rho_i v_i\right) - v^* \leq 0 \tag{5.2}$$

$$: \boldsymbol{KU} = \boldsymbol{F} \tag{5.3}$$

$$: \mathbf{0} \leq \boldsymbol{\rho}_{\min} \leq \boldsymbol{\rho} \leq \mathbf{1}, \tag{5.4}$$

where compliance is calculated, for the planar problem depicted in Figure 5.2, as

$$c(\boldsymbol{\rho}) = \boldsymbol{F}^T\boldsymbol{U} = \boldsymbol{U}^T\boldsymbol{KU} = \sum_{i=1}^{Nel}(\rho_i)^p \boldsymbol{u}_i^T \boldsymbol{k}_i^0 \boldsymbol{u}_i. \tag{5.5}$$

In the foregoing, c is the compliance, $\boldsymbol{\rho}$ is the vector of design variables (representing elemental densities) made up of elemental values ρ_i, $i = 1, 2, ..., Nel$. In order to prevent singularities in the finite element analysis, a lower bound on the densities is imposed, denoted $\boldsymbol{\rho}_{\min}$. Furthermore, v_Ω is the volume of the design domain Ω, v_i is the volume of each element, and v^* is an upper bound on the permissible volume fraction. The volume constraint (not the actual material volume) is denoted $v(\boldsymbol{\rho})$. Finally, $\boldsymbol{U}$ and $\boldsymbol{F}$ are the global assembled displacement and force vectors, $\boldsymbol{K}$ is the global stiffness matrix, and $\boldsymbol{u}_i$ and $\boldsymbol{k}_i^0$ are the elemental displacement vector and the stiffness matrix of a solid element respectively.

If the force is not design dependant, the sensitivity of compliance to the density of a given element ρ_i is

$$\frac{\partial c}{\partial \rho_i} = \boldsymbol{F}^T \frac{\partial \boldsymbol{U}}{\partial \rho_i}, \tag{5.6}$$

where $\frac{\partial \boldsymbol{U}}{\partial \rho_i}$ can be found using (5.3) as

$$\frac{\partial \boldsymbol{U}}{\partial \rho_i} = -\boldsymbol{K}^{-1}\frac{\partial \boldsymbol{K}}{\partial \rho_i}\boldsymbol{U}. \tag{5.7}$$

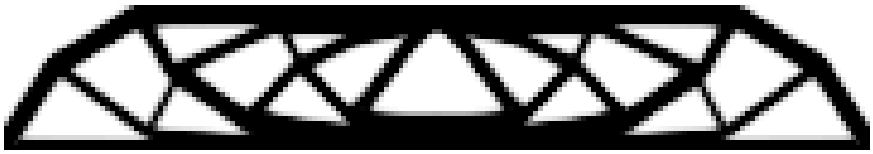

Figure 5.3: A reference optimal topology for the MBB beam discretized using 180×30 elements.

Now, combining (5.6) and (5.7) gives:

$$\frac{\partial c}{\partial \rho_i} = -\boldsymbol{F}^T \boldsymbol{K}^{-1} \frac{\partial \boldsymbol{K}}{\partial \rho_i} \boldsymbol{U}. \tag{5.8}$$

Equation (5.8) can be shown to further reduce to

$$\frac{\partial c}{\partial \rho_i} = -\boldsymbol{U}^T \frac{\partial \boldsymbol{K}}{\partial \rho_i} \boldsymbol{U} = -p(\rho_i)^{p-1} \boldsymbol{u}_i^T \boldsymbol{k}_i^0 \boldsymbol{u}_i, \tag{5.9}$$

which contains only elemental quantities.

Finally, the sensitivity of the volume constraint can simply be written as

$$\frac{\partial v}{\partial \rho_i} = \frac{v_i}{v_\Omega}. \tag{5.10}$$

For comparison, Figure 5.3 depicts a reference optimal topology for the MBB beam problem depicted in Figure 5.2. To avoid checkerboarding, the sensitivities of the objective function are filtered using the methods suggested by Sigmund [100]. The solution is computed using a heuristic updating scheme proposed by Bendsøe [4, 101], based on standard optimality criterion methods. The scheme for updating the elemental densities is expressed as:

$$\rho_i^{\text{new}} = \begin{cases} \max(\rho_{\min}, \rho_i - m) & \text{if} \quad \rho_i B_i^\eta \leq \max(\rho_{\min}, \rho_i - m) \\ \rho_i B_i^\eta & \text{if} \quad \max(\rho_{\min}, \rho_i - m) < \rho_i B_i^\eta < \min(1, \rho_i + m) \\ \min(1, \rho_i + m) & \text{if} \quad \min(1, \rho_i + m) \leq \rho_i B_i^\eta \end{cases} \tag{5.11}$$

where m is a move limit, $\eta (= \frac{1}{2})$ is a numerical damping coefficient and B_i is found from the optimality condition as

$$B_i = \frac{-\dfrac{\partial c}{\partial \rho_i}}{\lambda \dfrac{\partial v}{\partial \rho_i}}, \tag{5.12}$$

where λ is a Lagrange multiplier found using a bisection algorithm. A more complete derivation of B_i can be found, for example in [4].

In order to reduce the likelihood of convergence to local minima, the penalty parameter p is increased slowly from 1 to 3 during the optimization procedure. In the following paragraphs, some brief comments on checkerboarding in minimum compliance problems are presented.

(a) (b) (c)

Figure 5.4: MBB beam optimal designs for a 30×90 mesh employing: (a) Q4 elements, (b) Q9 elements, (c) Q4X elements.

5.4.2 Comments on checkerboarding

Checkerboarding is a numerical instability, commonly observed in reported solutions of minimum compliance problems. It is characterized by material being distributed in alternating solid and void elements in a checkerboard-like pattern. The numerical model of this material layout is poor, and appears over-stiff as detailed in [14, 102] and Chapter 7. Although filters are frequently used to reduce or eliminate this effect, the use of filters complicates interpretation of results, due to their largely heuristic nature. It is well known that under certain circumstances, checkerboarding is eliminated when higher order elements (Q8 or Q9) are used. These elements, however, greatly increase the time required to solve the structural problem due to the higher number of nodes per element and the reduced sparsity of the stiffness matrix.

A more detailed theoretical study of checkerboarding, investigating the effect of various planar element formulations, is presented in Chapter 7 and therefore only selected numerical results will be presented here. In each case, results are computed using the heuristic updating scheme based on optimality criteria, see (5.11). To reduce the likelihood of convergence to local minima, the penalty parameter is increased linearly from 1 to 3 in 33 iterations and held at $p = 3$ for a further 16 iterations.

Figure 5.4 illustrates the effect of element formulation on the optimal topology of the popular MBB beam problem. This problem is detailed in Section 5.4.1 and a reference solution employing the mesh independency filter due to Sigmund is depicted in Figure 5.3. Note that in Figure 5.4 only the topology of the symmetric model, see Figure 5.2(b), is depicted.

As is well known, Q4 elements are prone to checkerboard layouts, as depicted in Figure 5.4(a), while in most cases, Q9 elements eliminate checkerboards in the optimal design, see Figure 5.4(b). Elements with drilling DOFs are shown here to significantly reduce the amount of checkerboarding in the optimal layout, as depicted in Figure 5.4(c). In fact, in a number of test problems employing elements with drilling DOFs, checkerboarding has only been observed in diagonal structural members, similar to those in Figure 5.4(c).

Although checkerboarding is not completely eliminated upon application of elements with drilling DOFs, the resulting topology is considered more usable than that found using Q4 elements. Major features of the topology, found using elements with drilling DOFs, will not be lost after a 'smoothing' post-processing step, unlike the result found with Q4 elements. It is however explained in Chapter 7, that it is not possible completely prevent checkerboarding

by mere application of elements with drilling DOFs. Additionally, it is shown that only if the skew-symmetric part of the displacement gradient is non-zero will checkerboarding be (slightly) alleviated.

Finally, in an attempt to highlight the numerical cost benefits of employing lower order elements, the time required to solve for $\boldsymbol{U}$ in $\boldsymbol{KU} = \boldsymbol{F}$, was recorded for one iteration of the MBB beam problem, using Q4, Q9, and elements with drilling DOFs. When the computational effort (in CPU seconds) is normalized with respect to that of the Q4 results, the effort using elements with drilling DOFs is 1.80, while the relative effort with Q9 elements is 11.19, illustrating the significant saving achieved when using lower order elements.

We now return to the presentation of the various topology optimization problem formulations used to evaluate the proposed schemes.

5.4.3 Compliant mechanism design using topology optimization and SIMP

Compliant mechanism design employing topology optimization, involves seeking the optimal material distribution within a design domain which optimizes a given objective function (usually maximizing a certain displacement) while subject to a limit on the available material. To illustrate, the popular force inverter problem is used, with the problem graphically depicted in Figure 5.5. The goal is to maximise the output displacement, in the direction opposite to the applied force. The problem may be formulated, similar to the minimum compliance problem, as

$$\max_{\boldsymbol{\rho}} \; u_{\text{out}}(\boldsymbol{\rho}) \tag{5.13}$$

$$\text{such that} \;\; : v(\boldsymbol{\rho}) = \frac{1}{v_\Omega}\left(\sum_{i=1}^{Nel} \rho_i v_i\right) - v^* \leq 0 \tag{5.14}$$

$$: \boldsymbol{KU} = \boldsymbol{F} \tag{5.15}$$

$$: \mathbf{0} \leq \boldsymbol{\rho}_{\min} \leq \boldsymbol{\rho} \leq \mathbf{1}, \tag{5.16}$$

where u_{out} is the output displacement. The output displacement can be extracted from the solution of the equilibrium equations (5.15) and is given by

$$u_{\text{out}} = \boldsymbol{L}^T \boldsymbol{U}. \tag{5.17}$$

In (5.17), $\boldsymbol{L}$ is a unit vector in the desired output direction within the finite element space. In the case of the force inverter depicted in Figure 5.5, $\boldsymbol{L}$ is a vector with a single non-zero (unit) entry corresponding to the DOF which extracts u_{out} from $\boldsymbol{U}$.

In a process similar to that used to compute the sensitivities of compliance, the sensitivity of u_{out} to the design variables $\boldsymbol{\rho}$ can be found using (5.15) and (5.17):

$$\frac{\partial u_{\text{out}}}{\partial \rho_i} = \boldsymbol{L}^T \frac{\partial \boldsymbol{U}}{\partial \rho_i}, \tag{5.18}$$

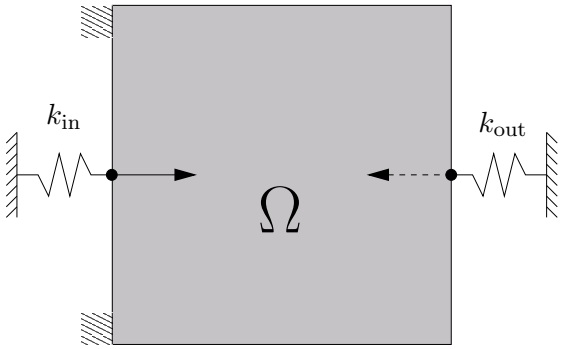

Figure 5.5: Compliant mechanism design of a force inverter.

where from (5.15),

$$\frac{\partial \boldsymbol{U}}{\partial \rho_i} = -\boldsymbol{K}^{-1}\frac{\partial \boldsymbol{K}}{\partial \rho_i}\boldsymbol{U}. \tag{5.19}$$

Combining (5.18) and (5.19) results in

$$\frac{\partial u_{\text{out}}}{\partial \rho_i} = -\boldsymbol{L}^T\boldsymbol{K}^{-1}\frac{\partial \boldsymbol{K}}{\partial \rho_i}\boldsymbol{U}, \tag{5.20}$$

which can, using the fact that $\boldsymbol{K}$ is symmetric and positive definite, in turn be rewritten as

$$\frac{\partial u_{\text{out}}}{\partial \rho_i} = -\boldsymbol{\lambda}^T\frac{\partial \boldsymbol{K}}{\partial \rho_i}\boldsymbol{U}. \tag{5.21}$$

In this case, $\boldsymbol{\lambda}$ is the solution of the adjoint problem

$$\boldsymbol{K}\boldsymbol{\lambda} = \boldsymbol{L}. \tag{5.22}$$

Finally, the sensitivity of u_{out} can be written in terms of only elemental quantities as

$$\frac{\partial u_{\text{out}}}{\partial \rho_i} = -p(\rho_i)^{p-1}\boldsymbol{\lambda}_i^T\boldsymbol{k}_i^0\boldsymbol{u}_i, \tag{5.23}$$

where $\boldsymbol{\lambda}_i$ is the elemental vector (for element i) of displacements associated with the adjoint load, $\boldsymbol{k}_i^0$ is the stiffness matrix of solid element i and $\boldsymbol{u}_i$ is the displacements of the original problem for element i.

An illustrative reference solution to the force inverter problem is depicted in Figure 5.6. Once again, the heuristic updating scheme, with some minor adjustments to improve stability, is employed in the solution. In this particular solution, the formation of one-node hinges are clearly visible even though the mesh-independency filter of Sigmund is again employed.

5.4.4 Mirror scanning design using topology optimization and SIMP

In this section a traditional topology optimization procedure, using standard filtering techniques, is employed in the design of a prototype mirror microscanning device. The objective

Figure 5.6: A reference optimal topology for the force inverter problem using 48×48 elements.

of the designed mechanism is to rotate a mirror about a single axis, and thereby accurately position the reflected image. Our design employs two 18×5×5mm piezoelectric stack actuators in a push-pull configuration.

Since this application represents a prototype design, the size and shape of a representative design domain is simply estimated. The focus of this work is not on the optimal placement of the piezoelectric actuator, since this issue has already been addressed, see Frecker [103] for examples. Therefore, in order to determine a suitable position for the piezoelectric stack, topology optimization trials, with various stack positions, were performed.

After determining a suitable stack position, the optimization problem was run several times with random starting points. Due to the global nature of the problem, approximately 70% of the randomly seeded designs resulted in a double-lever mechanism, while the remainder terminated in local inferior optima. Therefore, in order to ensure the required load-path for this type of mechanism in the initial stages of the optimization procedure, a double-lever mechanism is seeded as a starting point. These topology optimization trials further revealed that an output rotation of around 1° is comfortably realized, which translates to a tip displacement of approximately 0.5mm. The selected initial design with fixed stack position is shown in Figure 5.7. The figure identifies the design domain as well as passive (solid and void) regions.

In the results to follow, anti-symmetry is used to model the mechanism as illustrated in Figure 5.7(b), and the optimization problem is solved with the method of moving asymptotes (MMA) due to Svanberg [10]. The sensitivities of the objective functions have once again been modified with the mesh independency filter of Sigmund [100] to avoid checkerboarding. In the remainder of this section, the formulation of, and results for, the three different problem formulations are presented.

Mirror scanning device: Formulation 1

The first formulation seeks to simply maximize the output rotation subject to a constraint on the amount of available material. The required output rotation may be computed given the length of the mirror and the tangential displacement. The problem formulation can be

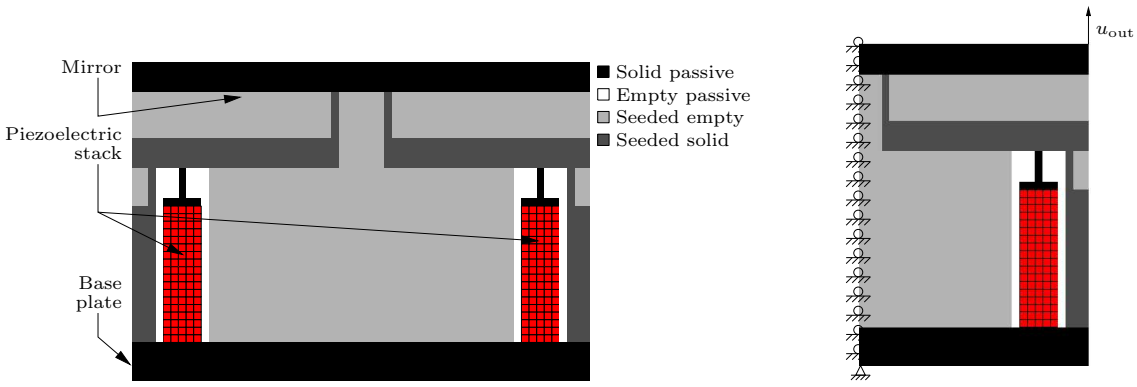

(a) (b)

Figure 5.7: Design domain and problem definition for mirror scanning device: (a) Full initial design, (b) anti-symmetric finite element model.

written as:

$$\min_{\boldsymbol{\rho}} \; f_1(\boldsymbol{\rho}) = -\left(\frac{u_{\text{out}}}{u_{\text{req}}}\right)^2 \tag{5.24}$$

$$\text{such that} \;\; : v(\boldsymbol{\rho}) = \frac{1}{v_\Omega}\left(\sum_{i=1}^{Nel} \rho_i v_i\right) - v^* \leq 0 \tag{5.25}$$

$$: \begin{bmatrix} \boldsymbol{K}_{uu} & \boldsymbol{K}_{u\phi} \\ \boldsymbol{K}_{u\phi}^T & \boldsymbol{K}_{\phi\phi} \end{bmatrix} \begin{Bmatrix} \boldsymbol{U} \\ \boldsymbol{\phi} \end{Bmatrix} = \begin{Bmatrix} \boldsymbol{F} \\ \boldsymbol{Q} \end{Bmatrix} \tag{5.26}$$

$$: \mathbf{0} \leq \boldsymbol{\rho}_{\min} \leq \boldsymbol{\rho} \leq \mathbf{1}. \tag{5.27}$$

The output rotation is maximized by maximizing the output tip displacement u_{out} due to the actuator input. The vertical output displacement is monitored at the top right vertex of the mirror, see Figure 5.7. As mentioned earlier, an output displacement of u_{req}=0.5mm is required to achieve a rotation of 1°. The displacement is normalized with respect to the required value and squared so that the direction of the displacement is not prescribed, and optimization algorithmic scaling issues are avoided.

In this case, the equilibrium equations (5.26) include the piezoelectric terms arising from the piezoelectric actuators, where $\boldsymbol{\phi}$ represents the electric potential and $\boldsymbol{Q}$ the nodal charge. The upper bound on the volume fraction is $v^* = 0.5$. Note that only $\boldsymbol{K}_{uu}$ is a function of the design variables $\boldsymbol{\rho}$ since the piezoelectric elements are considered passive solid elements.

The sensitivity of (5.24) can easily be found, using a process similar to that used to calculate the sensitivity of the output displacement for the force inverter problem, given in (5.23). Using the chain rule:

$$\frac{\partial f_1}{\partial \rho_i} = -2\frac{u_{\text{out}}}{{u_{\text{req}}}^2}\left(\frac{\partial u_{\text{out}}}{\partial \rho_i}\right). \tag{5.28}$$

In this case however, u_{out} is derived from the voltage applied to the electrodes of the piezoelectric actuators, and not directly due to any applied forces.

In the system of equations (5.26), the *unknown* displacement and potential vectors $\boldsymbol{U}$ and $\boldsymbol{\phi}$ respectively, are sought. The vectors $\boldsymbol{F}$ and $\boldsymbol{Q}$ represent not only the applied forces and charges (there are none in this case), but also reactions due to *prescribed* displacement and electric potential boundary conditions. Using static condensation, (5.26) can be rewritten in terms of only the unknown displacements as:

$$\hat{\boldsymbol{K}}\boldsymbol{U} = \hat{\boldsymbol{F}}, \tag{5.29}$$

where the equivalent stiffness matrix is given by

$$\hat{\boldsymbol{K}} = \boldsymbol{K}_{uu} - \boldsymbol{K}_{u\phi}\boldsymbol{K}_{\phi\phi}^{-1}\boldsymbol{K}_{u\phi}^{T}, \tag{5.30}$$

and where the equivalent force vector is given by

$$\hat{\boldsymbol{F}} = \boldsymbol{F} - \boldsymbol{K}_{u\phi}\boldsymbol{K}_{\phi\phi}^{-1}\boldsymbol{Q}. \tag{5.31}$$

This solution strategy, in which electric potentials are condensed from the unknown output vector, also prevents poor scaling which results if displacements and potentials are solved simultaneously [69]. Finally, the unknown potentials can be recovered (if necessary) as

$$\boldsymbol{\phi} = \boldsymbol{K}_{\phi\phi}(\boldsymbol{Q} - \boldsymbol{K}_{u\phi}^{T}\boldsymbol{U}). \tag{5.32}$$

Therefore, instead of solving for the adjoint equation as in (5.22), the solution to the adjoint equation

$$\hat{\boldsymbol{K}}\boldsymbol{\lambda} = \boldsymbol{L}, \tag{5.33}$$

is required, where $\boldsymbol{L}$ is an appropriate adjoint load vector. In terms of elementwise quantities, it can be shown that the sensitivities reduce to

$$\frac{\partial u_{\text{out}}}{\partial \rho_i} = -p(\rho_i)^{p-1}\boldsymbol{\lambda}_i^{T}\boldsymbol{k}_i^{0}\boldsymbol{u}_i, \tag{5.34}$$

where the subscript i once again indicates elemental quantities.

Mirror scanning device: Formulation 2

Using the first formulation large displacements may be obtained at the expense of mechanism stiffness. Such a mechanism may not be robust or stable enough for practical applications. The problem formulation can therefore be modified so that only the required output displacement is attained. In so doing, an additional requirement can be prescribed, i.e. that the structure should be as stiff as possible.

In this second formulation, a mechanism with minimum compliance is sought, subject to a prescribed output rotation being maintained. The required output rotation is, as before, translated to a required tangential displacement of $u_{\text{req}} = 0.5\text{mm}$. The compliance is computed using a point force applied to the output displacement point. Note that since

anti-symmetry is used to model the device, this force in fact simulates a force couple. Additionally, there is no constraint on volume imposed.

The problem can be written in standard form as:

$$\min_{\boldsymbol{\rho}} \; f_2(\boldsymbol{\rho}) = \frac{c}{c_0} \tag{5.35}$$

$$\text{such that} \; : 1 - \left(\frac{u_{\text{out}}}{u_{\text{req}}}\right) \leq 0 \tag{5.36}$$

$$: \hat{\boldsymbol{K}}\boldsymbol{U} = \hat{\boldsymbol{F}} \tag{5.37}$$

$$: \boldsymbol{K}_{uu}\bar{\boldsymbol{U}} = \boldsymbol{L} \tag{5.38}$$

$$: \mathbf{0} \leq \boldsymbol{\rho}_{\min} \leq \boldsymbol{\rho} \leq \mathbf{1}, \tag{5.39}$$

where c_0, the compliance of the initial design, is again introduced to prevent poor scaling of the optimization problem. The compliance is expressed as

$$c = \boldsymbol{L}^T\bar{\boldsymbol{U}} = \bar{\boldsymbol{U}}^T\boldsymbol{K}_{uu}\bar{\boldsymbol{U}}, \tag{5.40}$$

where the displacements $\bar{\boldsymbol{U}}$ are computed by solving the short circuited system given in (5.38), and where $\boldsymbol{L}$ is the adjoint load used to determine u_{out}. The sensitivity of c in this case can easily be shown to be

$$\frac{\partial c}{\partial \rho_i} = -p(\rho_i)^{p-1}\bar{\boldsymbol{u}}_i{}^T\boldsymbol{k}_i^0\bar{\boldsymbol{u}}_i, \tag{5.41}$$

where $\bar{\boldsymbol{u}}_i$ are again appropriate elemental displacements and $\boldsymbol{k}_i^0$ represents stiffness matrix of the solid element.

Mirror scanning device: Formulation 3

In this final problem formulation, the minimum natural frequency of the structure is maximized, again subject to the prescribed tangential displacement of $u_{\text{req}} = 0.5$mm being maintained. Since the 'rotational' stiffness of the structure is of particular interest, anti-symmetric boundary conditions are again employed to model only half of the structure. Finally, as with Formulation 2 there is no constraint imposed on the available volume of material.

The problem can be expressed as:

$$\min_{\boldsymbol{\rho}} \; f_3(\boldsymbol{\rho}) = -\frac{\lambda_{\min}}{\lambda_0} \tag{5.42}$$

$$\text{such that} \; : 1 - \left(\frac{u_{\text{out}}}{u_{\text{req}}}\right) \leq 0 \tag{5.43}$$

$$: \hat{\boldsymbol{K}}\boldsymbol{U} = \hat{\boldsymbol{F}} \tag{5.44}$$

$$: \boldsymbol{K}_{uu}\boldsymbol{\Phi}_j = \lambda_j\boldsymbol{M}\boldsymbol{\Phi}_j, \quad \forall\; j = 1, 2, ..., Ndof \tag{5.45}$$

$$: \mathbf{0} \leq \boldsymbol{\rho}_{\min} \leq \boldsymbol{\rho} \leq \mathbf{1}, \tag{5.46}$$

where λ_j is the j-th short circuited eigenvalue with corresponding eigenvector $\boldsymbol{\Phi}_j$ and $Ndof$ is the total number of degrees of freedom. The eigenvectors are normalised so that

$$\boldsymbol{\Phi}_j^T \boldsymbol{M} \boldsymbol{\Phi}_j = 1, \quad \forall\ j = 1, 2, ..., Ndof. \tag{5.47}$$

Neglecting possible issues with duplicate or multiple eigenvalues (and the resulting non-differentiability issues), the sensitivities of λ_j can be computed using (5.45) as

$$\frac{\partial \boldsymbol{K}_{uu}}{\partial \rho_i}\boldsymbol{\Phi}_j + (\boldsymbol{K}_{uu} - \lambda_j \boldsymbol{M})\frac{\partial \boldsymbol{\Phi}_j}{\partial \rho_i} = \frac{\partial \lambda_j}{\partial \rho_i}\boldsymbol{M}\boldsymbol{\Phi}_j + \lambda_j \frac{\partial \boldsymbol{M}}{\partial \rho_i}\boldsymbol{\Phi}_j. \tag{5.48}$$

By premultiplying by $\boldsymbol{\Phi}_j^T$, making use of the symmetry of $\boldsymbol{K}_{uu}$ and $\boldsymbol{M}$, and substituting (5.45) and (5.47), the sensitivity of λ_j to ρ_i can be shown to be

$$\frac{\partial \lambda_j}{\partial \rho_i} = \boldsymbol{\Phi}_j^T \left(\frac{\partial \boldsymbol{K}_{uu}}{\partial \rho_i} - \lambda_j \frac{\partial \boldsymbol{M}}{\partial \rho_i} \right) \boldsymbol{\Phi}_j. \tag{5.49}$$

This sensitivity can be written with elemental quantities only as

$$\frac{\partial \lambda_j}{\partial \rho_i} = \boldsymbol{\phi}_{j\ i}^T \left(p(\rho_i)^{p-1} \boldsymbol{k}_i^0 - \lambda_j \boldsymbol{m}_i^0 \right) \boldsymbol{\phi}_{j\ i}, \tag{5.50}$$

where $\boldsymbol{\phi}_{j\ i}$ is the elemental component of element i, corresponding to the j^{th} eigenvector, and $\boldsymbol{m}_i^0$ is the mass matrix of the i^{th} solid element.

The modified SIMP material model, for removing localized eigenmodes in low density areas, suggested by Pedersen [104], has been used. Specifically, mass and stiffness terms are interpolated using the following relations:

$$\text{mass:} \quad \boldsymbol{m}_i = \rho_i \boldsymbol{m}_i^0 \quad \text{for } 0 \leq \rho_{\min} \leq \rho_i \leq 1 \tag{5.51}$$

$$\text{stiffness:} \quad \boldsymbol{k}_i = \rho_i^3 \boldsymbol{k}_i^0 \quad \text{for } 0.1 < \rho_i \leq 1 \tag{5.52}$$

$$: \quad \boldsymbol{k}_i = \tfrac{\rho_i}{100} \boldsymbol{k}_i^0 \quad \text{for } 0 \leq \rho_{\min} \leq \rho_i \leq 0.1. \tag{5.53}$$

Reasonable results are achieved without making special provision for multiple eigenvalues. If problems were encountered, the techniques described in [105] could be employed. Alternatively, a bound-formulation could be applied in which the formulation is typically modified as follows

$$\max_{\boldsymbol{\rho}} \ \beta \tag{5.54}$$

$$\text{such that} \ : [\alpha]^j \lambda_j \geq \beta, \quad \forall\ j = 1, 2, ..., Ndof \tag{5.55}$$

$$: \boldsymbol{K}_{uu}\boldsymbol{\Phi}_j = \lambda_j \boldsymbol{M}\boldsymbol{\Phi}_j, \quad \forall\ j = 1, 2, ..., Ndof, \tag{5.56}$$

where for example $\alpha = 0.95$. This additional constraint ensures that consecutive eigenvalues are at least a certain fraction smaller than the previous. It may however, prevent eigenmodes from switching order during the iteration process [4].

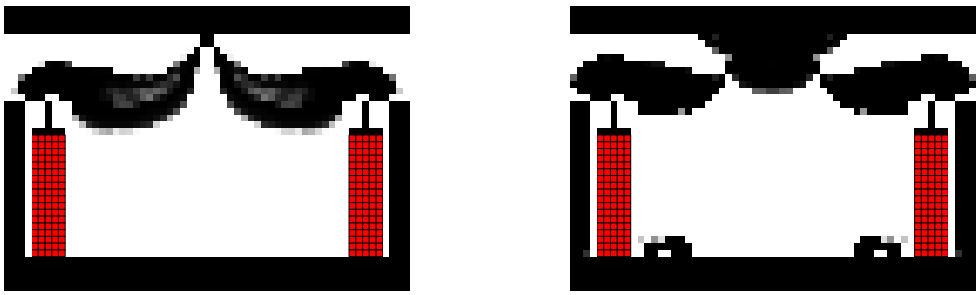

(a) (b)

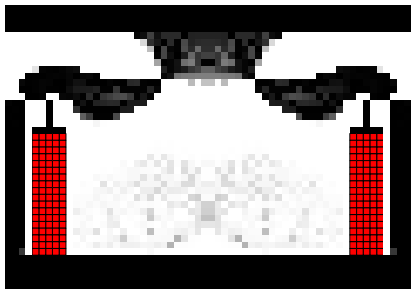

(c)

Figure 5.8: Optimal topologies for: (a) Formulation 1, (b) Formulation 2, (c) Formulation 3. Although anti-symmetry is used in the finite element model, the complete design is shown.

Numerical results

The optimal topologies for the three different problem formulations are depicted in Figure 5.8. Figures 5.8(a), 5.8(b) and 5.8(c) depict the optimal topologies resulting from formulations 1, 2 and 3, respectively. In each case, standard Q4 elements are used in the finite element solution, and the mesh-independency scheme of Sigmund is used to prevent checkerboarding.

As expected, each of the three designs result in similar double-lever mechanisms, although their connection points to the mirror, vary. The designs resulting from formulations 2 and 3 in particular, are very similar. Furthermore, since formulations 2 and 3 do not have a restriction on the amount of available material, superfluous features in the area between the two piezoelectric stacks are obtained, as illustrated in Figures 5.8(b) and 5.8(c).

In each case depicted in Figure 5.8, the optimal design is unacceptible due to the formation of one-node connected hinges. These mechanisms all exploit the unrealistic flexability of the one-node connected hinges to attain the required mobility. After interpretation and post-processing of these designs, it is likely that significantly lower mobility than precicted, will be achieved due to the higher stiffness of realistic hinges. Schemes which prevent their formation (or improve their finite element model) within the topology optimization procedure are therefore sought.

5.5 New schemes to prevent checkerboarding and one-node hinges

In this section, two new schemes to deal with one-node connected hinges and diagonal members are detailed. Results containing diagonal members have been illustrated in Section 5.4.2, when no scheme for checkerboard prevention is employed. Furthermore, in Sections 5.4.3 and 5.4.4 it has been demonstrated that one-node hinges are possible even if Sigmund's mesh independency filter is used to prevent checkerboarding.

In particular, we attempt to show how elements with drilling DOFs may be exploited in formulating schemes to overcome (or improve the modelling of) one-node hinges and diagonal members. The first scheme is based on the NoHinge scheme proposed by Poulsen [15]. Poulsen's scheme is modified to incorporate a measure of rotation so that distinction can be made between a hinge undergoing rotation, and a diagonal member in tension.

The second scheme attempts to perform the 'post-processing step' of interpreting the final topology automatically during the optimization process. Since a one-node hinge is often interpreted as a thin beam, it seems reasonable to directly use beam finite elements in areas where one-node hinges or diagonal members occur.

5.5.1 Scheme I: A modified scheme based on NoHinge

The rotations at one-node hinges are usually large, and since rotations are computed at each node associated with Q4X elements, they present a natural measure to detect excessive rotations at suspect nodes.

However, since the rotations (and displacements) calculated at nodes surrounded by empty elements can be large, but are considered irrelevant, a density function is necessary to eliminate rotations and displacements calculated at these nodes. In the current scheme, the NoHinge method proposed by Poulsen [15] is used as an appropriate density function. Combining the scheme of Poulsen with a measure of rotation, results in a scheme which effectively detects and prevents checkerboarding and, in particular, one-node connected hinges. However, the new scheme is also capable of distinguishing between a one-node hinge and a *diagonal structural member* subjected to purely axial loads

Poulsen developed a local function h that efficiently detects one-node connected hinges. The scheme is a function of (the densities of) the four elements surrounding each interior node in the finite element mesh. His scheme makes use of the fact that a one-node hinge is not *quasi-monotonic* in density around a node.

Each local (non-negative) h function is simply summed, resulting in a global measure H which is added to the topology optimization problem as a single additional constraint. This scheme was shown by Poulsen to eliminate both one-node connected hinges and checkerboarding.

The local (density) function, h, which detects one-node connected hinges is defined as

$$h(a,b,c,d) = m(a,b,d) \cdot m(a,c,d) \cdot m(b,a,c) \cdot m(m,d,c), \tag{5.57}$$

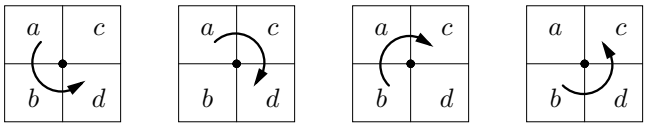

Figure 5.9: Four paths around node to check for quasi-monotonicity.

where a, b, c, d are the material density values in the elements surrounding the node, as indicated in Figure 5.9, and m is defined as

$$m(a, b, c) = |b - a| + |c - b| - |c - a|. \tag{5.58}$$

It is propsed here to modify this local function h, and to define a new funtion, denoted h', as follows

$$h'_{ij} = |\psi_{ij}| h_{ij}, \tag{5.59}$$

where i and j are pointers to the location of an interior node at row i and column j in the finite element mesh, and ψ_{ij} is the rotation at interior node i, j. For implementation in a gradient-based optimization environment, the absolute value function is replaced with a continuous approximation. For example, $|x|$ would be replaced by the approximate function A, where

$$A(x) = \sqrt{x^2 + \epsilon^2} - \epsilon, \tag{5.60}$$

where ϵ is an appropriately small number. The modified descriptor function H' based on the modified local function h' is therefore defined as

$$H'(\boldsymbol{\rho}) = \sum_{j=1}^{k-1} \sum_{i=1}^{l-1} h'(\rho_{i\ j}, \rho_{i+1\ j}, \rho_{i\ j+1}, \rho_{i+1\ j+1}, \psi_{ij}), \tag{5.61}$$

where k is the number for rows of elements and l is the number of element columns in the regular finite element mesh. As in the scheme of Poulsen, this modified descriptor function is added to the original topology optimization function as a single additional constraint function:

$$H'(\boldsymbol{\rho}) - \delta \leq 0, \tag{5.62}$$

where δ is a prescribed tolerance. Note that in applications where engineering materials are used, the rotations may be relatively small, and may therefore need to be scaled.

In (5.59), the sensitivity of each h_{ij} is given by Poulsen [15] and the sensitivities of each ψ_{ij} can be found using the adjoint method. A significant drawback of this method is therefore the additional computational effort required for sensitivity calculations. For each iteration (if no active set type strategy is used to minimize the computational cost) there are as many additional adjoint loads required as internal nodes.

5.5.2 Scheme II: A new scheme to improve checkerboard, one-node hinge and diagonal member modelling

In this section, the second of the two new schemes is presented. Instead of explicitly preventing the formation of checkerboard, one-node hinge and diagonal member layouts as before,

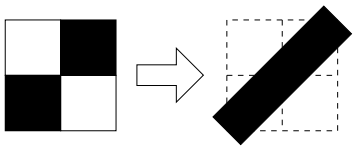

Figure 5.10: Post-processed interpretation of a 2×2 hinge.

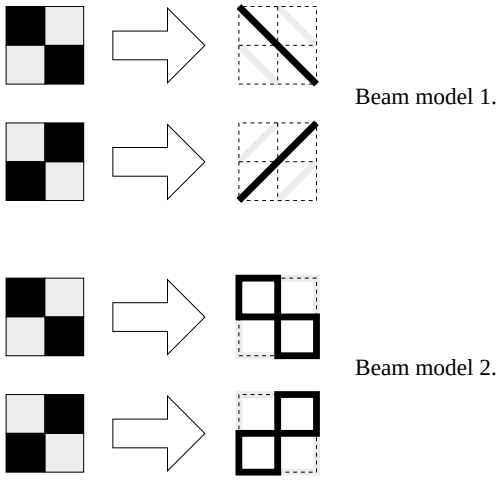

Figure 5.11: Two different beam models of a hinge.

this scheme aims at improving the finite element model of these layouts by replacing selected elements with a more representative beam model.

Traditional Q4 elements possess only translational DOFs and therefore combining beam elements and Q4 elements in a single model often calls for *ad hoc* modelling 'tricks', or the use of MPC's. Planar elements with drilling DOFs however, allow for the direct connection of beam and plane elements.

The use of beam elements in conjunction with elements with drilling DOFs, to improve the modelling of, in particular one-node hinges, is explored. We argue that instead of eliminating these layouts, an alternative is to use an improved finite element model.

The idea is therefore to replace undesirable 2-D planar element layouts with an equivalent beam model, which represents a reasonable post-processed or interpreted model of the original 2-D element layout. A reasonable interpretation of a one-node hinge is depicted in Figure 5.10. Note that the interpreted geometry preserves the volume of material in the original layout.

Herein however two possible beam models for representation of a one-node hinge are evaluated, as depicted in Figure 5.11. The first model replaces the planar elements with diagonal beams as suggested in Figure 5.10. In a second model, the planar elements are replaced with a box-like beam structure, similar to the 2-D element's layout. Although both are valid interpretations of a one-node hinge, the most natural and easiest to manufacture is the diagonal beam (beam model 1 in Figure 5.11).

The steps involved in the proposed strategy to automatically detect and replace problematic

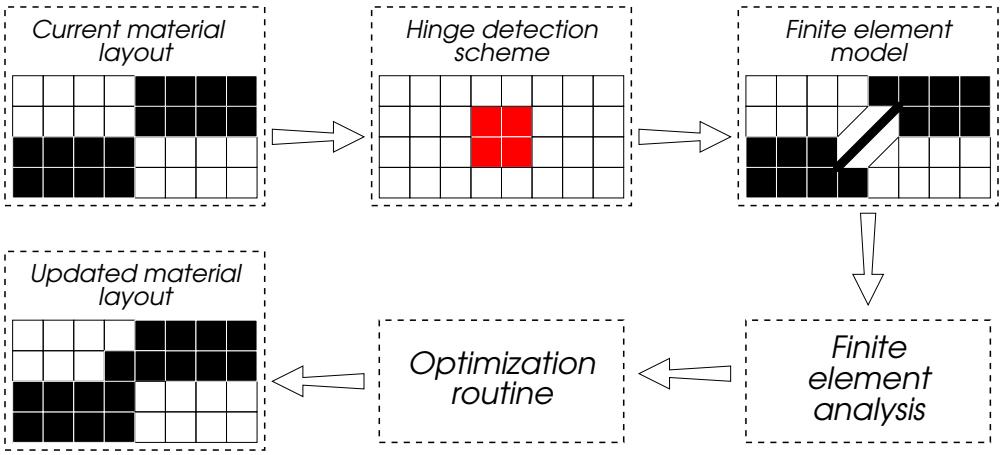

Figure 5.12: Beam replacement scheme.

planar elements by beam elements is schematically depicted in Figure 5.12. Firstly, it is assumed that the vector of design variables describing the material layout are arranged in a fixed grid, as is usually the case in topology optimization procedures. Next, possible hinges or diagonal members are identified, based solely on the material distribution. Then, depending on whether or not unsuitable material distributions are detected, selected planar elements are removed from the finite element model, and replaced with an equivalent beam model. This assembly of beam and planar finite elements is analysed using the finite element method, and the results passed to the optimization procedure. Finally, the optimization procedure makes a preciction of an improved material layout, and the process is repeated. If an updated design is predicted with no unsuitable material layouts, as is the case illustrated in Figure 5.12, planar elements are not replaced by beam elements, making the process of element replacement completely reversable.

The suggested process by which 2-D planar elements are replaced by their equivalent beam model, is similar to the way in which multiple materials have been used in topology optimization [106]. Instead of a second density measure however, a *function* which returns 1 if the beam model is to be used, and 0 if the planar element is appropriate, is used. This scalar function is denoted $\mathcal{H}$, with $0 \leq \mathcal{H} \leq 1$, and essentially indicates whether an element forms part of a one-node hinge or not. The elemental stiffness matrix, denoted $\boldsymbol{k}^e$, is accordingly calculated as

$$\boldsymbol{k}^e_{i,j} = \rho^p_{i,j}(\mathcal{H}_{i,j}\boldsymbol{k}^0_{\text{frame}} + (1 - \mathcal{H}_{i,j})\boldsymbol{k}^0_{\text{Q4X}}), \quad i = 1, 2, \ldots, N, \ j = 1, 2, \ldots, M, \tag{5.63}$$

where the subscript i, j denotes the i^{th} row and j^{th} column in a grid of elements with N rows and M columns. The density associated with the element is denoted $\rho_{i,j}$, while p is a penalty parameter used in the SIMP method. The beam and the 2-D planar element's stiffness matrices are denoted $\boldsymbol{k}^0_{\text{frame}}$ and $\boldsymbol{k}^0_{\text{Q4X}}$ respectively.

As a first step towards calculating $\mathcal{H}_{i,j}$, a local function to detect a one-node hinge at each interior node in the mesh is required. Our local function shall be denoted $\tilde{h}$ and uses the four orthogonal basis vectors $\boldsymbol{\phi}^k$, $k = 1, 2, 3, 4$, depicted in Figure 5.13 see [98]. The basis

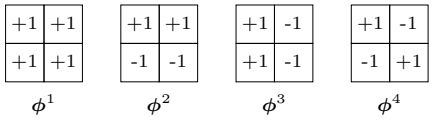

Figure 5.13: Orthogonal basis vectors.

vectors are given explicitly as

$$\begin{array}{rcrrrr} \boldsymbol{\phi}^1 & = & [1 & 1 & 1 & 1] \\ \boldsymbol{\phi}^2 & = & [1 & -1 & 1 & -1] \\ \boldsymbol{\phi}^3 & = & [1 & 1 & -1 & -1] \\ \boldsymbol{\phi}^4 & = & [1 & -1 & -1 & 1] \end{array} \tag{5.64}$$

where $\boldsymbol{\phi}^4$ represents the basis for a one-node hinge. A vector of element densities in a given patch of four elements at interior nodes i, j, is given by

$$\boldsymbol{v}_{i,j} = [\rho_{i,j} \quad \rho_{i+1,j} \quad \rho_{i,j+1} \quad \rho_{i+1,j+1}], \tag{5.65}$$

where the relationship between the elements and nodes is depicted in Figure 5.14. Now, the four components of the density vector $\boldsymbol{v}_{i,j}$ in each of the basis vector directions is given by the dot product of $\boldsymbol{v}_{i,j}$ with $\boldsymbol{\phi}^k$, $k = 1, 2, 3, 4$. In order to ensure only positive quantities in the calculation of the local $\tilde{h}$ function, the dot products are squared and the result denoted ζ^k, $k = 1, 2, 3, 4$:

$$\zeta^k_{i,j} = (\boldsymbol{v}_{i,j} \cdot \boldsymbol{\phi}^k)^2, \quad k = 1, 2, 3, 4. \tag{5.66}$$

The local scalar function to identify a one-node hinge for the four elements around interior node i, j is finally introduced as

$$\tilde{h}_{i,j} = \left(\frac{\zeta^4_{i,j}}{\zeta^1_{i,j}}\right)\left(1 - \frac{\zeta^2_{i,j}}{\zeta^1_{i,j}}\right)\left(1 - \frac{\zeta^3_{i,j}}{\zeta^1_{i,j}}\right). \tag{5.67}$$

It is clear from this function that $0 \leq \tilde{h}_{i,j} \leq 1$. Poulsen [15] defined a similar function (NoHinge) using the nonmonotonic behaviour of a one-node hinge around a given node, see equation (5.57). Unfortunately his function decreases sharply as the density of the elements decrease. Our new function effectively detects one-node hinges even when made up of elements with intermediate density. Incidentally, Rozvany [99] independently suggested a number of different functions to overcome the problems associated with Poulsen's function.

As depicted in Figure 5.14, an arbitrary interior element i, j can be involved in four different local $\tilde{h}$ functions, any of which could be a potential one-node hinge. A vector of local functions to which element i, j contributes, is defined as

$$\boldsymbol{H}_{i,j} = \left[\tilde{h}_{i-1,j-1} \quad \tilde{h}_{i,j-1} \quad \tilde{h}_{i-1,j} \quad \tilde{h}_{i,j}\right]. \tag{5.68}$$

Special attention is now required for boundary elements. For example, considering an element in the 1st row and 1st column, the functions $\tilde{h}_{0,0}$, $\tilde{h}_{1,0}$ and $\tilde{h}_{0,1}$ do not exist. Each local $\tilde{h}$ in (5.68) is therefore defined by

$$\tilde{h}_{k,l} = \begin{cases} \tilde{h}_{k,l} & \text{if } h_{k,l} \text{ exists, and} \\ \emptyset & \text{otherwise} \end{cases} \tag{5.69}$$

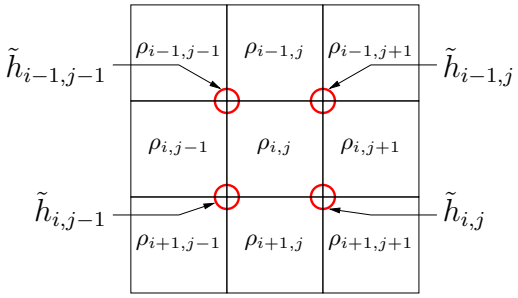

Figure 5.14: Patch of nine elements around element i, j.

where $\emptyset$ denotes an empty set. So, for example, $\boldsymbol{H}_{1,1} = \begin{bmatrix} \emptyset & \emptyset & \emptyset & \tilde{h}_{1,1} \end{bmatrix} = \begin{bmatrix} \tilde{h}_{1,1} \end{bmatrix}$. The measure quantifying whether element i, j takes part in a one-node hinge or not, may now simply be defined as the maximum term in the $\boldsymbol{H}_{i,j}$ vector (5.68).

$$\mathcal{H}_{i,j} = ||\boldsymbol{H}_{i,j}||_{\infty}. \tag{5.70}$$

Note that $\mathcal{H}_{i,j}$ is a function of only the four element densities defining the maximum local $\tilde{h}$ function.

As illustrated in Figure 5.11, beam model 1 is dependant on the orientation of the element densities. Therefore, once each element's $\mathcal{H}_{i,j}$ has been calculated, the orientation of the beam model needs to be determined. To decide which of the two diagonal beams is more appropriate, the sign of $(\boldsymbol{v}_{i,j} \cdot \boldsymbol{\phi}^4)$ can be used. Beam model 2 is not dependant on the arrangement of the elements.

A possible complication in an optimization environment is the discontinuous nature of $\mathcal{H}_{i,j}$. In order to alleviate this discontinuity, the infinity norm in (5.70) is approximated by a continuous function. A p-norm is not appropriate since values of $\mathcal{H} > 1$ should be avoided, and the p-norm converges to the infinity norm from above for $p \geq 1$. The function

$$\hat{\mathcal{H}}_{i,j} = \frac{(||\boldsymbol{H}_{i,j}||_2)^2}{||\boldsymbol{H}_{i,j}||_1}, \tag{5.71}$$

satisfies our requirements. $\hat{\mathcal{H}}_{i,j}$, is a function of all 9 elements depicted in Figure 5.14. For this reason the orientation of a diagonal beam model (beam model 1 in Figure 5.11) cannot easily be determined. Therefore, only the box-like model (beam model 2 in Figure 5.11) will be used for this measure. Finally, in order to prevent $||\boldsymbol{H}_{i,j}||_1$ from becoming zero, a small perturbation on the $\tilde{h}$ functions is necessary, therefore $\epsilon \ll 1$ is added to (5.67).

5.6 Numerical examples and applications

In this section, the merits of the two newly introduced scheme are evaluated using the test problems introducted in Section 5.4.

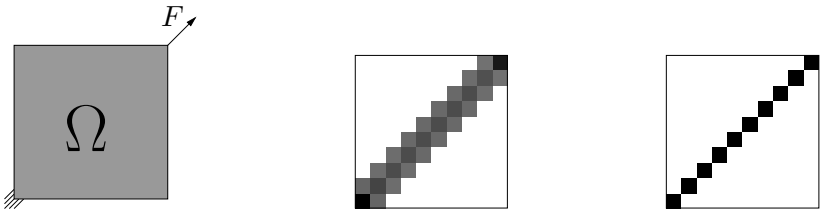

(a) (b) (c)

Figure 5.15: Illustration of the effect of the proposed scheme to overcome one-node hinges: (a) The design problem, (b) optimal design using the scheme of Poulsen, (c) optimal design using the proposed scheme.

5.6.1 Application of Scheme I

A potential drawback of the original scheme of Poulsen is the possibility of undue penalization of an optimal design. An example of this situation is depicted in Figure 5.15, where the square design domain is discretized into a 10×10 mesh, with loads and constraints as depicted, and a prescribed volume fraction of $v^* = 0.1$. Although this design problem is probably not practically significant, a similar situation could occur locally in topology optimization problems, especially if a coarse discretization is used.

Figure 5.15(a) depicts the design problem. Figure 5.15(b) depicts the optimal design found using the scheme of Poulsen, in which one-node hinges are prevented, and unduly penalized. Figure 5.15(c) depicts the optimal design using the modified scheme proposed herein (Scheme I), in which the local functions h' are expressed in terms of the absolute value of rotation at the applicable node. In so-doing only those one-node hinges that actually act as hinges (viz. associated with large rotations) are avoided. For the simple problem depicted in Figure 5.15, zero rotations arise due to the applied load. Therefore no penalization is required or enforced.

For this problem the optimal topology using the original scheme of Poulsen has to violate either the volume constraint or the additional constraint imposed by NoHinge. For the modified scheme, since zero rotation is induced along the diagonal, both the volume constraint and the constraint on H' can be satisfied exactly.

Figure 5.16 depicts the application of the original scheme of Poulsen [15] and our modified scheme suggested herein to the force inverter compliant mechanism with a 48×48 mesh and volume constraint $v^* = 0.3$. A reference solution was presented in Figure 5.6 illustrating the formation of one-node connected hinges. The stronger penalization of one-node hinges with large rotations (enlarged view Figure 5.16(b)) which is induced with the modified method, forces the density distribution around the hinge towards relatively large areas with intermediate densities, as compared to the original scheme of Poulsen (Figure 5.16(a)). Having said that, both solutions can be accommodated in a post-processing step and are quite similar.

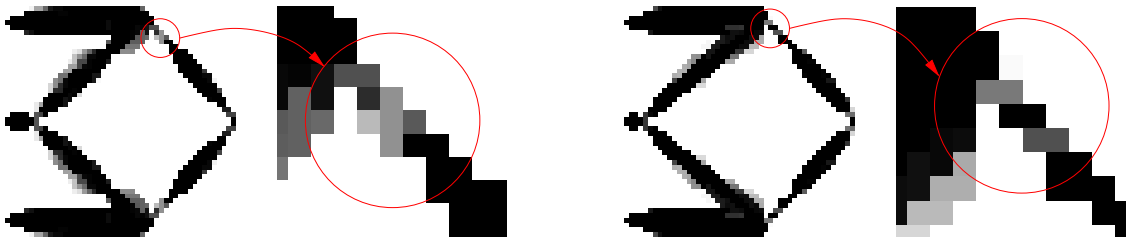

(a) (b) (c) (d)

Figure 5.16: Application of different filters to the force inverter: (a) optimal design using new method, (b) enlarged view of potential hinge, (c) optimal design using original method of Poulsen [15], (d) enlarged view of potential hinge.

5.6.2 Application of Scheme II

In this section the second scheme (Scheme II) is firstly validated on a number of benchmark problems to determine the modelling accuracy. Thereafter, the scheme is used in a topology optimization infrastructure to solve the popular MBB beam problem, and finally the compliant mirror scanning device.

Numerical accuracy benchmark problems

In an attempt to determine the applicability of this new method, some accuracy benchmarking evaluations of the alternative finite element models are conducted. In the tables to follow, results for both measures $\mathcal{H}$ (calculated in (5.70)) and $\hat{\mathcal{H}}$ (from (5.71)) are presented. 'Beam 1' refers to the diagonal beam model, denoted beam model 1 in Figure 5.11. 'Beam 2' refers to the box-like beam model, labeled beam model 2 in Figure 5.11. Considering the box-like beam representation (Beam 2), the ratio of horizontal to vertical beam element heights is equal to the aspect ratio of the 2-D element. In the presentation of the results, Q4 is used to denote the results employing traditional planar elements *without* drilling DOFs, whereas Q4X identifies results for planar elements *with* drilling DOFs. Furthermore, V refers to the volume of the beam representation and V^0 to the volume of the original 2-D element. To determine the sensitivity of the scheme to beam thickness, beam representations with two different volumes, namely $V = V^0$ and $V = 2V^0$, will be evaluated.

The first test problem, used to benchmark the modelling accuracy, is depicted in Figure 5.17(a) with the applied load as shown. It represents a square domain modelled with $(n+1)\times(n+1)$ square elements, and an $n\times n$ diagonal member. The black elements in the figure are solid ($\rho = 1$) while all other elements are void and have a density of $\rho = \rho_{\min} = 10^{-3}$. A penalty parameter of $p = 3$ in (5.63), is used. The displacements calculated with the various elements are normalized with respect to a finite element analysis, using a refined mesh, of the post-processed geometry shown in Figure 5.17(a).

Table 5.1 presents the normalized tip displacements of a diagonal member subject to the load in Figure 5.17(a), using various elements, and for different mesh refinements. For this problem the model employing diagonal beam elements (Beam 1) is relatively accurate, even

	n=2	n=4	n=8	n=16
$\mathcal{H}$, Beam1, $V{=}V^0$	1.6265	1.3203	1.1602	1.0811
$\mathcal{H}$, Beam2, $V{=}V^0$	1.9217	2.9930	3.5756	3.8807
$\mathcal{H}$, Beam2, $V{=}2V^0$	0.30913	0.44165	0.51366	0.55126
$\hat{\mathcal{H}}$, Beam2, $V{=}V^0$	1.8674	2.9192	3.5131	3.8309
$\hat{\mathcal{H}}$, Beam2, $V{=}2V^0$	0.32815	0.46079	0.52669	0.55927
Q4X	5.9252	3.4241	2.2835	1.9220
Q4	$8.4119{\times}10^6$	$2.2008{\times}10^6$	$4.2153{\times}10^5$	$7.0902{\times}10^4$

Table 5.1: Normalised tip displacement of a diagonal member.

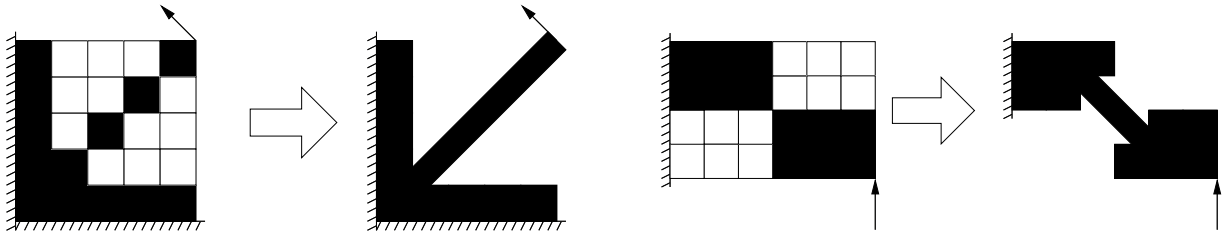

(a) (b)

Figure 5.17: Modelling accuracy benchmark problems: (a) Diagonal member, (b) one-node hinge.

for the extreme case of a diagonal member with only two elements ($n = 2$). The results indicate that the box beam section with the same volume as the original element ($V = V^0$) over-predicts the displacement, while a box section with twice the original volume ($V = 2V^0$) is too stiff. Similar results for both functions $\mathcal{H}$ and $\hat{\mathcal{H}}$ employing the box-like beam model (Beam 2) are calculated. Finally, the diagonal member modeled with Q4X elements, is not sufficiently accurate to approximate the interpreted geometry. Q4 elements, possess no stiffness in this configuration, with only the void elements preventing the singularity.

Table 5.2 presents the results of modelling the one-node hinge depicted in Figure 5.17(b), for the load shown. The first column presents the normalised vertical displacement of the node

	$n_{\text{bisect}}{=}0$	$n_{\text{bisect}}{=}1$	$n_{\text{bisect}}{=}2$	$n_{\text{bisect}}{=}3$
$\mathcal{H}$, Beam1, $V{=}V^0$	2.6086	2.3400	2.2747	2.2719
$\mathcal{H}$, Beam2, $V{=}V^0$	2.3251	2.4760	2.5342	2.5440
$\mathcal{H}$, Beam2, $V{=}2V^0$	0.43379	0.41329	0.40839	0.40584
$\hat{\mathcal{H}}$, Beam2, $V{=}V^0$	2.3177	2.4684	2.5263	2.5362
$\hat{\mathcal{H}}$, Beam2, $V{=}2V^0$	0.43525	0.41499	0.41011	0.40756
Q4X	2.9994	2.7231	2.7123	2.7202
Q4	$3.5400{\times}10^6$	$1.0266{\times}10^6$	$2.6914{\times}10^5$	$6.8014{\times}10^4$

Table 5.2: Normalised displacement of a one-node hinge.

	Formulation 1	Formulation 2	Formulation 3
Q4	3.7718×10^{-3}	4.1903×10^{-4}	4.1904×10^{-4}
Q4X	1.9901×10^{-4}	2.6926×10^{-4}	2.7286×10^{-4}
$\hat{\mathcal{H}}$, Beam2, $V{=}2V^0$	5.1435×10^{-5}	1.1554×10^{-4}	1.1136×10^{-4}

Table 5.3: Output displacement of optimal mirror mechanisms.

to which the load is applied, using the discretization shown in the figure. Results are then presented for the number of mesh bisections of the original mesh given by n_{bisect}. Results are again normalized with respect to a detailed finite element analysis of the post-processed geometry depicted in Figure 5.17(b).

For this problem, the model employing diagonal beams (Beam 1) is relatively inaccurate when compared to the previous test problem. Again the model employing the box-like beam model over-predicts the displacement if the volume of the original 2-D element is conserved and is too stiff if the beam representation's volume is doubled. In this case, the model simply using elements with drilling DOFs (Q4X) predicts a similar displacement to the model containing the diagonal beam element. Again, the Q4 elements possess very little stiffness for this bending-dominated load.

Finally, the new scheme is used to re-evaluate the optimal topologies (of the mirror scanning device) presented in Section 5.4.4. For brevity, only the results of the box-like beam model with twice the 2-D element's volume is presented in Table 5.3. The Q4X elements, which have been shown in the benchmark problems to under-predict the stiffness of the interpreted design, produce substantially lower output displacements than the original model with Q4 elements. This is especially true for the design resulting from optimization Formulation 1. Notably, the beam model employed here severely penalizes the working of the mechanism, containing one-node hinges and therefore seems a promising method to penalise the formation of one-node hinges in topology optimization results.

Topology optimization implementation

The developed scheme is now used in a topology optimization infrastructure. The first benchmark topology optimization test problem is the well known MBB beam, detailed in Section 5.4.1. Exploiting the symmetry of the problem, only half the beam is modelled.

Figure 5.18(a) depicts the results using Q4 elements with no filters or other devices. The checkerboarding problem is clearly illustrated. In Figure 5.18(b) the checkerboard layout is eliminated using the filter of Sigmund [100] with a filter radius of 1.2 element lengths. Figures 5.18(c) to 5.18(e) show the results using the proposed scheme with various beam element models. From these figures, it is apparent that the beam models are sufficiently flexible to alleviate checkerboard layouts. Moreover, the results achieved using the new scheme are also far less defuse than results computed using filtering.

Finally, the new scheme is applied in the design of the mirror mechanism discussed in Section 5.4.4. The optimization is performed for the second problem formulation (Formulation 2 in Section 5.4.4). The optimal topology in this case, depicted in Figure 5.19, closely resem-

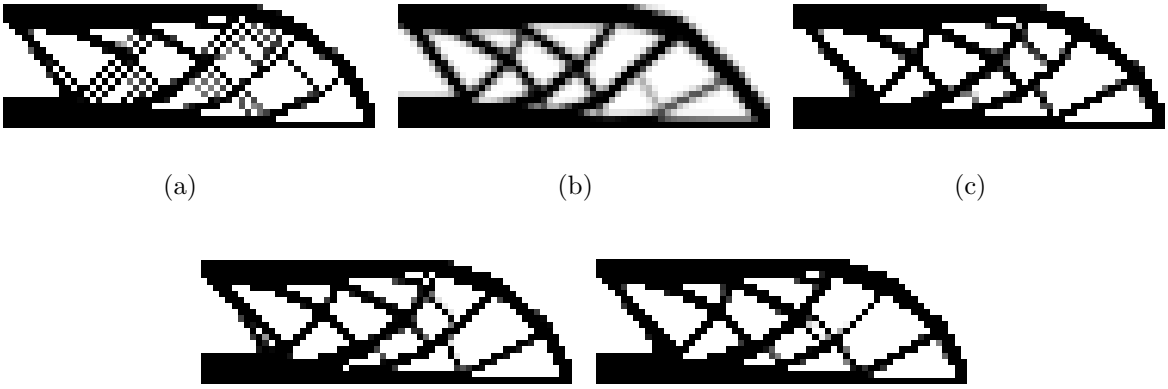

Figure 5.18: MBB beam solutions using: (a) Q4 elements, (b) Q4 with filter of Sigmund, (c) $\hat{\mathcal{H}}$, Beam2, $V{=}V^0$, (d) $\hat{\mathcal{H}}$, Beam2, $V{=}2V^0$, (e) $\hat{\mathcal{H}}$, Beam1, $V{=}V^0$.

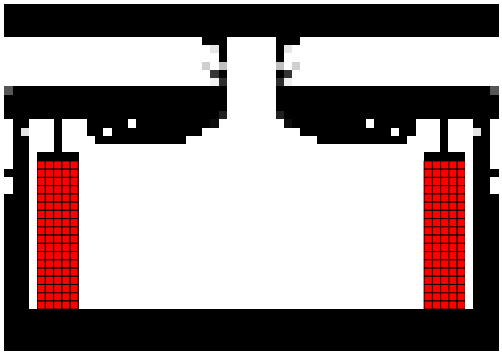

Figure 5.19: Mirror mechanism design using new scheme, $\hat{\mathcal{H}}$, Beam2, $V{=}2V^0$.

bles the starting design, and is quite different from the results achieved with Q4 elements and standard filtering techniques, see Figure 5.8(b). Notably, one-node hinges have been sufficiently 'stiffened' such that their existence is practically infeasible.

Upon further investigation, no feasible discrete (0-1) solution has been found for this specific discretization, despite extensive numerical experimentation. That is to say, the required displacement can only be achieved by inclusion of one-node connected hinges or by the introduction of elements with intermediate desities.

Therefore the prediction from the initial topology optimization study, suggesting that a 0.5mm displacement is attainable with 1mm thick hinges is misleading since the unrealistic flexiblity of one-node hinges are exploited to achieve this displacement.

The optimal design using the scheme suggested herein (depicted in Figure 5.19), rather compromises on the hinge densities to achieve the required flexibility, indicating that thinner hinges are required. The suggestion is therefore that a finer mesh is required in order to allow for thinner hinges.

5.6.3 Discussion of results

Our two proposed schemes have been applied to solve a number of topology optimization problems. The first scheme, Scheme I, based on the NoHinge method of Poulsen, was shown to clearly distinguish between diagonal members subjected to axial loads and hinges undergoing rotation. However, when applied to practical topology optimization problems, such as the force inverter problem, results closely resemble those of the NoHinge scheme. A significant drawback of our method is the additional adjoint loads required for the constraint sensitivity calculations.

Considering the second scheme, Scheme II, the results of the benchmark accuracy evaluations emphasize that the direct connection between a beam element to a *single* node of a planar element (with drilling DOFs) should be avoided since moments cannot accurately be transfered. Such a situation occurs in the case of the diagonal beam model (denoted Beam model 1 in Figure 5.11), and the unpredictable behaviour is illustrated by the difference in accuracy of the results presented in Tables 5.1 and 5.2.

A preferable situation occurs in the case of the box-like structure (Beam model 2 in Figure 5.11) since this structure allows for the transmission of moments from the beam representation to the 2-D elements predictably. However this beam representation does not accurately predict the displacement of the favoured interpretation of a hinge depicted in Figure 5.10. It is worthwhile noting however, that the accuracy of the box-like beam model would be considerably better if a comparison with respect to a box-like post-processed design were carried out. However, the manufacture of such a structure would be more complex than than the diagonal beam-type interpretation. Some work is therefore still required to develop an improved beam model which accurately predicts the response of the post-processed one-node hinge (depicted in Figure 5.10).

Nevertheless this scheme remains a promising alternative to filtering methods. It is demonstrated that this scheme effectively 'softens' checkerboard layouts preventing their formation. Furthermore, one-node connected hinges are shown to be sufficiently 'stiffened' such that their formation is infeasible in compliant mechanism design problems. An additional salient feature of this scheme applied in a topology optimization environment, is that it does not require any additional constraints and therefore optimality criteria methods can be used to solve simple minimum compliance problems. What is more, unlike topology optimization performed with a ground structure of beam elements, the majority of the resulting design using this method, is continuous.

5.7 Conclusions

In this chapter the benefits of using membrane finite elements with drilling degrees of freedom (DOFs) in topology optimization applications has been demonstrated. These elements increase numerical accuracy and analysis capability, while not excessively increasing the computational effort.

Although a detailed study of the checkerboarding instability is carried out in Chapter 7, it is shown here, via numerical experiments, that employing these elements significantly reduces

the amount of checkerboarding obtained in optimal topologies.

In addition, elements with drilling DOFs present a natural way of detecting and/or penalizing one-node connected hinges and diagonal members. Alternatively, they can be used to improve on the numerical modelling of one-node hinges and diagonal members. Two new schemes to treat these material layouts have been suggested, exploiting drilling DOFs.

The first scheme is based on NoHinge, a scheme originally proposed by Poulsen [15]. Our modified scheme however, uses the rotations computed at internal nodes to distinguish between material layouts which are behaving as a hinge (rotating) and a diagonal structural member subjected to axial loads. This scheme however, requires a somewhat numerically expensive constraint sensitivity computation, and its practical application is therefore somewhat limited.

A second scheme to model a one-node hinge, such that the computed response is similar to a reasonable interpretation of the material layout, is presented. A function has been developed which indicates whether or not an element takes part in a layout with unsuitable numerical representation. Thereafter, selected elements are replaced by an equivalent beam model which is numerically better behaved. Since this process is dictated by the material distribution at each iteration, it is reversible so that planar elements which have formerly been replaced by beam elements, may again become planar elements and *vice versa*. Using this new method, it has been demonstrated that it is relatively easy to stiffen a one-node hinge in compliant mechanism design (or soften checkerboard layouts), thereby preventing their formation.

Finally, topology optimization has been employed in the design of a mirror scanning device, employing three different problem formulations. The first seeks to simply maximize the output rotation, while the other two maximize some measure of stiffness subject to a required output rotation being maintained. Each of the resulting optimal topologies, computed using standard Q4 elements and filtering techniques, contain a number one-node hinges and are therefore not acceptable. The most promising scheme (Scheme II) has therefore finally been applied in the design of the device. The design employing our new scheme effectively penalized one-node hinges in critical areas, thereby preventing their formation.

Chapter 6

Effect of element formulation on membrane, plate and shell topology optimization problems

6.1 Summary

In this chapter the effects of membrane, plate and flat shell finite element formulations on optimal topologies are investigated. Two membrane components are considered. The first is a standard 4-node bilinear quadrilateral with only two translational degrees of freedom per node. The other is a 4-node element with three degrees of freedom per node, which properly accounts for in-plane (drilling) rotations. Plate elements selected for evaluation include Discrete Kirchhoff Quadrilateral (DKQ) elements as well as two Mindlin-Reissner based elements, one employing Selective Reduced Integration (SRI), and the other an Assumed Natural Strain (ANS) formulation, to overcome transverse shear locking. The flat shell elements studied, consist of an assemblage of these membrane and plate components.

Since DKQ elements are shear rigid, they are only well suited to thin plate problems. Mindlin-Reissner based elements, on the other hand, are shear flexible and may therefore be used in the analysis of thin to moderately thick plate problems. For popular benchmark topology optimization plate problems, both Mindlin-Reissner elements are shown to recover thin plate results computed using DKQ elements. However, a new benchmark problem is introduced to illustrate the deficiencies of Mindlin-Reissner elements, employing SRI on transverse shear terms, without hourglass control. On the other hand, elements with an ANS formulation are shown to be stable and robust.

For membrane and shell problems, elements which properly account for in-plane rotations are shown to be insensitive to the penalty parameter which enforces the relationship between in-plane rotations and displacements. Conversely, it is illustrated that a simple, but *ad hoc*, treatment of drilling degrees of freedom for standard bilinear membrane elements is sensitive to the introduced parameter for a number of popular shell problems. A benchmark problem which further highlights this sensitivity, in the form of a pretwisted beam, is also introduced.

6.2 Introduction

Due to the competitive nature of industry, designers are increasingly expected to produce optimal, or near optimal, designs. What is more, they are expected to do so rapidly to ensure that superior products are launched timeously. This, in part, explains the recent significant attention that structural optimization has received from research institutes and industry alike.

The advent of inexpensive computers, capable of performing complex calculations extremely quickly, has made it feasible to optimize even complex nonlinear structures with reasonable discretization. Structural optimization could therefore in future (and of course within reason), largely automate the design process and deliver optimal solutions, making what is now mostly a trial-and-error design improvement strategy redundant.

Sizing and shape optimization rely on the engineer or designer's judgment and experience to select an acceptably good starting design, since in both cases the topology is fixed throughout. Topology optimization is seen as particularly powerful since it is capable of exploring different topologies during the optimization process. Topology optimization can therefore generate optimal, sometimes unintuitive designs while simultaneously generating the optimal shape.

Topology optimization has been receiving unprecedented attention of late. This is particularly evident at specialized structural and multidisciplinary optimization meetings, such as the recent WCSMO6 congress held in Rio de Janeiro, Brazil, where topology optimization drew significant attention. All this research effort has led to many advances in topology optimization, especially in the types of problems which can now be addressed.

The recent revival of interest is largely credited the early paper of Bendsøe and Kikuchi [107] who employed homogenization techniques to perform generalized shape optimization. Even before this, a pivotal role was played by the problem of variable thickness plate design, see for example the original work of Cheng and Olhoff [108].

In this work the popular SIMP (Simple Isotropic Material with Penalization) material parameterization is employed in order to demonstrate the effect of element selection in topology optimization. Bendsøe [109] is largely credited for the introduction of the SIMP material model, which was independently derived by Zhou and Rozvany [110] and Rozvany *et al.* [111].

Special attention is paid to plate and shell problems in this chapter. It is therefore appropriate to give some background on topology optimization of plate and shell problems at this point. There has been a plethora of work in this field, so this is by no means an exhaustive review of all work done. A more thorough review can be found in, for example the book of Bendsøe and Sigmund [4].

Tenek and Hagiwara [112] employed homogenization techniques to generate optimal isotropic single layer and multilayer anisotropic plate topologies. They minimize the structural strain energy subject to a volume constraint, employing sequential linear programming to solve the optimization problem. The finite elements used in their work are based on Mindlin-Reissner plate theory, and are four noded bilinear quadrilateral elements with only 5 degrees of freedom (DOFs) per node (the in-plane rotation is omitted since only flat problems are

considered).

Their work was extended by Tenek and Hagiwara [113] so that the topology optimization of plates, as well as single and doubly curved shell structures are considered. Again, strain energy was minimized subject to a volume constraint. Both homogenization as well as optimal thickness distribution problems are considered. Again, simple four noded quadrilateral elements with 5 DOFs per node were employed with Selective Reduced Integration (SRI) to alleviate shear locking. They rely on the cubic relation between element stiffness and element thickness in bending to prevent intermediate densities.

There are of course numerous other authors who have used homogenization methods to solve topology optimization problems for plate and shell structures, for example see Díaz *et al.* [114], Krog and Olhoff [115], or see Bendsøe and Sigmund [4] for a more complete list of references.

Recently Hinton and co-workers [116, 117] have addressed the topology optimization problem of plate and shell structures using SIMP-like material models. A resizing algorithm based on Optimality Criteria (OC) methods is used to perform the iterative optimization. The Mindlin-Reissner based element used in their work is detailed in [118], and employs SRI on shear terms to overcome transverse shear locking. Since then SIMP-like material parameterizations have become very popular in this type of problem, see for example Pedersen [119], Jog [120] (who incidentally implement the MITC4 and MITC9 elements of Bathe and co-workers [16]) and Stegmann and Lund [121], who also use MITC elements.

Other interesting developments include simultaneous shape and topology optimization as performed by Ansola *et al.* [1, 2] and the hybrid (Homogenization-Evolutionary) method developed by the ADOPT group, see for example [122, 123, 124] which has been used in static and vibration problems of plate and shell structures.

Meanwhile, many advances have been made in finite element technology, which have a direct bearing on topology optimization, since most of the applications in topology optimization employ the finite element method as an analysis tool. Often, however, little attention is paid to the actual finite element formulation in the application. In this chapter, the abilities of the more sophisticated finite element formulations are leveraged in a topology optimization setting.

Element selection is an important part of finite element analysis, relying on the experience of the analyst to select a suitable element type. There are several different models for physical structural elements, e.g. beam, two dimensional planar, plate and shell, or solid models. Each of these models may have several different formulations, e.g. displacement-based, hybrid and mixed formulations, etc. perhaps with various interpolations or other mechanisms to improve element accuracy.

In this chapter, flat shell finite elements as an assembly of plate and membrane elements are considered. These elements can only be effective if the membrane and plate components are independently accurate and robust. To illustrate this point, it is demonstrated that the use of dubious, ad-hoc treatments of, in particular in-plane rotations and methods to overcome shear locking could lead to misleading ‘optimal’ topologies.

Flat shell elements are simpler than generally curved shell elements, both in terms of formu-

lation and computer implementation. Since the element Jacobian matrix is constant through the thickness, analytical through thickness integration is possible. Furthermore, in flat shell elements the inclusion of drilling DOFs is straightforward and, if required, element out of plane warp can be handled on the element level with the aid of warp corrections to the nodal DOFs.

Flat shell elements generally allow for 6 DOFs per node, two in-plane displacements and one in-plane rotation (membrane contributions) and the remaining two out of plane rotations and single out of plane displacement (plate bending components). The membrane component of a the flat shell element is considered first.

In general, membrane elements only require two displacement DOFs per node to adequately describe the kinematics. However, in membrane and shell elements, the additional rotational DOFs are highly desirable. They allow for the modeling of, for instance, folded plates and beam-slab intersections. Due to the enriched displacement field, these elements are also significantly more accurate than their counterparts with translational DOFs only [21]. For bending dominated problems for example, drilling DOFs enhance the accuracy of 4-node elements to a level comparable to that of 8- or 9-node elements, while the 4-node element with translational DOFs only (Q4) is notoriously inaccurate. Since provision is generally made for the in-plane rotation, regardless of how it is derived, including drilling DOFs in flat shell element formulations is largely (numerically) free of charge. Further detail regarding these elements can be found in Chapters 2 and 3.

As a flat shell element is constituted of membrane and plate components a suitable plate component is also crucial to the formulation. Successful quadrilateral isotropic plate and shell elements are mostly based on discrete Kirchhoff-Love theory (e.g. the Discrete Kirchhoff Quadrilateral (DKQ) [125]) or first order shear deformation theory of Mindlin-Reissner. The discrete Kirchhoff-Love theory allows only for shear rigid formulation and existence of the integral expressions of the stiffness matrices requires C^1 continuity of interpolation functions. The Mindlin-Reissner theory includes shear deformation and only C^0 continuity of the shape functions is required. For a large range of engineering problems, especially layered composites, exclusion of shear deformation leads to unacceptable results and the Mindlin-Reissner plate formulation is preferred.

However, 4-node displacement-based plate elements derived from Mindlin-Reissner theory are prone to severe locking associated with the transverse shear deformation and therefore require modifications in the finite element interpolation to alleviate this shear locking. Shear locking was overcome in a number of elements through the use of reduced or Selective Reduced Integration (SRI) schemes. For 4-node plate bending elements, these integration schemes, however, result in the appearance of spurious zero energy modes. A number of elements with stabilization methods [89] overcome this problem, however these elements generally require adjustable parameters.

Although these elements are reported to be highly accurate, alternative methods such as assumed strain or mixed methods are based on variational principles and are theoretically better founded. A number of elements based on Mindlin-Reissner theory exist. They differ mainly with respect to the assumptions in the finite element interpolation or in the handling of kinematic locking phenomena. One of the most efficient element formulations appears to

be the Assumed Natural Strain (ANS) formulation of Bathe and Dvorkin [126, 127], which has some similarities to the elements proposed by MacNeal [128] and Hughes and Tezduyar [129], and are also known as MITCn (Mixed Interpolation of Tensorial Components) elements, with n the number of nodes.

In this work it is illustrated that, for the SIMP method, Kirchhoff and Mindlin-Reissner based elements result in different topologies for thick plate problems. SRI, as a method to overcome shear locking, is also analyzed and compared to an ANS formulation. Finally, an investigation of the effect of drilling DOFs in membrane and shell elements is reported on.

In the longer term, the aim is to suggest suitable element formulations for work in piezoelectric actuators, to be used in micropositioning applications[1]. We should, nonetheless be mindful of the dangers inherent in the linear assumption [130] in plate and shell formulations, and its effect in topology optimization [121]. However since micropositioning applications with extremely small displacements are of interest, the linear assumption is applicable here. Ultimately this research is to be used for the selection of suitable piezoelectric finite element formulations for topological optimization applications, similar to those in for example [131].

This chapter is set out as follows: In Section 6.3 a discussion of the topology optimization problem formulation, and the material parameterization used, is briefly presented. In Section 6.4 a short summary of the finite element formulations used in this work are offered. Section 6.5 presents the findings of the numerical experiments carried out on membrane, plate and shell problems. Finally, some concluding remarks are presented in Section 6.6.

6.3 Topology optimization problem formulation

In this section, a discussion of the topology optimization formulation used for evaluation, is briefly presented. Minimum compliance membrane, plate and shell problems are specifically focused on. Some details of the material parameterization of multilayer designs are given. Also presented is a very short description of the optimality criteria based updating scheme employed, as well as the filtering strategy employed to address the mesh dependency problem.

6.3.1 Material parameterization

The discretized finite element model is parameterized using the popular Simple Isotropic Material with Penalization (SIMP) method [4], in which material properties are scaled with an artificial density parameter ρ, as will be detailed in this section. As a simple example, the elastic modulus is parameterized as

$$E = \rho^p E^0, \tag{6.1}$$

where ρ is an artificial density parameter with $0 \leq \rho \leq 1$ and p (usually $1 < p \leq 6$) is a penalty exponent which renders intermediate densities uneconomical, encouraging the design to a discrete solution. Finally, E is the modified (parameterized) modulus of elasticity of a region with artificial density ρ. The materials actual elastic modulus is given by E^0.

[1] However, for the time being, only linear elastic finite element formulations are considered.

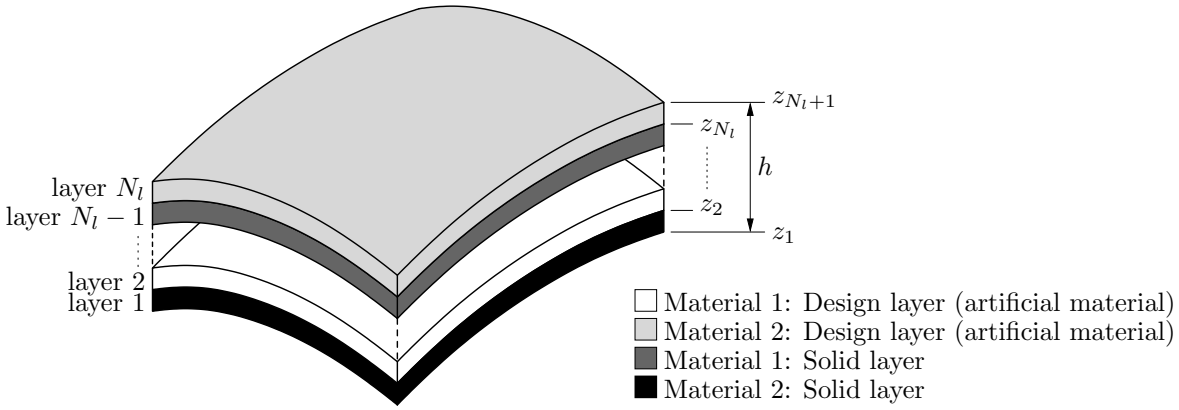

Figure 6.1: A schematic representation of a general material layup for topology optimization problems.

As in Lee *et al.* [116] and Stegmann and Lund [121] numerical experiments with multilayer shell models are performed. Perforated plates and shells as well as reinforcement, honeycomb or general multilayer structures are therefore allowed for. Only layups of isotropic materials are considered, although extension to orthotropic materials with constant [121] or variable [132] material coordinates is also possible.

Perfect bonding between adjacent layers is assumed, allowing for the use of a single element through the thickness. Although the same material is used for each layer, material properties can of course vary due to layerwise artificial density variations. The constitutive relations are computed using classical laminate theory by analytical through the thickness integration.

For the isotropic materials used in this study, the stress resultant form of the constitutive equations can be calculated by pre-integration through the thickness. Thus for for a laminate of thickness h with N_l layers, the relations between the stress resultants and strains for multilayer shells can be expressed as [116]

$$\begin{Bmatrix} \boldsymbol{N} \\ \boldsymbol{M} \\ \boldsymbol{Q} \end{Bmatrix} = \begin{bmatrix} \boldsymbol{\mathcal{A}}(\rho) & \boldsymbol{\mathcal{B}}(\rho) & \mathbf{0} \\ \boldsymbol{\mathcal{B}}(\rho) & \boldsymbol{\mathcal{D}}(\rho) & \mathbf{0} \\ \mathbf{0} & \mathbf{0} & \boldsymbol{\mathcal{G}}(\rho) \end{bmatrix} \begin{Bmatrix} \boldsymbol{\epsilon}_{\mathrm{m}} \\ \boldsymbol{\kappa} \\ \boldsymbol{\gamma} \end{Bmatrix}, \tag{6.2}$$

where $\boldsymbol{\epsilon}_{\mathrm{m}}$, $\boldsymbol{\kappa}$ and $\boldsymbol{\gamma}$ are the membrane, bending and transverse shear strains respectively and $\boldsymbol{N}$, $\boldsymbol{M}$ and $\boldsymbol{Q}$ are the corresponding stress resultants.

Figure 6.1 schematically shows the problem considered. Although an identical material for each layer is used, the general case in which each layers material type may vary, even without artificial density effects, is presented. Specifically, the submatrices in (6.2) are calculated for each element as:

Membrane stiffness:

$$\boldsymbol{\mathcal{A}}(\boldsymbol{\rho}) = \int_{-\frac{h}{2}}^{\frac{h}{2}} \boldsymbol{C}(\boldsymbol{\rho}, z)\mathrm{d}z = \sum_{i=1}^{N_l} {\rho_i}^p \boldsymbol{C}_i(z_{i+1} - z_i). \tag{6.3}$$

Membrane-bending stiffness:

$$\boldsymbol{\mathcal{B}}(\boldsymbol{\rho}) = \int_{-\frac{h}{2}}^{\frac{h}{2}} \boldsymbol{C}(\boldsymbol{\rho}, z) z \mathrm{d}z = \frac{1}{2} \sum_{i=1}^{N_l} \rho_i{}^p \boldsymbol{C}_i (z_{i+1}^2 - z_i^2). \tag{6.4}$$

Bending stiffness:

$$\boldsymbol{\mathcal{D}}(\boldsymbol{\rho}) = \int_{-\frac{h}{2}}^{\frac{h}{2}} \boldsymbol{C}(\boldsymbol{\rho}, z) z^2 \mathrm{d}z = \frac{1}{3} \sum_{i=1}^{N_l} \rho_i{}^p \boldsymbol{C}_i (z_{i+1}^3 - z_i^3). \tag{6.5}$$

Transverse shear stiffness:

$$\boldsymbol{\mathcal{G}}(\boldsymbol{\rho}) = \int_{-\frac{h}{2}}^{\frac{h}{2}} \boldsymbol{D}(\boldsymbol{\rho}, z) \mathrm{d}z = \sum_{i=1}^{N_l} \rho_i{}^p \boldsymbol{D}_i (z_{i+1} - z_i). \tag{6.6}$$

For plane stress, $\boldsymbol{C}_i$ and $\boldsymbol{D}_i$ are given by

$$\boldsymbol{C}_i = \frac{E_i^0}{(1-\nu_i^2)} \begin{bmatrix} 1 & \nu_i & 0 \\ \nu_i & 1 & 0 \\ 0 & 0 & \frac{(1-\nu_i)}{2} \end{bmatrix}, \text{ and} \tag{6.7}$$

$$\boldsymbol{D}_i = \frac{k\ E_i^0}{2(1+\nu_i)} \begin{bmatrix} 1 & 0 \\ 0 & 1 \end{bmatrix}. \tag{6.8}$$

In the foregoing, E_i^0 is the elastic modulus and ν_i the Poisson's ratio of the material in layer i, and k is the shear correction factor. The artificial density of layer i is denoted ρ_i. Note that layers that are *a priori* solid or void, and therefore do not form part of the design problem, are simply accounted for by setting $\rho_i = 1$ for solid layers or $\rho_i = \rho_{\min}$ for void layers. The vector containing the density in the N_l layers is denoted $\boldsymbol{\rho}$.

Usually, topology optimization problems impose a constraint on the amount of material or resource which can be utilized. The volume of a given element can be computed (assuming a constant area A through the thickness) as

$$V_e(\boldsymbol{\rho}) = \int_{-\frac{h}{2}}^{\frac{h}{2}} A(\boldsymbol{\rho}) \mathrm{d}z = \sum_{i=1}^{N_l} \rho_i\ A(z_{i+1} - z_i). \tag{6.9}$$

The volume of the entire structure is then easily computed as the sum of all element volumes:

$$V = \sum_{e=1}^{N_{el}} V_e, \tag{6.10}$$

where N_{el} represents the total number of elements in the assembly. In this work the design volume, or the volume of the design domain, will also be referred to. This is calculated as the difference between the total volume (6.10) and the volume of the elements or layers which are prescribed to be solid or void. In other word, the design volume is the volume of all the layers which are a function of the design variables (artificial densities).

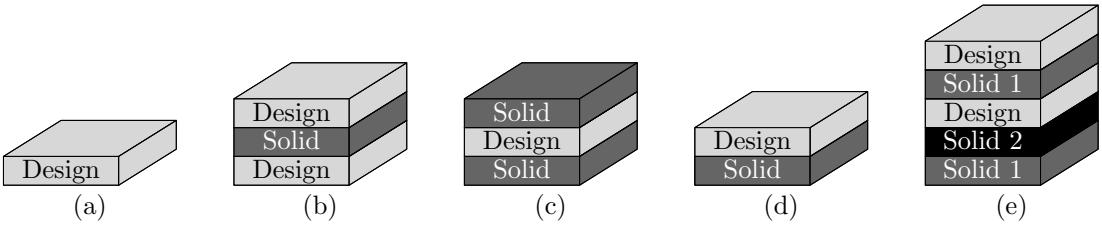

Figure 6.2: Various multilayer models with solid and design layers. (a) Single layer model, (b) Ribbed layup, (c) Honeycomb layup, (d) eccentric stiffened material model and (e) general asymmetric layup.

6.3.2 Layer models

Numerous laminate material models are possible using the material parameterization described in Section 6.3.1. Some of the popular schemes which have been used by other researchers are shown in Figure 6.2. Specifically, the examples depicted in Figure 6.2 are:

1. Single layer material model, depicted in Figure 6.2(a). This represents the classical topology optimization problem for plate and shell problems, and allows for the introduction of holes through the entire thickness (perforated plates/shells).

2. Three layer ribbed or rib stiffened material model, graphically represented in Figure 6.2(b). This model maintains an inner layer which is *a priori* solid with outer layers consisting of artificial material, allowing for the introduction of stiffening zones concentric to the shell mid-surface.

3. Three layer honeycomb model schematically depicted in Figure 6.2(c). This layup maintains two solid outer layers of equal thickness, concentric to the mid-surface, and an inner layer consisting of artificial material. This material description allows for core design. Although Stegmann *et al.* [121] question the practical interpretation of such a design problem, this material model will be employed as a benchmark for comparison with previously published results.

4. Other more general material models. Models 1 to 3 above, all result in symmetric material distributions, and therefore result in no membrane-bending coupling, i.e. $\boldsymbol{\mathcal{B}} = \mathbf{0}$. For problems such as the two-layer eccentric stiffener in Figure 6.2(d) and the general asymmetric laminate in Figure 6.2(e), coupling between membrane and bending actions becomes important. Although these material models present no real conceptual difficulty, we restrict ourselves to models 1 to 3 above. The effect of numerically adjustable parameters and element formulation on these more 'traditional' problems are to be investigated, especially since piezoelectric actuators usually result in symmetric layups as, for example, the case of piezoelectric bimorphs.

6.3.3 Problem formulation and sensitivities

In this work, the traditional topology optimization problem of minimizing compliance is considered. The minimum compliance problem may be written as

$$\min_{\boldsymbol{\rho}} c(\boldsymbol{\rho}) \tag{6.11}$$

$$\text{such that : } \sum_{e=1}^{N_{el}} V_e \leq V^*, \tag{6.12}$$

$$: \boldsymbol{KQ} = \boldsymbol{F}, \tag{6.13}$$

$$: 0 < \rho_{\min} \leq \rho_e \leq 1, \quad e = 1, 2, \ldots, N_{el} \tag{6.14}$$

where c is the compliance given by $c(\boldsymbol{\rho}) = \boldsymbol{F}^T\boldsymbol{Q}(\boldsymbol{\rho})$, and where the displacements are determined from $\boldsymbol{Q}(\boldsymbol{\rho}) = \boldsymbol{K}(\boldsymbol{\rho})^{-1}\boldsymbol{F}$. In this problem, the force vector $\boldsymbol{F}$ is independent of the artificial density. The allowable volume is denoted V^*. The sensitivity of the linear volume constraint in (6.12) can easily be determined. The sensitivity of the compliance (6.11) can be calculated using the adjoint method [4]. It can easily be shown that

$$\frac{\partial c}{\partial \rho_e} = -\boldsymbol{Q}^T \frac{\partial \boldsymbol{K}}{\partial \rho_e}\boldsymbol{Q}, \quad e = 1, 2, \ldots, N_{el}. \tag{6.15}$$

This problem has been presented in some detail in Chapter 5, Section 5.4.1. Note that in the treatment above, each element e in the finite element mesh has only one corresponding density variable ρ_e. In the case of the three layer stiffening model, for example, this variable scales the material properties of the two outer layers simultaneously. Each layer's material properties could of course be scaled independently, and therefore in up to N_l variables for each element (without any solid or void layers) are possible. However, only the former procedure is considered here.

6.3.4 Design update and filtering strategies

In Section 6.3.3 it was described how the function value and constraint functions are evaluated. In this section the design updating scheme as well as the treatment of some numerical difficulties in topology optimization are briefly discussed.

The design update is carried out using the standard fixed-point updating scheme based on the conditions of optimality [4], i.e.

$$\rho_{k+1} = \begin{cases} \max\{(1-\zeta)\rho_k, \rho_{\min}\}, & \text{if } \rho_k B_k^{\eta} \leq \max\{(1-\zeta)\rho_k, \rho_{\min}\} \\ \min\{(1+\zeta)\rho_k, 1\}, & \text{if } \min\{(1+\zeta)\rho_k, 1\} \leq \rho_k B_k^{\eta} \\ \rho_k {B_k}^{\eta} & \text{otherwise} \end{cases} \tag{6.16}$$

where $B_k = -\frac{\partial c}{\partial \rho_k}{\lambda_k}^{-1}$, λ_k is the Lagrange multiplier enforcing the volume constraint and determined using a simple bisection method, and where $\zeta = 0.2$ is a move limit and $\eta = \frac{1}{2}$ is a tuning parameter. The density distribution at iteration k is denoted ρ_k. Although the optimal topology calculated using this scheme is known to be somewhat sensitive to the

parameters ζ and η [116], the aforementioned settings are exclusively used for all results presented herein. In this way, the effect of element formulation on optimal topology is isolated.

The final implementational issue is that of mesh dependency. In order to overcome this problem, as well as the checkerboarding problem (see [4, 13, 100] for details) the sensitivity filtering method of Sigmund [100] is used, with a filter radius of 1.2 element side lengths in all cases.

6.4 Finite element formulations

In this section, the formulations of the various shell finite elements used in the numerical experiments, are briefly outlined. Flat shell finite elements, which can be thought of as an assemblage of membrane and plate components, are employed.

Without presenting details of the various finite element formulations at this point, the resulting discretized system can be described using

$$\boldsymbol{K}\boldsymbol{Q} = \boldsymbol{F}, \tag{6.17}$$

which usually results from minimization of appropriate functionals based on linear elasticity assumptions. Here $\boldsymbol{F}$ is a vector representing the global forces and moments, and $\boldsymbol{Q}$ is the associated vector of global displacements and rotations. $\boldsymbol{K}$ is the global stiffness matrix, comprising all the assembled elemental stiffness matrices:

$$\boldsymbol{K} = \mathbf{A}_{e=1}^{Nel} \boldsymbol{k}_e, \tag{6.18}$$

where $\mathbf{A}$ represents the assembly operator and $\boldsymbol{k}_e$ the elemental stiffness matrix in the global coordinate system. In this chapter, membrane, plate and shell problems are considered, and therefore some details of the formulation of shell elements, which can be used to solve all of the presented test problems, are presented. Each shell finite element, with associated elemental displacements and rotations, can be further decomposed as

$$\boldsymbol{k}\,\boldsymbol{q} = \begin{bmatrix} \boldsymbol{k}_{\mathrm{m}} & \boldsymbol{k}_{\mathrm{mp}} \\ \boldsymbol{k}_{\mathrm{mp}}^T & \boldsymbol{k}_{\mathrm{p}} \end{bmatrix} \begin{Bmatrix} \boldsymbol{q}_{\mathrm{m}} \\ \boldsymbol{q}_{\mathrm{p}} \end{Bmatrix}; \qquad \begin{aligned} \boldsymbol{k}_{\mathrm{p}} &= \boldsymbol{k}_{\mathrm{b}} + \boldsymbol{k}_{\mathrm{s}} \\ \boldsymbol{k}_{\mathrm{mp}} &= \boldsymbol{k}_{\mathrm{mb}} + \boldsymbol{k}_{\mathrm{ms}} \end{aligned} \tag{6.19}$$

where $\boldsymbol{k}$ represents the stiffness matrix in a locally defined coordinate system, with related local nodal displacements and rotations $\boldsymbol{q}$. The partitioned membrane and plate stiffness matrices are denoted $\boldsymbol{k}_{\mathrm{m}}$ and $\boldsymbol{k}_{\mathrm{p}}$, respectively. The coupling stiffness between membrane and plate actions is denoted $\boldsymbol{k}_{\mathrm{mp}}$.

As indicated in (6.19), the plate component of the stiffness matrix is composed of bending ($\boldsymbol{k}_{\mathrm{b}}$) and transverse shear ($\boldsymbol{k}_{\mathrm{s}}$) components. Similarly the coupling between plate actions can be decomposed into coupling between membrane and bending ($\boldsymbol{k}_{\mathrm{mb}}$) and that between membrane and transverse shear ($\boldsymbol{k}_{\mathrm{ms}}$). It is usually assumed that there is no coupling between membrane and transverse shear, or between bending and transverse shear components. The local shell stiffness matrix can therefore be rewritten as

$$\boldsymbol{k} = \begin{bmatrix} \boldsymbol{k}_{\mathrm{m}} & \boldsymbol{k}_{\mathrm{mp}} \\ \boldsymbol{k}_{\mathrm{mp}}^T & \boldsymbol{k}_{\mathrm{p}} \end{bmatrix}. \tag{6.20}$$

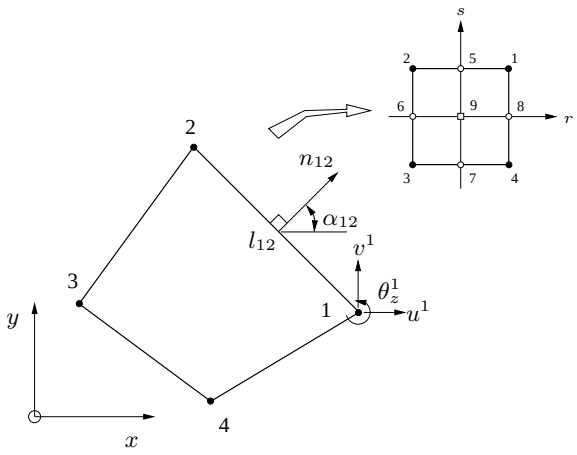

Figure 6.3: Quadrilateral element with drilling degrees of freedom.

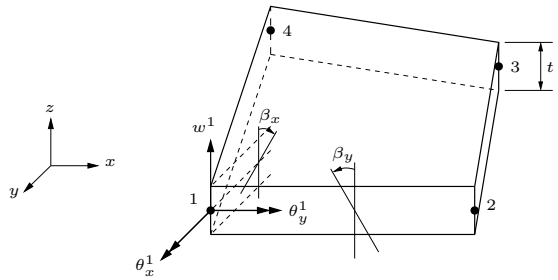

Figure 6.4: Quadrilateral Mindlin-Reissner plate element.

In the foregoing, the associated local displacements $\boldsymbol{q}$ are decomposed into terms associated with membrane actions, $\boldsymbol{q}_{\rm m}$, and those associated with the plate component, $\boldsymbol{q}_{\rm p}$. Specifically, $\boldsymbol{q}_{\rm m} = [\boldsymbol{u}\ \boldsymbol{v}\ \boldsymbol{\theta}_z]^T$, where $[\boldsymbol{u}\ \boldsymbol{v}]^T$ represent the in-plane nodal displacements only, and $\boldsymbol{\theta}_z$ denotes the in-plane rotations or drilling DOFs at each node. A quadrilateral membrane element with drilling DOFs is schematically depicted in Figure 6.3. The plate transverse displacement and rotations are given by $\boldsymbol{q}_{\rm p} = [\boldsymbol{w}\ \boldsymbol{\theta}_x\ \boldsymbol{\theta}_y]^T$, as shown in Figure 6.4.

For clarity, some detail of the membrane and plate components of the elemental stiffness matrix are now presented separately in the local coordinate system.

6.4.1 Membrane elements

Two membrane finite element formulations are employed in this work. The first is the traditional Q4 displacement based element which neglects in-plane rotations. The rotations can, however, be accommodated by an extremely simple, but *ad hoc* treatment. This method has no theoretical basis, and is used to illustrate the pitfalls of an improper treatment of element deficiencies.

The second membrane element is based on the variational formulation due to Hughes and

Brezzi [18], with the finite element implementation investigated by Ibrahimbegovic *et al.* [21]. This formulation, detailed in Chapter 2, is based on a rigorous mathematical foundation, and represents a robust, accurate membrane element.

Standard displacement based membrane element

The first membrane element is the standard displacement-based quadrilateral element with bilinear displacement interpolations, see for example [17]. The potential energy functional used to derive the elemental stiffness matrix is given by:

$$\Pi_{\mathrm{m}}^{\mathrm{Q4}}(\boldsymbol{u}_{\mathrm{m}}) = \frac{1}{2}\int_V {\boldsymbol{\epsilon}_{\mathrm{m}}}^T \boldsymbol{C}_{\mathrm{m}} \boldsymbol{\epsilon}_{\mathrm{m}} \mathrm{d}V - \frac{1}{2}\int_V {\boldsymbol{u}_{\mathrm{m}}}^T \boldsymbol{f} \mathrm{d}V, \tag{6.21}$$

where

$${\boldsymbol{\epsilon}_{\mathrm{m}}}^T = \left[\frac{\partial u}{\partial x}\ ;\quad \frac{\partial v}{\partial y}\ ;\quad \frac{\partial u}{\partial y} + \frac{\partial v}{\partial x}\right], \tag{6.22}$$

and $\boldsymbol{C}_{\mathrm{m}}$ is the constitutive relation. The displacement field is denoted $\boldsymbol{u}_{\mathrm{m}} = [u\ v]^T$ and $\boldsymbol{f}$ is the body force vector field. Surface tractions and point forces can be considered in the standard fashion [17].

The element stiffness matrix which results from this functional, is given by

$$\boldsymbol{k}_{\mathrm{m}}^{\mathrm{Q4}}(\rho) = \int_A [\boldsymbol{B}_{\mathrm{m}}^{\mathrm{Q4}}]^T \boldsymbol{\mathcal{A}}(\rho) \boldsymbol{B}_{\mathrm{m}}^{\mathrm{Q4}} \mathrm{d}A, \tag{6.23}$$

where $\boldsymbol{B}_{\mathrm{m}}^{\mathrm{Q4}}$ is the strain-displacement operator and $\boldsymbol{\mathcal{A}}(\rho)$ is the through thickness integrated constitutive relation given in (6.3). Note that $\boldsymbol{\mathcal{A}}$ is a function of the artificial density introduced in the SIMP material parameterization procedure.

This element formulation neglects the in-plane rotational field, θ_z, and possesses only two degrees of freedom per node. The dimension of $\boldsymbol{k}_{\mathrm{m}}^{\mathrm{Q4}}$ is therefore only 8×8. For planar problems this treatment is adequate. However, for general shell problems the additional in-plane rotational DOF is required. A method which is sometimes used to account for the in-plane rotation is simply to add a small fictitious stiffness to each drilling DOF. This is done by simply replacing the on-diagonal 4×4 null matrix with the matrix $\boldsymbol{k}_{\theta z}$ given in (6.25).

$$\boldsymbol{k}_{\mathrm{m}}^{\mathrm{Q4}\alpha} = \begin{bmatrix} \boldsymbol{k}_{\mathrm{m}}^{\mathrm{Q4}} & \boldsymbol{0}_{8\times 4} \\ \boldsymbol{0}_{4\times 8} & \boldsymbol{k}_{\theta z} \end{bmatrix}, \tag{6.24}$$

$$\text{where } \boldsymbol{k}_{\theta z} = \alpha V E(\rho) \begin{bmatrix} 1 & -\frac{1}{3} & -\frac{1}{3} & -\frac{1}{3} \\ & 1 & -\frac{1}{3} & -\frac{1}{3} \\ & & 1 & -\frac{1}{3} \\ & \text{symm} & & 1 \end{bmatrix}, \tag{6.25}$$

where α is an adjustable parameter, V is the volume of the element and $E(\rho)$ is the elastic modulus which is a function of the element artificial density. As in Cook *et al.* [17] the added matrix provides each drilling DOF with a fictitious stiffness, but offers no resistance to the mode $\theta_z^1 = \theta_z^2 = \theta_z^3 = \theta_z^4$, or any other rigid mode.

This *ad hoc* treatment results in no coupling between in-plane displacements and in-plane rotations, and will probably be sensitive to element aspect ratio and distortion. Although this method is heuristic, it is tempting since implementation is trivial. Of course there are numerous other ways of treating drilling DOFs suggested in the literature, see for example [23, 24, 33]. Most methods result in a rank deficient stiffness matrix and therefore require some form of stability control which introduces other adjustable parameters to avoid potential spurious results.

Membrane element with drilling DOFs

The second membrane element accounts for in-plane rotations based on their continuum mechanics definition. The approach relies on a variational formulation employing an independent rotation field, as presented by Hughes and Brezzi [18]. The original element formulation with drilling DOFs was presented by Reissner [40]. However, the formulation of Reissner lacks stability in the discrete form. The variational problem of Reissner was modified by Hughes and Brezzi [18] in order to preserve the stability of the discrete problem. It utilizes the skew-symmetric part of the stress tensor as a Lagrange multiplier to enforce equality of independent rotations and the skew-symmetric part of the displacement gradient in a weak sense. The stress tensor is therefore not *a priori* assumed to be symmetric.

Hughes and Brezzi show that a displacement-based functional can be derived by eliminating the skew-symmetric part of stress from a mixed-type functional. Employing a notation similar to that in [22], the result is the modified functional

$$\Pi_{\mathrm{m}}^{\mathrm{Q4}\gamma}(\boldsymbol{u}_{\mathrm{m}}, \theta_z) = \frac{1}{2}\int_V {\boldsymbol{\epsilon}_{\mathrm{m}}}^T \boldsymbol{C}_{\mathrm{m}} \boldsymbol{\epsilon}_{\mathrm{m}} \mathrm{d}V + \frac{1}{2}\gamma \int_V (\omega_{xy} - \theta_z)^2 \mathrm{d}V - \frac{1}{2}\int_V {\boldsymbol{u}_{\mathrm{m}}}^T \boldsymbol{f} \mathrm{d}V, \tag{6.26}$$

where ω_{xy} is the skew-symmetric part of the displacement gradient, given by

$$\omega_{xy} = \frac{\partial v}{\partial x} - \frac{\partial u}{\partial y}, \tag{6.27}$$

see Chapter 2 for details. The translations are related to the in-plane rotations by γ, overcoming the rank deficiency present in many formulations with drilling DOFs. The patch test is passed for all $\gamma > 0$. The functional in (6.26) requires only interpolation of displacements and rotations. The stationary point can be found in the usual manner. The independent rotations are interpolated using standard bilinear functions, while the in-plane displacement approximation is taken as an Allman-type interpolation [23].

In matrix form the first term of $\Pi_{\mathrm{m}}^{\mathrm{Q4}\gamma}$ can be shown to reduce to

$$\tilde{\boldsymbol{k}}_{\mathrm{m}}^{\mathrm{Q4}\gamma} = \int_A \left[\boldsymbol{B}_{\mathrm{m}}^{\mathrm{Q4}\gamma} \;\; \boldsymbol{G}_{\mathrm{m}}^{\mathrm{Q4}\gamma}\right]^T \boldsymbol{\mathcal{A}}(\rho) \left[\boldsymbol{B}_{\mathrm{m}}^{\mathrm{Q4}\gamma} \;\; \boldsymbol{G}_{\mathrm{m}}^{\mathrm{Q4}\gamma}\right] \mathrm{d}A, \tag{6.28}$$

where $\tilde{\boldsymbol{k}}_{\mathrm{m}}^{\mathrm{Q4}\gamma}$ is a 12×12 matrix. This is in fact the QC9 or QC9(8) element (depending on the integration scheme employed to integrate the element area Ω^e). This rank deficient element was reported by Stander and Wilson [95] further to the work of Taylor and Simo [37].

To eliminate the rank deficiency, the following penalty term, in matrix form, corresponding to the second term of $\Pi_{\mathrm{m}}^{\mathrm{Q4}\gamma}$ is derived:

$$\boldsymbol{p}_{\mathrm{m}}^{\gamma} = \gamma(\rho) \int_A \begin{Bmatrix} \boldsymbol{b}_{\mathrm{m}}^{\mathrm{Q4}\gamma} \\ \boldsymbol{g}_{\mathrm{m}}^{\mathrm{Q4}\gamma} \end{Bmatrix} \begin{bmatrix} \boldsymbol{b}_{\mathrm{m}}^{\mathrm{Q4}\gamma} & \boldsymbol{g}_{\mathrm{m}}^{\mathrm{Q4}\gamma} \end{bmatrix} \mathrm{d}A \tag{6.29}$$

$$\text{where } \gamma(\rho) = \alpha G(\rho), \tag{6.30}$$

with G the shear modulus which is a function of the artificial density variable, and α an adjustable parameter as in (6.25). Quite a number of studies have reported a suitable value of γ. In their original work, Hughes and Brezzi [18] suggest a value of $\gamma = G$, the shear modulus. Recently, however, it has been shown that lower values of γ, such as $\gamma = G \times 10^{-2}$ gives better results [20, 58] and Chapter 2. Again, γ is a function of the element's artificial density ρ.

The element stiffness matrix therefore becomes

$$\boldsymbol{k}_{\mathrm{m}}^{\mathrm{Q4}\gamma} = \tilde{\boldsymbol{k}}_{\mathrm{m}}^{\mathrm{Q4}\gamma} + \boldsymbol{p}_{\mathrm{m}}^{\gamma}, \tag{6.31}$$

$\boldsymbol{p}_{\mathrm{m}}^{\gamma}$ is integrated by a single point Gaussian quadrature. By fully integrating $\tilde{\boldsymbol{k}}_{\mathrm{m}}^{\mathrm{Q4}\gamma}$ and combining with $\boldsymbol{p}_{\mathrm{m}}^{\gamma}$, spurious zero energy modes are prevented [21]. No additional devices (e.g. see [24]) are needed. The same holds if a modified 8-point quadrature, or 5-point rule [52], is employed to integrate $\tilde{\boldsymbol{k}}_{\mathrm{m}}^{\mathrm{Q4}\gamma}$ [21].

The forms of $\boldsymbol{B}_{\mathrm{m}}^{\mathrm{Q4}\gamma}$, $\boldsymbol{G}_{\mathrm{m}}^{\mathrm{Q4}\gamma}$, $\boldsymbol{b}_{\mathrm{m}}^{\mathrm{Q4}\gamma}$ and $\boldsymbol{g}_{\mathrm{m}}^{\mathrm{Q4}\gamma}$ can be found in, for example [21, 52] or in Chapter 2.

Membrane locking correction

The membrane locking appearing in elements with drilling DOFs was alleviated in [21] by employing Taylor's correction [38]. The final modified membrane strain relationship of the correction is given by,

$$\bar{\boldsymbol{\epsilon}} = \boldsymbol{B}_{\mathrm{m}}^{\mathrm{Q4}\gamma}[\boldsymbol{u}\ \boldsymbol{v}]^T + \left(\boldsymbol{G}_{\mathrm{m}}^{\mathrm{Q4}\gamma} - \frac{1}{V_e} \int_{\mathrm{V}} \boldsymbol{G}_{\mathrm{m}}^{\mathrm{Q4}\gamma} \mathrm{dV} \right) \boldsymbol{\theta}_z, \tag{6.32}$$

where $[\boldsymbol{u}\ \boldsymbol{v}]$ and $\boldsymbol{\theta}_z$ are the nodal values for displacement and rotation respectively, and $\boldsymbol{B}_{\mathrm{m}}^{\mathrm{Q4}\gamma}$ and $\boldsymbol{G}_{\mathrm{m}}^{\mathrm{Q4}\gamma}$ are the same as those in (6.28), and their explicit form is shown in, for example [21]. Finally, V_e is the element volume.

6.4.2 Plate elements

In the numerical study to follow, three different plate elements are employed. The first is the popular Discrete Kirchhoff Quadrilateral (DKQ) element based on the Kirchhoff assumptions for thin plates, in which transverse shear is neglected. The other two elements are Mindlin-Reissner based elements, and differ only in the way in which shear locking is overcome.

Discrete Kirchhoff Quadrilateral plate element

DKQ plate elements are commonly used in the analysis of thin plate problems. Since transverse shear deformation (TSD) is not permitted (γ_{xz}=γ_{yz}=0) this plate, and of course the resulting shell, is transversely shear rigid.

The formulation of the DKQ element is based on the functional (after integration through the thickness)

$$\Pi_{\mathrm{p}}^{\mathrm{DKQ}}(\boldsymbol{\beta}, w) = \frac{1}{2}\int_A \boldsymbol{\kappa}^T \boldsymbol{C}_{\mathrm{b}} \boldsymbol{\kappa}\ \mathrm{d}A - \int_A w\ p\ \mathrm{d}A, \tag{6.33}$$

$$\text{such that : } \beta_x = \frac{\partial w}{\partial x} \text{ and } \beta_y = \frac{\partial w}{\partial y}, \tag{6.34}$$

where

$$\boldsymbol{\kappa}^T = [\frac{\partial \beta_x}{\partial x}\ ;\ \frac{\partial \beta_y}{\partial y}\ ;\ \frac{\partial \beta_x}{\partial y} + \frac{\partial \beta_y}{\partial x}], \tag{6.35}$$

is the curvature, $\boldsymbol{C}_{\mathrm{b}}$ is the moment-curvature relation, p is the lateral load including surface and body forces and w is the lateral displacement. Furthermore, $\theta_x = \frac{\partial w}{\partial y} = \beta_y$ and $\theta_y = -\frac{\partial w}{\partial x} = -\beta_x$, as shown in Figure 6.4.

To circumvent the difficulty of the required C^1 continuity, the lateral displacements w and the rotations of the normals to the undeformed mid-surface in the x, z and y, z planes (β_x and β_y respectively) are assumed independently. Discrete approximations to the constraint in (6.34) are imposed by discrete elimination.

The stiffness matrix of the DKQ element is defined in the standard manner for displacement models as [125]

$$\boldsymbol{k}_{\mathrm{p}}^{\mathrm{DKQ}} = \int_A [\boldsymbol{B}_{\mathrm{b}}^{\mathrm{DKQ}}]^T \boldsymbol{\mathcal{D}}(\rho) \boldsymbol{B}_{\mathrm{b}}^{\mathrm{DKQ}} \mathrm{d}A, \tag{6.36}$$

where the specific form of $\boldsymbol{B}_{\mathrm{b}}^{\mathrm{DKQ}}$ can be found in, for example Batoz and Tahar [125] and the bending rigidity matrix $\boldsymbol{\mathcal{D}}$ is a function of the artificial density ρ, as shown in (6.5).

Mindlin-Reissner plate element with selective reduced integration

Two Mindlin-Reissner plate elements based on first order shear deformation of Mindlin and Reissner are evaluated. Both are derived from the following functional which has been pre-integrated through the thickness:

$$\Pi_{\mathrm{p}}^{\mathrm{MR}}(\boldsymbol{\beta}, w) = \frac{1}{2}\int_A \boldsymbol{\kappa}^T \boldsymbol{C}_{\mathrm{b}} \boldsymbol{\kappa}\ \mathrm{d}A + \frac{1}{2}\int_A \boldsymbol{\gamma}^T \boldsymbol{C}_{\mathrm{s}} \boldsymbol{\gamma}\ \mathrm{d}A - \int_A w\ p\ \mathrm{d}A, \tag{6.37}$$

where $\boldsymbol{\kappa}$ is given in (6.35), $\boldsymbol{C}_{\mathrm{b}}$ is the moment-curvature relationship, $\boldsymbol{C}_{\mathrm{s}}$ is the constitutive relation between shear forces and transverse shear, including the shear correction term accounting for the quadratic transverse shear stress consistent with classical theory. Finally the transverse shear strains are defined as,

$$\boldsymbol{\gamma}^T = [\frac{\partial w}{\partial x} - \beta_x\ ;\ \frac{\partial w}{\partial y} - \beta_y]. \tag{6.38}$$

Assuming independent bilinear interpolations for the transverse displacement and section rotations, the resulting stiffness matrix for a Mindlin-Reissner plate element can be written as

$$\boldsymbol{k}_{\mathrm{p}}^{\mathrm{MR}} = \boldsymbol{k}_{\mathrm{b}}^{\mathrm{MR}} + \boldsymbol{k}_{\mathrm{s}}^{\mathrm{MR}} = \int_A [\boldsymbol{B}_{\mathrm{b}}^{\mathrm{MR}}]^T \boldsymbol{\mathcal{D}}(\rho) \boldsymbol{B}_{\mathrm{b}}^{\mathrm{MR}} \mathrm{d}A + \int_A [\boldsymbol{B}_{\mathrm{s}}^{\mathrm{MR}}]^T \boldsymbol{\mathcal{G}}(\rho) \boldsymbol{B}_{\mathrm{s}}^{\mathrm{MR}} \mathrm{d}A, \tag{6.39}$$

where the standard forms of $\boldsymbol{B}_{\mathrm{b}}^{\mathrm{MR}}$ and $\boldsymbol{B}_{\mathrm{s}}^{\mathrm{MR}}$ can be found in, for example [17]. It is well known that full integration of the stiffness matrix terms in (6.39) results in severe locking for thin plates [16, 22, 17]. A simple method to overcome the locking phenomenon is to employ a selective reduced integration (SRI) scheme on the shear part of the stiffness matrix $\boldsymbol{k}_{\mathrm{s}}^{\mathrm{MR}}$. This procedure will be employed to calculate the first Mindlin-Reissner plate stiffness matrix, i.e.

$$\boldsymbol{k}_{\mathrm{p}}^{\mathrm{SRI}} = \boldsymbol{k}_{\mathrm{b}}^{\mathrm{MR}} + \tilde{\boldsymbol{k}}_{\mathrm{s}}^{\mathrm{MR}}, \tag{6.40}$$

where $\boldsymbol{k}_{\mathrm{b}}^{\mathrm{MR}}$ is calculated using a 4-point scheme and $\tilde{\boldsymbol{k}}_{\mathrm{s}}^{\mathrm{MR}}$ is evaluated using a single point integration scheme. A potential problem with this method of overcoming locking due to the parasitic shear, is the introduction of spurious zero-energy modes. Two spurious modes are introduced if SRI is employed, one of which is not communicable. No hourglass control, e.g. see [93], will be used in order to demonstrate how this mode becomes problematic in topology optimization problems.

Mindlin Reissner plate element with assumed natural strain

The second Mindlin-Reissner-based plate element overcomes the effects of shear locking by assuming a mixed interpolation of transverse displacement, section rotations and transverse strains. In particular the Assumed Natural Strain (ANS) formulation of Bathe and Dvorkin [126, 127] is considered here. The element of Bathe and Dvorkin has some similarities to the elements of MacNeal [128] and Hughes and Tezduyar [129].

This element has the advantage that it doesn't have any numerically adjustable factors (often required for hourglass control). Furthermore, it contains no spurious zero-energy modes, and passes all appropriate patch tests.

The stiffness matrix derived from this interpolation procedure finally results in the stiffness matrix

$$\boldsymbol{k}_{\mathrm{p}}^{\mathrm{ANS}} = \boldsymbol{k}_{\mathrm{b}}^{\mathrm{MR}} + \boldsymbol{k}_{\mathrm{s}}^{\mathrm{ANS}} = \boldsymbol{k}_{\mathrm{b}}^{\mathrm{MR}} + \int_A [\boldsymbol{B}_{\mathrm{s}}^{\mathrm{ANS}}]^T \boldsymbol{\mathcal{G}}(\rho) \boldsymbol{B}_{\mathrm{s}}^{\mathrm{ANS}} \mathrm{d}A, \tag{6.41}$$

where the bending part of the stiffness matrix is identical to that of $\boldsymbol{k}_{\mathrm{p}}^{\mathrm{SRI}}$, but the shear part of the stiffness matrix is derived including the ANS interpolations and evaluated using full integration. The strain operator $\boldsymbol{B}_{\mathrm{s}}^{\mathrm{ANS}}$ can be derived as described in [16, 126].

6.4.3 Membrane-bending components

For non-symmetric laminates, coupling between membrane and bending constitutive components becomes significant, i.e. $\boldsymbol{\mathcal{B}}$ in (6.4) is non-zero. Naturally, this part of the partitioned stiffness matrix, denoted $\boldsymbol{k}_{\mathrm{mb}}$ in (6.20), is a function of the specific membrane and plate components which constitute a given shell element.

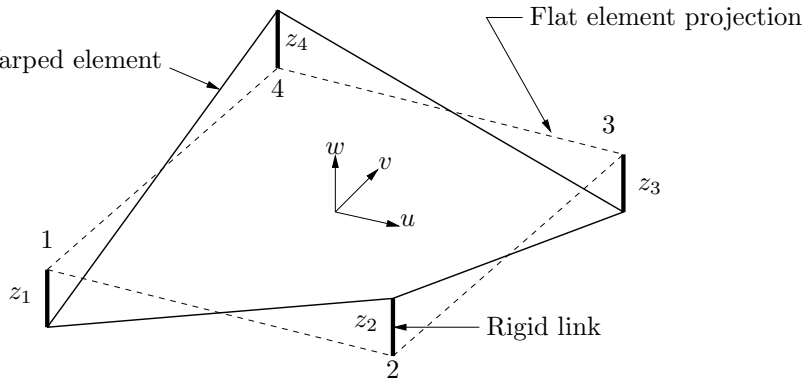

Figure 6.5: Warped and projected shell element.

The $\boldsymbol{k}_{\text{mb}}$ submatrix can simply be computed by premultiplying $\boldsymbol{\mathcal{B}}$ by the membrane strain-displacement operator, and postmultiplying by the bending strain-displacement operator. For simplicity however, in the numerical experiments presented herein only symmetric layups are considered, and consequently no coupling between membrane and bending actions is present.

6.4.4 Warp correction and local-global transformation

Where necessary, the effect of out-of-plane warp is corrected by using, the so-called 'rigid link correction' of Taylor [38], is employed to transform the nodal variables to the projected flat element variables. Figure 6.5 schematically shows the local warped and flat projected elements.

Ultimately, this corrected local element stiffness matrix $\boldsymbol{k}$ is transformed to the global coordinate system to yield,

$$\boldsymbol{k}^g = \boldsymbol{T}^T \boldsymbol{k} \boldsymbol{T} \tag{6.42}$$

where $\boldsymbol{T}$ is an appropriate transformation matrix.

6.4.5 Shell element denotation

Formulations of two membrane and three plate elements have been presented, which allows for a total of six different flat shell elements. In this section the denotations used for the various tested elements are presented.

The two membrane components are denoted:

- Q4α - The standard Q4 displacement based four node quadrilateral element with the *ad hoc* treatment of drilling DOFs. The Q4α stiffness matrix is given in (6.24).
- Q4γ - The four node membrane element based on the variational formulation of Hughes and Brezzi [18], and with local stiffness matrix given by (6.31).

The three plate components are denoted:

- DKQ - The plate element based on the Kirchhoff-Love thin plate assumption of shear rigidity. The stiffness matrix in local coordinates is presented in (6.36).
- SRI - The irreducible Mindlin-Reissner based element with selective reduced integration on transverse shear terms, and stiffness matrix given by (6.40).
- ANS - The assumed natural strain plate element based on Mindlin-Reissner assumptions, suggested by Bathe and Dvorkin [126], in which each of the natural strain components is independently interpolated. The elemental plate stiffness matrix is given in (6.41).

Shell elements will be denoted using first the membrane, followed by the plate designations. Recalling the form of the partitioned stiffness matrix in local coordinates, as presented in (6.20), the element made up of Q4α membrane and DKQ plate components can be represented as Q4αDKQ, with elemental stiffness matrix:

$$\boldsymbol{k}^{\mathrm{Q4}\alpha\mathrm{DKQ}} = \begin{bmatrix} \boldsymbol{k}_{\mathrm{m}}^{\mathrm{Q4}\alpha} & \boldsymbol{k}_{\mathrm{mb}}^{\mathrm{Q4}\alpha\mathrm{DKQ}} \\ (\boldsymbol{k}_{\mathrm{mb}}^{\mathrm{Q4}\alpha\mathrm{DKQ}})^T & \boldsymbol{k}_{\mathrm{p}}^{\mathrm{DKQ}} \end{bmatrix}. \tag{6.43}$$

Each partitioned matrix in (6.43) is 12×12 in size.

6.5 Numerical Examples

Several different finite element implementations are numerically tested in a SIMP topology optimization setting. A number of popular benchmark problems, which have been used mostly by researchers to verify effectiveness or correctness of implementation, are investigated. Some new problems, which highlight possible element deficiencies, are also introduced. Membrane, plate and shell problems are considered. In particular, we wish to investigate:

- The sensitivity of optimal topologies to parameters related to drilling DOFs in membrane and shell structures.
- The effect of employing Selective Reduced Integration (SRI) in Mindlin-Reissner plate elements, compared to mathematically sound and reliable procedures for overcoming shear locking.
- The difference in optimal topologies generated using elements based on Kirchhoff theory, compared to those using Mindlin-Reissner theory for thick and thin plate structures.

In each case, a uniform material distribution which exactly satisfies the volume constraint is chosen as an initial design or starting point. As detailed in Section 6.3.4 the mesh independency filter, due to Sigmund [100], is used to prevent checkerboarding. A filter radius equal to 1.2 times the element side length is utilized.

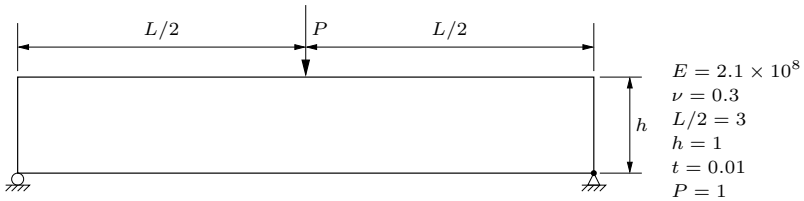

Figure 6.6: MBB beam geometry and constraints.

A stopping criterion based on the number of iterations only has been implemented. Therefore, in the discussion to follow the final topology, i.e. the topology after 100 iterations will be referred to as the optimal topology. In some cases numerical deficiencies cause singularities which result in the gradient of strain energy in particular elements to become very close to zero or even positive. In such circumstances, these spurious values are replaced manually by zero. This problem occurs only when SRI plate elements are used, and instances where the correction is made, are explicitly pointed out.

The remainder of this section details the results of the investigation into membrane, plate and finally shell problems. After each subsection, a brief discussion of the results is presented in which the most important points are emphasized.

6.5.1 Membrane example

Since the use of elements with drilling DOFs based on sound mathematical theory is advocated, it is important to determine the sensitivity of optimal topologies using elements with drilling DOFs, to the adjustable parameter α in Q4γ elements, see (6.30). For the purpose of this study, the popular MBB beam problem is selected.

MBB beam

The geometry, material properties, restraints and loading are all depicted in Figure 6.6. Although symmetry is used to model the structure, the complete topology is reported. In total 2700 square elements are used, 90 elements along the length of the finite element model, $L/2$ and 30 elements in the height h. Of course, since only membrane components are evaluated, only the single layer material model is tested. The available volume fraction is half of the design domain. In order to stabilize the convergence, the penalty exponent is stepped from 1 to 3. Also, the objective is normalized with respect to the starting value of compliance in order to improve the problem scaling.

Figure 6.7 depicts the sensitivity of the optimal compliance calculated using the Q4γ element to the value of the adjustable parameter α, see (6.30). Note that for the Q4γ membrane element, a value of $\alpha = 1$ corresponds the the value of γ suggested by Hughes and Brezzi [18]. However, recently a number of studies have suggested that a value of $\alpha = 10^{-2}$ results in more accurate solutions, see for example [20, 58] and Chapter 2. Therefore the upper bound of $\alpha = 10^2$ which is tested, is significantly higher than the optimal value suggested in

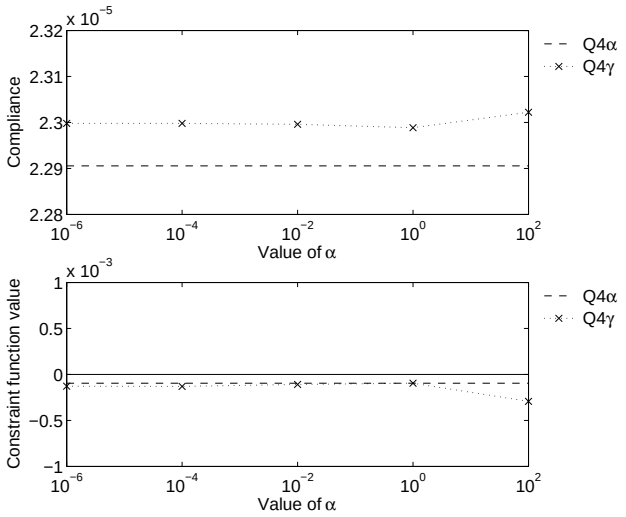

Figure 6.7: Compliance and constraint function values for optimal topologies as a function of α for the MBB beam problem.

the studies listed above. However, Hughes and Brezzi [18] showed that elements based on their variation formulation are convergent for all values of $\alpha > 0$.

It is clear from this figure that the optimal value of compliance computed using Q4γ elements is not significantly sensitive to the value of α. In fact, the slight increase in compliance around $\alpha = 10^2$ can be attributed to a corresponding decrease in volume, depicted in Figure 6.7, at this point rather than an elemental phenomenon. For this example, the optimal topology calculated using Q4α elements is of course insensitive to the value of α. In fact, for all 2-D planar analyses the correction in (6.24) is unnecessary since the standard Q4 element ($\boldsymbol{k}_{\mathrm{m}}^{\mathrm{Q4}}$ in (6.24)) is sufficient to capture the planar kinematics. Also plotted in the figure is the constraint function value at the various values of α tested.

Figure 6.8 depicts the optimal topologies corresponding to each point in Figure 6.7. Clearly, the optimal topology calculated using the Q4α element and the Q4γ elements are (visually) identical for the range of α tested. The indication is, therefore that Q4γ elements are reliable in membrane topology optimization problems over a wide range of α values. Furthermore, the actual value of compliance resulting from these optimal topologies is stable over a wide range of α values. An element with $\alpha = 0$ can be shown to be rank deficient and cannot always be relied upon to deliver accurate results. Nevertheless, for completeness this problem is evaluated for $\alpha = 0$, and satisfactory results are still found.

Readers interested in the convergence histories for the topologies depicted in Figure 6.8 are referred to Appendix B.1.1.

6.5.2 Analysis of membrane results

Based on the membrane example presented, a number of remarks can be made:

(a) Q4α element. (Same for all α.)

(b) Q4γ element, $\alpha = 0$.

(c) Q4γ element, $\alpha = 10^{-6}$.

(d) Q4γ element, $\alpha = 10^{-4}$.

(e) Q4γ element, $\alpha = 10^{-2}$.

(f) Q4γ element, $\alpha = 10^{0}$.

(g) Q4γ element, $\alpha = 10^{2}$.

Figure 6.8: Optimal topologies of MBB beam for various values of α.

- For membrane problems, Q4α and Q4γ elements produce almost identical topologies.
- As expected, the optimal topologies computed with Q4α elements are not a function of the adjustable parameter α, for 2-D planar problems.
- The optimal topologies calculated using Q4γ elements are insensitive to scaling parameter α over a wide range of values.
- The actual value of compliance (objective function value) of the optimal topologies generated with Q4γ elements are relatively insensitive to the numerical value of α over the range tested.

6.5.3 Plate examples

In order to determine the sensitivity of optimal topologies calculated using various plate elements and the SIMP method, a number of popular plate benchmark problems are considered. Additionally, a new problem which demonstrates the deficiencies associated with SRI is proposed. The geometry, material properties and support conditions for the plate example problems are depicted in Figure 6.9.

Both thick and thin plates are studied, with various layer models, i.e. single layer (see Figure 6.2(a)), rib stiffened design (as in Figure 6.2(b)) and honeycomb design (schematically depicted in Figure 6.2(c)). Each of these problems is analyzed using Discrete Kirchhoff Quadrilateral (denoted DKQ) elements, Mindlin-Reissner based elements with selective reduced integration on shear terms (denoted SRI) and Mindlin-Reissner based elements with assumed natural strain interpolations (denoted here as ANS) elements.

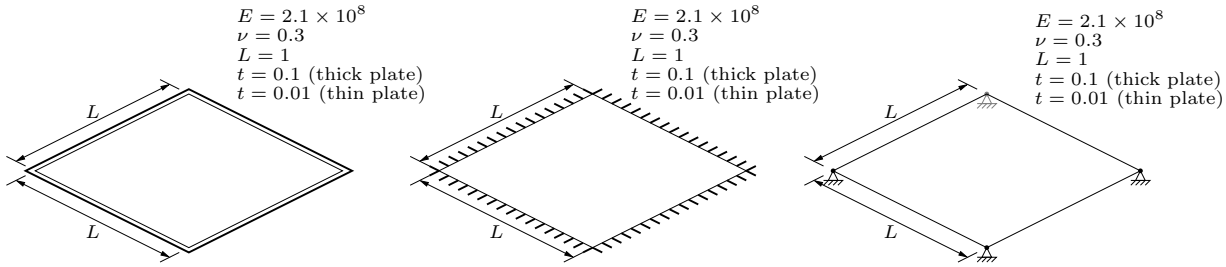

(a) Simply supported square plate subjected to center point load.

(b) Clamped square plate subjected to center point load.

(c) Corner supported square plate subjected to center point load.

Figure 6.9: Example plate problems, geometry and constraints.

In each of the multilayer examples to follow, the layup comprises three layers, with layers 1 and 3 (the outer layers) having thickness $\frac{t}{4}$ and a center layer with thickness of $\frac{t}{2}$ where t is the total thickness of the laminate. For the thick plates, thickness is set to $t = 0.1$ and for the problems considering thin plates $t = 0.01$ is used. These aspect ratios are in line with those used by Zienkiewicz and Taylor [22] to classify thick and thin plates.

In each plate example, the problem symmetry is exploited by modeling only a quarter of the plate using 900 square elements in total (i.e. a discretization of 30×30). Again, although only a quarter of the structure is modeled, the full topology is reported. The available volume for the volume constraint is set, in each case, to half of the design volume (i.e. the sum of the volume of the design layers).

Simply supported plate with center point load

The geometry and constraints for the first plate problem are depicted in Figure 6.9(a). The problem consists of a square plate which is simply supported, and subjected to a unit point load applied to the center of the plate. For brevity, only the single layer results will be detailed in this section. Interested readers are referred to Appendix B.2.1 which contains the results for the multilayer material models.

The compliance, together with the corresponding optimal topologies are plotted as a function of plate thickness for the three different plate elements used in the study. Figure 6.10(a) depicts the compliance as a function of plate thickness plotted on a log-log scale for the three different plate elements. From Figure 6.10(a) it was confirmed that the DKQ optimal compliance results, follow a cubic trend almost exactly with only slight variations due to numerical noise and truncation. Furthermore, Figure 6.11 confirms that the DKQ optimal topologies are insensitive to plate thickness.

Figure 6.10(b) depicts the results on a linear scale, normalized with respect to the (cubic) DKQ results. At the thin plate limit (t=0.01), very little difference is observed between the compliance of the different designs. From this figure, it is clear that the SRI plate

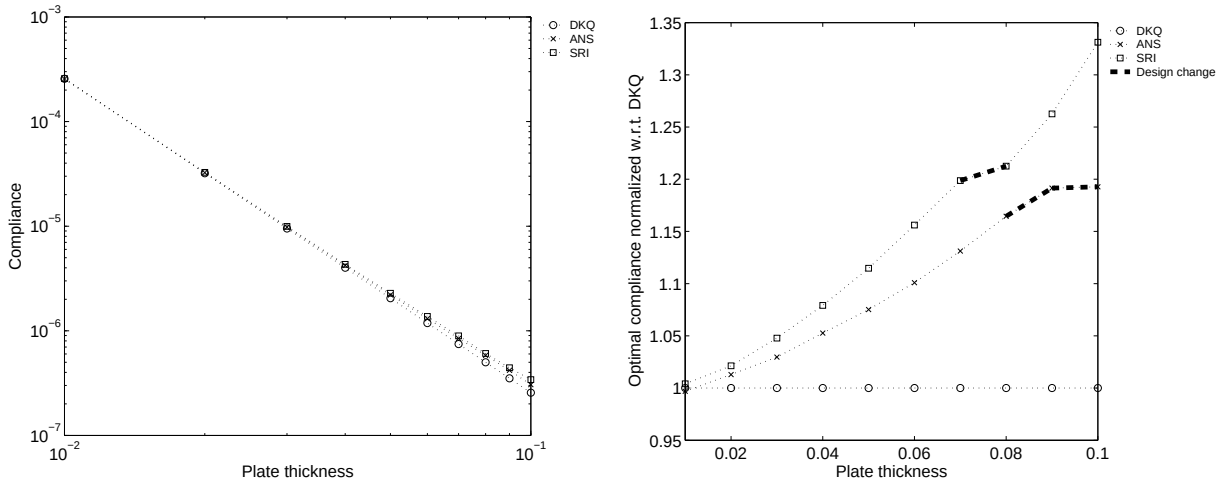

(a) Compliance on log-log scale.

(b) Compliance normalized with respect to DKQ's cubic relation.

Figure 6.10: Optimal topology compliance as a function of plate thickness for the simply supported plate problem.

element is less stiff than the ANS element since higher values of compliance are computed at each thickness, even when topologies are similar. Also indicated on the figure are the thickness ranges over which design changes occur, corresponding to the changes in the slope of the curve. In both cases the design is significantly changed when the compliance of the structure is approximately 1.2 times that of the DKQ result. Since the slope of the SRI curve is greater than that of ANS, this point is reached at a lower thickness for the SRI element and does not occur as gradually as the ANS element. Figure 6.11 depicts the actual topologies corresponding to the points on the curves in Figures 6.10(a) and 6.10(b).

The conclusion is therefore that the differences in topology resulting from SRI and ANS elements, is due to the SRI element being 'softer' (in transverse shear) than the ANS element. Since the bending terms are identical, the softer shear terms of the SRI elements offer less resistance and therefore relatively more strain energy is accommodated by these terms.

Clamped plate with center point load

The geometry for this problem is depicted in Figure 6.9(b). The load considered is again a unit point load applied to the center of the plate. This problem has been considered by a number of authors [4, 115], and our thin plate results compare favorably with theirs.

Results similar to those found for the simply supported plate with centre point load are found for this problem. Therefore, since no real insight is gained through presentation of these results, interested readers are simply referred to Appendix B.2.2. However, the results presented in Appendix B.2.2 are significant in that they are similar to those presented by

previous works that have considered this problem, e.g. Krog and Olhoff [115] and therefore confirm the correctness of our model and optimization routine.

Corner supported plate with center point load

The final plate geometry with restraints is depicted in Figure 6.9(c). It represents a corner supported plate (i.e. transverse displacement is constrained at the four corner nodes only). For this problem, the first load case considered, is again a center point load as before. The single layer, ribbed and honeycomb material models are again analyzed. Once again for brevity only selected results are presented in this section, with the results from the remaining material models and plate thicknesses given in Appendix B.2.3. In particular, only results for the thin ribbed material model are presented.

The tables accompanying each figure, tabulate the difference in compliance between the optimal topologies, analyzed using the three plate elements utilized in this study. The values represent the percentage difference between the compliance of the optimal topology computed with a given element, and the compliance calculated using the remaining two elements. Of course, there is no difference between the compliance of the optimal topology calculated with any element and itself, accounting for the zero terms on the diagonal of each table.

Figure 6.12 depicts the results for the thin ribbed model subjected to a center point load. Although all optimal topologies are similar, the convergence history of using SRI elements, depicted in Figure 6.12(f) indicates that some numerical problems occurred. In fact, during iteration 73 elements with negative compliance (or positive compliance sensitivity) were encountered. Table 6.1 confirms that there is not a significant difference between the various optimal topologies.

	Optimal topology generated using:		
	DKQ	ANS	SRI
Analysed with DKQ	0.0000	-0.0088	1.5140
Analysed with ANS	0.0281	0.0000	1.3180
Analysed with SRI	-0.4786	-0.5854	0.0000
Constraint value	-3.3392e-05	1.5709e-05	-2.9578e-05

Table 6.1: Percentage difference: Corner supported square plate subjected to center point load, ribbed model, $t = 0.01$.

Corner supported plate subjected to uniform distributed load

In the previous plate problems which have been presented there appears to be little or no difference between the results computed using the ANS and SRI Mindlin-Reissner based elements. A problem is now tested for which SRI is known to have difficulty solving [133].

In this problem the same corner supported geometry and restraints, depicted in Figure 6.9(c), are used but the applied load in this case is uniformly distributed over the plate

surface. In order to ensure that the load is not design dependent, only the ribbed and honeycomb material models are considered. Again, to illustrate, results are shown only for the thin ribbed material model (similar to the previous example), while the results of the other material models are contained in Appendix B.2.4.

Figure 6.14 demonstrates that the optimal topologies calculated using the DKQ and ANS elements are, once again, similar. The convergence history of the SRI element depicted in Figure 6.14(f) is extremely erratic due to the element instability. Indeed, many iterations resulted in elements with slightly negative or near zero compliance. As a result, the optimal topology calculated using SRI elements is completely different to the other two elements results. Table 6.2 emphasizes that the compliance of the DKQ and ANS topologies, computed using SRI elements, is completely spurious. In order to explain this, the displaced shape of the optimal topology generated using DKQ elements, analyzed using SRI elements is plotted in Figure 6.13. The hourglass mode which is known to propagate through SRI meshes can clearly be seen.

	Optimal topology generated using:		
	DKQ	ANS	SRI
Analysed with DKQ	0.0000	0.2396	79.4795
Analysed with ANS	-0.0308	0.0000	79.1851
Analysed with SRI	3583.5656	921450354.1646	0.0000
Constraint value	-2.4021e-05	1.6275e-05	6.2786e-05

Table 6.2: Percentage difference: Corner supported square plate subjected to uniform distributed load, ribbed model, $t = 0.01$.

6.5.4 Analysis of plate results

For the results which have been presented in this section, a number of observations and remarks can be made:

- Since the DKQ element is shear rigid, it is not capable of distinguishing between thick and thin plate topology optimization problems. As a result, identical topologies result for any plate thickness.
- The ANS elements have been shown to be reliable and stable. They are capable of reproducing thin plate results similar to those computed using DKQ elements, but are also sensitive to plate thickness.
- The SRI plate element is 'softer' than the ANS element in transverse shear. The SRI element is therefore more sensitive to plate thickness than the ANS elements. The result is that occasionally this sensitivity to thickness drives the SRI element to better designs than that of the ANS or DKQ elements. However, the fact that the SRI element possesses a communicable spurious mode makes it an unreliable element in certain circumstances.

- In cases where SRI elements manifest the propagating spurious mode, the actual topology calculated using SRI elements is not of concern. The conclusion is that there are cases (even in linear static problems) for which SRI is not suitable. Therefore, the use of SRI elements with no hourglass control is not recommended in topology optimization.
- Finally, the correctness of the thick plate results should be tested with an analysis of solid slab-like structures. However, the purpose of this work is simply to show that the thin and thick plate results differ.

6.5.5 Shell examples

Finally, some results for the analysis of thin shell examples are presented. The flat shell elements are constructed as an assemblage of the two membrane elements presented in Section 6.4.1, and the DKQ plate element presented in Section 6.4.2. Since the effect of plate formulation on optimal topologies has already been demonstrated, the effect of membrane component, and especially the inclusion of drilling DOFs, in shell elements is now studied. Therefore, in order to ensure that the results are not a function of the plate formulation, only shell elements with shear rigid plate components are evaluated. It is thereby guaranteed that only thin shell results are recovered, since DKQ elements have just been shown to be insensitive to plate thickness.

Two problems are presented, the first being a cylindrical shell example, which has been studied by several authors [116, 134]. The second problem, with geometry in the shape of a pretwisted beam, is introduced here to highlight the element dependenceny of optimal shell topologies.

Cylindrical shell

The first shell problem is depicted in Figure 6.15. The geometry, restraints, applied loads and material properties are all depicted in the figure. The symmetry of the problem is exploited by only modeling one quarter of the structure with a 30×30 discretization. A volume constraint of half of the design volume is again imposed. Once again, for brevity only single layer results are presented with ribbed and honeycomb results presented in Appendix B.3.1.

Figure 6.16 depicts the optimal compliance values for the single layered material model, as a function of scaling parameter α (see (6.25) for the Q4α membrane component and (6.30) for the Q4γ component). The row of encircled topologies represent the optimal topologies generated using the Q4αDKQ element at each value of α. Above these, are depicted the optimal topologies at the same α value, calculated using Q4γDKQ elements.

Figure 6.16 illustrates that distinctly different topologies are recovered for relatively high values of α, i.e. $\alpha = 1$ and $\alpha = 100$, when the Q4αDKQ element is employed in the finite element analysis. On the other hand, the optimal topologies generated using Q4γDKQ elements are shown to be insensitive to the scaling value of α. The figure also shows that the actual value of compliance is far more sensitive to α when using Q4αDKQ elements than Q4γDKQ elements. The notable decrease in compliance at high values of α, when using

Q4αDKQ elements, is due to the artificially high stiffness of the drilling DOFs which, due to the curvature, is propagated through the structure.

Pretwisted shell

The final shell example is depicted in Figure 6.17. The problem is that of a pretwisted beam, which is clamped at the root, with two point loads applied at the vertices opposite the fixed end. The full geometry is modeled with a 40×40 discretization. A volume constraint of half of the design volume is imposed. For brevity, only the single layer results will be presented. This problem has previously been shown to be sensitive to the value of α [135].

Figure 6.18 depicts the optimal topologies employing Q4αDKQ and Q4γDKQ elements together with the corresponding optimal topologies. For this problem, the range of values of α for which the Q4αDKQ and Q4γDKQ elements result in similar topologies is much smaller than the cylindrical shell problem. In fact, values of $\alpha = 10^{-6}$, 10^{-4} and 10^{2}, each result in different topologies when the finite element model employs Q4αDKQ elements! In contrast, the Q4γDKQ element is once again shown to be stable for all tested values of α.

6.5.6 Analysis of shell results

Based on the results presented in this section the following remarks are appropriate:

- The optimal topologies computed using Q4γDKQ elements are shown to be insensitive, over a wide range, to the scaling value of α. In fact, the only perceivable difference in compliance over the range of tested values of α is a result of the slight difference in volume.

- In contrast, the optimal topologies resulting from the use of the Q4αDKQ elements are shown to be a function of α, and that the sensitivity to α appears to be problem dependent. Authors [17] suggests that if the *ad hoc* correction for absence of drilling DOFs (as in the membrane part of the Q4αDKQ) is made, that a value should be chosen which is small enough not to affect the finite element analysis, while being large enough to alleviate any spurious modes. It is shown here that even if a small value of α is selected, preventing numerical instabilities, different topologies result from those calculated from elements with true drilling DOFs. In fact, the only tested value of α which consistently results in the same results as the Q4γDKQ element is 10^{-2}.

6.6 Conclusions

Numerical experiments have been performed in order to determine the effect of finite element formulation on membrane, plate and shell topology optimization problems. It is shown that, for given topology optimization algorithmic settings, the resultant optimal topology is a function of the element type. It should be noted however, that 'optimal' topologies are known to be a function of the algorithm settings [116]. Therefore, the global optimal topologies

of the evaluated problems are not necessarily reported here. Having said that, optimal topologies presented herein closely resemble previously reported results, where comparison is possible. The implication of this study is therefore that the global optimal topology for a given problem could be a function of the type of element which is used in the analysis.

For membrane problems, it is demonstrated that both standard Q4 (Q4α) and element with drilling degrees of freedom (DOFs) (Q4γ elements) results in identical optimal topologies. The Q4γ elements are shown to be largely insensitive, over a large range of values, to the penalty parameter which enforces the definition of in-plane rotation in terms of in-plane displacements.

The plate examples presented confirmed that, since the DKQ element is shear rigid, optimal topologies computed using these elements are not sensitive to plate thickness. Elements employing an Assumed Natural Strain (ANS) formulation are shown to be robust and reliable. The ANS elements consistently recovered thin plate results similar to the DKQ results. Mindlin-Reissner elements with Selective Reduced Integration (SRI) on transverse shear terms are shown to be 'softer' in transverse shear than the ANS Mindlin-Reissner based elements and are therefore more sensitive to plate thickness. However, the SRI element possesses a spurious communicable mode which occasionally renders this element unstable. A plate example is introduced which exemplifies this problem.

Finally, the effect of parameters related to drilling DOFs of shell problems are studied. It is shown that optimal topologies computed with elements with drilling degrees of freedom based on sound mathematical theory are insensitive to the penalty parameter over a wide range. On the other hand, elements with an *ad hoc* treatment of drilling degrees of freedom are found to be far more sensitive to adjustable parameters. This sensitivity to the adjustable parameter is a furthermore shown to be problem dependent. A new shell example, in the form of a pretwisted beam, is introduced to highlight this dependence.

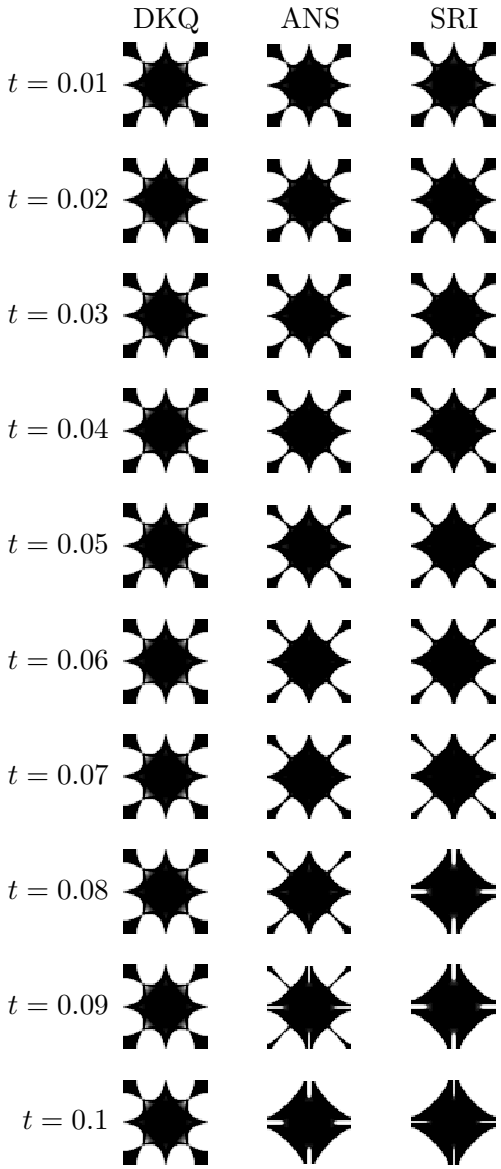

Figure 6.11: Optimal topologies of a simply supported plate subjected to center point load for various plate thicknesses, computed using different plate elements.

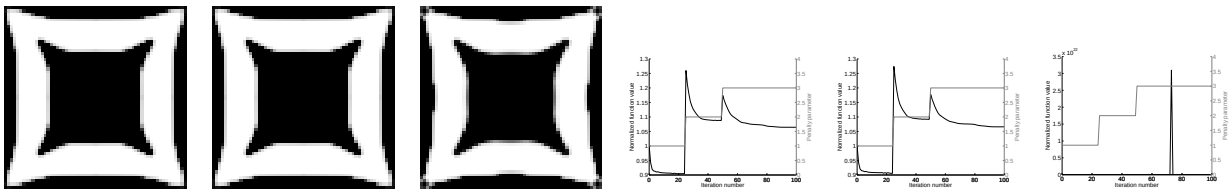

(a) DKQ. (b) ANS. (c) SRI. (d) DKQ. (e) ANS. (f) SRI.

Figure 6.12: Optimal topologies of a corner supported square plate subjected to center point load, ribbed model, $t = 0.01$: (a)-(c) optimal topologies, (d)-(f) convergence histories.

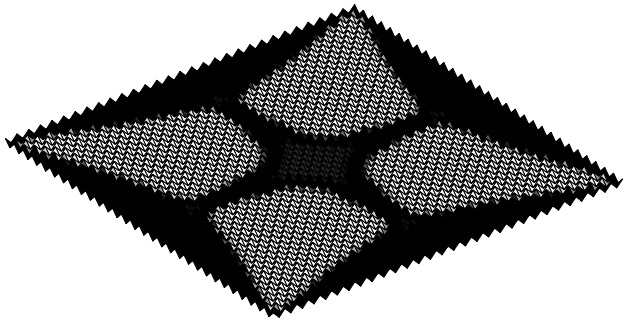

Figure 6.13: Optimal topology, computed using DKQ, of the corner supported plate subjected to distributed load with thin ribbed material model: Displaced shape analyzed using SRI elements, amplification factor 3×10^{-10}.

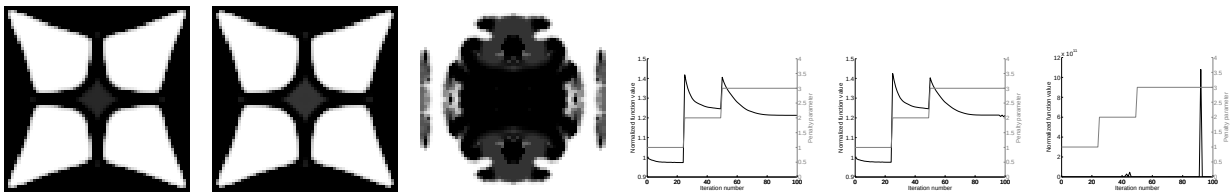

(a) DKQ. (b) ANS. (c) SRI. (d) DKQ. (e) ANS. (f) SRI.

Figure 6.14: Optimal topologies of a corner supported square plate subjected to uniform distributed load, ribbed model, $t = 0.01$: (a)-(c) optimal topologies, (d)-(f) convergence histories.

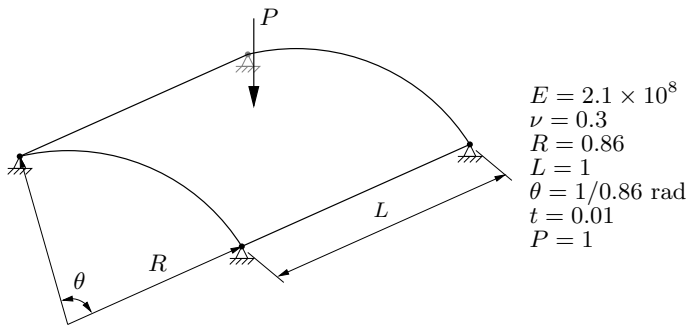

Figure 6.15: Corner supported cylinder geometry and constraints.

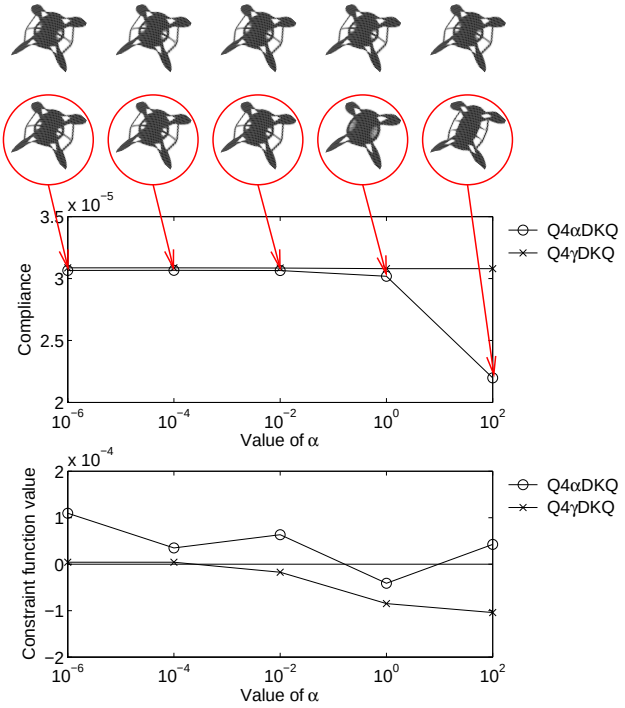

Figure 6.16: Optimal topologies of a corner supported cylinder with single layer material model. Above are the optimal topologies solved employing the standard Q4γDKQ element. On the second row are the optimal topologies employing Q4αDKQ for various values of scaling factor α. Also shown are the optimal function and constraint values for various values of scaling factor α.

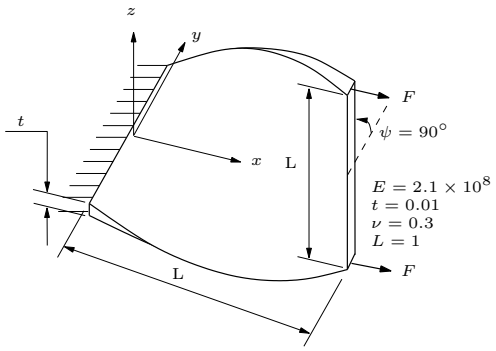

Figure 6.17: Pretwisted beam geometry and constraints.

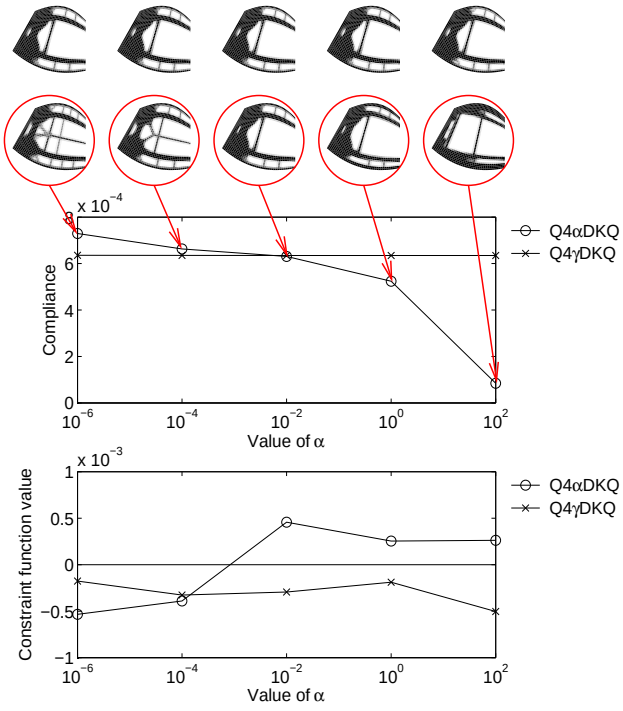

Figure 6.18: Optimal topologies of a pretwisted beam with single layer material model. Above are the optimal topologies solved employing the standard Q4γDKQ element. On the second row are the optimal topologies employing Q4αDKQ for various values of scaling factor α. Also shown are the optimal function and constraint values for various values of scaling factor α.

Chapter 7

Effect of reduced order integration schemes and elements with in-plane rotations on checkerboard patterns in topology optimization

7.1 Summary

In this chapter, the effect of different planar element formulations on the stiffness of a checkerboard patch of elements is investigated. Standard 4-node bilinear elements (Q4) as well as 4-node elements with drilling degrees of freedom (Q4X) are considered. Furthermore, the effect of reduced order integration schemes on quadratic Q8 and Q9 elements is examined. Employing a reduced 4-point integration scheme in elemental calculations of higher order elements leads to the introduction of spurious zero-energy modes, some of which are communicable. Here, it is shown how modified reduced order integration schemes suppress spurious modes, while simultaneously reducing the stiffness of a checkerboard patch of elements, thereby making checkerboarding unlikely in topology optimization applications. It is finally also shown how this reduced stiffness allows for the use of a larger penalty parameter in the SIMP material parameterization, making intermediate densities unattractive without risking the formation of checkerboard material layouts.

7.2 Introduction

Topology optimization has seen a resurgence in popularity in recent times, largely credited to the paper of Bendsøe and Kikuchi [107]. This increased research interest has led to many significant advances and has seen the use of topology optimization in a number of applications and fields. Examples include minimum compliance problems (against which most new procedures and theories are benchmarked) [109, 110], vibration problems [104, 136], compliant mechanism design [100, 137] and even multiphysics problems [106, 138].

However it was accepted relatively early on, during this recent progress, that there are several numerical issues which need to be carefully dealt with in order to achieve sensible results [14]. One of the numerical issues that has received significant attention is the problem of checkerboarding. Checkerboarding is characterised by a significant part of the material layout, forming a checkerboard pattern. That is, if the finite element method is employed and elemental densities are graphically represented on a finite element mesh, the resulting pattern is reminiscent of a checkerboard.

It is pertinent at this stage to emphasise that topology optimization is a challenging global optimization problem. It should therefore be qualified that, although checkerboarding is accepted as being a physical phenomenon, the severity of checkerboarding is dependant on a number of factors, including: optimization algorithm type and settings (such as step limit), objective function (checkerboarding is less prevalent in compliant mechanism design than minimum compliance problems), starting point, as well as problem discretization and, in the SIMP environment, whether or not continuation methods are applied or not. Furthermore, there have been numerous schemes suggested to eliminate checkerboarding from a design generated using topology optimization. Examples include [15, 98] as well as many of the restriction methods detailed in Appendix A. These schemes naturally also have an effect on the checkerboarding severity.

The checkerboarding problem was studied in detail by especially Jog and Haber [102] and Díaz and Sigmund [14]. By interpreting the layout problem as a mixed variational problem in density and displacement, Jog and Haber attribute this problem to a violation of the Babuska-Brezzi or LBB condition. Unfortunately, as reported by Díaz and Sigmund [14], the conditions under which the standard Babuska-Brezzi arguments are applied to mixed variational problems are not met by the layout optimization problem [139].

A different approach was adopted by Díaz and Sigmund. They suggest that the pattens can be explained on the basis of local behaviour. They show that numerical approximations introduced by the finite element method may, under certain circumstances, cause material arranged in a checkerboard fashion to appear artificially stiff. Under these conditions a local arrangement in a checkerboard-like fashion appears to be locally stiffer than any other arrangement of the two constitute materials with the same volume.

Díaz and Sigmund found that quadratic Q9 elements are less likely to checkerboard than standard bilinear Q4 elements. However, the numerical stability of higher order elements (such as Q8 or Q9) comes at a price. They are numerically more expensive than lower order (Q4) elements due to lower connectivity of Q4 elements. Nevertheless, with the advent of ever increasing computing power, this additional expense may become less significant in future. It is therefore still of interest to study the use of higher order elements to alleviate checkerboarding in topology optimization problems. The work of Díaz and Sigmund is built upon here, by exploring the use of reduced order integration schemes in higher order elements in order to further reduce the stiffness of a checkerboard patch of elements.

In the earlier days of the development of the finite element method, numerical integration schemes attracted significant attention (e.g. see [54, 86, 87, 88]), possibly due to the limitations of the computing devices available at the time.

Reduced integration schemes are less numerically expensive than higher order schemes. This

saving in computational effort on the element level comes at the expense of integration accuracy. However, the induced integration error is often on higher-order terms, which in some instances actually enhances finite element accuracy. In summary, reduced integration may be able to simultaneously reduce cost, reduce accuracy in the evaluation of integration expressions, and increase the accuracy of the finite element analysis. This principle was recently successfully applied by Long and Groenwold [140] who applied modified reduced order quadratures to quadratic Q8 and Q9 elements (see also Chapter 4).

It is well known that quadratic elements are less susceptible to checkerboarding than standard bilinear elements. Since planar elements with drilling degrees of freedom (DOFs) are based on a quadratic 'parent element', the stiffness of a checkerboard arrangement of elements with drilling DOFs is also briefly investigated.

This chapter is set out as follows: In Section 7.3 the modified numerical integration schemes employed in this study are briefly described. Section 7.4 presents a very brief discussion of element formulations with drilling degrees of freedom. The theory used by Díaz and Sigmund to estimate the stiffness of a checkerboard patch is summarised in Section 7.5. In Section 7.6 the numerical results of employing reduced order integration on elements with drilling degrees of freedom, and on higher order elements such as Q8 and Q9, are presented. Finally, conclusions are drawn in Section 7.7.

7.3 Modified reduced order quadrature integration rules

Reduced integration is frequently used in evaluating the element stiffness matrix of quadratically interpolated finite elements. Typical examples are the serendipity (Q8) and Lagrangian (Q9) membrane finite elements, for which a reduced 2×2 Gauss-Legendre integration rule is frequently used, as opposed to full 3×3 Gauss-Legendre integration. This 'softens' these element, thereby increasing accuracy, albeit at the introduction of spurious zero energy modes on the element level. This is in general not considered problematic for the 'hourglass' mode common to Q8 and Q9 elements, since this spurious mode is non-communicable. The remaining two zero energy modes occurring in the Q9 element are indeed communicable. However, in topology optimization for instance, conditions may arise where the spurious mode associated with the Q8 element becomes activated. To effectively suppress these modes altogether in elements employing quadratic interpolation fields, two modified quadratures have been employed [140]. As compared to fully integrated elements, the new rules enhance element accuracy due to the introduction of soft, higher-order deformation modes. For completeness, some detail regarding the schemes employed is presented. For further detail, the reader is referred to Chapter 4 and [140].

7.3.1 Numerical integration schemes

The schemes proposed in this section were originally proposed by Dovey [54]. Consider the area integral given by

$$I = \int_{-1}^{1} \int_{-1}^{1} F(r,s) \, \mathrm{d}r \, \mathrm{d}s, \tag{7.1}$$

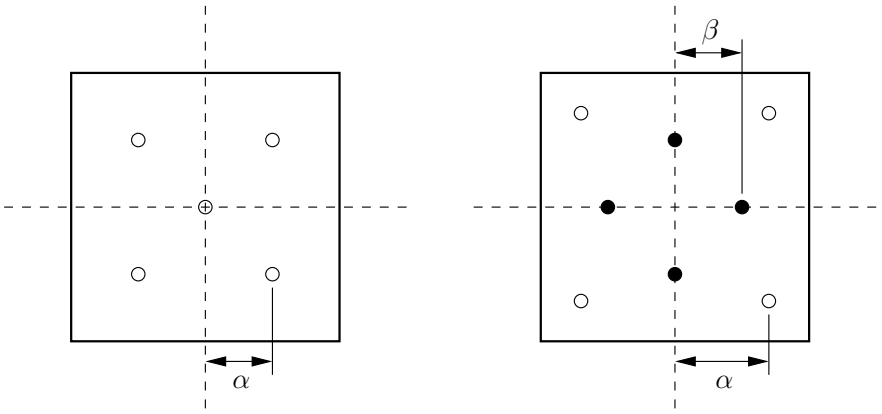

(a) 5-point scheme. (b) 8-point scheme.

Figure 7.1: Modified reduced order integration schemes.

where $F(r,s)$ is any polynomial function of r and s. Any polynomial expression of two variables can be expressed in the form

$$F(r,s) = \sum_{i,j} A_{ij} r^i s^j. \tag{7.2}$$

No limits are placed on the summation indices i and j as any arbitrary polynomial is being considered.

Let any N-point numerical integration rule be written as

$$I^* = \sum_{n=1}^{N} W_n F(r_n, s_n), \tag{7.3}$$

where I^* represents the numerical approximation to I. Integration point n is given by (r_n, s_n) and the associated weight is given as W_n.

Each term of (7.2) may be trivially integrated as follows:

$$\int_{-1}^{1}\int_{-1}^{1} A_{ij} r^i s^j \, dr ds = \begin{cases} \frac{2^2 A_{ij}}{(i+1)(j+1)} & i,j \text{ both even} \\ 0 & \text{otherwise} \end{cases} \tag{7.4}$$

Based on this exact integral, numerical approximations are proposed with leading error terms related to ever higher exponents.

7.3.2 A five-point rule

The 5-point rule is depicted in Figure 7.1(a). Due to symmetry, the weights W_α are identical. The rule is indicated by

$$I^* = W_0 F(0,0) + W_\alpha F(\pm\alpha, \pm\alpha). \tag{7.5}$$

The second term of (7.5) indicates four points when all combinations of positive and negative signs are taken. Now, combining (7.2) and (7.3), comparing with (7.4) and grouping terms including A_{00}, A_{20} and A_{02} and disregarding the centre weight (refer to Chapter 4 for details for details) leads to:

$$\alpha = 1/\sqrt{3}; \quad W_\alpha = 1 \quad \text{and} \quad W_0 = 0, \tag{7.6}$$

which is identical to the 2×2 Gaussian product rule. However, the center point may be retained by selecting a value for W_0 and computing W_α and α.

The scheme is now defined by

$$W_\alpha = 1 - W_0/4, \tag{7.7}$$

$$\alpha = \left(\frac{1}{3W_\alpha}\right)^{\frac{1}{2}}. \tag{7.8}$$

The scheme only has physical meaning while $0 \leq W_0 < 4$. The error in the A_{22} term is minimized as $W_0 \rightarrow 0$. In practice this implies that the 5-point scheme converges to the 2×2 Gaussian scheme as $W_0 \rightarrow 0$. It was however, shown by Long and Groenwold that it is preferable if W_0 is chosen such that $0 \leq W_0 \leq \frac{8}{3}$.

7.3.3 An eight-point rule

The 8-point rule is depicted in Figure 7.1(b). The rule is described by

$$I^* = W_\alpha F(\pm\alpha, \pm\alpha) + W_\beta \left[F(\pm\beta, 0) + F(0, \pm\beta)\right]. \tag{7.9}$$

As demonstrated in Chapter 4, the four equations associated with A_{00}, (A_{02} and A_{20}), A_{22} and (A_{04} and A_{40}) may be satisfied simultaneously and the solution is

$$\alpha = \sqrt{7/9}; \quad W_\alpha = 9/49; \quad \beta = \sqrt{7/15}; \quad W_\beta = 40/49. \tag{7.10}$$

This rule gives the same order of accuracy as the 3 x 3 Gaussian rule. A scheme of lower accuracy is defined by

$$W_\alpha = 1 - W_\beta, \tag{7.11}$$

$$\alpha = \left(\frac{1}{9W_\alpha}\right)^{\frac{1}{4}}, \tag{7.12}$$

$$\beta = \left(\frac{2/3 - 2W_\alpha\alpha^2}{W_\beta}\right)^{\frac{1}{2}}. \tag{7.13}$$

In this case both α and β are restricted to be between 0 and 1. This implies that W_β be chosen such that $0 < W_\beta < \frac{8}{9}$.

7.4 Elements with drilling degrees of freedom

In this section, a very brief account of formulations for elements with drilling degrees of freedom is presented. These membrane elements account for in-plane rotations based on a continuum mechanics definition of rotation. The approach relies on a variational formulation employing an independent rotation field, as presented by Hughes and Brezzi [18]. It utilizes the skew-symmetric part of the stress tensor as a Lagrange multiplier to enforce equality of independent rotations and the skew-symmetric part of the displacement gradient in a weak sense. The stress tensor is therefore not *a priori* assumed to be symmetric.

Hughes and Brezzi show that a displacement-based functional can be derived by eliminating the skew-symmetric part of stress from a mixed-type functional. Employing a matrix notation similar to that in [22], the result is the modified functional

$$\Pi_{\mathrm{m}}^{\mathrm{Q4}\gamma}(\boldsymbol{u}_{\mathrm{m}},\theta_z) = \frac{1}{2}\int_V \boldsymbol{\epsilon}_{\mathrm{m}}{}^T \boldsymbol{C}_{\mathrm{m}}\boldsymbol{\epsilon}_{\mathrm{m}}\mathrm{d}V + \frac{1}{2}\gamma\int_V(\omega_{xy}-\theta_z)^2\mathrm{d}V - \frac{1}{2}\int_V \boldsymbol{u}_{\mathrm{m}}{}^T\boldsymbol{f}\mathrm{d}V, \tag{7.14}$$

where ω_{xy} is the rotational part of the displacement gradient, given by

$$\omega_{xy} = \frac{\partial v}{\partial x} - \frac{\partial u}{\partial y}. \tag{7.15}$$

In the foregoing, $\boldsymbol{\epsilon}_{\mathrm{m}}$ represents the membrane strains, $\boldsymbol{C}_{\mathrm{m}}$ the membrane constitutive matrix, $\boldsymbol{u}_{\mathrm{m}}$ denotes the in-plane membrane displacement field $[u, v]$ and $\boldsymbol{f}$ the body forces.

The independent rotations θ_z, are interpolated using standard bilinear functions, while the in-plane displacement approximation is taken as an Allman-type interpolation [23].

In matrix form the first term of $\Pi_{\mathrm{m}}^{\mathrm{Q4}\gamma}$ can be shown to reduce to

$$\tilde{\boldsymbol{k}}_{\mathrm{m}}^{\mathrm{Q4}\gamma} = \int_A \left[\boldsymbol{B}_{\mathrm{m}}^{\mathrm{Q4}\gamma} \;\; \boldsymbol{G}_{\mathrm{m}}^{\mathrm{Q4}\gamma}\right]^T \boldsymbol{\mathcal{A}} \left[\boldsymbol{B}_{\mathrm{m}}^{\mathrm{Q4}\gamma} \;\; \boldsymbol{G}_{\mathrm{m}}^{\mathrm{Q4}\gamma}\right] \mathrm{d}A, \tag{7.16}$$

where $\tilde{\boldsymbol{k}}_{\mathrm{m}}^{\mathrm{Q4}\gamma}$ is a 12×12 matrix.

The penalty term, in matrix form, corresponding to the second term of $\Pi_{\mathrm{m}}^{\mathrm{Q4}\gamma}$ is derived:

$$\boldsymbol{p}_{\mathrm{m}}^{\gamma} = \gamma\int_A \begin{Bmatrix} \boldsymbol{b}_{\mathrm{m}}^{\mathrm{Q4}\gamma} \\ \boldsymbol{g}_{\mathrm{m}}^{\mathrm{Q4}\gamma} \end{Bmatrix} \left[\boldsymbol{b}_{\mathrm{m}}^{\mathrm{Q4}\gamma} \;\; \boldsymbol{g}_{\mathrm{m}}^{\mathrm{Q4}\gamma}\right] \mathrm{d}A, \tag{7.17}$$

$$\text{where } \gamma = \bar{\gamma}G, \tag{7.18}$$

with G the shear modulus which is a function of the artificial density variable, and $\bar{\gamma}$ an adjustable parameter as in (6.25).

The element stiffness matrix therefore becomes

$$\boldsymbol{k}_{\mathrm{m}}^{\mathrm{Q4}\gamma} = \tilde{\boldsymbol{k}}_{\mathrm{m}}^{\mathrm{Q4}\gamma} + \boldsymbol{p}_{\mathrm{m}}^{\gamma}. \tag{7.19}$$

$\boldsymbol{p}_{\mathrm{m}}^{\gamma}$ is integrated by a single point Gaussian quadrature. By fully integrating $\tilde{\boldsymbol{k}}_{\mathrm{m}}^{\mathrm{Q4}\gamma}$ and combining with $\boldsymbol{p}_{\mathrm{m}}^{\gamma}$, spurious zero energy modes are prevented [21]. No additional devices (e.g. see [24]) are required. The same holds if a modified 8-point quadrature, or 5-point rule [45], is employed to integrate $\tilde{\boldsymbol{k}}_{\mathrm{m}}^{\mathrm{Q4}\gamma}$.

The forms of $\boldsymbol{B}_{\mathrm{m}}^{\mathrm{Q4}\gamma}$, $\boldsymbol{G}_{\mathrm{m}}^{\mathrm{Q4}\gamma}$, $\boldsymbol{b}_{\mathrm{m}}^{\mathrm{Q4}\gamma}$ and $\boldsymbol{g}_{\mathrm{m}}^{\mathrm{Q4}\gamma}$ can be found in, for example [21]. Once again, for more detail regarding these elements, the reader is referred to Chapters 2 and 3.

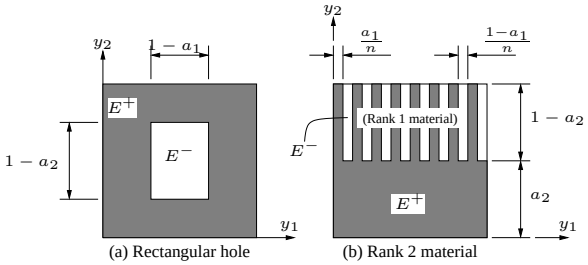

Figure 7.2: Example base cells often used in topology optimization.

7.5 On the stiffness of a checkerboard patch of elements

In this section the essential theory and results of Díaz and Sigmund [14] will be highlighted. Since much of the work presented in this section is based on their work, and in order to ensure continuity for those readers familiar with the work of Díaz and Sigmund, their notation will be used here. This section starts with a short summary of the minimum compliance topology optimization problem using homogenization theory and concludes with the main results from their paper.

7.5.1 Topology optimization using homogenization

Even with todays advanced computing power, a numerical analysis of a composite structure with complex microstructure, is infeasible if the microstructure itself is modelled. A cellular body, made of solids and voids, may be considered a simple such composite material. This is typically the type of material exploited to perform topology optimization.

Homogenization theory can be employed to replace a composite with periodic microstructure, with an effective material model. These materials are usually described in terms of a base cell, the smallest representative unit of material. Homogenization theory allows macroscopic material characterization, based solely on analysis of the microscopic base cell. Evaluation of the base cell can be performed analytically if the base cell is sufficiently simple in structure. Alternatively, a numerical analysis, usually involving the Finite Element Method (FEM), may be called for.

In a topology optimization setting, topology is most frequently described by a continuous density function which effectively transforms the problem into a material distribution problem using composite materials.

In general, the composite (base cell) is made up of a mixture of two isotropic materials, one strong with constitutive tensor E^+, and one weak with constitutive tensor $E^- \ll E^+$. The weak material typically represents a void, allowing admission or removal of holes in the structure.

Examples of two common base cells are depicted in Figure 7.2. The first is a square cell with rectangular hole, see Bendsøe and Kikuchi [107] and the second is a so-called Rank 2

material as studied by, for example Milton and Kohn [141].

The continuous density function, describing the material layout or topology, of these two base cells is given by the ratio of strong material volume to total base cell volume, in terms of cell parameters (a_1 and a_2 in Figure 7.2). The effective constitutive tensor $\bar{E}$, is then sought in terms of cell parameters a_1, a_2 and of course the two isotropic material property tensors E^+ and E^-.

The minimum compliance topology optimization problem consists of finding the material layout which minimises the mean compliance, while maintaining a bound on the amount of strong material:

$$\min_{\rho \in X_M} \min_{a \in X_\rho} f(u^*), \tag{7.20}$$

where $f(u^*)$ is the mean compliance at equilibrium, corresponding to displacement solution u^*.

$$X_M = \left\{ \rho \in L^\infty(\Omega) : \ 0 \leq \rho \leq 1, \ \int_\Omega \rho \ \mathrm{d}x \leq M \right\}, \tag{7.21}$$

where M is an upper bound on the amount of strong material, Ω is the structural domain and ρ is a scalar density function based on unit cell parameters $a = \{a_1, \ a_2\}$. Finally,

$$X_\rho = \left\{ a \in R^2 : \ a_1 + a_2 - a_1 a_2 = \rho, \ 0 \leq a_1, a_2 \leq 1 \right\}. \tag{7.22}$$

It is well known that the minimum compliance topology optimization problem can be cast in the form:

$$\max_{\rho \in X_M} \min_{u \in K} \left\{ \int_\Omega \max_{a \in X_\rho} \ w \ \mathrm{d}x - f(u) \right\}, \ \text{where} \tag{7.23}$$

$$K = \left\{ u^h \in H^1(\Omega) : \ u^h = 0 \text{ on } \Gamma^0 \right\}. \tag{7.24}$$

K represents the set of kinematically admissible displacement fields u and

$$w = \frac{1}{2} \bar{E}(a) \epsilon(u) \cdot \epsilon(u) \tag{7.25}$$

is the strain energy density resulting from strain field $\epsilon(u)$.

The implication of (7.23) is that for fixed density ρ and known strain field $\epsilon(u)$, the optimum local orthotropy is such that strain energy density is maximised [4, 14].

The finite element discretization of the problem in (7.23) can be written as

$$\max_{\rho^h \in X_R^h} \min_{u^h \in K^h} \left\{ \sum_{e=1}^{N} \frac{1}{2} \int_e \max_{a^e \in X_{\rho^e}} \ \bar{E}(a^e) \epsilon(u^e) \cdot \epsilon(u^e) \ \mathrm{d}x - f(u^h) \right\}, \tag{7.26}$$

assuming that Ω can be covered by N square finite elements. The density discretization ρ^h is assumed to be constant within each element e, taking value ρ^e. Standard shape functions $N_\alpha(x)$ are used to construct $u^h \subset K$, where elemental interpolations on element e are given by:

$$u^e = \sum_{\alpha=1}^{n} N_\alpha(x) u_\alpha^e, \ n = \text{number of nodes}, \tag{7.27}$$

and u_α^e are nodal DOFs.

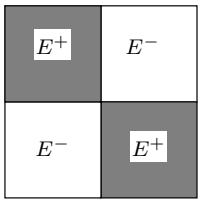

Figure 7.3: Checkerboard patch with average density ρ =1/2.

7.5.2 Effective properties of a checkerboard

Continuing to follow the procedure set out by Díaz and Sigmund, it is now demonstrated how the effective properties of a 'black-and-white' checkerboard patch of finite elements are computed. That is, the material distribution of a patch with average density $\rho = 1/2$. This represents a unit base cell Y which is divided into four equal quadrants Y^i such that $E = E^-$ in $Y^1 \cup Y^3$ and $E = E^+$ in $Y^2 \cup Y^4$, as shown in Figure 7.3.

The homogenized stiffness tensor is computed using the well-known formulae [4, 14, 141, 142, 143] by integration over the base cell area as

$$\bar{E}_{ijkl} = \int_Y \left\{ E_{ijkl} - E_{ijpq}\epsilon^*_{pq}[\chi^{(kl)}] \right\} \mathrm{d}y, \tag{7.28}$$

where the $Y-$periodic test fields $\chi_p^{(kl)}$ are found as the solution to the equilibrium equations

$$\int_Y E_{ijkl} \left\{ \epsilon^*_{pq}[\chi^{(kl)}] - \epsilon^{0^{(kl)}}_{pq} \right\} \frac{\partial v_i}{\partial y_j} \mathrm{d}y = 0, \tag{7.29}$$

for all $v \in V^h$, and $k, l = 1, 2$.

The finite element space V^h contains the same shape functions as those used to approximate the displacement field, defining

$$V^h = \left\{ v(y) \in R^2 : v(y) = N_\alpha(y) v^i_\alpha, \text{ if } y \in Y^i, \ i = 1, \ldots, 4 \right\}, \tag{7.30}$$

and where in the unit base cell, $v(0, y_2) = v(1, y_2)$ and $v(y_1, 0) = v(y_2, 1)$. The effective material tensor, given in (7.28) can be computed after solving (7.29) using three linearly independent test strains $\epsilon^{0^{(kl)}}_{pq}$ as discussed in, for example, [4, 141, 142, 143, 144].

In their paper, Díaz and Sigmund [14] find solutions to (7.28) and (7.29) using analytical integration of the finite element discretization. For an undistorted mesh of elements, this is equivalent to using full numerical integration, i.e. a 4 point Gauss quadrature for standard 4 noded elements and a 9 point scheme for 9 node elements.

They present the optimal strain energy density w^* for a known strain field $\bar{\epsilon}$ and average density $\rho = 1/2$ using: (*i*) rank 2 materials, (*ii*) materials with a base cell described by a rectangular hole, as well as (*iii*) SIMP parameterizations. They then use the foregoing theory to compare these results to the strain energy density calculated using a patch of 4 square elements, as depicted in Figure 7.3 with the same average density and applied strain field.

In particular, for rank 2 materials, it can be shown (see Díaz and Sigmund [14] and Jog *et al.* [145]) that the optimal strain energy density for fixed strain $\bar{\epsilon}$ and density $\rho = 1/2$ is given by:

$$w^*_{\text{Rank2}}(\bar{\epsilon}) = \frac{1}{2} \max_{a^e \in X, \rho^e = 1/2} \bar{E}_{\text{Rank2}}(a)\bar{\epsilon} \cdot \bar{\epsilon}, \tag{7.31}$$

where $\bar{E}_{\text{Rank2}}$ is the effective property tensor of the Rank 2 material and the a's are as depicted in Figure 7.2(b). For a void weak material ($E^- = 0$), $w^*_{\text{Rank2}}(\bar{\epsilon})$ may be expressed analytically (see Díaz and Sigmund [14]). This result is compared to

$$w^*_{\text{Q4}}(\bar{\epsilon}) = \frac{1}{2}\bar{E}_{\text{Q4}}\bar{\epsilon} \cdot \bar{\epsilon}, \text{ and} \tag{7.32}$$

$$w^*_{\text{Q9}}(\bar{\epsilon}) = \frac{1}{2}\bar{E}_{\text{Q9}}\bar{\epsilon} \cdot \bar{\epsilon}, \text{ where} \tag{7.33}$$

$\bar{E}_{\text{Q4}}$ and $\bar{E}_{\text{Q9}}$ are, respectively, the effective constitutive tensor of the 'black-and-white' patch of Q4 and Q9 elements, as depicted in Figure 7.3.

Similarly, for $\rho = 1/2$, the optimal strain energy density for a microstructure with a base cell described by a rectangular hole is given by

$$w^*_{\text{RHole}}(\bar{\epsilon}) = \frac{1}{2} \max_{a^e \in X, \rho^e = 1/2} \bar{E}_{\text{RHole}}(a)\bar{\epsilon} \cdot \bar{\epsilon}, \text{ and} \tag{7.34}$$

and for the SIMP material model,

$$w^*_{\text{SIMP}}(\bar{\epsilon}) = \frac{1}{2}\bar{E}_{\text{SIMP}}(\rho)\bar{\epsilon} \cdot \bar{\epsilon} = \frac{1}{2}\left(\frac{1}{2}\right)^p E^+\bar{\epsilon} \cdot \bar{\epsilon}, \tag{7.35}$$

where $\bar{E}_{\text{RHole}}$ and $\bar{E}_{\text{SIMP}}$ are the associated constitutive tensors. Given the preceding, the following relationships can be proven:

- For rank 2 layered materials (denoted Rank 2),

$$w^*_{\text{Q4}}(\bar{\epsilon}) \geq w^*_{\text{Rank 2}}(\bar{\epsilon}), \tag{7.36}$$
$$w^*_{\text{Q9}}(\bar{\epsilon}) < w^*_{\text{Rank 2}}(\bar{\epsilon}), \tag{7.37}$$

- For a square cell with rectangular hole (denoted RHole),

$$w^*_{\text{Q4}}(\bar{\epsilon}) > w^*_{\text{RHole}}(\bar{\epsilon}), \tag{7.38}$$
$$w^*_{\text{Q9}}(\bar{\epsilon}) < w^*_{\text{RHole}}(\bar{\epsilon}), \tag{7.39}$$

- For SIMP material model (denoted SIMP),

$$w^*_{\text{Q4}}(\bar{\epsilon}) = w^*_{\text{SIMP}}(\bar{\epsilon}), \text{ for } p = 1, \tag{7.40}$$
$$w^*_{\text{Q4}}(\bar{\epsilon}) > w^*_{\text{SIMP}}(\bar{\epsilon}), \text{ for } p > 1, \tag{7.41}$$
$$w^*_{\text{Q9}}(\bar{\epsilon}) < w^*_{\text{SIMP}}(\bar{\epsilon}), \text{ for } p < p^*_1(\nu), \tag{7.42}$$
$$w^*_{\text{Q9}}(\bar{\epsilon}) > w^*_{\text{SIMP}}(\bar{\epsilon}), \text{ for } p > p^*_2(\nu) \tag{7.43}$$

where

$$p_1^*(\nu) = \frac{\log\left(22/(6-5\nu)\right)}{\log(2)}, \text{ and} \tag{7.44}$$

$$p_2^*(\nu) = \frac{\log\left(2(6-5\nu)\right)}{\log(2)}. \tag{7.45}$$

Díaz and Sigmund suggest that checkerboarding is likely to occur if the strain energy density, based on the effective material tensor of a checkerboard patch of elements (e.g. $\bar{E}_{\text{Q4}}$, $\bar{E}_{\text{Q9}}$), is greater than that based on the effective material tensor of the relevant material parameterization (e.g. $\bar{E}_{\text{Rank2}}$, $\bar{E}_{\text{RHole}}$ or $\bar{E}_{\text{SIMP}}$). These relations can therefore be used to, not only explain why checkerboarding occurs, but also in the case of the SIMP material model, to recommend a suitable penalty parameter p.

7.6 Numerical results

In this section, some numerical results of the investigation are presented. Firstly, the effect of finite element formulation on the local χ field is explored qualitatively. Next, effective material properties of a checkerboard patch of elements are computed, employing various elements, and making use of various integration schemes. These effective properties are then used to compute strain energy densities for prescribed straining conditions. Finally, for the SIMP material model, the effects of integration scheme on the bounds of penalty parameter p_1^* and p_2^*, are investigated.

The following elements are considered in this study:

- *Q4*, a standard 4-node displacement based element.
- *Q4X*, a 4-node element with drilling degrees of freedom, based on the formulation presented in Section 7.4.
- *Q8*, the serendipity 8-node element based on the same formulation as Q4.
- *Q9*, the Lagrange 9-node element based on the the same formulation as Q4 and Q8.

The integration schemes evaluated are listed below:

- *4-point Gauss-Legendre scheme*, which is standard for evaluating Q4 elements and exact for undistorted elements. It is also commonly used to evaluate Q8 elements, although it leads to a spurious mode on the elements level.
- *5-point scheme*, with varying center weight W_0, see Section 7.3.2.
- *8-point scheme* with varying W_β, see Section 7.3.3.
- *9-point scheme Gauss-Legendre scheme*, which is the standard in evaluation of the Q9 element matrices and is also commonly used for Q8 elements.

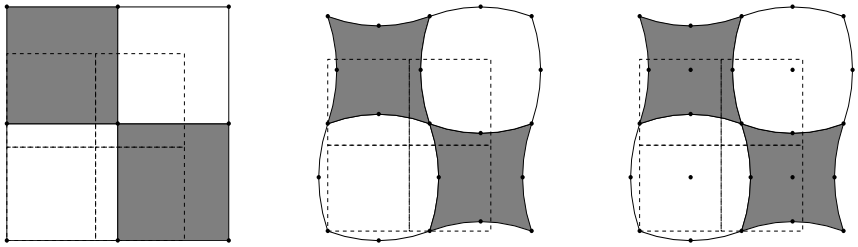

(a) Q4 and Q4X (b) Q8 (c) Q9

Figure 7.4: Local χ fields for various elements resulting from mean strain field $\bar{\epsilon}_{11} = \bar{\epsilon}_{22} = 1$ and $\bar{\epsilon}_{12} = 0$.

7.6.1 Effect of element formulation on local χ field

The solution to the cell problem (7.29) employing Q4 elements has been shown to be extremely simple, e.g. see [14]. The periodic deformation subjected to constant test strain is such that the strain in the patch is constant. That is to say,

$$\epsilon^*[\chi^{(kl)}] = 0. \tag{7.46}$$

To illustrate, the χ field for a patch of Q4 elements subjected to a constant prestrain $\bar{\epsilon}_{11} = \bar{\epsilon}_{22} = 1$, and $\bar{\epsilon}_{12} = 0$, is depicted in Figure 7.4(a).

It is now investigated whether the additional straining modes, associated with Q4X elements, result in non-constant patch strains when subjected to similar test strains. These elements are based on an 8-node parent element employing quadratic Allman-type shape functions as explained in Section 7.4. The side nodes (5-8) are then 'condensed' to the corner nodes (1-4) and related to corner nodal rotations. Q4X elements, therefore possess 3 degrees of freedom per node in total, i.e. 2 in-plane translations and an in-plane rotation.

Unfortunately, as with Q4 elements, only constant patch strains result for Q4X elements. This can be attributed to the fact that, in the solution of the cell problem, the rotational degrees of freedom are not activated by any of the test strains, and therefore neither are the higher order straining modes. The resulting local χ field is thus identical to that of Q4, as depicted in Figure 7.4(a).

In previous work, e.g. see [146] and Section 5.4.2, it has been shown that Q4X elements do in fact yield slightly different results in terms of checkerboarding than Q4 elements. This is probably due to the fact that for realistic problems with complex strain fields, the skew-symmetric part of the displacement gradient becomes non-zero. Under these circumstances Q4X appears to be less stiff than standard Q4 elements, tending to effectively suppress the formation of large areas of checkerboard material layout. To illustrate, Figure 7.5(a) depicts the optimal topology of the MBB beam employing Q4 elements and a ramping strategy to increase penalty parameter p linearly from 1 to 3 in 34 iterations, and held at $p = 3$ for a further 16 iterations after which the solution is terminated. Figure 7.5(b) depicts the results employing the same strategy, but this time employing Q4X elements. Clearly, the severity of checkerboarding is significantly reduced compared to the results employing Q4 elements.

However, in the limit of mesh refinement only constant strains are experienced, and under

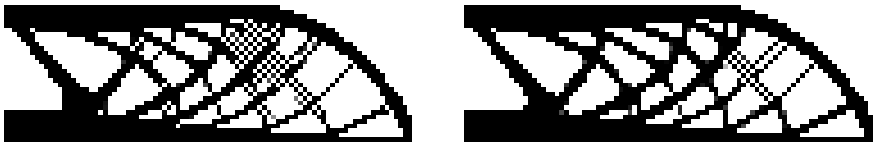

(a) Q4 elements. (b) Q4X elements

Figure 7.5: Optimal topologies of the MBB beam using symmetry and employing (a) Q4 and (b) Q4X elements.

these circumstances (fine meshes) more checkerboarding is expected. Numerical experiments have supported this conjecture. There is therefore no guarantee that Q4X elements will not checkerboard, especially when fine meshes are employed. However, elements with drilling degrees of freedom have been shown to be useful in topology optimization applications for specific problems, e.g. see [146, 77, 147]. Q4X elements are also more accurate and more stable than standard Q4 elements, at only a slight increase in numerical expense.

The local χ fields for Q8 and Q9 elements are distinctly different to those associated with the Q4 and Q4X elements. The material distribution results in nonzero local strain variations as shown in Figures 7.4(b) and (c) respectively.

The local χ fields for the Q8 and Q9 elements, depicted in Figure 7.4, are recognised as having a significant contribution from higher order staining modes. Recently, it has been shown that higher order deflection modes of quadratic elements can be softened by employing reduced order integration schemes. In the next section, these reduced order integration schemes are employed to compute effective material properties of checkerboards with the aim of reducing the strain energy density associated with prescribed strains $\bar{\epsilon}$.

7.6.2 Effect of element selection and integration scheme on effective properties of a checkerboard

A patch of 4 elements, arranged in a checkerboard as depicted in Figure 7.3, is used to determine the effect of element formulation, interpolation and integration scheme on the effective material properties computed using homogenization. In order to compare with results presented by Díaz and Sigmund, their material properties are used in similar calculations for Q4 and Q9 elements. Specifically, the weak material has constitutive tensor

$$E^- = 0, \tag{7.47}$$

and the strong material with constants

$$E^+_{1111} = E^+_{2222} = 1, E^+_{1122} = 0.3, E^+_{1212} = 0.35. \tag{7.48}$$

The variable weights selected for evaluation (for the 5- and 8-point schemes) are based on results presented in Chapter 4, wherein it was shown that employing a very small adjustable weight W could result in numerical instabilities, and therefore the use of values $W < 0.01$ are not recommended. Furthermore, in Chapter 4 settings of $W_0 = 0.1(8/3)$ and $W_\beta = 0.1(8/9)$

were suggested for improved stability and accuracy. It was also shown that a value of $W_\beta = 40/49$ results in a solution identical to employing a full 9-point integration scheme for undistorted elements. Values selected for evaluation are therefore $W_0 = 0.01$ and $8/30$ and $W_\beta = 0.01$, $8/90$ and $40/49$.

Effective material properties for the evaluated elements employing the various integration schemes and weights to solve (7.29) and then (7.28) are presented in Table 7.1.

Undistorted Q4 elements are exactly integrated using a 4 point Gauss quadrature, and all other (higher order in this case) integration schemes yield the same result. The resulting material constants are simply given by the average of the strong and weak material properties since $\epsilon^*[\chi^{(kl)}] = 0$ in (7.28).

A similar result is computed for the patch of Q4X elements, as expected, since Q4 and Q4X elements result in the same χ fields. The result is that the homogenised material properties of Q4X and Q4 are identical. Furthermore, the integration scheme employed has no effect since local strains are all constant. Note however, that employing a 4-point scheme results in a rank deficiency for Q4X elements.

Applying a reduced 4-point integration scheme in elemental calculations of Q8 elements is known to result in one spurious straining mode. For an assembly of 2 or more elements, this mode is largely non-communicable. However, as shown in, for example [17, 60, 140], the mode becomes communicable under certain circumstances, such as when elements are soft-supported (as may be the case in topology optimization applications), or in some dynamic problems (in which Escher modes appear). In the case considered here, the manner in which the two solid elements are connected in the patch (similar to a one-node hinge) also allows the mode to become communicable. In other words, the mode is not prevented from propagating between diagonal elements, since adjacent elements are empty.

Solution of the system of equations in (7.29) under these circumstances is obviously not recommended, due to the rank deficiency of the global stiffness matrix. However, for completeness singularity problems were suppressed in order to compute 'singular results'. Applying the 4-point scheme to the patch of Q8 elements and solving (7.29) and then (7.28) results in a constitutive tensor with all non-zero entries equal. This constitutive matrix is therefore rank deficient, and a strain of $\epsilon = \{\bar{\epsilon},\ \bar{\epsilon}, 0\}$ results in zero stress and therefore zero strain energy. This proves that application of the 4-point scheme in a topology optimization environment employing quadratic elements is not recommended.

The 5- and 8-point integration schemes are further evaluated with the weights suggested by Long and Groenwold [140]. The 5-point integration scheme has been shown, even at the low value of $W_0 = 0.01$, to suppress the spurious mode present when a 4-point scheme is employed. This result is mirrored by the results presented in Table 7.1. Application of the 8-point scheme, naturally also suppresses these modes. As shown in [140], application of the 8-point scheme with weight $W_\beta = 40/49$ yields identical results to a 9-point scheme for undistorted elements.

Identical results are computed when a patch of Q9, instead of Q8, elements are considered. However, application of a 4-point integration scheme to compute the element stiffness matrix of Q9 elements results in 3 spurious zero energy modes, two of which are communicable in an assemblage of elements. As a result, even application of the 5-point scheme results in a rank

deficient global stiffness matrix. Therefore, even though the computed results are similar for Q8 and Q9 elements, Q9 elements can only safely be used with 8- or 9-point integration schemes.

Finally, applying a full (9-point) integration scheme results in identical effective material properties for Q8 and Q9 elements. Since a 9-point scheme represents a full integration scheme for an undistorted quadratic element, the result is identical to solving the expressions analytically. This suggests that there is very little or no advantage in including the hierarchical bubble function, present in Q9 elements, in terms of checkerboarding of undistorted elements. Results for distorted elements may differ however.

7.6.3 Effect of integration scheme on strain energy density of quadratic elements

Since it was shown in Section 7.6.2 that both Q4 and Q4X elements result in identical effective material tensors independent of integration scheme, their results are not considered in this section. Results for Q4 elements may be found in the paper of Díaz and Sigmund [14]. Furthermore, since Q8 and Q9 elements produce identical results, as shown in Table 7.1, only results for Q8 elements will be presented here. Finally, due to the dominance of the SIMP material model in recent years, only results for SIMP will be focused upon in this subsection. However, these results are equally valid for other material parameterizations such as rank 2 materials.

The material parameterization for SIMP is extremely simple, with the equivalent material tensor given by

$$\bar{E}_{\text{SIMP}}(\rho) = \rho^p E^+, \text{ with } p \geq 1. \tag{7.49}$$

The minimum compliance problems can therefore be written as

$$\max_{\rho^h \in X_M} \min_{u^h \in K^h} \sum_{e=1}^{N} \frac{1}{2} \int_e (\rho^e)^p E^+ \epsilon(u^h) \cdot \epsilon(u^h) \mathrm{d}x - f(u^h), \tag{7.50}$$

with relevant space of density

$$X_M = \left\{ \rho \in L^\infty(\Omega) : \ 0 \leq \rho \leq 1, \ \int_\Omega \rho \ \mathrm{d}x \leq M \right\}. \tag{7.51}$$

For the SIMP problem, the strain energy density of a patch with average density ρ can simply be written as

$$w^*_{\text{SIMP}} = \frac{1}{2} (\rho)^p \, E^+ \bar{\epsilon} \cdot \bar{\epsilon}, \tag{7.52}$$

for prescribed strain $\bar{\epsilon}$. It can easily be shown that the strain energy density can be written in terms of principal strains as

$$\frac{w^*_{\text{SIMP}}}{E^+_{1111} \epsilon_I^2} = \frac{1}{2} (\rho)^p \left(1 + 2\nu\eta + \eta^2\right), \tag{7.53}$$

Table 7.1: Effective constitutive terms for different elements employing various integration schemes.

Element	Integration Scheme	Weight	$\bar{E}_{1111}$	$\bar{E}_{2211}=\bar{E}_{1122}$	$\bar{E}_{1211}=\bar{E}_{1112}$	$\bar{E}_{2222}$	$\bar{E}_{1222}=\bar{E}_{2212}$	$\bar{E}_{1212}$
Q4	4pt	–	5.0000e-01	1.5000e-01	-7.6328e-17	5.0000e-01	-6.9389e-18	1.7500e-01
Q4	5pt	$W_0 = 0.01$	5.0000e-01	1.5000e-01	-1.1102e-16	5.0000e-01	-6.9389e-18	1.7500e-01
Q4	5pt	$W_0 = 0.1\frac{8}{3}$	5.0000e-01	1.5000e-01	1.3032e-16	5.0000e-01	-2.6021e-18	1.7500e-01
Q4	8pt	$W_\beta = 0.01$	5.0000e-01	1.5000e-01	1.4658e-16	5.0000e-01	-4.5103e-17	1.7500e-01
Q4	8pt	$W_\beta = 0.1\frac{8}{9}$	5.0000e-01	1.5000e-01	1.6617e-16	5.0000e-01	-1.2040e-18	1.7500e-01
Q4	8pt	$W_\beta = \frac{40}{49}$	5.0000e-01	1.5000e-01	-1.3878e-17	5.0000e-01	0	1.7500e-01
Q4	9pt	–	5.0000e-01	1.5000e-01	-1.9452e-16	5.0000e-01	2.0046e-17	1.7500e-01
Q4X	4pt*	–	5.0000e-01	1.5000e-01	-4.8572e-17	5.0000e-01	3.4694e-17	1.7500e-01
Q4X	5pt	$W_0 = 0.01$	5.0000e-01	1.5000e-01	-2.7756e-17	5.0000e-01	-1.1796e-16	1.7500e-01
Q4X	5pt	$W_0 = 0.1\frac{8}{3}$	5.0000e-01	1.5000e-01	7.6328e-17	5.0000e-01	9.7145e-17	1.7500e-01
Q4X	8pt	$W_\beta = 0.01$	5.0000e-01	1.5000e-01	3.1225e-17	5.0000e-01	4.1633e-17	1.7500e-01
Q4X	8pt	$W_\beta = 0.1\frac{8}{9}$	5.0000e-01	1.5000e-01	1.0061e-16	5.0000e-01	2.7756e-17	1.7500e-01
Q4X	8pt	$W_\beta = \frac{40}{49}$	5.0000e-01	1.5000e-01	-1.0408e-17	5.0000e-01	2.7756e-17	1.7500e-01
Q4X	9pt	–	5.0000e-01	1.5000e-01	-1.0755e-16	5.0000e-01	-1.3878e-17	1.7500e-01
Q8	4pt*	–	1.1375e-01	1.1375e-01	-9.1901e-16	1.1375e-01	-3.1130e-15	1.1375e-01
Q8	5pt	$W_0 = 0.01$	1.1413e-01	1.1391e-01	2.9730e-16	1.1413e-01	1.0847e-16	1.1386e-01
Q8	5pt	$W_0 = 0.1\frac{8}{3}$	1.2428e-01	1.1814e-01	9.5590e-16	1.2428e-01	6.0057e-16	1.1682e-01
Q8	8pt	$W_\beta = 0.01$	1.1420e-01	1.1357e-01	-1.2468e-15	1.1420e-01	1.0146e-17	1.1376e-01
Q8	8pt	$W_\beta = 0.1\frac{8}{9}$	1.1783e-01	1.1211e-01	8.5974e-16	1.1783e-01	6.7693e-17	1.1387e-01
Q8	8pt	$W_\beta = \frac{40}{49}$	1.7184e-01	9.4066e-02	6.9568e-16	1.7184e-01	8.3630e-17	1.1582e-01
Q8	9pt	–	1.7184e-01	9.4066e-02	-5.0362e-16	1.7184e-01	-1.2759e-16	1.1582e-01
Q9	4pt*	–	1.1375e-01	1.1375e-01	2.9343e-17	1.1375e-01	-4.7436e-16	1.1375e-01
Q9	5pt*	$W_0 = 0.01$	1.1413e-01	1.1391e-01	-4.4465e-16	1.1413e-01	2.0281e-16	1.1386e-01
Q9	5pt*	$W_0 = 0.1\frac{8}{3}$	1.2428e-01	1.1814e-01	1.9876e-13	1.2428e-01	7.1124e-14	1.1682e-01
Q9	8pt	$W_\beta = 0.01$	1.1420e-01	1.1357e-01	-1.6860e-15	1.1420e-01	1.4914e-15	1.1376e-01
Q9	8pt	$W_\beta = 0.1\frac{8}{9}$	1.1783e-01	1.1211e-01	3.5281e-16	1.1783e-01	-8.8486e-17	1.1387e-01
Q9	8pt	$W_\beta = \frac{40}{49}$	1.7184e-01	9.4066e-02	-4.1730e-16	1.7184e-01	6.1592e-18	1.1582e-01
Q9	9pt	–	1.7184e-01	9.4066e-02	-6.1712e-16	1.7184e-01	1.2296e-16	1.1582e-01

* Singularity problems suppressed to perform the calulation. Use of this integration scheme is not recommended.

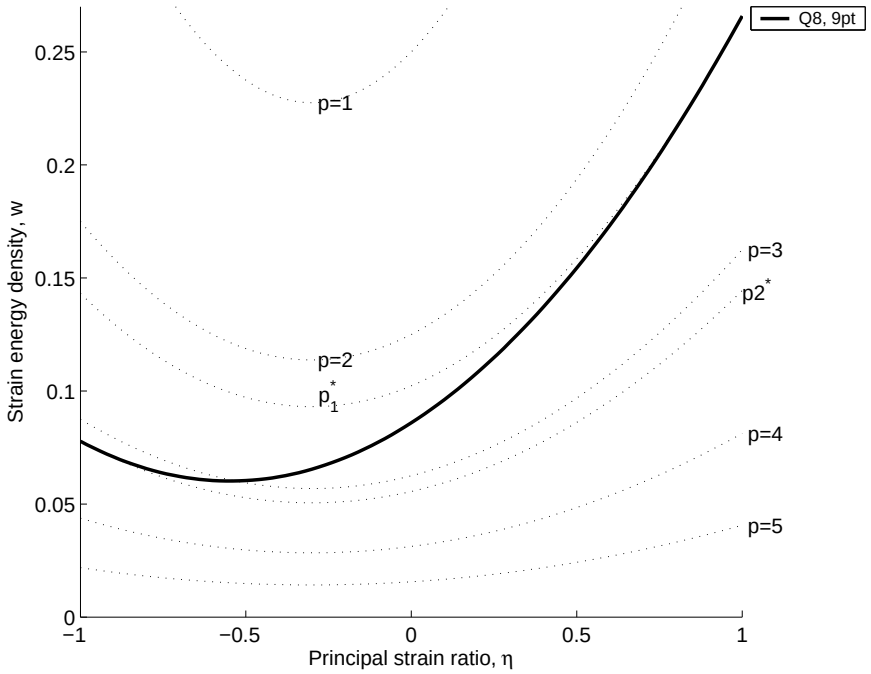

Figure 7.6: Strain energy density of fully integrated Q8 elements.

where η is the principal strain ratio $\eta = \frac{\epsilon_{II}}{\epsilon_I}$, with $|\epsilon_I| \geq |\epsilon_{II}|$, the principal strains.
Comparing this result to expressions for the (analytically or fully integrated) strain energy density of a patch of elements, given by

$$\frac{w^*_{Q4}}{E^+_{1111}\epsilon_I^2} = \frac{1}{4}\left(1 + 2\nu\eta + \eta^2\right), \tag{7.54}$$

for a checkerboard patch of Q4 elements, and

$$\begin{aligned}\frac{w^*_{Q9}}{E^+_{1111}\epsilon_I^2} =& \frac{1}{4}\left[\frac{(47 - 35\nu - 35\nu^2 + 25\nu^3)}{22(6 - 5\nu)} + \right.\\ & \frac{(50 - 26\nu - 70\nu^2 + 50\nu^3)}{22(6 - 5\nu)}\eta + \\ & \left.\frac{(47 - 35\nu - 35\nu^2 + 25\nu^3)}{22(6 - 5\nu)}\eta^2\right],\end{aligned} \tag{7.55}$$

for a patch consisting of Q9 elements, Díaz and Sigmund were able to prove the propositions in (7.40) to (7.43). Díaz and Sigmund conject that if w^*_{SIMP} is less than the strain energy density given by the equivalent patch of elements, checkerboarding is likely to occur.

The strain energy density given in (7.53) is now compared to numerically integrated counterparts of equations (7.54) and (7.55) computed using reduced order integration schemes and Q8 elements.

To illustrate, $w^*_{\text{Q8}}(\eta)$, computed using Q8 elements with full (9-point) integration, is plotted for unit E^+_{1111} and ϵ_I and for $\nu = 0.3$ in Figure 7.6. To reiterate, since Q8 and Q9 elements

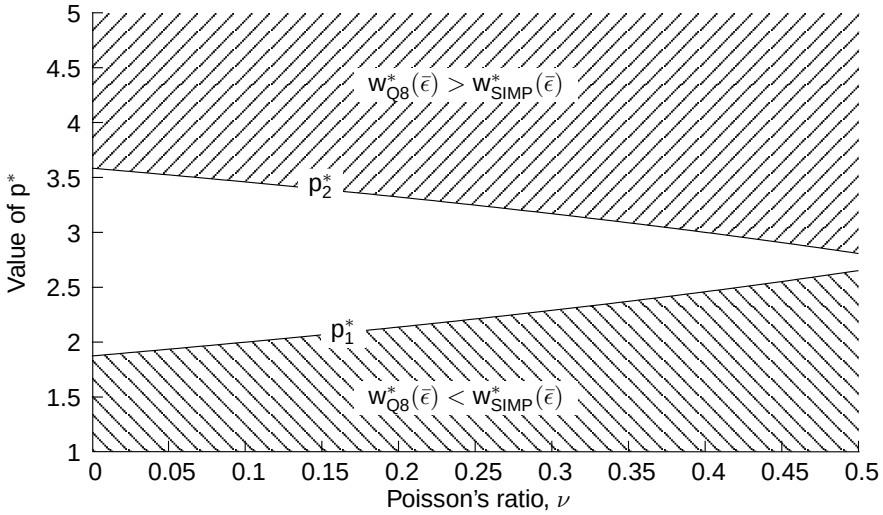

Figure 7.7: Variation of p^* for fully integrated Q8 elements.

result in identical effective material properties (see Table 7.1), the result of w^*_{Q9} is identical and given by (7.55), assuming the same integration scheme is employed. Also plotted in Figure 7.6, is $w^*_{\text{SIMP}}(\eta)$ computed using (7.53) for various values of penalty parameter p and $\rho = 1/2$. Clearly, for values of $1 \leq p < p^*_1$, $w^*_{\text{Q8}}(\eta) < w^*_{\text{SIMP}}(\eta)$, i.e. checkerboarding is unlikely, and when $p \geq p^*_2$, $w^*_{\text{Q8}}(\eta) \geq w^*_{\text{SIMP}}(\eta)$, i.e. checkerboarding is likely to occur (in both cases, independently of η).

For values of $p^*_1 < p < p^*_2$, $w^*_{\text{Q8}}(\eta)$ could be such that $w^*_{\text{Q8}}(\eta) < w^*_{\text{SIMP}}(\eta)$ or $w^*_{\text{Q8}}(\eta) > w^*_{\text{SIMP}}(\eta)$, depending on the strain being experienced. For example, if $p = 3$ in this example, $w^*_{\text{Q8}}(\eta) < w^*_{\text{SIMP}}(\eta)$ for $-1 \leq \eta \lessapprox -0.53$ and $w^*_{\text{Q8}}(\eta) > w^*_{\text{SIMP}}(\eta)$ for $-0.53 \lessapprox \eta \leq 1$.

Values of p^*_1 and p^*_2 can similarly be computed for each Poisson's ratio ν and plotted as shown in Figure 7.7. Values of p can therefore be selected using this figure so as to minimize the likelihood of checkerboarding. Since values of p as large as possible are desired (to penalize intermediate densities), a value of p^*_1 as large as possible is sought. If p^*_1 cannot be altered, the 'next best' would be to increase p^*_2.

Figures 7.8 and 7.9 depict the effect of applying the 5-point integration scheme on strain energy density, as a function of principal strain ratio η, for a patch of Q8 elements. The plot is for a material with $\nu = 0.3$, and as before, unit E^+_{1111} and ϵ_I. For clarity, only the 5-point scheme with weights $W_0 = 0.01$ and $W_0 = 8/30$ are depicted, together with the results computed using the 4-point and 9-point schemes for reference.

Clearly, applying the 5-point scheme with $W_0 = 0.01$ or $8/30$ significantly reduces the strain energy density associated with the considered straining modes. It can be shown that there is a monotonic increase in strain energy density with an increase in W_0. In fact, for weights close the the maximum permitted $8/3$, a higher strain energy density is estimated than the 9-point scheme.

Also shown in Figure 7.8 are the strain energy densities w^*_{SIMP}, calculated for different values of p. If $w^*_{\text{Q8}}(\bar{\epsilon}) > w^*_{\text{SIMP}}(\bar{\epsilon})$, checkerboarding is likely to occur. Therefore, application of reduced order integration schemes clearly reduces the likelihood of checkerboarding for

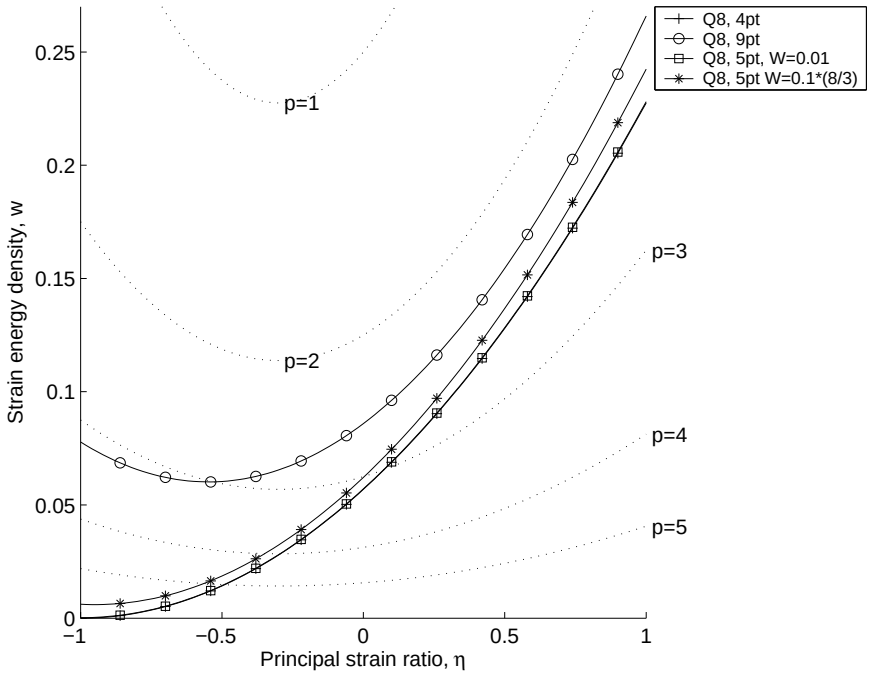

Figure 7.8: Strain energy density of Q8 elements with 5-point integration scheme.

a given p. Alternatively, it allows for the use of larger values of p without increasing the effective stiffness of the checkerboard patch of elements.

Finally, the minimum of w^*_{SIMP} computed using (7.53) occurs at $\eta = -\nu$, in this case $\eta = -0.3$. Increasing p simply decreases values of w^*_{SIMP}. However, computing the strain energy density of a patch of Q8 elements employing the various integration schemes, affects not only the value of $w^*_{\text{Q8}}(\eta)$, but also shifts the turning point towards $\eta = -1$ as the integration scheme becomes 'softer'. Unfortunately, this means that the gap between p^*_1 and p^*_2 is increased as will be shown in the next subsection.

For clarity, Figure 7.9 shows an enlargement of Figure 7.8, concentrating on the lower left corner. As described earlier, applying a 4-point integration scheme (which is equivalent to a 5-point scheme with $W_0 = 0$), results in zero strain energy being experienced at $\eta = -1$, corresponding to the rank deficiency in the constitutive matrix $\bar{E}$. Figure 7.9 also highlights the difference between the results employing the 4-point scheme and those using the 5-point scheme with $W_0 = 0.01$ and $8/30$, which is not clear in Figure 7.8.

Figures 7.10 and 7.11 depict the results for the same problem employing the 8-point scheme. Again, the results of the 4- and 9-point schemes are plotted together with results for w^*_{SIMP} for various values of p. Employing the 8-point scheme with $W_\beta = 40/49$ clearly produce identical results to those employing the 9-point scheme as expected. Again, employing low values of $W_\beta = 0.01$ and $8/90$ produce significantly lower values of strain energy density. Once again, an enlargement of Figure 7.10 is depicted in Figure 7.11. Slightly higher values of strain energy density are computed using the 8-point compared to the 5-point scheme for low weights, such as 0.01. This is significant, especially since the 5-point scheme is not recommended for Q9 elements.

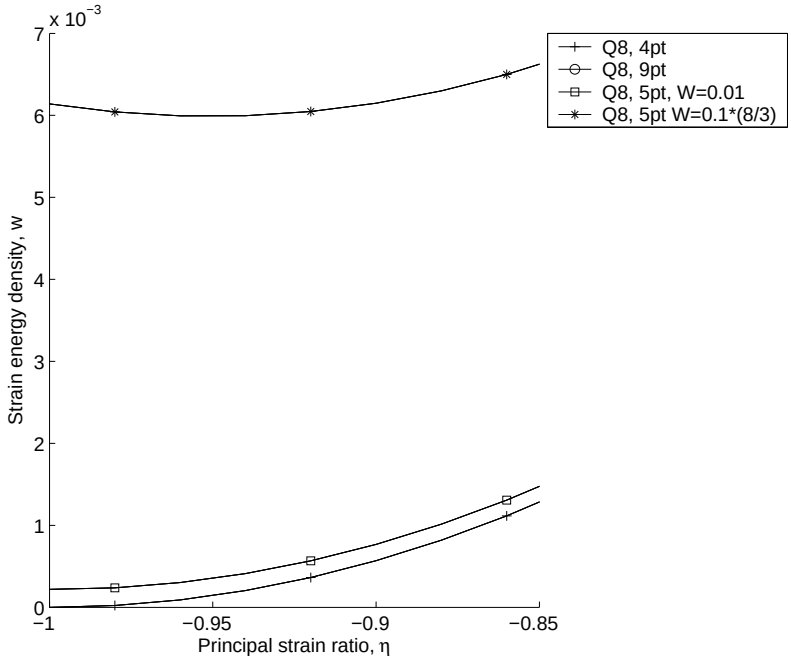

Figure 7.9: Zoom of strain energy density of Q8 elements with 5-point integration scheme.

7.6.4 Effect of integration scheme on penalty bounds p_1^* and p_2^*

Based on the computation of strain energy density for a checkerboard patch of Q8 elements compared to the expression for the SIMP material model in (7.53), limits of p can be determined for which $w^*_{\text{Q8}}(\bar{\epsilon}) < w^*_{\text{SIMP}}(\bar{\epsilon})$ (denoted $p_1^*(\nu)$) and $w^*_{\text{Q8}}(\bar{\epsilon}) > w^*_{\text{SIMP}}(\bar{\epsilon})$ (denoted $p_2^*(\nu)$) for each value of Poisson's ratio ν, as depicted in Figure 7.7.

In Figure 7.12, the values of $p_1^*(\nu)$ for Q8 elements employing the 5-point scheme are plotted, normalised with respect to the fully integrated equivalent, (shown in Figure 7.6). Also plotted as a reference are the values computed using 4- and 9-point integration schemes. The figure shows that employing the 5-point scheme with $W_0 = 0.01$ increases p_1^* significantly, almost to the level of the 4-point scheme. At a Poisson's ratio of $\nu = 0.3$ (common in engineering materials) an increase of approximately 10% is achieved employing this integration scheme. A slightly less marked increase is achieved employing the 5-point scheme with $W_0 = 8/30$.

Figure 7.13 depicts the results employing the 8-point scheme. In this case, the increase is approximately 10% for both weights $W_\beta = 0.01$ and $W_\beta = 8/90$. Once again, as expected, employing the 8-point scheme with a weight $W_\beta = 40/49$ results that are identical results to the results computed with the 9-point scheme.

Figures 7.14 and 7.15 depict the values of $p_2^*(\nu)$ for a patch of Q8 elements employing 5- and 8-point schemes, respectively. It was shown in Section 7.6.3, that for the 4-point scheme as $\eta \to -1$, $w^*_{\text{Q8}} \to 0$. This implies that $p_2^* \to \infty$. The results for the 4-point scheme are therefore not shown in Figures 7.14 and 7.15.

The scale of improvement for p_2^* is notably higher than that of p_1^*, with improvements of well over 300% for the 5-point scheme with $W_0 = 0.01$ and around 300% for the 8-point

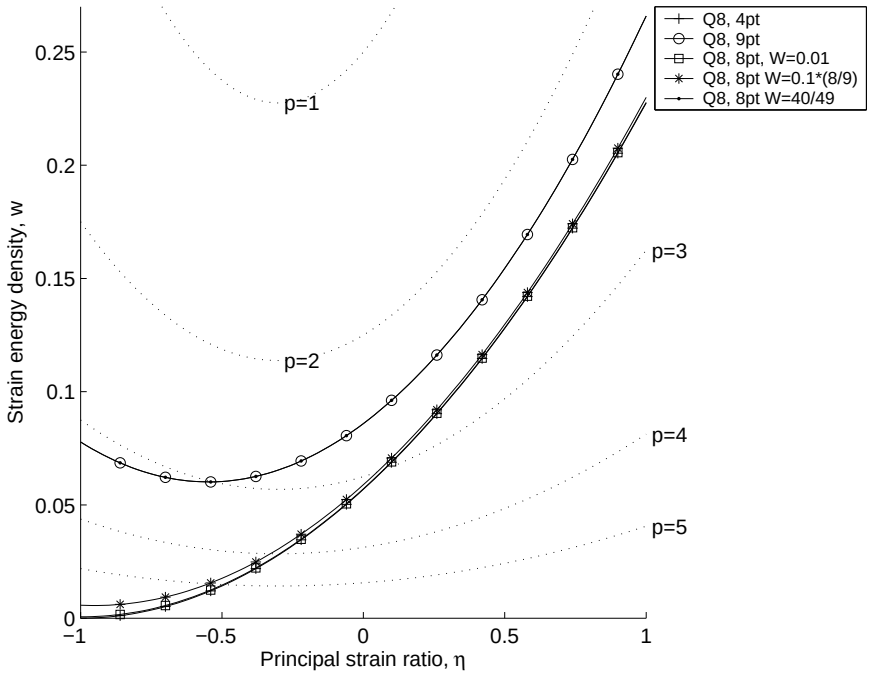

Figure 7.10: Strain energy density of Q8 elements with 8-point integration scheme.

scheme with $W_\beta = 0.01$. This results in a relatively wide range of values of p, for which checkerboarding likelihood depends on strain conditions. However, since reduced order integration does not add to element numerical cost (in fact cost is reduced) and accuracy is improved with no loss of stability, as shown in [140], it is recommend that our reduced order integration schemes be implemented for topology optimization problems.

7.7 Conclusions

Based on the theory of Díaz and Sigmund [14], the stiffness of checkerboard patches of various elements, employing different integration schemes have been assessed. Standard bilinear isoparametric 4-node elements and higher order 8- and 9-node elements as well as 4-node elements with in-plane rotational degrees of freedom are evaluated, employing full, reduced and modified reduced order integration schemes. The combinations of element and integration scheme which 'soften' the effective material tensor of a checkerboard patch of elements, effectively reducing the likelihood of checkerboarding in a topology optimization applications, are investigated.

Firstly, it is shown that both 4-node elements *with* drilling degrees of freedom (Q4X) and *without* (Q4) result in identical effective material properties for a checkerboard patch of elements. The additional degrees of freedom present in Q4X elements do not 'soften' the patch since none of the 3 linearly independent test strains applied to compute the effective material properties, activate the nodal in-plane rotations. It is however numerically demonstrated that for realistic problems, where nodal rotations are non-zero, checkerboarding is

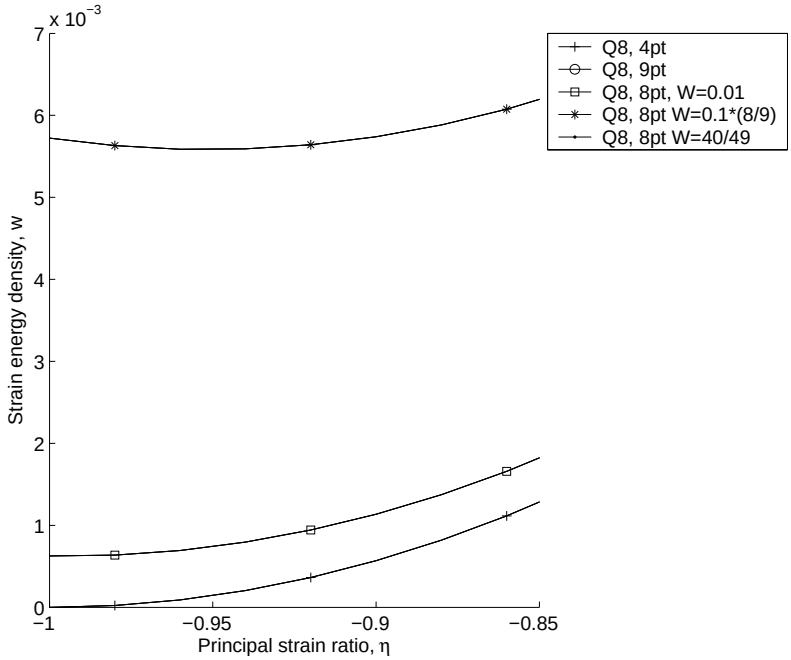

Figure 7.11: Zoom of strain energy density of Q8 elements with 8-point integration scheme.

notably reduced. However, since in the limit of mesh refinement only constant strain states are experienced, there is no guarantee that Q4X elements will unconditionally eliminate checkerboarding.

Next it is shown that undistorted higher order 8-node (Q8) and 9-node (Q9) elements result in identical effective material properties for the checkerboard patch of elements considered, if similar integration schemes are employed. It is shown that if a full (9-point) integration scheme is employed, both Q8 and Q9 elements result in effective material properties which are identical to the analytical solution computed by Díaz and Sigmund [14].

Q8 elements may be used with either 5-, 8- or 9-point integration schemes without the risk of introducing elemental rank deficiencies. Q9 elements are shown to be stable when using either 8- or 9-point schemes, with 4- and 5- point schemes resulting in communicable spurious modes.

The most significant improvements in terms of reducing the strain energy density (of a checkerboard patch) has been achieved by application of Q8 elements with a 5-point integration scheme with associated variable weight $W_0 = 0.01$. Employing this combination additionally increases the value of penalty which can be applied in the SIMP material parameterization without increasing the risk of checkerboarding. Specifically, p_1^*, the threshold at which checkerboarding is likely to occur independent of straining condition, is increased approximately 10%, while p_2^* is increased over 300% for common engineering materials This benefit is also cost-effective since employing the 5-point scheme simultaneously reduces computational cost, and increases the accuracy of the finite element approximation.

It is therefore recommended that Q8 elements with a 5-point integration scheme be used,

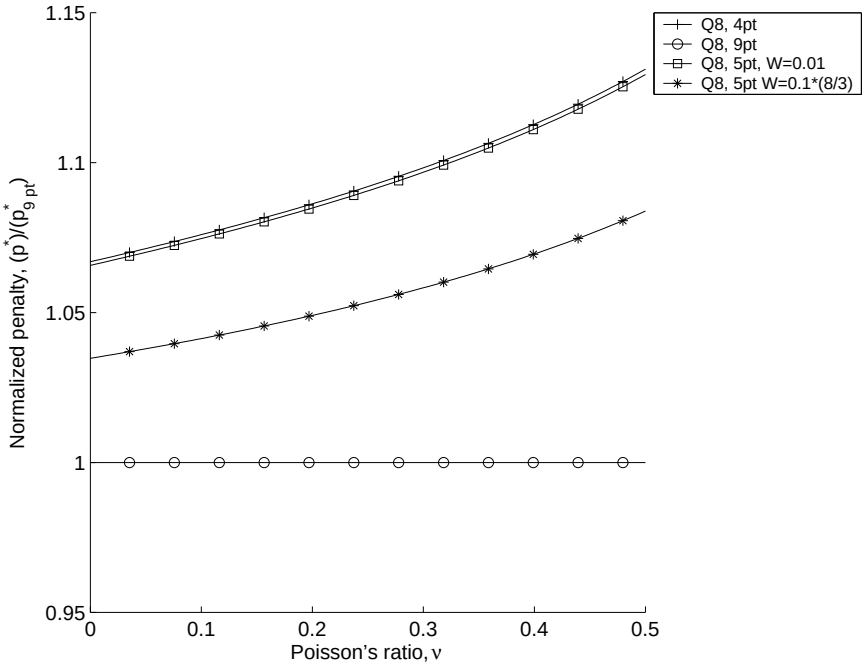

Figure 7.12: Effect of integration scheme setting on p_1^*: 5-point scheme.

instead of Q9 elements with full integration, when higher order elements are employed in SIMP topology optimization applications.

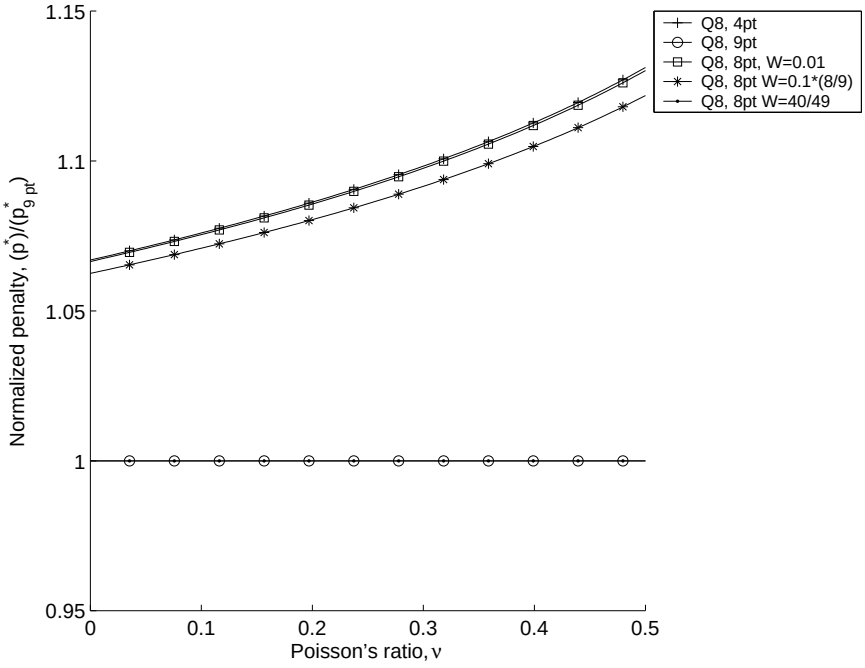

Figure 7.13: Effect of integration scheme setting on p_1^*: 8-point scheme.

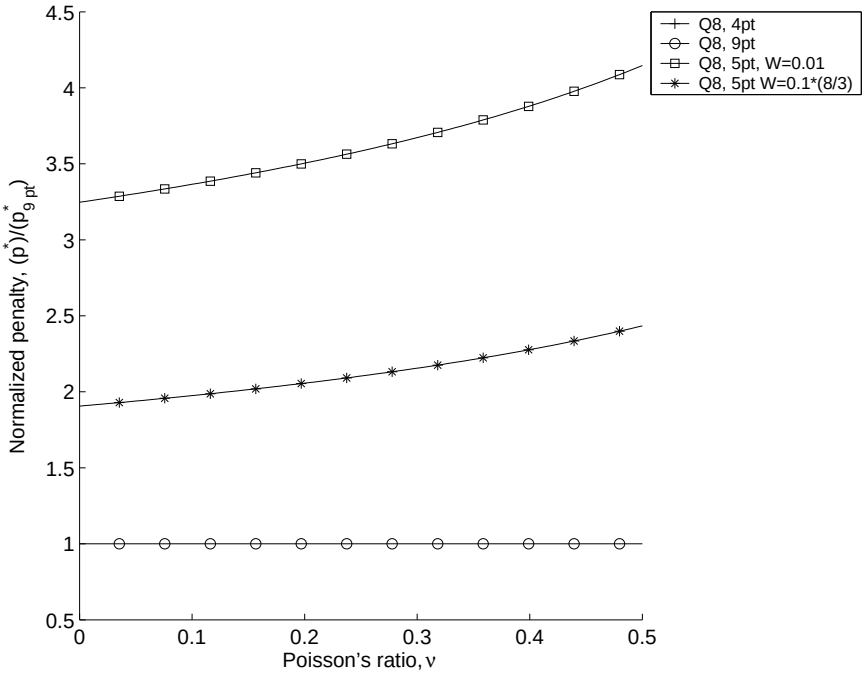

Figure 7.14: Effect of integration scheme setting on p_2^*: 5-point scheme.

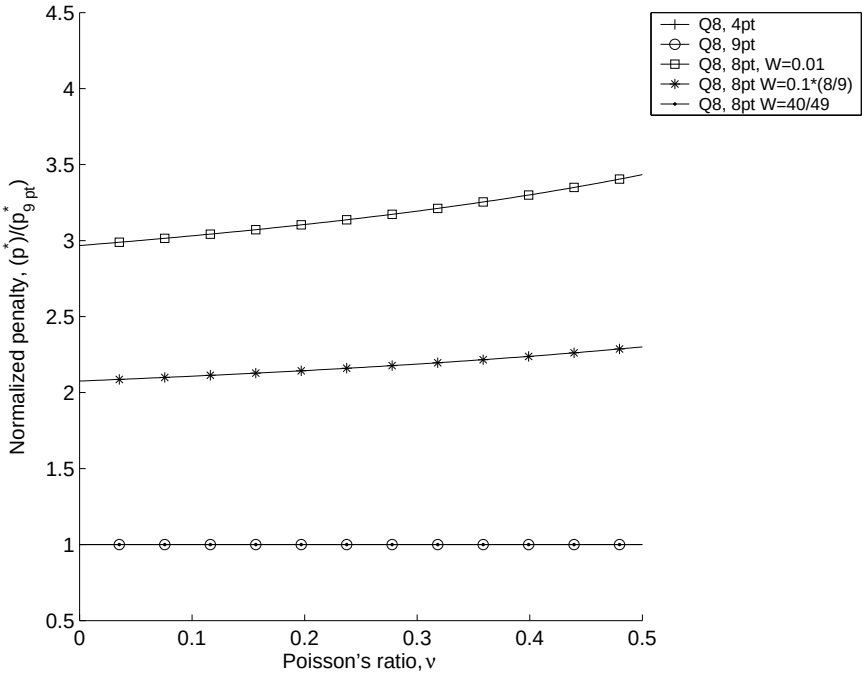

Figure 7.15: Effect of integration scheme setting on p_2^*: 8-point scheme.

Chapter 8

Conclusion

The stated objectives of this work were to:

1. Develop new finite elements, or elemental procedures, which not only improve model accuracy, robustness and/or efficiency, but can also be used in schemes which alleviate or eliminate the numerical instabilities, or improper modelling, associated with spurious material layouts in topology optimization.

2. Develop procedures which exploit the salient features of the new finite elements, or elemental procedures, in order to overcome or alleviate the numerical instabilities, or modelling deficiencies, leading to spurious material layouts in topology optimization.

These two main objectives formed the basis of this two part thesis. In the first part, emphasis is mainly concentrated on the development of planar finite elements and procedures. The stability of planar elastic elements with drilling degrees of freedom (DOFs) are considered, and piezoelectric finite elements with drilling DOFs are developed. Finally, reduced order integration schemes are applied to quadratic (Q8 and Q9) elements in order to enhance element accuracy.

In the second part of the thesis, the new finite elements, and elemental procedures, are applied in a topology optimization environment. Firstly, elements with drilling DOFs are exploited in the development of schemes to deal with problematic material layouts. The effect of element formulation on optimal topologies of membrane, plate and shell problems is then investigated. Finally it is shown how reduced order integration schemes soften checkerboard patches of higher order elements, making checkerboard material layouts less likely in optimal topologies.

In this final chapter, conclusions made during the course of the study, and evidence demonstrating that the objectives of the study have been met, are presented. Each chapter contains a presentation of specific scientific contributions made during the course of this study. As such, each chapter is intended to represent a self-contained work, which can be read in isolation of the remainder of the document. Therefore, the conclusions drawn from each chapter will also be presented separately.

8.1 PART I: Development of finite element technology

Effect of penalty parameter on elements with drilling DOFs
In Chapter 2, after a brief summary of historical developments in the formulation of elements with in-plane rotations, a numerical investigation into the effect of a penalty parameter in elements with drilling degrees of freedom is presented.

The parameter under investigation is usually denoted γ, and relates the in-plane translations and rotations. Rather than simply reporting on the quantitative influence of the penalty parameter γ on measures like displacement, rotation and stress, the skewness of the nonsymmetric part of the stress tensor is directly assessed. Results are presented for both isotropic and orthotropic constitutive relationships.

In general it is shown that, values smaller than $\gamma = \mu$, with μ the shear modulus, are desirable, even though the formulation is convergent for all values of γ. In implementing elements with drilling degrees of freedom based on the procedure suggested by Hughes and Brezzi [18], the skewness of the nonsymmetric part of the stress tensor, may directly be used to quantitatively assess the validity of selected values of γ.

Development of planar four node piezoelectric elements with drilling DOFs
In Chapter 3 a number of variational formulations accounting for piezoelectricity and in-plane rotations are presented. Two new functional families, namely M-type, which retains the skew-symmetric part of the stress tensor, and K-Type, in which the skew part of stress is eliminated, are introduced.

From the Hu-Washizu-like functionals (M- and K-type) irreducible formulations with only 'kinematic' independent variables, i.e. displacement and electric potential are developed. It is also shown how 'fully' mixed formulations, with stress and electric flux density assumed, are developed. Furthermore, 'degenerate' Hellinger-Reissner-like formulations with either stress or electric flux density assumed, are also presented. It is also illustrated how the family of functionals are related to one another.

The accuracy and robustness of these elements on a number of benchmark problems is demonstrated. The addition of drilling degrees of freedom enriches the interpolated displacement field, resulting in improved element performance. This is borne out by the improved accuracy and robustness of the irreducible elements with drilling DOFs over the standard bilinear piezoelectric element.

The improved performance of the mixed elements with drilling degrees of freedom is generally less marked when compared to existing mixed piezoelectric elements. In fact, it is difficult to conclusively state that any one of the elements used in the study is better in terms of accuracy than all the others, since none of the elements herein consistently outperforms all the other elements on all reported accuracy measures.

The 'fully mixed' elements, however, are shown to be accurate and stable, even at extreme element distortions. They also allow for improved modelling capabilities due to the additional rotational degree of freedom, e.g. compatibility with elastic elements with drilling degrees of freedom is ensured.

Modified reduced order quadratures for quadratic membrane elements
The use of modified reduced order quadrature integration rules in the evaluation of elemental matrices was the focus of Chapter 4. Modified reduced order quadrature rules as alternative numerical integration schemes for Q8 serendipity and Q9 Lagrange membrane finite elements are offered. For these elements, practitioners often either employ full integration, using order 3 Gauss rules, or reduced integration using an order 2 Gauss rule. However, full integration usually results in excessively stiff behavior while order 2 Gauss rules result in the introduction of spurious modes on the element level. Even though the spurious mode associated with the Q8 element is non-communicable, it remains undesirable, and may influence results in a number of situations of practical importance, e.g. vibration problems.

The 5 and 8 point schemes, proposed for respectively Q8 and Q9 elements, eliminate spurious zero energy modes, while element accuracy is enhanced as compared to order 3 Gauss rules, through the introduction of soft higher order deformation modes.

It is shown that for the Q8 element, both the 5 and 8 point rules can be used for integrating the element stiffness matrix. In each case the spurious mode is eliminated. Since the numerical cost of the 8 point scheme is higher than the 5 point scheme, with no other obvious benefits, it is recommended that Q8 elements be integrated using the 5 point rule. For the Q9 element, the 5 point rule is inadequate since only one of the three spurious modes is eliminated. It is therefore recommended that the 8 point rule be employed for elemental calculation of Q9 elements. Appropriate values for the variable weights which appear in the integration schemes are also suggested, so as to balance element accuracy and stability.

8.2 PART II: Application of finite element developments to topology optimization

Exploiting drilling DOFs to deal with checkerboarding, one-node hinges and diagonal members
The aim of Chapter 5 was to demonstrate that membrane finite elements with drilling DOFs can be exploited in schemes to treat problematic local material layouts, such as checkerboarding and one-node connected hinges. It is firstly demonstrated via numerical experimentation, that simply employing these elements in topology optimization problems, results in a significant reduction in the amount of checkerboarding in optimal topologies. The theoretical merits of this strategy are detailed in Chapter 7. In addition, drilling DOFs present a natural way of detecting and/or penalizing one-node connected hinges. It is therefore also shown how drilling DOFs can be used to improve on the numerical modelling of one-node hinges and diagonal structural members.

Two new schemes to deal with one-node hinges and diagonal members, exploiting drilling DOFs are suggested. The first scheme is based on NoHinge, a scheme originally proposed by Poulsen [15]. The modified scheme however, uses the rotations computed at internal nodes to distinguish between a material layout which is behaving as a hinge (in rotation) and a diagonal structural member subjected to only axial loads. This scheme however, requires

a somewhat numerically expensive constraint sensitivity computation. A second scheme in which a one-node hinge is modelled, such that the response is similar to a reasonable interpretation of the material layout, is also presented. A function which indicates whether or not an element takes part in a layout with unsuitable numerical representation, such as a one-node hinge, is developed. If such an element is detected, it is replaced by an equivalent beam model for improved modelling accuracy. Since the process is solely determined by the material layout, it is completely reversible. Using this new method, it is demonstrated that it is relatively easy to stiffen one-node hinges in compliant mechanism design, thereby penalizing their existence, and that this stiffening does not lead to checkerboarding.

This second scheme in particular seems a promising alternative to traditional methods which seek to simply eliminate these problematic material layouts altogether, and is therefore further applied in the design of a practical mirror scanning device. Firstly, standard filtering strategies are employed in the topology optimization of a mirror scanning device using three different problem formulations. The first seeks to simply maximize the output rotation, while the other two maximize some measure of stiffness subject to a required output rotation being maintained. Each of the resulting optimal topologies contain a number one-node hinges. Upon application of the newly proposed scheme, the formation of one-node hinges are however, effectively prevented.

Effect of finite element formulation on optimal topologies of generally curved shells structures

Chapter 6 presents an investigation into the effect of finite element formulation and elemental settings on optimal topologies of membrane, plate and shell minimum compliance problems. It is shown that for given optimization algorithm settings, the optimal topology which results is a function of the element type.

For membrane problems, it is demonstrated that both standard Q4 elements and element with drilling DOFs results in identical optimal topologies. Referring here to the stability of elements with drilling DOFs, studied in Chapter 2: Optimal topologies employing elements with drilling DOFs are shown to be largely insensitive to the value of the adjustable parameter γ over a large range of values.

Furthermore, the effect of the plate component of flat shell elements, is investigated. Results for Discrete Kirchhoff Quadrilateral (DKQ) elements, and two Mindlin-Reissner based elements, one employing Selective Reduced Integration (SRI) on transverse shear terms and the other employing an Assumed Natural Strain (ANS) formulation, are investigated and compared. The plate examples presented confirmed that, since the DKQ element is shear rigid, optimal topologies are not sensitive to plate thickness. Elements employing the ANS interpolations are shown to be robust reliable. The ANS elements consistently recovered thin plate results similar to the DKQ results. Mindlin-Reissner elements with SRI on transverse shear terms are shown to be 'softer' in transverse shear than the ANS Mindlin-Reissner based elements and are therefore more sensitive to plate thickness. However, the SRI element possesses a spurious communicable mode which occasionally renders this element unstable. A plate example is introduced which exemplifies the problem.

Finally, the effects of parameters related to drilling DOFs of shell problems are studied. It

is shown that optimal topologies computed with elements with drilling degrees of freedom based on sound mathematical theory are insensitive to the penalty parameter over a wide range. On the other hand, elements with an *ad hoc* treatment of drilling degrees of freedom are found to be far more sensitive to the adjustable parameter. This sensitivity to the adjustable parameter is furthermore shown to be problem dependent. This dependency is illustrated on a newly introduced benchmark problem in the form of a pretwisted beam.

Effect of reduced order integration schemes and elements with drilling DOFs on checkerboarding
The application of modified reduced order quadratures applied to quadratic membrane elements in a topology optimization environment, was the focus of Chapter 7.

Various elements, each employing different integration schemes, are assessed in term of the stiffness of a checkerboard patch of elements. The evaluation makes use of 4-node elements (with and without drilling degrees of freedom) as well as 8- and 9-node isoparametric elements, employing full and modified reduced order integration schemes. In particular, combinations of element and integration scheme which 'soften' the effective material tensor of a checkerboard patch of elements, (effectively reducing the likelihood of checkerboarding) are identified.

Firstly, it is shown that both 4-node elements with and without drilling degrees of freedom result in identical effective material properties for a checkerboard patch of elements. Since the additional straining modes associated with the drilling DOFs are not activated by the 3 linearly independent test strains applied to compute the effective material properties, elements with drilling DOFs do not affect the stiffness of a checkerboard patch. It is however numerically demonstrated that for realistic problems where nodal rotations are non-zero, checkerboarding is somewhat reduced. However, since in the limit of mesh refinement only constant strain states are experienced, there is no guarantee that elements with drilling DOFs will eliminate checkerboarding altogether.

Next it is shown that checkerboard layouts comprising higher order 8-node (Q8) and 9-node (Q9) elements employing modified reduced order integration schemes are significantly softened. The most significant improvements, in terms of softening, are achieved using the 5-point scheme in conjunction with Q8 elements. Employing this combination significantly reduces strain energy density associated with a checkerboard patch under prescribed strain. This benefit is also numerically cost-effective since employing the 5-point scheme simultaneously reduces computational cost, and increases the accuracy of the finite element approximation.

8.3 Suggested future work

Although the main objectives of the study have been successfully accomplished, the research topics have not been exhaustively addressed. For example, many of the (planar) finite element developments presented in this study could be extended to the more general three-dimensional case: The variational formulations presented in Chapter 3 are valid for planar

two-dimensional and general three-dimensional finite element development. Solid three-dimensional elastostatic elements with rotational degrees of freedom have previously been implemented by for example Choi *et al.* [148]. It should therefore also be possible to develop solid equivalents of the planar piezoelectric elements with rotational degrees of freedom presented in Chapter 3. Furthermore, in theory, it is possible to develop modified reduced order integration schemes, equivalent to those presented in Chapter 4 and to apply them in the calculation of solid three-dimensional finite elements to enhance element accuracy and reduce computational cost.

Naturally the two aforementioned solid finite element developments would also allow the schemes and theory presented in Chapters 5 and 7 to be extended to the three dimensional case if so desired.

Furthermore, in Chapter 5, two schemes exploiting elements with drilling degrees of freedom were presented. Although acceptable results were achieved, a more elegant beam representation of a one-node connected hinge (and a diagonal member) for the scheme denoted Scheme II in Section 5.5.2 would be helpful in improving the accuracy of the method.

Finally, the application of topology optimization in the synthesis of plate and shell compliant mechanisms for micropositioning problems could be attempted. A simple piezoelectric shell element has already been implemented, and its application in topology optimization problems awaits attention.

Bibliography

[1] R. Ansola, J. Canales, J.A. Tarrago, and J. Rasmussen. On simultaneous shape and material layout optimization of shell structures. *Struct. Multidisc. Optim.*, 24:175–184, 2002.

[2] R. Ansola, J. Canales, J.A. Tarrago, and J. Rasmussen. Combined shape and reinforcement layout optimization of shell structures. *Struct. Multidisc. Optim.*, 27:219–227, 2004.

[3] G.I.N. Rozvany, editor. *Topology Optimization in Structural Mechanics*. Springer-Verlag, Wien, New York, 1997.

[4] M.P. Bendsøe and O. Sigmund. *Topology Optimization: Theory, Methods and Applications*. Springer, Berlin, 2003.

[5] P. Duysinx and O. Sigmund. New developments in handling stress constraints in optimal material distributions. In *Proceedings of the 7th AIAA/USAF/NASA/ISSMO symposium on Multidisciplinary Design Optimization*, Saint Louis, Missouri, USA, September 1998.

[6] P. Duysinx and M.P. Bendsøe. Topology optimization of continuum structures with local stress constraints. *Int. J. Numer. Meth. Engng.*, 43:1453–1478, 1998.

[7] G.I.N. Rozvany. On design-dependent constraints and singular topologies. *Struct. Multidisc. Optim.*, 21:164 – 172, 2001.

[8] R.T. Haftka, Z. Gürdal, and M.P. Kamat. *Elements of structural optimization*. Kluwer Academic, Dordrecht, 2nd edition, 1990.

[9] J.A. Snyman. *Practical Mathematical Optimization: An introduction to the basic optimization theory and classical and new gradient-based algorithms*. Springer Science+Business Media, Inc., 233 Spring Street, New York, NY, 10013, USA, 2005.

[10] K. Svanberg. The method of moving asymptotes - a new method for structural optimization. *Int. J. Numer. Meth. Engng.*, 24:359–373, 1987.

[11] C. Niezrecki, D. Brei, S. Balakrishnan, and A. Moskalik. Piezoelectric actuation: State of the art. *The Shock and Vibration Digest*, 33:269–280, 2001.

[12] S.E. Park and T.R. Shrout. Ultrahigh strain and piezoelectric behavior in relaxor based ferroelectric single crystals. *Journal of Applied Physics*, 82:1804–1811, 1997.

[13] O. Sigmund and J. Petersson. Numerical instabilities in topology optimization: A survey on procedures dealing with checkerboards, mesh-dependencies and local minima. *Struct. Multidisc. Optim.*, 16:68 – 75, 1998.

[14] A. Díaz and O. Sigmund. Checkerboard patterns in layout optimization. *Struct. Optim.*, 10:40–45, 1995.

[15] T.A. Poulsen. A simple scheme to prevent checkerboard patterns and one-node connected hinges in topology optimization. *Struct. Multidisc. Optim.*, 24:396–399, 2002.

[16] K.-J. Bathe. *Finite Element Procedures*. Prentice-Hall International, Inc., Upper Saddle River, New Jersey 07458, 1996.

[17] R.D. Cook, D.S. Malkus, Plesha M.E., and R.J. Witt. *Concepts and applications of finite element analysis*. John Wiley and Sons, New York, 2002.

[18] T.J.R. Hughes and F. Brezzi. On drilling degrees of freedom. *Comput. Methods Appl. Mech. Engrg.*, 72:105–121, 1989.

[19] C.A. Felippa. A historical outline of matrix structural analysis: a play in three acts. *Computers and Structures*, 79:1313–1324, 2001.

[20] G. Pimpinelli. An assumed strain quadrilateral element with drilling degrees of freedom. *Finite Elements in Analysis and Design*, 41:267–283, 2004.

[21] A. Ibrahimbegovic, R.L. Taylor, and E.L. Wilson. A robust quadrilateral membrane finite element with drilling degrees of freedom. *Int. J. Numer. Meth. Engng.*, 30:445–457, 1990.

[22] O.C. Zienkiewicz and R.L. Taylor. *The Finite Element Method*, volume II: Solid and Fluid Mechanics Dynamics and Non-linearity. McGraw-Hill Book Company, London, 1991.

[23] D.J. Allman. A quadrilateral finite element including vertex rotations for plane elasticity analysis. *Int. J. Numer. Meth. Engng.*, 26:717–730, 1988.

[24] R.H. MacNeal and R.L. Harder. A refined four-noded membrane element with rotational degrees of freedom. *Computers and Structures*, 28:75–84, 1988.

[25] F. Frey. Shell finite elements with six degrees of freedom per node. In *ASME Winter Annual Meeting*, San Francisco, 1989.

[26] P.G. Bergan and C.A. Felippa. A triangular membrane element with rotational degrees of freedom. *Comput. Methods Appl. Mech. Engrg.*, 50:25–69, 1985.

[27] A.A. Groenwold. Finite element analysis of composite plates and shells. Master's thesis, University of Pretoria, Dept. of Mechanical and Aeronautical Engineering, Pretoria, South Africa, 1993.

[28] L. Jin. Analysis and evaluation of a shell finite element with drilling degrees of freedom. Master's thesis, University of Maryland at College Park, Dept. of Civil Engineering and Institute for System Research, 1994.

[29] A.C. Scordelis. Analysis of continuum box girder bridges. Technical Report SESM 67-2, University of California, Dept. of Civil Engineering, Berkley, CA, 1967.

[30] K.J. Willam. *Finite element analysis of cellular structures*. PhD thesis, University of California, Dept. of Civil Engineering, Berkley, CA, 1969.

[31] B. Irons and S. Ahmad. *Techniques of finite elements*. Ellis-Horwood, Cichester, U.K., 1980.

[32] D.J. Allman. A compatible triangular element including vertex rotations for plane elasticity analysis. *Computers and Structures*, 19:1–8, 1984.

[33] R.D. Cook. On the allman triangle and a related quadrilateral elements. *Computers and Structures*, 22:1065–1067, 1986.

[34] P. Jetteur. A shallow shell element with in-plane rotational degrees of freedom. IREM Internal Report 86/3, Ecole Polytechnique Fédérale de Lausanne, 1986.

[35] P. Jetteur. Improvement of the quadrilateral "JET" shell element for a particular class of shell problems. IREM Internal Report 87/1, Ecole Polytechnique Fédérale de Lausanne, 1987.

[36] S. Jaamei. "Jet" thin shell finite element with drilling rotations. IREM Internal Report 88/7, Ecole Polytechnique Fédérale de Lausanne, 1988.

[37] R.L. Taylor and J.C. Simo. Bending and membrane elements for analysis of thick and thin shells. In G.N. Pande and J. Middleton, editors, *Proceedings of the NUMETA 85 Conference*, Swansea, 7-11 Jan. 1985.

[38] R.L. Taylor. Finite element analysis of linear shell problems. In J.R. Whiteman, editor, *The Mathematics of Finite Elements and Applications VI, MAFELAP*, pages 191–203, Academic Press Limited, London, 1987.

[39] J.C. Simo, D.D. Fox, and M.S. Rifai. On a stress resultant geometrically exact shell model Part II: The linear theory; computational aspects. *Comput. Methods Appl. Mech. Engrg.*, 73:53–92, 1989.

[40] E. Reissner. A note on variational principles in elasticity. *International Journal of Solids and Structures*, 1:93–95, 1965.

[41] T.J.R. Hughes, F. Brezzi, A. Masud, and I. Harari. Finite element with drilling degree of freedom: Theory and numerical evaluation. In R. Gruber, J. Periaux, and R.P. Shaw, editors, *Proceedings of the fifth International Symposium on Numerical Methods in Engineering*, volume 1, pages 3–17, Springer-Verlag, Berlin, 1989.

[42] A. Ibrahimbegovic and E.L. Wilson. A unified formulation for triangular and quadrilateral flat shell finite elements with six nodal degrees of freedom. *Communications in Applied Numerical Methods*, 7:1–9, 1991.

[43] S. Geyer and A.A. Groenwold. Two hybrid stress membrane finite element families with drilling rotations. *Int. J. Numer. Meth. Engng.*, 53:583–601, 2002.

[44] T.J.R. Hughes, A. Masud, and I. Harari. Numerical assessment of some membrane elements with drilling degrees of freedom. *Computers and Structures*, 55:297–314, 1995.

[45] S. Geyer and A.A. Groenwold. On reduced integration and locking of flat shell finite elements with drilling rotations. *Commun. Num. Meth. Eng.*, 19:85–97, 2003.

[46] T.H.H. Pian. Derivation of element stiffness matrices by assumed stress distributions. *AIAA J.*, 2:1333–1336, 1964.

[47] T.H.H. Pian. State-of-the-art development of the hybrid/mixed finite element method. *Fin. Elem. Anal. Des.*, 21:5–20, 1995.

[48] M.A. Aminpour. An assumed-stress hybrid 4-node shell element with drilling degrees of freedom. *Int. J. Numer. Meth. Engng.*, 33:19–38, 1992.

[49] G. Rengarajan, M.A. Aminpour, and N.F. Knight. Improved assumed-stress hybrid shell element with drilling degrees of freedom for linear stress, buckling and free vibration analyses. *Int. J. Numer. Meth. Engng.*, 38:1917–1943, 1995.

[50] K.Y. Sze and A. Ghali. Hybrid plane quadrilateral element with corner rotations. *ASCE Journal of Structural Engineering*, 119:2552–2572, 1993.

[51] K.Y. Sze, C. Wanji, and Y.K. Cheung. An efficient quadrilateral plane element with drilling degrees of freedom using orthogonal stress modes. *Computers and Structures*, 42:695–705, 1992.

[52] A.A. Groenwold and N. Stander. An efficient 4-node 24 d.o.f. thick shell finite element with 5-point quadrature. *Engineering Computations*, 12:723–748, 1995.

[53] A.A. Groenwold and N. Stander. A 24 d.o.f. 4-node flat shell finite element for general unsymmetric orthotropic layered composites. *Engineering Computations*, 15:518–543, 1998.

[54] H.H. Dovey. *Extension of three dimensional analysis to shell structures using the finite element idealization.* Report no. UC SESM 74-2, Ph-D dissertation, University of California, Berkeley, 1974.

[55] C.A. Felippa. *Advanced Finite Element Methods (ASEN 5367): Course Material*. Aerospace Engineering Sciences - University of Colorado at Boulder, 2006. Available at http://www.colorado.edu/engineering/CAS/courses.d/AFEM.d/Home.html.

[56] T. Mura and T. Koya. *Variational Methods in Mechanics*. Oxford University Press, Inc., 200 Madison Avenue, New York, New York, 10016, 1992.

[57] T.J.R. Hughes. *The finite element method: Linear static and dynamic analysis*. Prentice-Hall, London, 1987.

[58] C.S. Long, S. Geyer, and A.A. Groenwold. A numerical study of the effect of penalty parameters for membrane elements with independent rotation fields and penalized equilibrium. *Finite Elements in Analysis and Design*, 42:757–765, 2006.

[59] J.C. Simo and M.S. Rifai. A class of mixed assumed strain methods and the method of incompatible modes. *Int. J. Numer. Meth. Engng.*, 29:1595–1638, 1990.

[60] O.C. Zienkiewicz and R.L. Taylor. *The Finite Element Method*, volume I: Basic Formulation and Linear Problems. McGraw-Hill Book Company, London, 1989.

[61] S. Di and E. Ramm. On alternative hybrid stress 2D and 3D elements. *Engineering Computations*, 11:49–68, 1994.

[62] T.H.H. Pian and K. Sumihara. Rational approach for assumed stress finite elements. *Int. J. Numer. Meth. Engng.*, 20:1685–1695, 1984.

[63] A.A. Groenwold, Q.Z. Xiao, and N.J. Theron. Accurate solution of traction free boundaries using hybrid stress membrane elements with drilling degrees of freedom. *Comput. Struct.*, 82:2071–2081, 2004.

[64] K.Y. Sze, X.-M. Yang, and L.-Q. Yao. Stabilized plane and axisymmetric piezoelectric finite element models. *Finite Elements in Analysis and Design*, 40:1105–1122, 2004.

[65] C.C. Wu, K.Y. Sze, and Y.Q. Huang. Numerical solutions on fracture of piezoelectric materials by hybrid element. *International Journal of Solids and Structures*, 38:4315–4329, 2001.

[66] A.A. Cannarozzi and F. Ubertini. Some hybrid variational methods for linear electroelasticity problems. *International Journal of Solids and Structures*, 38:2573–2596, 2001.

[67] P. Heyliger. A note on the static behaviour of simply-supported laminated piezoelectric cylinders. *International Journal of Solids and Structures*, 34:3781–3794, 1997.

[68] S. Kapuria, S. Sengupta, and P.C. Dumir. Three-dimensional solution for simply-supported piezoelectric cylindrical shell for axisymmetric load. *Comput. Methods Appl. Mech. Engrg.*, 140:139–155, 1997.

[69] H. Allik and T.J.R. Hughes. Finite element method for piezoelectric vibration. *Int. J. Numer. Meth. Engng.*, 2:151–157, 1970.

[70] A. Benjeddou. Advances in piezoelectric finite element modeling of adaptive structural elements: a survey. *Computers and Structures*, 76:347–363, 2000.

[71] J.S. Yang. Mixed variational principles for piezoelectric elasticity. In B. Antar, R. Engels, A.A. Prinaris, T.H. Moulden, and O. Zanaboni, editors, *Developments in Theoretical and Applied Mechanics*, volume XVI, pages II.1.31–38, University of Tennessee Space Institute, Tennessee, 1992.

[72] E.P. EerNisse. Variational method for electroelastic vibration analysis. *IEEE Transactions on Sonics and Ultrasonics*, SU-14:153–160, 1967.

[73] R. Holland and E.P. EerNisse. Variational evaluation of admittances of multielectroded three-dimensional piezoelectric structures. *IEEE Transactions on Sonics and Ultrasonics*, SU-15:119–132, 1968.

[74] K.Y. Sze, L.Q. Yao, and S. Yi. A hybrid stress ANS solid-shell element and its generalization for smart structure modelling. Part II - smart structure modelling. *Int. J. Numer. Meth. Engng.*, 48:565–582, 2000.

[75] K.Y. Sze and L.Q. Yao. Modelling smart structures with segmented piezoelectric sensors and actuators. *Journal of Sound and Vibration*, 235:495–520, 2000.

[76] K.Y. Sze and Y.S. Pan. Hybrid finite element models for piezoelectric materials. *Journal of Sound and Vibration*, 226:519–547, 1999.

[77] C.S. Long, P.W. Loveday, and A.A. Groenwold. Design of a piezoelectric mirror scanning device using topology optimization. In *Proc. Sixth World Congress on Structural and Multidisciplinary Optimization*, Rio de Janeiro, Brazil, May 2005. Paper no. 4031.

[78] T. Ikeda. *Fundamentals of Piezoelectricity*. Oxford University Press, Oxford, 1996.

[79] M. Liu. Finite element analysis for cracked piezoelectric material. Master's thesis, Dept. of Modern Mechanics, Univ. of Sci. and Tech. of China, Hefei, 1998.

[80] C.S. Long, P.W. Loveday, and A.A. Groenwold. Planar four node piezoelectric elements with drilling degrees of freedom. *Int. J. Numer. Meth. Engng.*, 65:1802–1830, 2006.

[81] T.J.R. Hughes, A. Masud, and I. Harari. Numerical assessment of some membrane elements with drilling degrees of freedom. *Computers and Structures*, 55:297–314, 1995.

[82] T.J.R. Hughes, A. Masud, and I. Harari. Dynamic analysis and drilling degrees of freedom. *Int. J. Numer. Meth. Engng.*, 38:3193–3210, 1995.

[83] H.S. Tzou. *Piezoelectric Shells: Distributed Sensing and Control of Continua*. Kluwer Academic Publishers, Netherlands, 1993.

[84] V.M. Franco Correia, M.A. Aguiar Gomes, A. Suleman, C.M. Mota Soares, and C.A. Mota Soares. Modelling and design of adaptive composite structures. *Comput. Methods Appl. Mech. Engrg.*, 185:325–346, 2000.

[85] R.H. MacNeal and R.L. Harder. A proposed standard set of problems to test finite element accuracy. *Finite Elements in Analysis and Design*, 1:3–20, 1985.

[86] O.C. Zienkiewicz, R.L. Taylor, and J.M. Too. Reduced integration techniques in general analysis of plates and shells. *Int. J. Numer. Meth. Engng.*, 3:275–290, 1971.

[87] B.M. Irons. Quadrature rules for brick based finite elements. *Int. J. Numer. Meth. Engng.*, 3:293–294, 1971.

[88] A.K. Gupta and B. Mohraz. A method of computing numerically integrated stiffness matrices. *Int. J. Numer. Meth. Engng.*, 5:83–89, 1972.

[89] T. Belytschko and B.E. Engelman. On flexurally superconvergent four-node quadrilaterals. *Computers and Structures*, 25:909–918, 1987.

[90] T. Belytschko, C.S. Tsay, and W.K. Liu. A stabilization matrix for the bilinear Mindlin plate element. *Comp. Meth. Applied Mech. Eng.*, 29:313–327, 1981.

[91] T. Belytschko and C.S. Tsay. A stabilization procedure for the quadrilateral plate with one-point quadrature. *Int. J. Numer. Meth. Engng.*, 19:405–419, 1983.

[92] X.J. Wang and T. Belytschko. A study of stabilization and projection in the 4-node Mindlin plate element. *Int. J. Numer. Meth. Engng.*, 28:2223–2238, 1989.

[93] W.K. Liu, J.S-J Ong, and Uras R.A. Finite element stabilization matrices - A unification approach. *Comp. Meth. Applied Mech. Eng.*, 53:13–46, 1985.

[94] T.J.R. Hughes, M. Cohen, and M. Haroun. Reduced and selective integration techniques in the finite element analysis of plates. *Nucl. Eng. Design*, 46:203–222, 1978.

[95] N. Stander and E.L. Wilson. A 4-node quadrilateral membrane element with in-plane vertex rotations and modified reduced quadrature. *Engineering Computations*, 6:266–271, 1989.

[96] K.-J Bathe and E.N. Dvorkin. A formulation of general shell elements - The use of mixed interpolation of tensorial components. *Int. J. Numer. Meth. Engng.*, 22:697–722, 1986.

[97] N. Bićanić and E. Hinton. Spurious modes in two-dimensional isoparametric elements. *Int. J. Numer. Meth. Engng.*, 14:1545–1557, 1979.

[98] T.A. Poulsen. Topology optimization in wavelet space. *Int. J. Numer. Meth. Engng.*, 53:567–582, 2002.

[99] G.I.N. Rozvany, V. Pomezanski, Z. Gaspar, and O.M. Querin. Some pivotal issues in structural topology optimization. In *Proceeding of the 6th World Congress on Structural and Multidisciplinary Optimization*, Rio de Janeiro, Brazil, May 2005. Paper no. 5951.

[100] O. Sigmund. On the design of compliant mechanisms using topology optimization. *Mechanics of Structures and Machines*, 25:495–526, 1997.

[101] O. Sigmund. A 99 line topology optimization code written in Matlab. *Struct. Multidisc. Optim.*, 21:120–127, 2001.

[102] C.S. Jog and R.B. Haber. Stability of finite element models for distributed-parameter optimization and topology design. *Comput. Methods Appl. Mech. Engrg.*, 130:203–226, 1996.

[103] M.I. Frecker. Review of current research activities in optimization of smart structures and actuators. In V. S. Rao, editor, *Proc. SPIE Vol. 4693, p. 112-123, Smart Structures and Materials 2002: Modeling, Signal Processing, and Control, Vittal S. Rao; Ed.*, pages 112–123, Jul 2002.

[104] N.L. Pedersen. Maximization of eigenvalues using topology optimization. *Struct. Multidisc. Optim.*, 20:2–11, 2000.

[105] A.P. Seyranian, E. Lund, and N. Olhoff. Multiple eigenvalues in structural optimization problems. *Struct. Optim.*, 8:207–227, 1994.

[106] O. Sigmund. Design of multiphysics actuators using topology optimization - Part II: Two-material structures. *Comput. Methods Appl. Mech. Engrg.*, 190:6605–6627, 2001.

[107] M.P. Bendsøe and N. Kikuchi. Generating optimal topologies in structural design using a homogenization method. *Comput. Methods Appl. Mech. Engrg.*, 71:197–224, 1988.

[108] K.-T. Cheng and N. Olhoff. An investigation concerning optimal design of solid elastic plates. *International Journal of Solids and Structures*, 17:305–323, 1981.

[109] M.P. Bendsøe. Optimal shape design as a material distribution problem. *Struct. Optim.*, 1:193–202, 1989.

[110] M. Zhou and G.I.N. Rozvany. The COC algorithm, Part II: Topological, geometrical and generalized shape optimization. *Comp. Meth. Appl. Mech. Engng.*, 89:309–336, 1991.

[111] G.I.N. Rozvany, M. Zhou, and T. Birker. Generalized shape optimization without homogenization. *Struct. Optim.*, 4:250–252, 1992.

[112] L.H. Tenek and I. Hagiwara. Optimization of material distribution within isotropic and anisotropic plates using homogenization. *Comput. Methods Appl. Mech. Engrg.*, 109:155–167, 1992.

[113] L.H. Tenek and I. Hagiwara. Optimal rectangular plate and shallow shell topologies using thickness distribution or homogenization. *Comput. Methods Appl. Mech. Engrg.*, 115:111–124, 1994.

[114] A.R. Díaz, R. Lipton, and C.A. Soto. A new formulation of the problem of optimum reinforcement of reissner-mindlin plates. *Comput. Methods Appl. Mech. Engrg.*, 123:121–139, 1995.

[115] L.A. Krog and N. Olhoff. Optimum topology and reinforcement design of disk and plate structures with multiple stiffness and eigenfrequency objectives. *Computers and Structures*, 72:535–563, 1999.

[116] S.J. Lee, J.E. Bae, and E. Hinton. Shell topology optimization using layered artificial material model. *Int. J. Numer. Meth. Engng.*, 47:843–867, 2000.

[117] F. Belblidia, J.E.B. Lee, S. Rechak, and E. Hinton. Topology optimization of plate structures using single- or three-layered artificial material model. *Advances in Engineering Software*, 32:159–168, 2001.

[118] W. Kanok-Nukulchai. A simple and efficient finite element for general shell analysis. *Int. J. Numer. Meth. Engng.*, 14:179–200, 1979.

[119] N.L. Pedersen. Topology optimization of laminated plates with prestress. *Computers and Structures*, 80:559–570, 2002.

[120] C.S. Jog. Topology design of structures subjected to periodic loading. *Journal of Sound and Vibration*, 253:687–709, 2002.

[121] J. Stegmann and E. Lund. Nonlinear topology optimization of layered shell structures. *Struct. Multidisc. Optim.*, 29:349 – 360, 2005.

[122] F. Belblidia and S. Bulman. Constrained adaptive topology optimization for vibrating shell structures. *Struct. Multidisc. Optim.*, 22:167–176, 2001.

[123] S. Bulman, J. Sienz, and E. Hinton. Comparisons between algorithms for structural topology optimization using a series of benchmark studies. *Computers and Structures*, 79:1203–1218, 2001.

[124] F. Belblidia and S. Bulman. A hybrid topology optimization algorithm for static and vibrating shell structures. *Int. J. Numer. Meth. Engng.*, 54:835–852, 2002.

[125] J.-L. Batoz and M. Ben Tahar. Evaluation of a new quadrilateral thin plate bending element. *Int. J. Numer. Meth. Engng.*, 18:1655–1677, 1982.

[126] K.-J. Bathe and E.N. Dvorkin. A four-node plate bending element based on Mindlin/Reissner plate theory and a mixed interpolation. *Int. J. Numer. Meth. Engng.*, 21:367–383, 1985.

[127] E. Dvorkin and K.-J. Bathe. A continuum mechanics based four node shell element for general nonlinear analysis. *Engineering Computations*, 1:77–88, 1984.

[128] R.H. MacNeal. Derivation of element stiffness matrices by assumed strain distribution. *Nuclear Engineering Design*, 70:3–12, 1982.

[129] T.J.R. Hughes and T.E. Tezduyar. Finite elements based upon mindlin plate theory, with particular reference to the 4-node bilinear isoparametric element. *Journal of Applied Mechanics*, 48:587–595, 1981.

[130] S.J. Lee and E. Hinton. Dangers inherited in shells optimized with linear assumptions. *Computers and Structures*, 78:473–486, 2000.

[131] M. Kögl and E.C.N. Silva. Topology optimization of smart structures: design of piezoelectric plate and shell actuators. *Smart Mater. Struct.*, 14:387–399, 2005.

[132] J. Stegmann and E. Lund. Discrete material optimization of general composite shell structures. *Int. J. Numer. Meth. Engng.*, 62:2009–2027, 2005.

[133] M.K. Rao and U. Shrinivasa. A set of pathological tests to validate new finite elements. *Sadhana*, 26:549–590, 2001.

[134] J. Stegmann and E. Lund. Nonlinear topology optimization of layered shell structures. *Struct. Multidisc. Optim.*, 29:349–360, 2005.

[135] C.S. Long, A.A. Groenwold, and P.W. Loveday. Implications of finite element formulation in optimal topology design. In A. Zingoni, editor, *Progress in Structural Engineering, Mechanics and Computation*, pages 1015–1019, Cape Town, South Africa, July 2004.

[136] A.R. Díaz and N. Kikuchi. Solutions to shape and topology eigenvalue optimization problems using a homogenization method. *Int. J. Numer. Meth. Engng.*, 35:1487–1502, 1992.

[137] T.E. Bruns and Tortorelli D.A. Topology optimization of non-linear elastic structures and compliant mechanisms. *Comput. Methods Appl. Mech. Engrg.*, 190:3443–3459, 2001.

[138] O. Sigmund. Design of multiphysics actuators using topology optimization - Part I: One-material structures. *Comput. Methods Appl. Mech. Engrg.*, 190:6577–6604, 2001.

[139] M.P. Bendsøe. *Optimization of structural topology, shape, and material*. Springer, Berlin, 1995.

[140] C.S. Long and A.A. Groenwold. Reduced modified quadrature for quadratic membrane finite elements. *Int. J. Num. Meth. Eng.*, 61:837–855, 2004.

[141] Hassani B.; Hinton E. A review of homogenization and topology opimization II-analytical and numerical solution of homogenization equations. *Computers and Structures*, 69:719–738, 1998.

[142] Hassani B.; Hinton E. A review of homogenization and topology optimization I-homogenization theory for media with periodic structure. *Computers and Structures*, 69:707–717, 1998.

[143] Hassani B.; Hinton E. A review of homogenization and topology optimization III-topology optimization using optimality criteria. *Computers and Structures*, 69:739–756, 1998.

[144] O. Sigmund. Materials with prescribed constitutive parameters: an inverse homogenization problem. *International Journal of Solids and Structures*, 31:2313–2329, 1994.

[145] C.S. Jog, R.B. Haber, and M.P. Bendsøe. A displacement-based topology design method with self-adaptive layered materials. In M.P. Bendsøe and C.A. Mota Soares, editors, *Topology Design of Structures*, Dordrecht, The Netherlands, 1993. Kluwer Academic Publishers.

[146] C.S. Long, P.W. Loveday, and A.A. Groenwold. On membrane elements with drilling degrees of freedom in topology optimization. In *Proc. Fifth World Congress on Structural and Multidisciplinary Optimization*, Lido di Jesolo, Venice, Italy, May 2003. Paper no. 83.

[147] C.S. Long, P.W. Loveday, and A.A. Groenwold. Topology optimization of generally curved shells. *Finite Elements in Analysis and Design*, 2006. To be submitted.

[148] C.-K. Choi, K.-Y. Chung, and E.-J. Lee. Mixed formulated 13-node hexahedral elements with rotational degrees of freedom: MR-H13 elements. *Structural Engineering and Mechanics*, 11:105–122, 2001.

[149] H.A. Eschenauer and N. Olhoff. Topology optimization of continuum structures: A review. *Applied Mechanics Reviews*, 54:331–390, 2001.

[150] T.E. Bruns. A reevaluation of the simp method with filtering and an alternative formulation for solid-void topology optimization. *Struct. Multidisc. Optim.*, 30:428–436, 2005.

[151] Y.Y. Kim and G.H. Yoon. Multi-resolution multi-scale topology optimization - a new paradigm. *International Journal of Solids and Structures*, 37:5529–5559, 2000.

[152] M.P. Bendsøe and O. Sigmund. Material interpolation schemes in topology optimization. *Archives of Applied Mechanics*, 69:635–654, 1999.

[153] S. Min, N. Kikuchi, Y.C. Park, S. Kim, and S. Chang. Optimal topology design of structures under dynamic loads. *Struct. Optim.*, 17:208–218, 1999.

[154] S. Min, S. Nishiwaki, and N. Kikuchi. Unified topology design of static and vibrating structures using multiobjective optimization. *Computers and Structures*, 75:93–116, 2000.

[155] S.J. Min and N. Kikuchi. Optimal reinforcement design of structures under the buckling load using the homogenization design method. *Structural Engineering and Mechanics*, 5:565–576, 1997.

[156] T. Borrvall and J. Petersson. Topology optimization of fluids in Stokes flow. *International Journal for Numerical Methods in Fluids*, 41:77–107, 2003.

[157] J.S. Jensen and O. Sigmund. Topology optimization of two-dimensional waveguides. In *Short papers of the 5th World Congress on Structural and Multidisciplinary Optimization WCSMO5*, pages 125–126, Lido de Jesolo, Venice, Italy, May 2003.

[158] M. Zhou and G.I.N. Rozvany. On the validity of ESO type methods in topology optimization. *Struct. Multidisc. Optim.*, 21:80–83, 2001.

[159] T. Borrvall and J. Petersson. Topology optimization using regularized intermediate density control. *Comput. Methods Appl. Mech. Engrg.*, 190:4911–4928, 2001.

[160] L. Ambrosio and G. Buttazzo. An optimal design problem with perimeter penalization. *Calculus of Variations and Partial Differential Equations*, 1:55–69, 1993.

[161] P. Duysinx. Layout optimization: A mathematical programming approach. Technical Report DCAMM Report No. 540, Technical University of Denmark, 1997.

[162] M. Beckers. Methodes du perimetre et des filtres pour l'optimisation topologique en variable discretes. Technical Report Technical Report OF-38, LTAS, University of Li'ege, 1996.

[163] J. Petersson and O. Sigmund. Slope constrained topology optimization. *Int. J. Numer. Meth. Engng.*, 41:1417–1434, 1998.

[164] T.P. Poulsen. A new scheme for imposing a minimum length scale in topology optimization: The MOLE method. In *Proceedings of the Fourth World Congress of Structural and Multidisciplinary Optimization*, Dalian, China, June 4-8 2001.

[165] O. Sigmund. *Design of material structures using topology optimization*. PhD thesis, Technical University of Denmark, 1994.

[166] G.K. Ananthasuresh, S. Kota, and Y. Gianchandani. A methodical approach to the design of compliant micromechanisms. In *Solid-state sensor and actuator workshop*, pages 189–192, 1994.

[167] C.B.W. Pedersen, T. Buhl, and O. Sigmund. Topology synthesis of large-displacement compliant mechanisms. *Int. J. Numer. Meth. Engng.*, 2001.

[168] S. Nishiwaki, K. Saitou, S. Min, and N. Kikuchi. Topological design considering flexibility under periodic loads. *Struct. Multidisc. Optim.*, 19:4–16, 2000.

[169] G.K. Lau, H. Du, and M.K. Lim. Use of functional specifications as objective functions in topological optimization of compliant mechanism. *Comput. Methods Appl. Mech. Engrg.*, 190:4421–4433, 2001.

[170] S.P. Gurav, M. Langelaar, and F. van Keulen. Uncertainty-based design optimization of shape memory alloy microgripper using combined cycle-based alternating anti-optimization and nested parallel computing. In *Proceedings of the 6th World Congresses of Structural and Multidisciplinary Optimization*, Rio de Janeiro, Brazil, May 2005. Paper no. 181.

[171] S. Canfield and M. Frecker. Topology optimization of compliant mechanical amplifiers for piezoelectric actuators. *Struct. Multidisc. Optim.*, 20:269–279, 2000.

[172] E.C.N. Silva and S. Nishiwaki. Multi-flexible micromanipulator design by using topology optimization. In *Proceedings of SPIE Smart Structures and Materials 2003 - Modeling, Signal Processing, and Control Conference*, volume 5049, pages 483–494, San Diego, U.S.A., 2003.

[173] E.C.N. Silva, S. Nishiwaki, J.S.O. Fonseca, and N. Kikuchi. Optimization methods applied to material and flextensional actuator design using the homogenization method. *Comput. Methods Appl. Mech. Engrg.*, 172:241–271, 1999.

[174] O. Sigmund and S. Torquato. Design of smart composite materials using topology optimization. *Smart Materials and Structures*, 8:365–379, 1999.

[175] Y. Li, X. Xin, N. Kikuchi, and Saitou K. Optimal shape and location of piezoelectric materials for topology optimization of flextensional actuators. In *Proceedings of the Genetic Evolutionary Computation Conference*, San Francisco, CA., U.S.A., July 2001.

[176] H. Du, G.K. Lau, M.K. Lim, and J. Qui. Topological optimization of mechanical amplifiers for piezoelectric actuators under dynamic motion. *Smart Materials and Structures*, 9:788–800, 2000.

Appendix A

A brief introduction to topology optimization

This appendix presents a very brief introduction to topology optimization as a material distribution problem. This brief review stems mainly from the review papers of Eschenauer and Olhoff [149], Frecker [103] and the book of Bendsøe and Sigmund [4]. For a more detailed review, the interested reader is therefore referred to these works and their references. This approach is characterised by the constitutive tensor of a material being parameterized within a predefined design domain Ω in order to determine the material domain Ω_{mat}, such that a given objective function is optimized.

Two of the most popular material models which parameterise the constitutive tensor are the homogenization and the SIMP (Simple Isotropic Material with Penalization) methods. Of course, a number of alternative approaches have been proposed. For example [98, 150, 151].

The SIMP material model has become very popular in recent times. The SIMP (Simple Isotropic Material with Penalization) was originally independently proposed by Bendsøe [109] and Zhou and Rozvany [110].

The SIMP material model modifies the elasticity tensor by simply premultiplying by a density $0 \leq \rho \leq 1$, raised to a power p, with $p > 1$:

$$E_{ijkl} = \rho(\boldsymbol{x})^p E^0_{ijkl}, \tag{A.1}$$

where E^0_{ijkl} is the elasticity tensor of the solid base material. The volume, on the other hand, is linearly dependant on ρ:

$$v(\rho) = \int_\Omega \rho(\boldsymbol{x}) \mathrm{d}V. \tag{A.2}$$

The penalty power makes intermediate densities uneconomical, since the stiffness of regions with intermediate densities are significantly reduced, while volume is contributed to linearly.

If $p = 1$ in A.1, the problem is converted to one where the energy depends linearly on ρ. In [13], it is noted that this linear problem provides the "most relaxed" problem and provides a useful bound on the maximum structural efficiency. An example of this type of problem is the variable thickness sheet problem.

Although the SIMP model is often referred to as an artificial or fictitious model since it was argued that intermediate densities could not be physically interpreted (as they can in the homogenization method). However, it was shown in [152] that the SIMP model can indeed be considered a realistic material model if p satisfies:

$$p \geq \max\left\{\frac{2}{1-\nu^0}, \frac{4}{1+\nu^0}\right\} \text{ in 2-D,} \tag{A.3}$$

$$p \geq \max\left\{\frac{15(1-\nu^0)}{7-5\nu^0}, \frac{3(1-\nu^0)}{2(1-2\nu^0)}\right\} \text{ in 3-D.} \tag{A.4}$$

That is to say, materials constructed from composites (materials with microstructure) which satisfy the Hashin-Shtrikman bounds. The Hashin-Shtrikman bounds for two-phase materials impose limits on materials properties achievable by constructing materials with microstructure from two linear elastic materials.

The simplicity and ease of implementation of the SIMP material model has seen topology optimization being adopted by a significant number of different elasticity problems and even different fields and problems, including : vibration and dynamics [104, 153, 154], buckling [155], flow [156], Micro Electro Mechanical Systems (MEMS) and multiphysics problems [106, 138], and even wave propagation problems [157].

A typical material distribution topology optimization problem can be stated as: Find the subdomain Ω_{mat} with a limited volume ($\bar{v}$) in Ω which minimizes a given objective function f (for example compliance). In order to solve the problem as a material distribution problem, a density function ρ is introduced which is 1 in Ω_{mat} and 0 elsewhere. Mathematically, this problem can be written as:

$$\begin{aligned} &\min_{\rho} f(\rho) \\ &\text{subject to} : v(\rho) = \int_{\Omega} \rho \, \mathrm{d}V \leq \bar{v} \\ &\qquad\qquad : \rho(\boldsymbol{x}) = 0 \text{ or } 1, \ \forall \boldsymbol{x} \in \Omega \\ &\qquad\qquad : \text{Physical laws} \end{aligned} \tag{A.5}$$

These problems are mostly solved using the finite element method. The discrete form of the problem can therefore be written as:

$$\begin{aligned} &\min_{\boldsymbol{\rho}} f(\boldsymbol{\rho}) \\ &\text{subject to} : v(\boldsymbol{\rho}) = \frac{1}{v_\Omega} \sum_{i=1}^{Nel} \rho_i v_i \leq v^* \\ &\qquad\qquad : \rho_i = 0 \text{ or } 1, \ \forall i = 1, 2, \ldots, Nel \\ &\qquad\qquad : \text{Physical laws} \end{aligned} \tag{A.6}$$

where v^* is an upper bound on the permissible volume fraction and Nel is the number of elements in the finite element mesh.

Of course numerous other methods to solve topology optimization problems exist. Examples include:

- *Evolutionary methods* which are related to fully stressed design methods and typically involve the iterative addition of elements in regions where they are predicted to be effective and removal from ineffective areas. Typically sensitivity information is not required or used in these methods. Although these methods are usually relatively easy to implement, Eschenauer and Olhoff [149] warn that evolutionary structural optimization-type methods are heuristic and have been shown to fail for even simple problems [158].

- Employing *topological derivatives* and *bubble methods* extends the use of boundary variation shape optimization techniques to topology optimization. Principally, the sensitivity to the addition of an infinitesimally small hole (a change in topology) at a certain point in the design domain is estimated. The topological derivative is used where necessary to alter the topology, while standard shape optimization techniques are used to manipulate the interior and exterior boundary shapes.

  Level set methods have also become quite popular of late. Essentially, as explained by Bendsøe and Sigmund [4], the contours of a parameterized family of level-set functions are used to define and alter the boundaries of a structure.

  Although these methods are theoretically sound, they are rather complex and are difficult to implement. Furthermore, although they have been demonstrated on problems such as the minimum compliance problem, they are difficult to extend to practical problems such as compliant mechanism design.

- Since discrete (0-1) solutions are ultimately sought from the topology optimization routine, it seems attractive to tackle the problem using *discrete variables*. Easily implemented gradient-free optimization algorithms such as Genetic Algorithms (GA's) and Particle Swarm Optimization Algorithms (PSOA's) have previously been applied to problems in topology optimization. However, these methods have had little success since, due to the large scale of the problems, a restrictively large number of (relatively numerically expensive) function evaluations are required.

Once again, a more detailed survey of these methods can be found in for example [149, 4].

A.1 Implementional issues

There are several known implementational issues which need to be dealt with appropriately if topology optimization procedures are to yield sensible results. These issues include: *existence* of solution (*mesh dependency*), *checkerboarding*, *one-node connected hinges*, *non-uniqueness*, and *local minima*. In this section, some of the work that has been published in open literature to deal with these issues, will be highlighted.

A.1.1 Mesh dependency

Problem (A.5) is well know to lack solution in general. A somewhat simplified explanation for this is that for a given design, with known volume, allowing the addition of new holes

(without increasing the volume) generally increases the efficiency of the allowable optimal design. More specifically, the set of feasible designs is not closed. This nonexistence problem (mesh dependence in the discrete case (A.6)) can be overcome by either relaxation or by restriction of the design domain.

Problem relaxation involves expanding the set of permissible designs to achieve existence. Bendsøe and Kikuchi [107] famously relaxed the problem by permitting composite microstructure using a homogenization method. The homogenization method describes global behaviour in terms of a microscopic base cell. Using this method, each elements effective density is allowed to vary such that $0 \leq \rho_i \leq 1$, $\forall i = 1, 2, \ldots Nel$, based on the parameterization of the base cell. Using this procedure however, can result in large areas of intermediate density which can be physically interpreted, but are difficult to manufacture.

Methods do exist to explicitly penalize intermediate densities, e.g. see [13, 159]. The problem with this explicit penalization of intermediate densities is however, that one is essentially reverting back to the problem in (A.6) which lacks solution!

More detail on topology optimization using homogenization methods can be found in Section 7.5.1. The detail of this method will therefore not be repeated here since the focus of this study is on the SIMP method.

The other method to overcome the non-existence problem is to restrict the set of admissible designs. Restriction methods involve decreasing the size of the set of feasible designs. In doing so, the set of all possible designs is sufficiently closed.

For detailed reviews of restriction methods, the reader is referred to [4, 13]. Since many of these methods also have the effect of reducing checkerboarding, some details of methods to deal with the mesh dependency problem will be presented here.

Perimeter control

The basic idea of this method is to (as the name suggests) restrict the perimeter of the solid domain Ω_{mat}. Roughly speaking, the perimeter is the sum of the perimeters of all the holes and the perimeter of boundary. Importantly, existence to topology optimization problems with a restriction on the perimeter was proven by Ambrosio and Buttazzo [160].

Haber *et al.* developed the first numerical implementation of this method. They impose a constraint on the total variation, which is in fact the perimeter of the solid domain if $\rho = 1$ in Ω_{mat} and $\rho = 0$ elsewhere. The discrete form of the total variation is:

$$P = \sum_{k=1}^{K} l_k \left(\sqrt{< \rho >_k^2 + \epsilon^2} - \epsilon \right), \tag{A.7}$$

where $< \rho >_k$ is the jump in material density over element interface k of length l_k. $K \approx 2Nel$ is the number of element interfaces and ϵ is a small number used to produce a differential function in place of the absolute value. Other workers who have made contributions are Duysinx [161] for continuous variables and Beckers [162] who worked with discrete variables. This method results in the inclusion of only one additional constraint which can easily be accommodated by general purpose optimizers such as MMA.

A reported drawback of this method is that that perimeter constraint is relatively difficult to approximate, resulting in fluctuations in the design variables. This is reported to be related to the choice of asymptotes of MMA [4]. These implementational issues were alleviated by an inner loop procedure for the relatively inexpensive perimeter approximation by Duysinx [161]. Furthermore, the choice of the actual bounding value is not easily physically justifiable.

Global gradient constraint

Bendsøe [139] proved existence of solution when including this bound in topology optimization problems. The global constraint simply involves imposing a bound on the norm of the ρ function in the Sobolov space $H^1(\Omega)$,

$$||\rho||_{H^1} = \left(\int_{Omega} (\rho^2 + |\nabla \rho|^2 \mathrm{d}V) \right)^{1/2} \leq M. \tag{A.8}$$

This method also only involves one additional constraint function, however Bendsøe and Sigmund [4] report that implementation of A.8 also involves some experimentation with a range of values for bound M to achieve acceptable results.

Local gradient constraint

Petersson and Sigmund [163] proved existence of solution for, as well as numerically implemented, a scheme introducing local gradient constraints. Point-wise bounds on the spacial derivatives of function ρ are imposed:

$$|\frac{\partial \rho}{\partial x_i}| \leq G, i = 1, 2, 3 \text{ (in three dimensions)}. \tag{A.9}$$

This scheme (which essentially constrains the L^∞ norm of the gradient of ρ) has the advantage that the gradient constraint provides a well defined length scale. That is to say, the transition from solid, to void, back to solid requires a distance of at least $2/G$. However, implementation of this scheme results in (up to) $2Nel$ additional constraints for the optimization problem, making large scale implementation difficult.

MOLE method

Recently a scheme named 'MOLE' (MOnoticity based minimum LEngth scale) has been proposed by Poulsen [164]. In essence, the idea is to pass a circular filter over the design domain and measure the monotonicity of the density function (horizontally, vertically and at +/- 45°). If a non-monotonic density distribution is detected at a smaller length scale than desired, a constraint function becomes non-zero. A permissible tolerance is placed on this function, resulting in only one additional constraint being added to the optimization problem.

Filtering of elemental densities

In a discrete implementation, this scheme modifies each elements density as some weighted sum of the surrounding elements within a certain distance [4]. Features larger than the filter size are implicitly penalised, since any non-uniformities within the filter area will result in a 'grey' element which is uneconomical in the SIMP model.

Implementation requires sensitivities of each element to take into account the mutual energy of elements within the filter radius. Therefore, although no additional constraints are added to the optimization problem, but bookkeeping in the computation of sensitivities may be somewhat involved.

Filtering sensitivities

A method which has been widely used by numerous authors is to filter the sensitivity information of the optimization problem. Although the method is purely heuristic, it is extremely efficient and has been shown to provide very good results for a wide range of problems, for examples see [4], with very little additional computational expense. Furthermore no additional constraints are added to the optimization problem, and therefore standard optimality criteria methods can be used.

The filter was originally proposed by Sigmund [100, 165] and not only does this scheme impose a sensible length scale on the problem but also eliminates checkerboarding. The scheme works by modifying the sensitivities as follows:

$$\frac{\hat{\partial} f}{\partial \rho_k} = (\rho_k)^{-1} \frac{1}{\sum_{i=1}^{Nel} \hat{H}_i} \sum_{i=1}^{Nel} \hat{H}_i \rho_i \frac{\partial f}{\partial \rho_i}, \tag{A.10}$$

where a linear convolution operator $\hat{H}_i$ can be written as

$$\hat{H}_i = r_{\min} - \text{dist}(k,i), \{i \in Nel | \text{dist}(k,i) \leq r_{\min}\}, k = 1, 2, \ldots, Nel, \tag{A.11}$$

and $\text{dist}(k,i)$ is the distance between the centroid of elements k and i, and $\hat{H}_i$ is zero outside the filter area.

A.1.2 Checkerboarding, one-node connected hinges

The checkerboarding phenomena is described in detail in Chapter 7, and therefore only a condensed treatment will be presented here. The checkerboarding problem is characterised by material distributions in "optimal topologies" being distributed in alternating solid and void elements. Checkerboarding is largely as a result of poor numerical modelling of this spurious material distribution, as shown by Díaz and Sigmund [14] and Jog and Haber [102]. In essence, the numerical behaviour of this material distribution is over-stiff.

The one-node connected hinge is characterised by four elements surrounding a node, where two diagonally opposite elements are solid and the other two are void. Although it is reported

that the mesh-independency sensitivity filtering scheme also eliminates checkerboarding, one-node connected hinges are still possible, and are in fact somewhat common when applied in the design of compliant mechanisms. The reason is that in compliant mechanism design, solid state hinges are employed to achieve the required motion and the numerical model of a on-node hinge employing standard Q4 elements is ideal (if unrealistic and inaccurate) since it offers zero resistance to bending.

Methods to overcome the problems of checkerboarding or one-node hinges (or both) are numerous, and therefore only selected popular methods with be presented here.

Higher order elements

It was shown by Díaz and Sigmund [14] and by Jog and Haber [102] that checkerboarding is to a large extent eliminated when higher order (Q8 or Q9 planar) elements are employed with the homogenization material model. However, as was shown in Chapter 7, checkerboarding is only prevented in the SIMP model for a limited range of values for the penalty power p. A significant drawback is that higher order elements are significantly more numerically expensive than standard elements.

Patches

An alternative is to eliminate checkerboarding in a patch of elements. Patches are comprised of four regular elements with a common node in the centre of the patch. The complete mesh is therefore made up of $P_x \times P_y$ patches or $2P_x \times 2P_y$ elements. Each patch of four elements can be viewed as a single "super-element".

Four orthogonal basis functions are defined for the patch, similar to those described in Section 5.5.2, one of which defines a pure checkerboard pattern. The ρ function is then restricted to lie within a reduced, checkerboard-free space. This is achieved by, for each patch, modifying the updated design variables by removing the component associated with the pure checkerboard basis function [4].

Alternatively wavelet methods can be employed to directly work in a space without checkerboarding [98, 151]. It was shown that this method can be used to prevent checkerboarding as well as to obtain some geometry control.

Filters

The scheme employed to impose mesh-independency, introduced by Sigmund [100] also efficiently alleviates the checkerboarding problem.

NoHinge

Poulsen [15] developed a simple scheme to avoid the formation of one-node connected hinges and checkerboard patterns. This scheme results in a single additional constraint based on a

measure of non-monotonicity of density around each interior node in the mesh. This method is the basis of the new scheme developed in Section 5.5.2.

Other Methods

Most of the restriction methods described in the previous section also alleviate the effects of checkerboarding.

A.1.3 Other complications

Other common complications in topology optimization problems are multiple (local) optima and non-uniqueness. If one observes the many different optimal solutions which have been published for, for example the MBB beam problem, it is clear that there are many local optima present in these problems. This is due to the fact that most topology optimization problems are non-convex. A popular method to alleviate non-convexity is the use of continuation methods, in which problems are gradually changed from (artificial) convex or nearly convex problems to the original non-convex problem. An example would be raising the penalty exponent p from 1 to higher values gradually, or gradually raising the value of filter radius until the desired value is reached.

Problems with multiple optimal solutions (with the same objective value) are termed non-unique. An example commonly cited is that of a structure under uniaxial tension, in which only the cross-sectional area is of importance and not the topology. The only sensible way to deal with this problem is to impose manufacturing preference constraints.

A.2 Compliant mechanism design

Since the ultimate application of the scheme developed in this investigation, is a piezoelectrically driven mirror scanning device designed using topology optimization, a brief review of previous work in the field is appropriate.

This review is not meant to be an exhaustive review, but is simply meant to give some background to problems previously considered in this field. Again, for a more comprehensive review the reader is referred to the book of Bendsøe and Sigmund [4] and to the review article by Frecker [103].

Compliant mechanisms achieve their mobility via the solid-state flexibility of different regions (components) within a single connected structure[1]. The fact that they are solid-state makes their use especially attractive when piezoelectric actuators are used. Piezoelectric actuators are capable of relatively small strokes (usually in the order of μm), which can easily be lost to any play in the system.

Original works in the field are credited to Ananthasuresh *et al.* [166] and Sigmund [100]. Since then, numerous works have appeared, e.g. see [101, 138]. Mechanisms able to gen-

[1] Of course the mechanism itself can include multiple parts e.g. actuation mechanism connected to a mechanical amplifier.

erate specific prescribed paths have been developed by (for example Pedersen *et al.* [167]. Optimization of mechanisms for dynamic response has been considered by for example Min and Kikuchi [168]. In most of these works, the output load is modelled using a spring with specific stiffness against which the mechanism works.

In [169], instead of using a spring for the output to work against, various alternative function specifications are investigated. Examples include, mechanical advantage, geometrical advantage and work ratio.

Topology optimization of smart structures is now specifically considered, especially those employing piezoelectric actuation. Notably, far less attention has been paid to other smart materials, such as shape memory alloys [170].

Canfield and Frecker [171] used a ground structure approach to design mechanical amplifiers for piezoelectric stack actuators by maximizing geometrical advantage or maximizing mechanical efficiency. The ground structure approach results in relatively sparse structures which are not easily manufacturable.

In Silva and Nishiwaki [172] a micromanipulator is designed using the homogenization topology optimization method. This multi-flexible structure requires various prescribed output displacements at different points in the domain for various excitations due to piezoelectric actuators.

Silva *el al.* [173] also used the homogenization method in the design of piezoelectric composite material microstructures. They maximize given performance measures by designing a material microstructure with prescribed material properties. Sigmund and Torqato [174] employed a similar procedure to design and manufacture piezoelectric material microstructures, except that the SIMP method is employed.

In Li *et al.* [175], the optimal shape and location of piezoelectric materials within the (optimal) compliant mechanism were generated. The placement of the piezoelectric material was performed in an outer loop, optimized with a G.A. and the compliant mechanism optimization carried out (for fixed location) in an inner loop.

Generally, mechanisms obtained using linear modelling in the topology optimization infrastructure do not behave optimally when subjected to large input/output displacements. For these applications geometrically non-linear modelling is required to generate optimal compliant mechanisms which produce the required motion. This problem was considered by for example Bruns *et al.* [137] and Pedersen *et al.* [167]. Non-linear modelling is not necessary for our applications driven by a piezoelectric actuator since free strains in the stacks employed are typically in the order of $0.1-0.2\%$.

Finally, topology optimization of mechanical amplifiers subjected to dynamic motion was considered by [176].

Appendix B

Additional plate and shell results

In order to maintain the conciseness of Chapter 6, only the most important and immediately relevant results were presented within the chapter itself. In this appendix supplemental results are presented which corroborate the evidence and support the conclusions drawn during the course of the investigation. The additional results that are referred to, but not explicitly given in Chapter 6, are therefore presented herein.

B.1 Additional membrane results

Firstly, the supplemental membrane results are given. For details of the considered problem, the reader is referred to Section 6.5.1.

B.1.1 MBB beam

The geometry, material properties, restraints and loading are all depicted in Figure 6.6. Although symmetry is used to model the structure, the complete topology is reported. In total 2700 square elements are used, 90 elements along the length of the finite element model, $L/2$ and 30 elements in the height h. Of course, since only membrane components are evaluated, only the single layer material model is tested. The available volume fraction is half of the design domain.

Figure B.1 depicts the convergence histories for the topologies shown in Figure 6.8. In order to stabilize the convergence, the penalty exponent is stepped from 1 to 3 as shown on the convergence history plots. Also, the objective is normalized with respect to the starting value of compliance in order to improve the problem scaling.

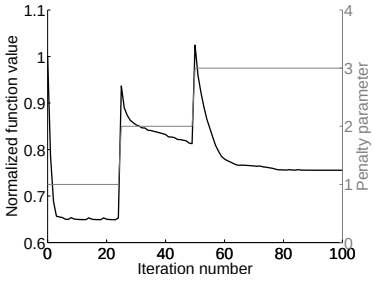

(a) Q4 element. (same for all α)

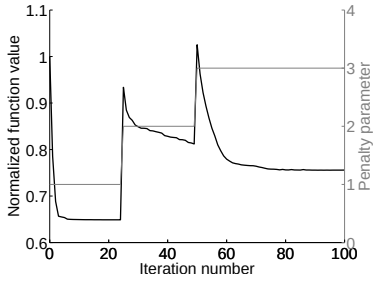

(b) Q4γ element, $\alpha = 0$.

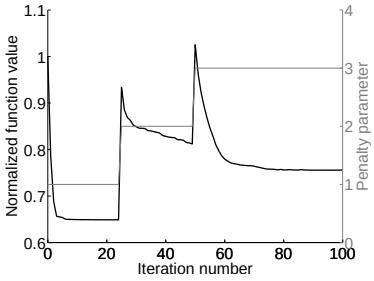

(c) Q4γ element, $\alpha = 10^{-6}$.

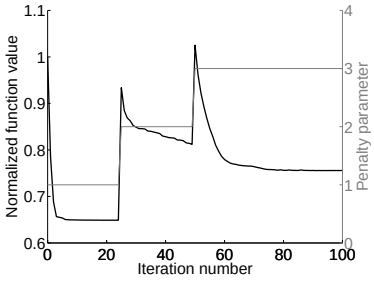

(d) Q4γ element, $\alpha = 10^{-4}$.

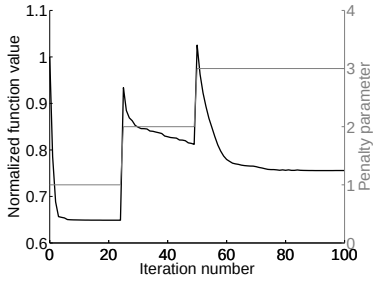

(e) Q4γ element, $\alpha = 10^{-2}$.

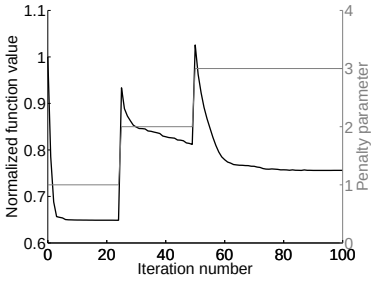

(f) Q4γ element, $\alpha = 10^{0}$.

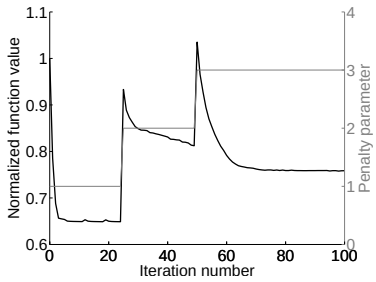

(g) Q4γ element, $\alpha = 10^{2}$.

Figure B.1: Convergence histories for MBB beam for various values of α.

B.2 Additional plate results

In this section, supplemental plate results are detailed. For more information about the considered problems, see Section 6.5.3 herein.

B.2.1 Simply supported square plate with centre point load

The geometry and constraints for the first plate problem are depicted in Figure 6.9(a). The problem consists of a square plate which is simply supported, and subjected to a unit point load applied to the center of the plate. Three material models are analyzed, namely single layer, ribbed and honeycomb material models.

The results for this problem are depicted in Figures B.2 to B.7. Figures B.2 and B.3 depict respectively the optimal topologies and convergence histories for the thin and thick single layer models. Figures B.4 and B.5 represent the optimal topologies for the thin and thick ribbed material models, with corresponding convergence histories. The results for the thin and thick honeycomb material models are depicted in Figures B.6 and B.7, respectively.

The tables accompanying each figure, tabulate the difference in compliance between the optimal topologies, analyzed using the three plate elements utilized in this study. The values represent the percentage difference between the compliance of the optimal topology computed with a given element, and the compliance calculated using the remaining two elements. Of course, there is no difference between the compliance of the optimal topology calculated with any element and itself, accounting for the zero terms on the diagonal of each table.

Single layer material model

Figure B.2 illustrates that similar topologies are computed using each of the different elements when considering the thin simply supported plate, with single layer material model. Table B.1, further shows that the solutions obtained from the two Mindlin-Reissner elements (in particular the ANS element) are marginally better than the result obtained using the DKQ element. A possible explanation for the slight improvement on the DKQ results, is that the regions of intermediate density (which contribute little to the compliance) are less pronounced in the two Mindlin-Reissner elements. The correctness of these results may be confirmed when compared to previously published results for similar problems [3, 115, 4].

Figure B.3 contains the results for the thick single layer problem. In this case the topology obtained using the DKQ element differs from the topologies obtained using the two Mindlin-Reissner elements. Since the DKQ element is shear rigid, the thick optimal topology is identical to the thin result as expected. Table B.2 shows, the compliance of the structure generated using DKQ elements has approximately 18% higher compliance (lower stiffness) than the topology computed with ANS elements, when both are modelled using ANS elements. The DKQ result has a 24% higher compliance than the result obtained with SRI elements, when both are analysed using SRI elements. Although the 18% and 24% differences cannot directly be compared since the percentage differences are calculated relative

	Optimal topology generated using:		
	DKQ	ANS	SRI
Analysed with DKQ	0.0000	-0.4871	-0.0641
Analysed with ANS	0.6021	0.0000	0.2734
Analysed with SRI	0.7677	-0.1193	0.0000
Constraint value	5.5924e-05	-4.4603e-05	-6.8271e-05

Table B.1: Percentage difference: Simply supported square plate subjected to center point load, single layer model, $t = 0.01$.

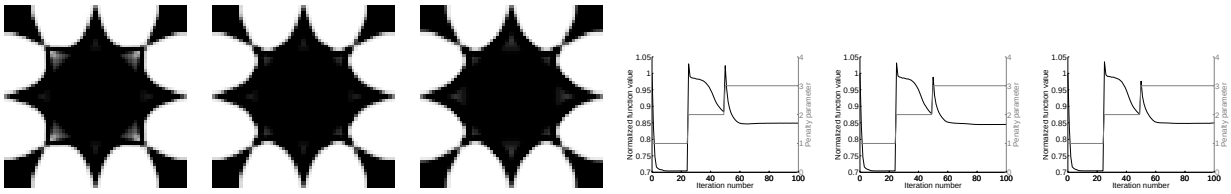

(a) DKQ. (b) ANS. (c) SRI. (d) DKQ. (e) ANS. (f) SRI.

Figure B.2: Optimal topologies of a simply supported square plate subjected to center point load, single layer model, $t = 0.01$: (a)-(c) optimal topologies, (d)-(f) convergence histories.

to different designs, the discrepency is significant. This difference is likely as a result of the SRI element being softer than the ANS elements in transverse shear.

	Optimal topology generated using:		
	DKQ	ANS	SRI
Analysed with DKQ	0.0000	1.3109	3.1641
Analysed with ANS	17.5832	0.0000	1.1297
Analysed with SRI	24.3415	-0.4341	0.0000
Constraint value	5.5924e-05	1.1389e-05	-7.5900e-06

Table B.2: Percentage difference: Simply supported square plate subjected to center point load, single layer model, $t = 0.1$.

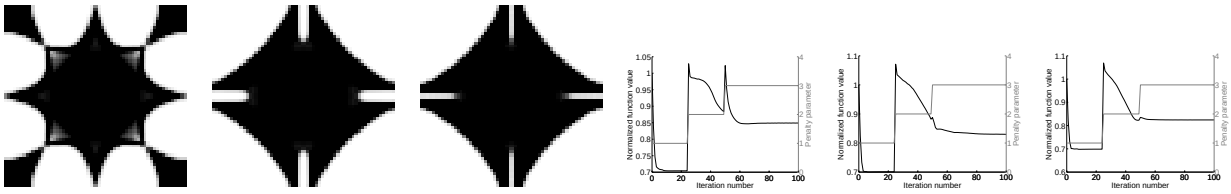

(a) DKQ. (b) ANS. (c) SRI. (d) DKQ. (e) ANS. (f) SRI.

Figure B.3: Optimal topologies of a simply supported square plate subjected to center point load, single layer model, $t = 0.1$: (a)-(c) optimal topologies, (d)-(f) convergence histories.

Ribbed material model

Figures B.4 and B.5, together with Tables B.3 and B.4 indicate that the ribbed design solutions are similar for the thin and thick structures. The shape of the thick Mindlin-Reissner solutions differ slightly from the thin results, but the difference in compliance, presented in Table B.4, is insignificant.

	Optimal topology generated using:		
	DKQ	ANS	SRI
Analysed with DKQ	0.0000	-0.1651	-0.2534
Analysed with ANS	0.1721	0.0000	-0.0868
Analysed with SRI	0.2514	0.0823	0.0000
Constraint value	7.0194e-05	2.4505e-05	-2.5642e-06

Table B.3: Percentage difference: Simply supported square plate subjected to center point load, ribbed model, $t = 0.01$.

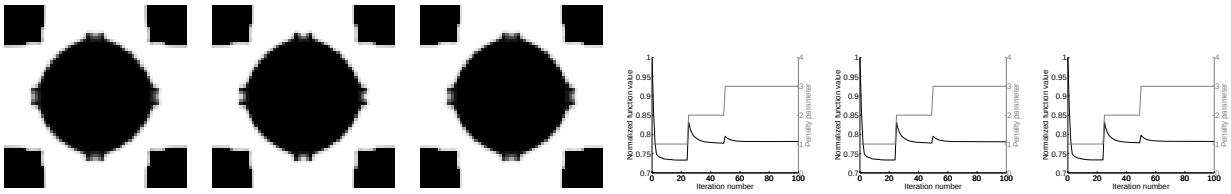

(a) DKQ. (b) ANS. (c) SRI. (d) DKQ. (e) ANS. (f) SRI.

Figure B.4: Optimal topologies of a simply supported square plate subjected to center point load, ribbed model, $t = 0.01$: (a)-(c) optimal topologies, (d)-(f) convergence histories.

	Optimal topology generated using:		
	DKQ	ANS	SRI
Analysed with DKQ	0.0000	1.4849	1.5135
Analysed with ANS	0.4956	0.0000	0.0404
Analysed with SRI	0.5351	-0.0030	0.0000
Constraint value	7.0194e-05	-1.1443e-04	4.4419e-05

Table B.4: Percentage difference: Simply supported square plate subjected to center point load, ribbed model, $t = 0.1$.

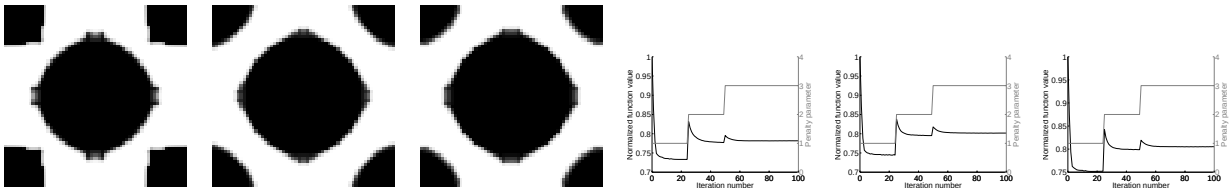

(a) DKQ. (b) ANS. (c) SRI. (d) DKQ. (e) ANS. (f) SRI.

Figure B.5: Optimal topologies of a simply supported square plate subjected to center point load, ribbed model, $t = 0.1$: (a)-(c) optimal topologies, (d)-(f) convergence histories.

Honeycomb material model

Considering the honeycomb layered model, the Mindlin-Reissner elements recover the same topology as the Kirchhoff element for the thin structure. For the thick plate however, although the percentage difference in function values presented in Table B.6 are very small, the optimal topologies calculated using using each element differ. What is more, Table B.6 confirms that the optimal topology generated with each element, is superior to the topologies calculated using the remaining two elements. This illustrates that the 'optimal' (shape or) topology is dependent on which element is employed in the finite element analysis. Again, the assumption is that the difference, especially between the two Mindlin-Reissner elements is due to the ANS element being slightly stiffer than the SRI element in transverse shear.

	Optimal topology generated using:		
	DKQ	ANS	SRI
Analysed with DKQ	0.0000	0.0006	0.0004
Analysed with ANS	-0.0005	0.0000	-0.0002
Analysed with SRI	-0.0003	0.0002	0.0000
Constraint value	1.3423e-04	-1.7928e-04	-1.8889e-04

Table B.5: Percentage difference: Simply supported square plate subjected to center point load, honeycomb model, $t = 0.01$.

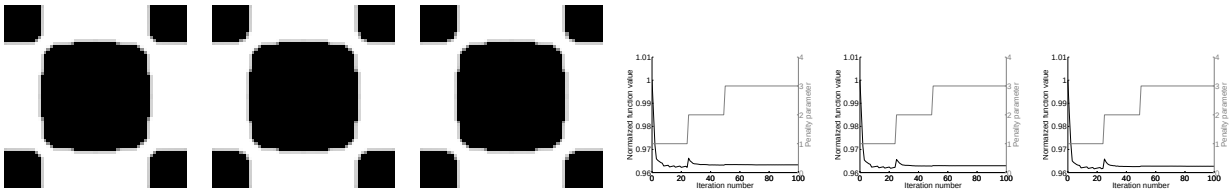

(a) DKQ. (b) ANS. (c) SRI. (d) DKQ. (e) ANS. (f) SRI.

Figure B.6: Optimal topologies of a simply supported square plate subjected to center point load, honeycomb model, $t = 0.01$: (a)-(c) optimal topologies, (d)-(f) convergence histories.

	Optimal topology generated using:		
	DKQ	ANS	SRI
Analysed with DKQ	0.0000	0.1873	0.5094
Analysed with ANS	0.1218	0.0000	0.0522
Analysed with SRI	0.4893	0.1351	0.0000
Constraint value	1.3423e-04	1.6512e-04	-9.2279e-05

Table B.6: Percentage difference: Simply supported square plate subjected to center point load, honeycomb model, $t = 0.1$.

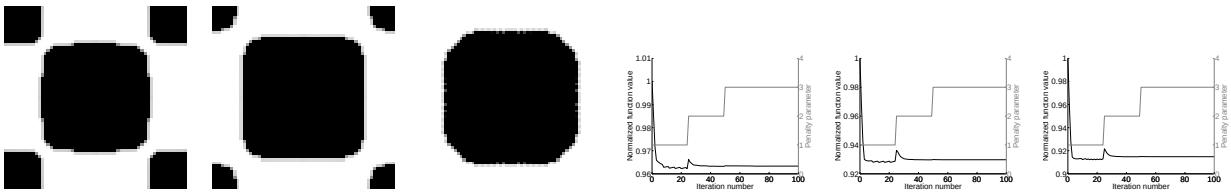

(a) DKQ. (b) ANS. (c) SRI. (d) DKQ. (e) ANS. (f) SRI.

Figure B.7: Optimal topologies of a simply supported square plate subjected to center point load, honeycomb model, $t = 0.1$: (a)-(c) optimal topologies, (d)-(f) convergence histories.

B.2.2 Clamped square plate with centre point load

The geometry for this problem is depicted in Figure 6.9(b). The load considered is again a unit point load applied to the center of the plate. This problem has been considered by a number of authors [4, 115], and our thin plate results compare favorably with theirs.

Single layer material model

The results for this problem are contained in Figures B.8 to B.13, and Tables B.7 to B.12. Figures B.8 and B.9, together with Tables B.7 and B.8 present the results for the thin and thick single layer models, respectively. Figures B.10 and B.11 and Tables B.9 and B.10 present the analysis thin and thick ribbed material models. The results for the thin and thick honeycomb material models are presented in Figures B.12 and B.13 with corresponding analysis in Tables B.11 and B.12, respectively.

From Figure B.8 and Table B.7 it is evident that, for the thin single layer material model, almost identical topologies are achieved for all elements. Although there is no visible difference between the three topologies, the negative values in the third column of Table B.7 indicate that the SRI result is marginally superior. The thick plate model on the other hand, results in slightly different topologies when Mindlin-Reissner elements are used compared to the result with the DKQ element. The finite element model is highly constrained, which could explain the slightness in difference between the thin and thick results. Nevertheless, the effect on the compliance is significant, with a 14% improvement on the thin topology's compliance compared to the result using ANS elements, when analysed with ANS elements and a 37% improvement when compared to the SRI results, analysed with SRI elements. Again, although the 14% and 37% difference cannot be directly compared (because the differences are computed with respect to different optimal topologies) the indication is that the ANS elements are slightly more stiff in transverse shear than the SRI elements.

	Optimal topology generated using:		
	DKQ	ANS	SRI
Analysed with DKQ	0.0000	-0.1317	-0.3028
Analysed with ANS	0.1733	0.0000	-0.1513
Analysed with SRI	0.6954	0.7259	0.0000
Constraint value	-5.5042e-05	3.1765e-05	-7.8998e-05

Table B.7: Percentage difference: Clamped square plate subjected to center point load, single layer model, $t = 0.01$.

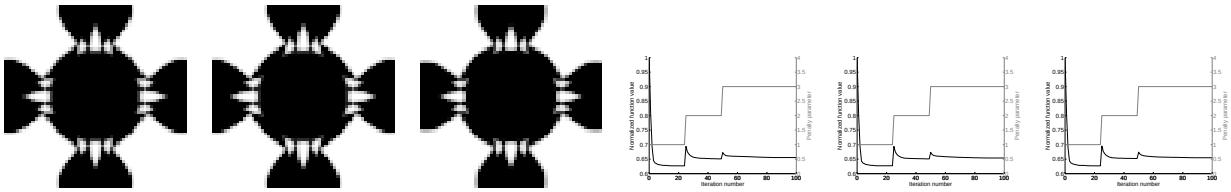

(a) DKQ. (b) ANS. (c) SRI. (d) DKQ. (e) ANS. (f) SRI.

Figure B.8: Optimal topologies of a clamped square plate subjected to center point load, single layer model, $t = 0.01$: (a)-(c) optimal topologies, (d)-(f) convergence histories.

	Optimal topology generated using:		
	DKQ	ANS	SRI
Analysed with DKQ	0.0000	1.3371	2.4424
Analysed with ANS	13.9028	0.0000	-0.0229
Analysed with SRI	37.0471	0.8543	0.0000
Constraint value	-5.5042e-05	-7.2254e-05	8.2104e-06

Table B.8: Percentage difference: Clamped square plate subjected to center point load, single layer model, $t = 0.1$.

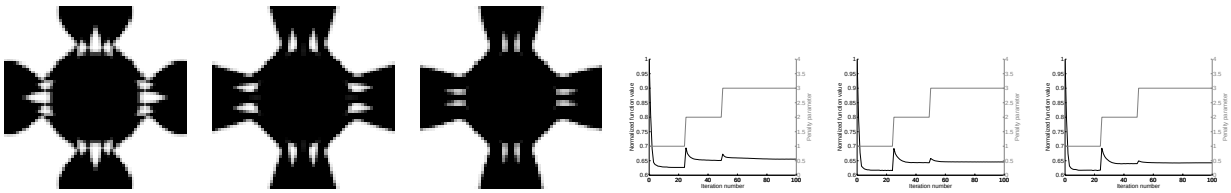

(a) DKQ. (b) ANS. (c) SRI. (d) DKQ. (e) ANS. (f) SRI.

Figure B.9: Optimal topologies of a clamped square plate subjected to center point load, single layer model, $t = 0.1$: (a)-(c) optimal topologies, (d)-(f) convergence histories.

Ribbed material model

For the ribbed material model, the thin and thick structures result in the same topologies for all elements as depicted in Figures B.10 and B.11. However, again the shape of the Mindlin-Reissner results differs slightly from the DKQ results for the thick plate. The values of compliance for the thin and thick plates are again similar for all elements, as shown in Tables B.9 and B.10.

	Optimal topology generated using:		
	DKQ	ANS	SRI
Analysed with DKQ	0.0000	0.0028	0.0115
Analysed with ANS	-0.0026	0.0000	0.0099
Analysed with SRI	-0.0098	-0.0069	0.0000
Constraint value	7.4645e-05	-2.9307e-05	-4.0355e-05

Table B.9: Percentage difference: Clamped square plate subjected to center point load, ribbed model, $t = 0.01$.

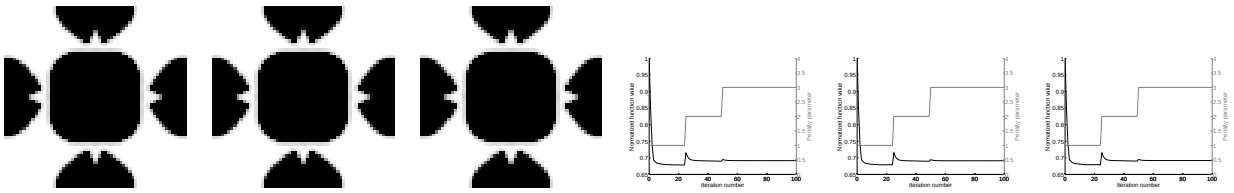

(a) DKQ. (b) ANS. (c) SRI. (d) DKQ. (e) ANS. (f) SRI.

Figure B.10: Optimal topologies of a clamped square plate subjected to center point load, ribbed model, $t = 0.01$: (a)-(c) optimal topologies, (d)-(f) convergence histories.

	Optimal topology generated using:		
	DKQ	ANS	SRI
Analysed with DKQ	0.0000	0.5273	0.5113
Analysed with ANS	0.1536	0.0000	0.0024
Analysed with SRI	0.2054	0.0593	0.0000
Constraint value	7.4645e-05	-9.2086e-05	7.4218e-05

Table B.10: Percentage difference: Clamped square plate subjected to center point load, ribbed model, $t = 0.1$.

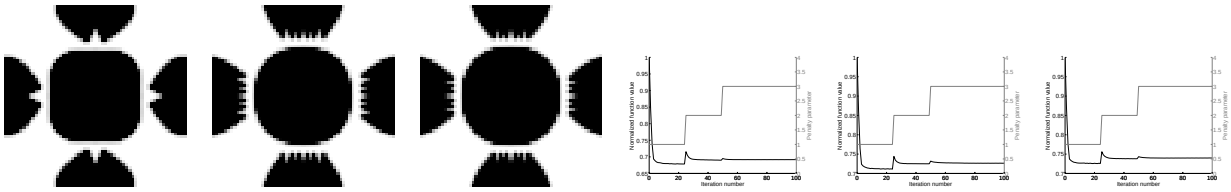

(a) DKQ. (b) ANS. (c) SRI. (d) DKQ. (e) ANS. (f) SRI.

Figure B.11: Optimal topologies of a clamped square plate subjected to center point load, ribbed model, $t = 0.1$: (a)-(c) optimal topologies, (d)-(f) convergence histories.

Honeycomb material model

Although in the case of the honeycomb material model, the optimal topologies for the thick plate generated using Mindlin-Reissner elements (see Figure B.13) are different to the results for the thin plate (depicted in Figure B.12), the result on the compliance is modest. However, the compliance results presented in Table B.12 do confirm that the optimal topology calculated using Mindlin-Reissner elements is lower than the DKQ topology for thick plates, whereas the DKQ result is indeed superior for thin plate problems.

	Optimal topology generated using:		
	DKQ	ANS	SRI
Analysed with DKQ	0.0000	-0.0060	0.0057
Analysed with ANS	0.0063	0.0000	0.0119
Analysed with SRI	-0.0058	-0.0120	0.0000
Constraint value	-5.9377e-05	-1.8208e-04	-1.3014e-04

Table B.11: Percentage difference: Clamped square plate subjected to center point load, honeycomb model, $t = 0.01$.

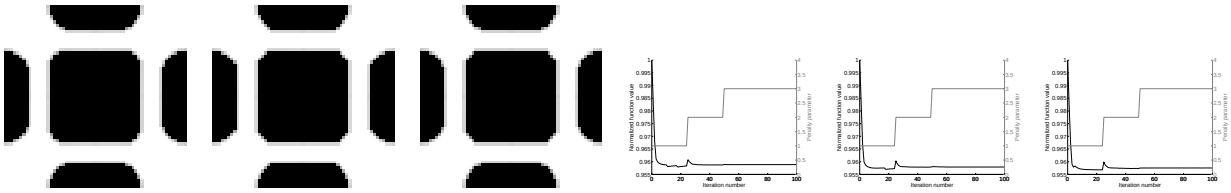

(a) DKQ. (b) ANS. (c) SRI. (d) DKQ. (e) ANS. (f) SRI.

Figure B.12: Optimal topologies of a clamped square plate subjected to center point load, honeycomb model, $t = 0.01$: (a)-(c) optimal topologies, (d)-(f) convergence histories.

	Optimal topology generated using:		
	DKQ	ANS	SRI
Analysed with DKQ	0.0000	0.2895	0.3975
Analysed with ANS	0.6686	0.0000	0.0097
Analysed with SRI	1.2910	0.0929	0.0000
Constraint value	-5.9377e-05	7.6439e-06	-1.0764e-04

Table B.12: Percentage difference: Clamped square plate subjected to center point load, honeycomb model, $t = 0.1$.

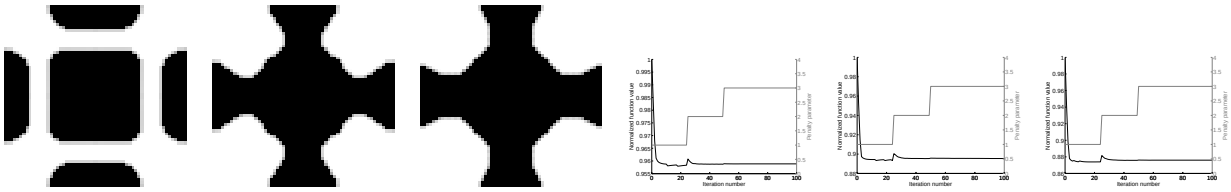

(a) DKQ. (b) ANS. (c) SRI. (d) DKQ. (e) ANS. (f) SRI.

Figure B.13: Optimal topologies of a clamped square plate subjected to center point load, honeycomb model, $t = 0.1$: (a)-(c) optimal topologies, (d)-(f) convergence histories.

B.2.3 Corner supported square plate with centre point load

The final plate geometry with restraints is depicted in Figure 6.9(c). It represents a corner supported plate (i.e. transverse displacement is constrained at the four corner nodes only). For this problem, the first load case considered, is again a center point load as before. Again the single layer, ribbed and honeycomb material models are analyzed.

Figures B.14 to B.19 with corresponding Tables B.13 to B.18 present the results for the corner supported square plate subjected to a center point load, for the single layer, ribbed and honeycomb material models.

Single layer material model

In Figure B.14 the optimal topologies for the thin, single layer material model are depicted. Once again, the topologies of all three elements are very similar. Although the SRI elements convergence history shows that some numerical problems were encountered during the optimization process, the final topology is not significantly affected. Albeit similar topologies are computed for the DKQ and ANS elements, Table B.13 indicates that the DKQ topology shows a 1% improvement over the optimal ANS results, when analysed using ANS elements.

	Optimal topology generated using:		
	DKQ	ANS	SRI
Analysed with DKQ	0.0000	1.2686	1.8995
Analysed with ANS	-1.0090	0.0000	0.5854
Analysed with SRI	2.1438	2.5740	0.0000
Constraint value	-5.2618e-05	-5.2688e-05	-3.4714e-05

Table B.13: Percentage difference: Corner supported square plate subjected to center point load, single layer model, $t = 0.01$.

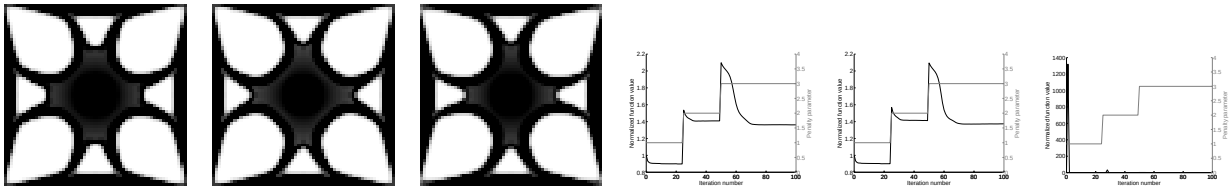

(a) DKQ. (b) ANS. (c) SRI. (d) DKQ. (e) ANS. (f) SRI.

Figure B.14: Optimal topologies of a corner supported square plate subjected to center point load, single layer model, $t = 0.01$: (a)-(c) optimal topologies, (d)-(f) convergence histories.

The results for the thick single layer material model are depicted in Figure B.15. In this case, the SRI result is distinctly different from the results using the other two elements.

Table B.14 shows that the compliance of the SRI result is approximately 4.5% lower than the DKQ result when both designs are analysed with DKQ elements and approximately 8.5% better than the ANS result when analysed using ANS elements. In this specific case the SRI element clearly realised the best design. This is again, probably due to the SRI element being 'softer' in transverse shear than the other two elements, which results in the optimizer searching different parts of the design domain. For this specific problem, the optimalilty criteria based algorithm appears to have terminated in local optima for the DKQ and ANS elements.

	Optimal topology generated using:		
	DKQ	ANS	SRI
Analysed with DKQ	0.0000	2.6995	-4.6636
Analysed with ANS	3.4167	0.0000	-8.5961
Analysed with SRI	16.4448	10.6660	0.0000
Constraint value	-5.2541e-05	2.3863e-05	2.5479e-05

Table B.14: Percentage difference: Corner supported square plate subjected to center point load, single layer model, $t = 0.1$.

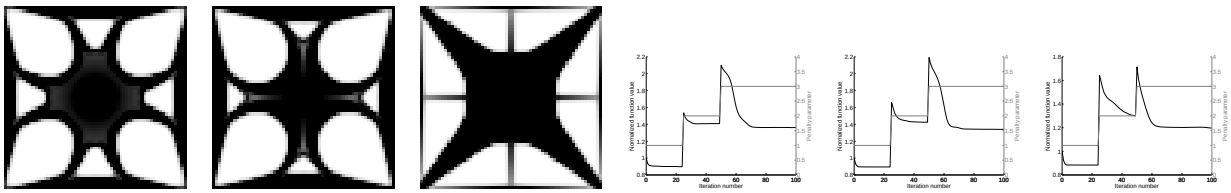

(a) DKQ. (b) ANS. (c) SRI. (d) DKQ. (e) ANS. (f) SRI.

Figure B.15: Optimal topologies of a corner supported square plate subjected to center point load, single layer model, $t = 0.1$: (a)-(c) optimal topologies, (d)-(f) convergence histories.

To confirm this, the same problem was run with identical finite element settings using the well-known MMA algorithm of Svanberg [10]. The optimal topologies for the MMA run are depicted in Figure B.16 with analysis of results in Table B.15. Ironically upon employing MMA as optimizer the results are reversed and the ANS element finds a superior design! Although for this specific problem the optimality criteria based updating scheme is unable to find the globally optimal solution for the ANS or DKQ elements, the effect of the finite element employed on 'optimal topology' is clearly demonstrated. This problem in particular serves also as a demonstration of the complexity (in global optimization terms) of the topology optimization problem.

	Optimal topology generated using:		
	DKQ	ANS	SRI
Analysed with DKQ	0.0000	-4.9705	3.4879
Analysed with ANS	15.2086	0.0000	10.0908
Analysed with SRI	6.5512	-9.4479	0.0000
Constraint value	-2.8216e-03	-9.8052e-04	-1.5108e-03

Table B.15: Percentage difference

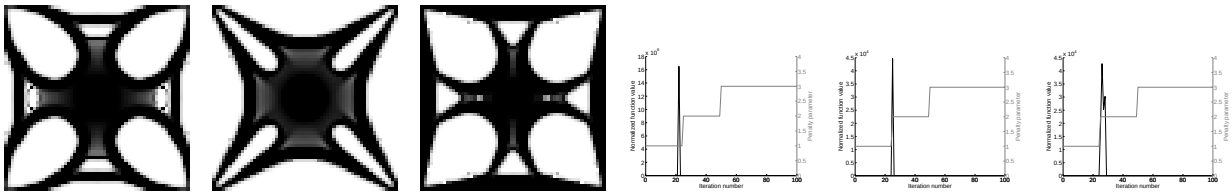

(a) DKQ. (b) ANS. (c) SRI. (d) DKQ. (e) ANS. (f) SRI.

Figure B.16: Optimal topologies of a corner supported square plate subjected to center point load, single layer model, $t = 0.1$: (a)-(c) optimal topologies, (d)-(f) convergence histories. Solved using MMA not OC.

Ribbed material model

Note that the results for the thin ribbed material model are presented and discussed in Section 6.5.3 on page 168. Considering the thick plate results for the ribbed material model, depicted in Figure B.17, again a distinctly different topology results from the use of Mindlin-Reissner elements. The numerical problems encountered with the SRI elements in the thin plate analysis are not experienced in this case. The negative values in the first row of Table B.16 indicate that the thick plate results is marginally superior, even for thin plates.

	Optimal topology generated using:		
	DKQ	ANS	SRI
Analysed with DKQ	0.0000	-0.2379	-0.1029
Analysed with ANS	4.2660	0.0000	0.0515
Analysed with SRI	4.4234	-0.0099	0.0000
Constraint value	-3.3457e-05	-2.8658e-05	-2.1399e-06

Table B.16: Percentage difference: Corner supported square plate subjected to center point load, ribbed model, $t = 0.1$.

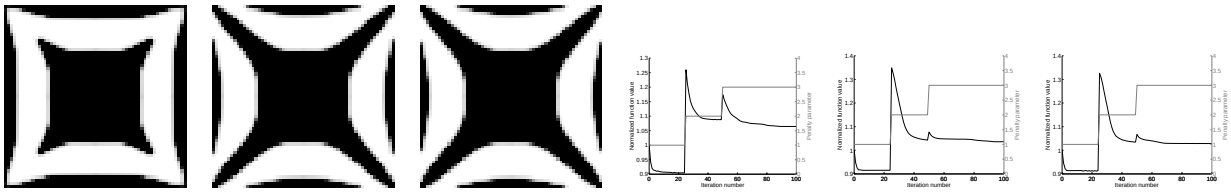

(a) DKQ. (b) ANS. (c) SRI. (d) DKQ. (e) ANS. (f) SRI.

Figure B.17: Optimal topologies of a corner supported square plate subjected to center point load, ribbed model, $t = 0.1$: (a)-(c) optimal topologies, (d)-(f) convergence histories.

Honeycomb material model

The results for the corner supported plate subjected to center point load with the thin honeycomb material model are depicted in Figure B.18. Again, although all converged topologies are similar, the iteration history of the SRI element suggests that some numerical instabilities occurred. In this case, many elements with negative compliance (or positive compliance gradient) were encountered at iteration 90. Figure B.19 illustrates how each of the element used to analyze the thick honeycomb material model, result in different topologies. In this case, the SRI element did not encounter any numerical problems in the iteration history. Although the SRI and ANS topologies (and shapes) are different, the compliance of the two structures is very similar. However, this problem demonstrates that even the two Mindlin-Reissner based elements result in different optimal shapes and topologies even though no numerical problems were encountered during the optimization history.

	Optimal topology generated using:		
	DKQ	ANS	SRI
Analysed with DKQ	0.0000	0.0331	0.0469
Analysed with ANS	0.0046	0.0000	0.0103
Analysed with SRI	0.0184	0.0065	0.0000
Constraint value	-1.5311e-04	3.8396e-05	-2.0403e-04

Table B.17: Percentage difference: Corner supported square plate subjected to center point load, honeycomb model, $t = 0.01$.

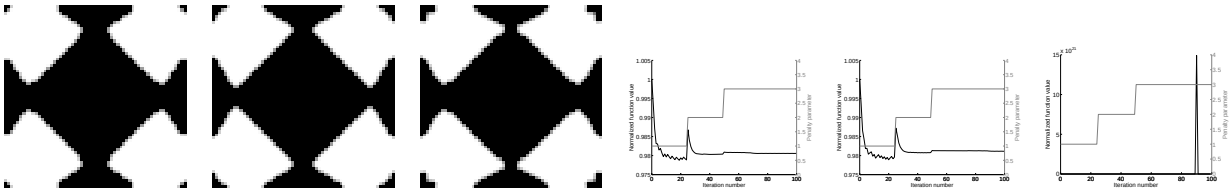

(a) DKQ. (b) ANS. (c) SRI. (d) DKQ. (e) ANS. (f) SRI.

Figure B.18: Optimal topologies of a corner supported square plate subjected to center point load, honeycomb model, $t = 0.01$: (a)-(c) optimal topologies, (d)-(f) convergence histories.

	Optimal topology generated using:		
	DKQ	ANS	SRI
Analysed with DKQ	0.0000	0.3268	0.6250
Analysed with ANS	1.8237	0.0000	0.1043
Analysed with SRI	3.3749	0.0978	0.0000
Constraint value	-1.5311e-04	2.7573e-04	6.2309e-05

Table B.18: Percentage difference: Corner supported square plate subjected to center point load, honeycomb model, $t = 0.1$.

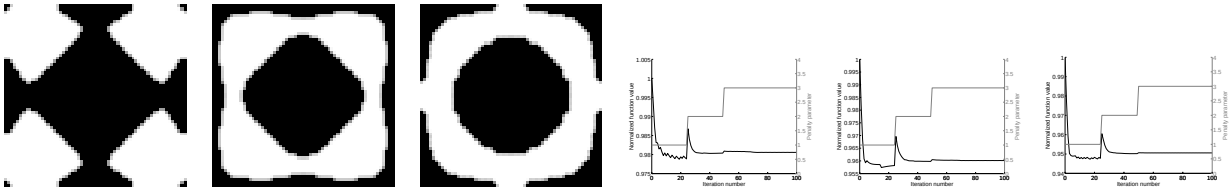

(a) DKQ. (b) ANS. (c) SRI. (d) DKQ. (e) ANS. (f) SRI.

Figure B.19: Optimal topologies of a corner supported square plate subjected to center point load, honeycomb model, $t = 0.1$: (a)-(c) optimal topologies, (d)-(f) convergence histories.

B.2.4 Corner supported square plate with distributed load

In this problem the same corner supported geometry and restraints, depicted in Figure 6.9(c), are used but the applied load in this case is uniformly distributed over the plate surface. In order to ensure that the load is not design dependent, only the ribbed and honeycomb material models are considered. The results for the thin ribbed material model are not repeated here since they are presented in Section 6.5.3, on page 168.

Figure B.20 depicts the optimal topologies for the thick ribbed models, with analysis in Table B.19. The results for the honeycomb material model are shown in Figures B.21 and B.22 with compliance results presented in Tables B.20 and B.21.

Ribbed material model

For the thick plate, again DKQ results in the same topology as the thin plate analysis, while the result of the ANS element is distinctly different. The compliance of the DKQ result is almost 3% higher than that of the ANS result when analysed with ANS plate elements. Again, the SRI element has an extremely irratic convergence history and a completely spurious, unsymmetric optimal topology results.

	Optimal topology generated using:		
	DKQ	ANS	SRI
Analysed with DKQ	0.0000	0.6072	34.2893
Analysed with ANS	2.7370	0.0000	34.5983
Analysed with SRI	121.3774	713.3591	0.0000
Constraint value	3.0994e-05	-3.2532e-05	-3.4844e-05

Table B.19: Percentage difference: Corner supported square plate subjected to uniform distributed load, ribbed model, $t = 0.1$.

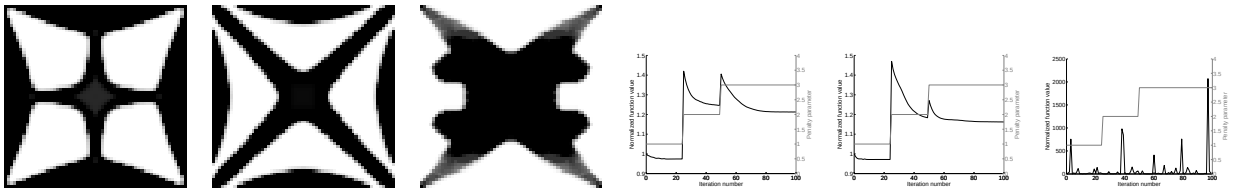

(a) DKQ. (b) ANS. (c) SRI. (d) DKQ. (e) ANS. (f) SRI.

Figure B.20: Optimal topologies of a corner supported square plate subjected to uniform distributed load, ribbed model, $t = 0.1$: (a)-(c) optimal topologies, (d)-(f) convergence histories.

Honeycomb material model

Similar observations can be made for the honeycomb layered models, depicted in Figures B.21 and B.22, with compliance analysis in Tables B.20 and B.21. The displaced shape of the thick honeycomb topologies computed with DKQ and ANS elements respectively, and analyzed using SRI elements, are plotted in Figures B.23 and B.24. In both the thin and thick honeycomb material models (especially the thin model), the compliance of the final topology computed with SRI elements is extremely large, due to the propagating mode. Therefore, the DKQ and ANS optimal topologies appear to be much better in Table B.20 since they are compared to a structure with almost zero stiffness.

	Optimal topology generated using:		
	DKQ	ANS	SRI
Analysed with DKQ	0.0000	0.0031	1.5821
Analysed with ANS	-0.0017	0.0000	1.9462
Analysed with SRI	-99.6858	-99.6666	0.0000
Constraint value	1.9059e-04	1.7756e-04	-8.6728e-03

Table B.20: Percentage difference: Corner supported square plate subjected to uniform distributed load, honeycomb model, $t = 0.01$.

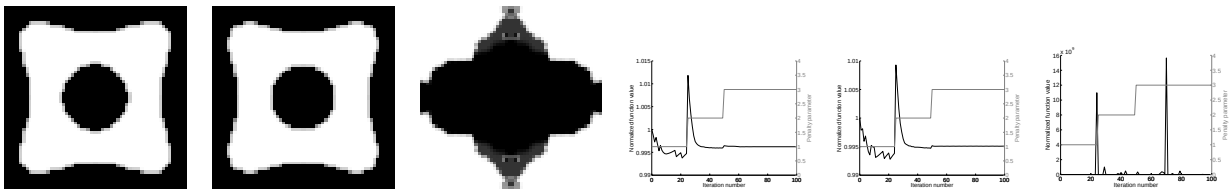

(a) DKQ. (b) ANS. (c) SRI. (d) DKQ. (e) ANS. (f) SRI.

Figure B.21: Optimal topologies of a corner supported square plate subjected to uniform distributed load, honeycomb model, $t = 0.01$: (a)-(c) optimal topologies, (d)-(f) convergence histories.

	Optimal topology generated using:		
	DKQ	ANS	SRI
Analysed with DKQ	0.0000	0.1147	1.5020
Analysed with ANS	0.2618	0.0000	2.1867
Analysed with SRI	2344.5765	-22.7655	0.0000
Constraint value	1.9057e-04	4.6099e-05	7.0618e-04

Table B.21: Percentage difference: Corner supported square plate subjected to uniform distributed load, honeycomb model, $t = 0.1$.

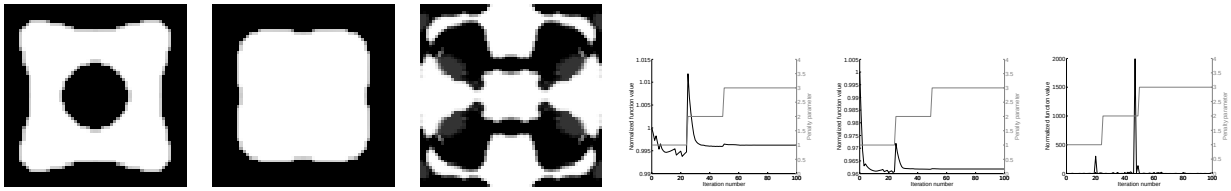

(a) DKQ. (b) ANS. (c) SRI. (d) DKQ. (e) ANS. (f) SRI.

Figure B.22: Optimal topologies of a corner supported square plate subjected to uniform distributed load, honeycomb model, $t = 0.1$: (a)-(c) optimal topologies, (d)-(f) convergence histories.

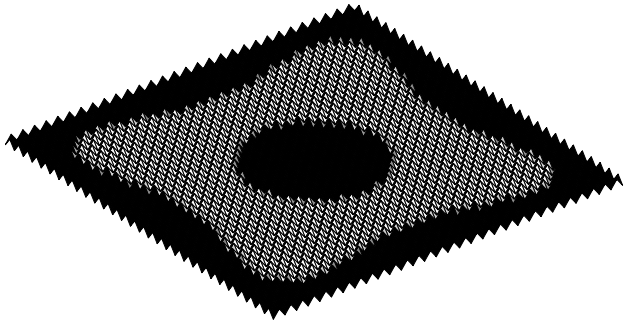

Figure B.23: Optimal topology, computed using DKQ, of the corner supported plate subjected to distributed load with thick honeycomb material model: Displaced shape analyzed using SRI elements, amplification factor 1×10^{-4}.

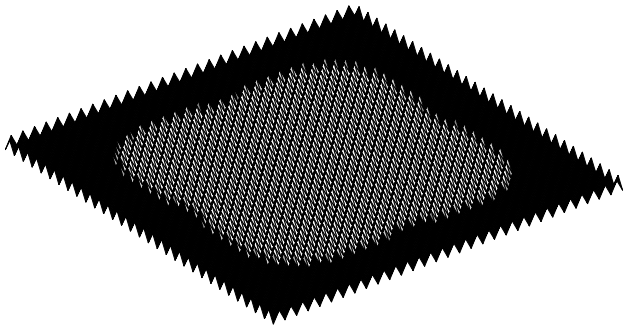

Figure B.24: Optimal topology, computed using ANS, of the corner supported plate subjected to distributed load with thick honeycomb material model: Displaced shape analyzed using SRI elements, amplification factor 1×10^{-4}.

B.3 Additional shell results

In the final section of this appendix, results not included in Section 6.5.5 are offered.

B.3.1 Cylindrical shell

The first shell problem is depicted in Figure 6.15. The geometry, restraints, applied loads and material properties are all depicted in the figure. The symmetry of the problem is exploited by only modeling one quarter of the structure with a 30×30 discretization. Once again, results are reported for the single layer, ribbed and honeycomb material models. A volume constraint of half of the design volume is again imposed.

Single layer material model

Figures B.25 and B.26 present details of the optimal topologies depicted in Figure 6.16, and their corresponding convergence histories. Since the x-axis of Figure 6.16 is plotted on a logarithmic scale, the topology at $\alpha = 0$ could not be included.

Figures B.25(a) and B.25(g) depict the optimal topologies for $\alpha = 0$ using the Q4αDKQ and Q4γDKQ elements respectively, with convergence histories in Figures B.26(a) and B.26(g), respectively. Notably, the Q4αDKQ has numerical instabilities if no stiffness is allotted to the rotational DOFs. No such problem is encountered when employing the Q4γDKQ element. The stability of the Q4γDKQ element at $\alpha = 0$ is due to the fact that α (which only scales γ) eliminates the penalty matrix $\boldsymbol{p}_{\mathrm{m}}^{\gamma} = \mathbf{0}$ in (6.29). However, enough stiffness is present to prevent numerical problems in the topology optimization environment. Of course this does not mean that the value of compliance will be very accurately calculated, and since this element is rank deficient its use in general should be avoided.

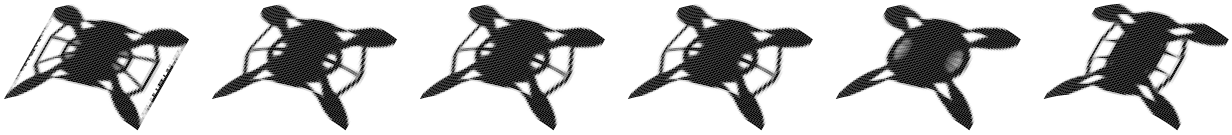

(a) Q4αDKQ element, $\alpha = 0$.

(b) Q4αDKQ element, $\alpha = 10^{-6}$.

(c) Q4αDKQ element, $\alpha = 10^{-4}$.

(d) Q4αDKQ element, $\alpha = 10^{-2}$.

(e) Q4αDKQ element, $\alpha = 10^{0}$.

(f) Q4αDKQ element, $\alpha = 10^{2}$.

(g) Q4γDKQ element, $\alpha = 0$.

(h) Q4γDKQ element, $\alpha = 10^{-6}$.

(i) Q4γDKQ element, $\alpha = 10^{-4}$.

(j) Q4γDKQ element, $\alpha = 10^{-2}$.

(k) Q4γDKQ element, $\alpha = 10^{0}$.

(l) Q4γDKQ element, $\alpha = 10^{2}$.

Figure B.25: Optimal topologies of corner supported cylinder with single layer material model for various values of α.

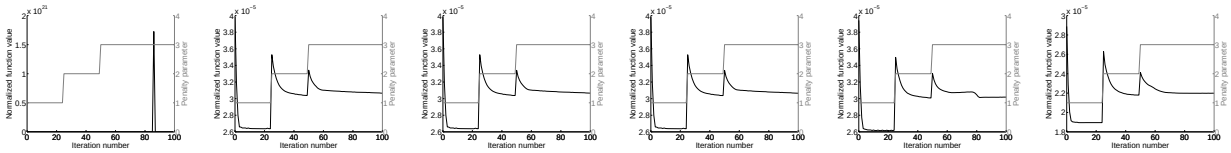

(a) Q4αDKQ element, $\alpha = 0$.

(b) Q4αDKQ element, $\alpha = 10^{-6}$.

(c) Q4αDKQ element, $\alpha = 10^{-4}$.

(d) Q4αDKQ element, $\alpha = 10^{-2}$.

(e) Q4αDKQ element, $\alpha = 10^{0}$.

(f) Q4αDKQ element, $\alpha = 10^{2}$.

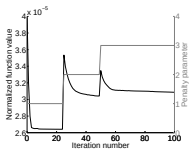

(g) Q4γDKQ element, $\alpha = 0$.

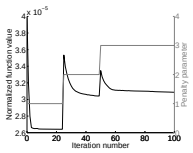

(h) Q4γDKQ element, $\alpha = 10^{-6}$.

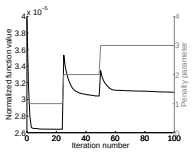

(i) Q4γDKQ element, $\alpha = 10^{-4}$.

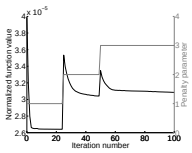

(j) Q4γDKQ element, $\alpha = 10^{-2}$.

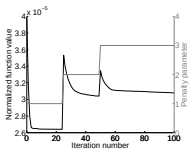

(k) Q4γDKQ element, $\alpha = 10^{0}$.

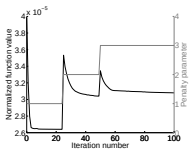

(l) Q4γDKQ element, $\alpha = 10^{2}$.

Figure B.26: Convergence histories for corner supported cylinder with single layer material model for various values of α.

Ribbed material model

Figure B.27 depicts the optimal topologies, as well as the function and constraint values, for the ribbed material model as a function of scaling parameter α. Again, the results for the Q4αDKQ element differ from the Q4γDKQ results at high values of α. Conversely, the optimal topologies calculated using the Q4γDKQ element are relatively insensitive to α.

Figures B.29(a) once again indicate that, with α is set to zero, an unstable convergence history results for the Q4αDKQ element is recorded, although the a 'correct' optimal topology results. Figure B.29(g) confirms that no such problems are encountered when employing the Q4γDKQ element.

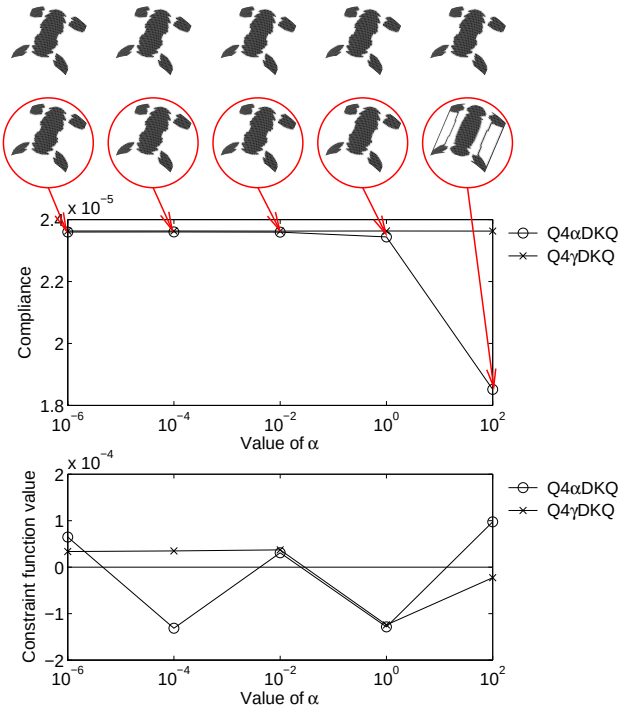

Figure B.27: Optimal topologies of a corner supported cylinder with ribbed material model. Above are the optimal topologies solved employing the standard Q4γDKQ element. On the second row are the optimal topologies employing Q4αDKQ for various values of scaling factor α. Also shown are the optimal function and constraint values for various values of scaling factor α.

(a) Q4αDKQ element, $\alpha = 0$.

(b) Q4αDKQ element, $\alpha = 10^{-6}$.

(c) Q4αDKQ element, $\alpha = 10^{-4}$.

(d) Q4αDKQ element, $\alpha = 10^{-2}$.

(e) Q4αDKQ element, $\alpha = 10^{0}$.

(f) Q4αDKQ element, $\alpha = 10^{2}$.

(g) Q4γDKQ element, $\alpha = 0$.

(h) Q4γDKQ element, $\alpha = 10^{-6}$.

(i) Q4γDKQ element, $\alpha = 10^{-4}$.

(j) Q4γDKQ element, $\alpha = 10^{-2}$.

(k) Q4γDKQ element, $\alpha = 10^{0}$.

(l) Q4γDKQ element, $\alpha = 10^{2}$.

Figure B.28: Optimal topologies of corner supported cylinder with ribbed material model for various values of α.

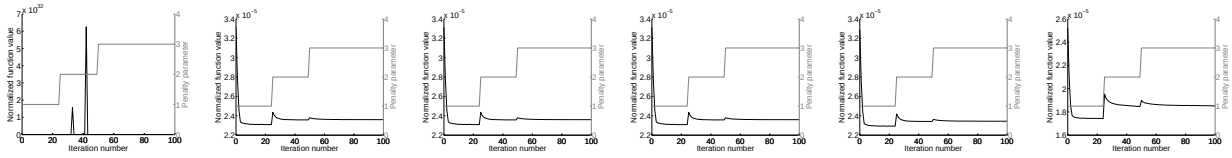

(a) Q4αDKQ element, $\alpha = 0$.

(b) Q4αDKQ element, $\alpha = 10^{-6}$.

(c) Q4αDKQ element, $\alpha = 10^{-4}$.

(d) Q4αDKQ element, $\alpha = 10^{-2}$.

(e) Q4αDKQ element, $\alpha = 10^{0}$.

(f) Q4αDKQ element, $\alpha = 10^{2}$.

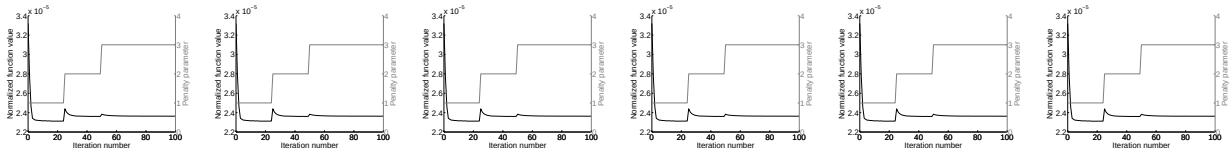

(g) Q4γDKQ element, $\alpha = 0$.

(h) Q4γDKQ element, $\alpha = 10^{-6}$.

(i) Q4γDKQ element, $\alpha = 10^{-4}$.

(j) Q4γDKQ element, $\alpha = 10^{-2}$.

(k) Q4γDKQ element, $\alpha = 10^{0}$.

(l) Q4γDKQ element, $\alpha = 10^{2}$.

Figure B.29: Convergence histories for corner supported cylinder with ribbed material model for various values of α.

Honeycomb material model

Finally, the optimal topologies for the honeycomb material model, are presented in Figure B.30. Again, the sensitivity of optimal topologies using Q4αDKQ elements is highlighted, in contrast to the Q4γDKQ element. Figure B.32(a) shows that although the optimal topology of the Q4αDKQ element corresponds to that using Q4γDKQ elements, some numerical instabilities are once again encountered when $\alpha = 0$ in the Q4αDKQ element.

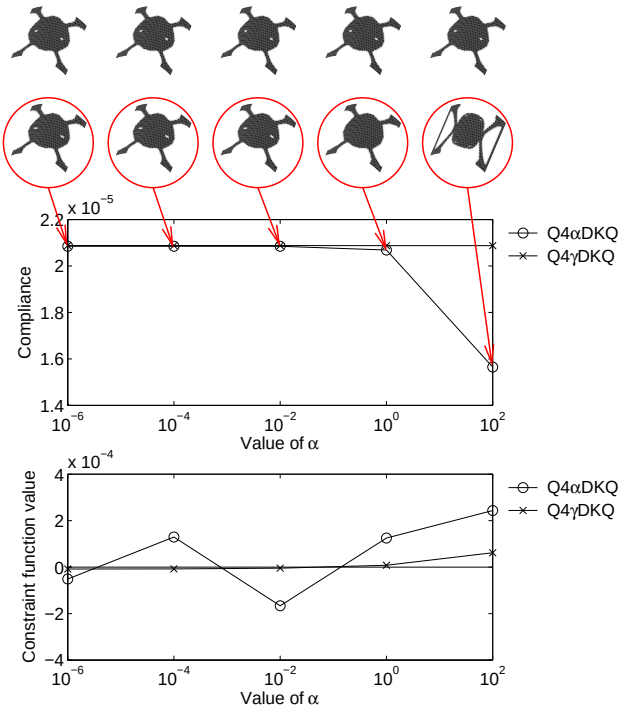

Figure B.30: Optimal topologies of a corner supported cylinder with honeycomb material model. Above are the optimal topologies solved employing the standard Q4γDKQ element. On the second row are the optimal topologies employing Q4αDKQ for various values of scaling factor α. Also shown are the optimal function and constraint values for various values of scaling factor α.

B.3.2 Pretwisted beam

The final shell example is depicted in Figure 6.17. The problem is that of a pretwisted beam, which is clamped at the root, with two point loads applied at the vertices opposite the fixed end. The full geometry is modeled with a 40×40 discretization. A volume constraint of half of the design volume is imposed. For brevity, only the single layer results will be presented. This problem has previously been shown to be sensitive to the value of α [135].

For this problem, the range of values of α for which the Q4αDKQ and Q4γDKQ elements result in similar topologies is much smaller than the cylindrical shell problem. In fact, Figure B.33 shows that values of $\alpha = 0,\ 10^{-6},\ 10^{-4}$ and 10^{-2}, each result in different topologies when

the finite element model employs Q4αDKQ elements! In contrast, the Q4γDKQ element is once again shown to be stable for all tested values of α.

Single layer material model

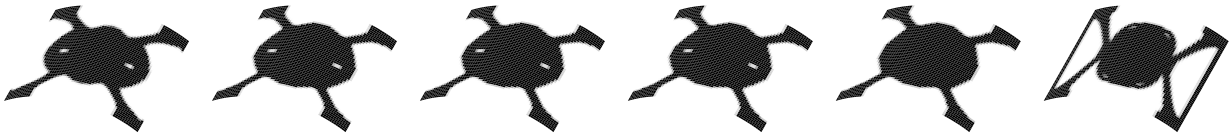

(a) Q4αDKQ element, $\alpha = 0$.

(b) Q4αDKQ element, $\alpha = 10^{-6}$.

(c) Q4αDKQ element, $\alpha = 10^{-4}$.

(d) Q4αDKQ element, $\alpha = 10^{-2}$.

(e) Q4αDKQ element, $\alpha = 10^{0}$.

(f) Q4αDKQ element, $\alpha = 10^{2}$.

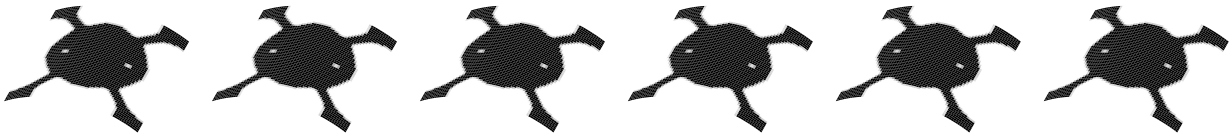

(g) Q4γDKQ element, $\alpha = 0$.

(h) Q4γDKQ element, $\alpha = 10^{-6}$.

(i) Q4γDKQ element, $\alpha = 10^{-4}$.

(j) Q4γDKQ element, $\alpha = 10^{-2}$.

(k) Q4γDKQ element, $\alpha = 10^{0}$.

(l) Q4γDKQ element, $\alpha = 10^{2}$.

Figure B.31: Optimal topologies of corner supported cylinder with honeycomb material model for various values of α.

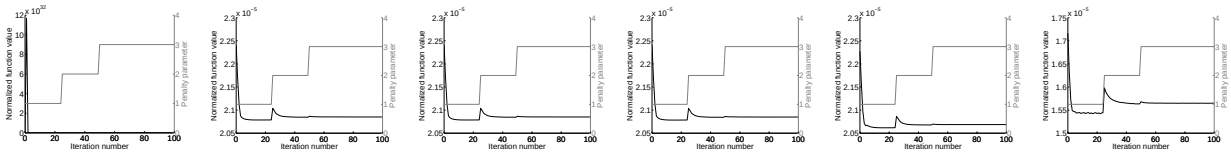

(a) Q4αDKQ element, $\alpha = 0$.

(b) Q4αDKQ element, $\alpha = 10^{-6}$.

(c) Q4αDKQ element, $\alpha = 10^{-4}$.

(d) Q4αDKQ element, $\alpha = 10^{-2}$.

(e) Q4αDKQ element, $\alpha = 10^{0}$.

(f) Q4αDKQ element, $\alpha = 10^{2}$.

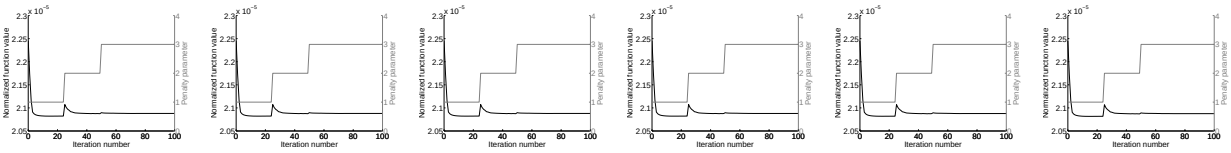

(g) Q4γDKQ element, $\alpha = 0$.

(h) Q4γDKQ element, $\alpha = 10^{-6}$.

(i) Q4γDKQ element, $\alpha = 10^{-4}$.

(j) Q4γDKQ element, $\alpha = 10^{-2}$.

(k) Q4γDKQ element, $\alpha = 10^{0}$.

(l) Q4γDKQ element, $\alpha = 10^{2}$.

Figure B.32: Convergence histories for corner supported cylinder with honeycomb material model for various values of α.

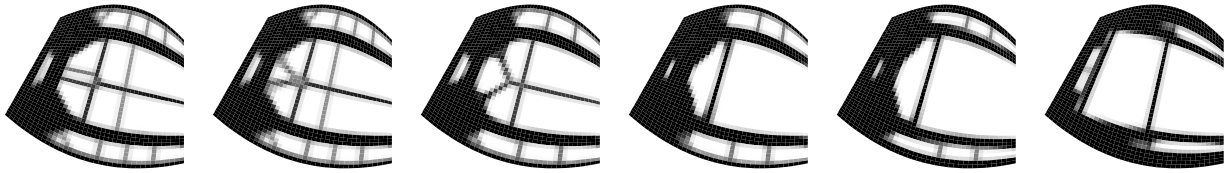

(a) Q4αDKQ element, $\alpha = 0$.

(b) Q4αDKQ element, $\alpha = 10^{-6}$.

(c) Q4αDKQ element, $\alpha = 10^{-4}$.

(d) Q4αDKQ element, $\alpha = 10^{-2}$.

(e) Q4αDKQ element, $\alpha = 10^{0}$.

(f) Q4αDKQ element, $\alpha = 10^{2}$.

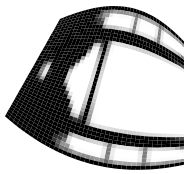

(g) Q4γDKQ element, $\alpha = 0$.

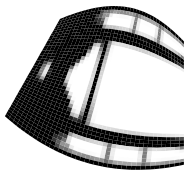

(h) Q4γDKQ element, $\alpha = 10^{-6}$.

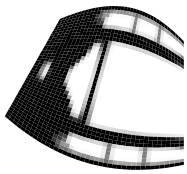

(i) Q4γDKQ element, $\alpha = 10^{-4}$.

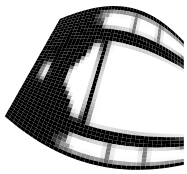

(j) Q4γDKQ element, $\alpha = 10^{-2}$.

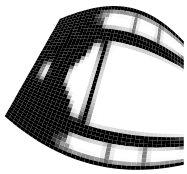

(k) Q4γDKQ element, $\alpha = 10^{0}$.

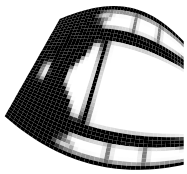

(l) Q4γDKQ element, $\alpha = 10^{2}$.

Figure B.33: Optimal topologies of pretwisted beam with single layer material model for various values of α.

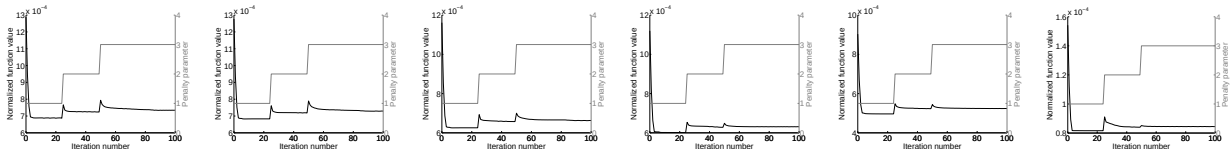

(a) Q4αDKQ element, $\alpha = 0$.

(b) Q4αDKQ element, $\alpha = 10^{-6}$.

(c) Q4αDKQ element, $\alpha = 10^{-4}$.

(d) Q4αDKQ element, $\alpha = 10^{-2}$.

(e) Q4αDKQ element, $\alpha = 10^{0}$.

(f) Q4αDKQ element, $\alpha = 10^{2}$.

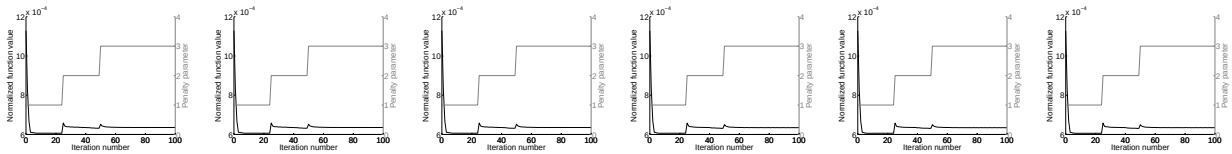

(g) Q4γDKQ element, $\alpha = 0$.

(h) Q4γDKQ element, $\alpha = 10^{-6}$.

(i) Q4γDKQ element, $\alpha = 10^{-4}$.

(j) Q4γDKQ element, $\alpha = 10^{-2}$.

(k) Q4γDKQ element, $\alpha = 10^{0}$.

(l) Q4γDKQ element, $\alpha = 10^{2}$.

Figure B.34: Convergence histories for pretwisted beam with single layer material model for various values of α.